Université du Luxembourg
Faculté des Sciences, de la Technologie et de la Communication

THÈSE

en vue de l'obtention du grade académique de

DOCTEUR DE L'UNIVERSITÉ DU LUXEMBOURG

EN SCIENCES DE L'INGÉNIEUR

par

Claude HOSTERT
né le 4 mars 1974 à Luxembourg

USE OF COMMERCIAL SIMULATION SOFTWARE FOR ANALYZING THE DYNAMICS OF AN INJECTION-MOLDING CLAMP UNIT

PhD-FSTC-0601

Jury de thèse

Dr Stefan MAAS, directeur de thèse
Professeur, Université du Luxembourg

Dr Raymond FREYMANN
Geschäftsführer BMW Group Forschung und Technik, München
Professeur honoraire, Technische Universität München

Dr Massimo MALVETTI, président
Professeur, Université du Luxembourg

Dr Rainer NORDMANN
Professeur, Technische Universität Darmstadt

Dr Arno ZÜRBES, président suppléant
Professeur, Université du Luxembourg

Date de la soutenance : Mercredi 6 septembre 2006
Lieu de la soutenance : Luxembourg

Je déclare sur l'honneur que cette thèse est le fruit de mon travail personnel et que la liste des moyens auxiliaires indiquée est exhaustive. Aucune partie de cette thèse n'a fait l'objet d'une soutenance antérieure.

Luxembourg, le

(signature)

Acknowledgements

I would like to express my gratitude to my supervisors Prof. Stefan Maas and Prof. Rainer Nordmann for their expertise and guidance throughout the thesis. I would also like to thank Prof. Arno Zürbes for his assistance at all levels of the research project.

I am very grateful to all the people of the University of Luxembourg, who directly or indirectly gave me support during the project. A special thank goes out to Guy Baum, Gilbert Klein, Guy Reichert and the SIU guys for their technical help.

I must also acknowledge Pierre Glaesener, Bernd Hardy and Harald Kollmeier for their useful comments or criticisms and for their contributions to this work. And I also not forget all the other people at HUSKY who provided me with all the necessary information and support.

I recognize that this research project would not have been possible without the scholarship of the Ministry of Culture, Higher Education and Research and the financial assistance of HUSKY and the University of Luxembourg.

And most of all, I would like to thank my parents for the moral and financial support they provided me during the last four years.

Table of Contents

1 Introduction

1.1 Mechatronic Systems Simulation

Basically, mechatronics is the combination of mechanical, electronic and controls engineering during the design or optimization process of a product in order to achieve the best balance between the mechanical system and its controls. If these subsystems are often treated independently, they are considered here as one system and are simulated and analyzed in a single model. In a more general way, products integrating different kinds of technologies, such hydraulics, pneumatics or those mentioned above, can be referred to as mechatronic systems.

Different approaches are possible for the analysis of hybrid systems. They depend, for example, on the nature of the system to be analyzed, on the required complexity of the model, or simply on the tools available to the engineer. The present work focuses on the implementation of commercial software packages and the combination of these tools for the simulation of mechatronic systems. These programs, developed for a specific field of application, allow the modeling of complex and nonlinear phenomena. They can be linked among each other and make integrated analyses possible. This approach becomes more and more feasible and makes its way into more common engineering applications due to the constant development of these tools and of more performing computer hardware. The software has been implemented and coupled at the University of Luxembourg and the resulting interdisciplinary tool has been applied to the dynamic simulation of the Quadloc™ clamp unit of an Husky injection molding machine.

The case studies presented in chapter 3, 4 and 5 show the potentials of such an integrated analysis. First of all, it gives a better understanding of the dynamic characteristics of the overall system. Then, the interactions between different subsystems, generally difficult to assess, can be investigated. Furthermore, the model allows to simulate with various design parameters and to predict the effect of modifications to these parameters on the performance of the overall system. All this is very helpful in order to work out improvements and is generally faster and cheaper than proceeding experimentally. Such a simulation is also a valuable tool in early design stages as it can serve as a fast method of evaluating different designs to meet the specified objectives and reduce the cost of prototyping.

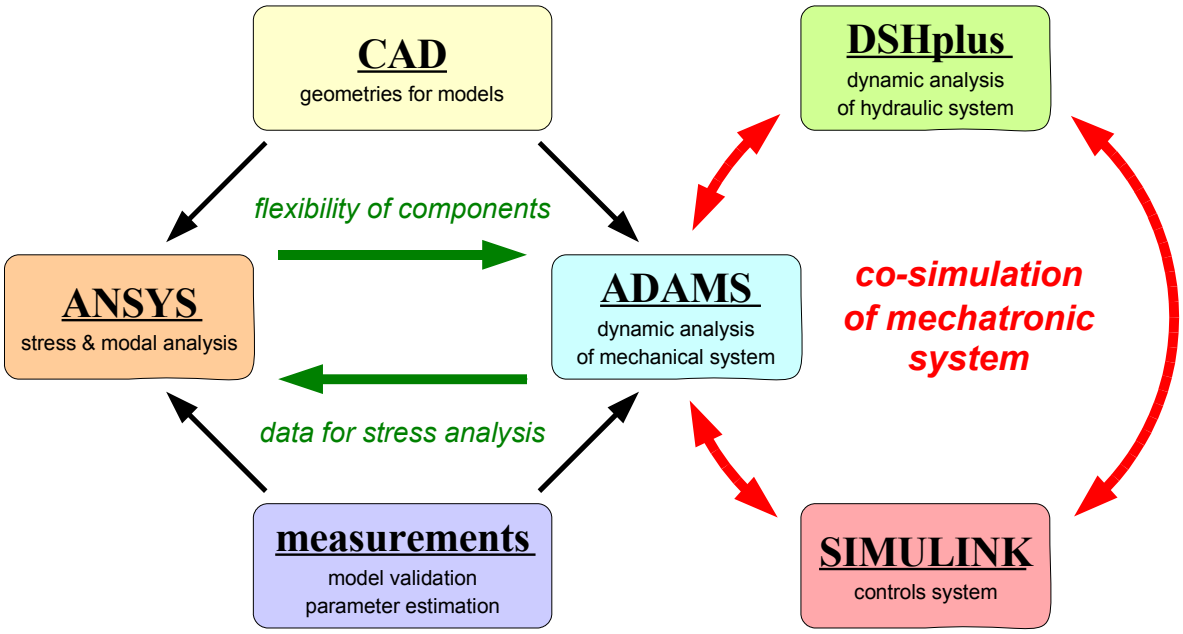

Figure 1-1: Simulation of clamp unit

Figure 1-1 shows the setup of the interdisciplinary simulation tool.[1] The Multi Body Simulation (MBS) software ADAMS, the Fluid Power Simulation (FPS) software DSHplus and the controls design tool SIMULINK are coupled for the dynamic simulation of the clamp unit. The Finite Element (FE) program ANSYS is primarily used to generate FE models that can be included in the MBS model in order to account for the flexibility of the structure if necessary. To "quickly and easily" generate these FE or MBS models, existing 3D CAD geometries are used. A more detailed presentation of the programs, the underlying theories and their coupling can be found in chapter 2. Finally, measurements, if available, can be of great help during the set-up of the simulation. They allow to validate the models, for example that the natural frequencies of the FE models correspond to the ones obtained from modal analysis measurements, and to determine and tune unknown parameters, like friction in the mechanical system or flow versus pressure drop characteristics of hydraulic components.

Of course, full complex models, such as flexible MBS models coupled with FPS and controls models, are not systematically generated right from the start. Basically, the more complicate the model is, the longer the computation time takes. Therefore, to begin with it is kept as simple as possible; generally independent mechanical, hydraulic or controls models are first of all created and validated. Then, complexity is added step by step until it reaches the desired accuracy. In this sense, the simulation programs and the co-simulation setup prove to be very flexible. For example, a simple hydraulic model can be easily replaced by a more complicate one without a complete reconfiguration of the co-simulation interface as long as the exchanged input- and output-parameters do not change.

1 The names of the programs implemented at the University of Luxembourg are explicitly mentioned for the sake of clearness. Of course, there exist programs by other software companies that offer similar or identical functionalities [1]. However, as these tools have not been tested, no further statement can be given here.

As stated earlier, different approaches are possible when simulating mechatronic systems. Since ADAMS was not available at the university right from the start, ANSYS was used to perform dynamic analyses. As long as non-linearities were not included in the FE model, relatively short computation times were achieved with the mode superposition method, but as soon as non-linearities were present, the calculation efforts became huge. Another disadvantage was that hydraulic or controls systems could not be directly incorporated into these FE models. On the other hand, flexible mechanical structures with hydraulic and controls systems can be modeled within SIMULINK as presented in [2, 3, 4]. However, the non-linearities due to the large displacement of the moving platen are difficult to represent. In contrary to ANSYS and SIMULINK, ADAMS inherently models such large non-linear motions. Additionally, it is possible to couple ADAMS with DSHplus and SIMULINK and to model the flexibility of the mechanical parts; even though limited compared to ANSYS. When including flexible components, the computation effort stays relatively moderate as through the component mode synthesis method the number of degrees of freedom of the FE model is considerably reduced. Hence, the simulation tool presented in figure 1-1 proved to be very efficient for the dynamic analysis of the clamp unit.

1.2 Injection Molding

1.2.1 Brief Overview

Injection molding is the process of forcing hot melted plastic into a mold cavity. Once the plastic has cooled down and consolidated, the finished part can be ejected. The process is generally used in mass-production and injection molded parts can be found in a wide range of applications, ranging from bottles, yogurt cups and syringes to computer parts, container bins and car bumpers. The beginning of injection molding can be traced back in the 19th century, but its lift off was in the 50th with the introduction of the screw as plasticizing and injection-pressure generating component [5]. In 2003, the consumption of polymers for plastics applications in Western Europe was over 39 million tons which is about 22.2 % of the worldwide plastic consumption. Packaging is the largest consumer of plastics, accounting for 37.2 % of all plastics consumed, followed by the household and domestic industry with 20.1 %, the building and construction industry with 18.5 %, the electrical and electronic industry with 8.5 %, the automotive industry with 8 % and the rest with 7.7 %. In Western Europe, 39 % of the recovered waste is recycled - 23 % through energy recovery and 14 % through mechanical recycling - the rest is incinerated or landfilled [6].

Husky was founded in 1953 - starting to design snowmobiles, thus the company's name - and build its first mold in 1958 and its first injection molding machine in 1961. The company has since specialized in providing integrated system solutions for the plastic industry. Husky engineers and manufactures a comprehensive range of injection molding equipment, including machines, molds, hot runners and robots. Manufacturing facilities are located on

campuses in Canada, the United States, Luxembourg and China. Additionally, over 40 service and sales offices and technical centers exist throughout the world. In fiscal 2004, sales were US$ 774 million, with over 60000 units sold and with approximately 3,000 people employed worldwide [7].

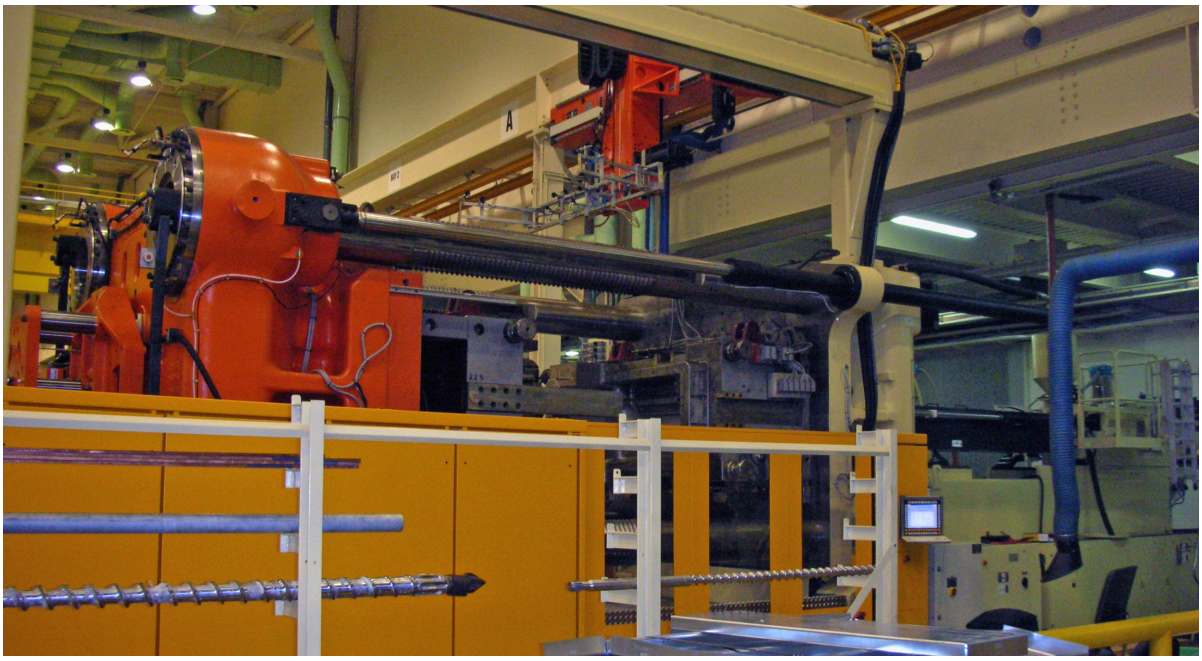

Figure 1-2: Quadloc™ injection molding machine with mold and robot

Basically, an injection molding machine consists of two parts: the injection unit and the clamp unit. The injection unit melts the plastic pellets, injects the material in the mold cavity and keeps it there under pressure. The clamp unit closes and opens the mold and generates the necessary force to keep the mold closed during the injection and holding-pressure phase. This process allows high production rates with repeatable tolerances using a wide range of materials [5]. The process can be broken down into 5 stages:

1. Clamping phase: once the mold is closed, the clamp unit has to generate a force capable of keeping the mold closed during the injection and holding-pressure phase. Different concepts exist which basically can be differentiated if the closing, opening and clamping are done mechanically or hydraulically.

2. Injection phase: the plastic pellets, loaded into a hopper on top of the injection unit, are fed into a heated barrel where the screw is located. Due to the heating and the friction between the pellets during screw rotation, the plastic is melted and homogenized. During this process, the screw conveys the material to the front of the injection. The pressure built-up at the nozzle pushes back the screw. When enough material is accumulated, the rotation stops and the injection process begins. The screw is then pushed forward and the plastic is injected into the mold (see figure 1-3). For some applications, two-stage injection units are used. Here the melted homogenized material is transferred from the screw to a plunger that injects the plastic.

3. Holding-pressure phase: after the injection process, a pressure is applied to make sure that all of the mold cavities are filled. The magnitude and duration of the holding-pressure have a major impact on the quality of the part.

4. Cooling phase: the plastic is allowed to cool and solidify within the mold. This may take a split of a second or several minutes depending on the size of the part.

5. Ejection phase: finally the mold is opened and rods eject the finished parts from the mold.

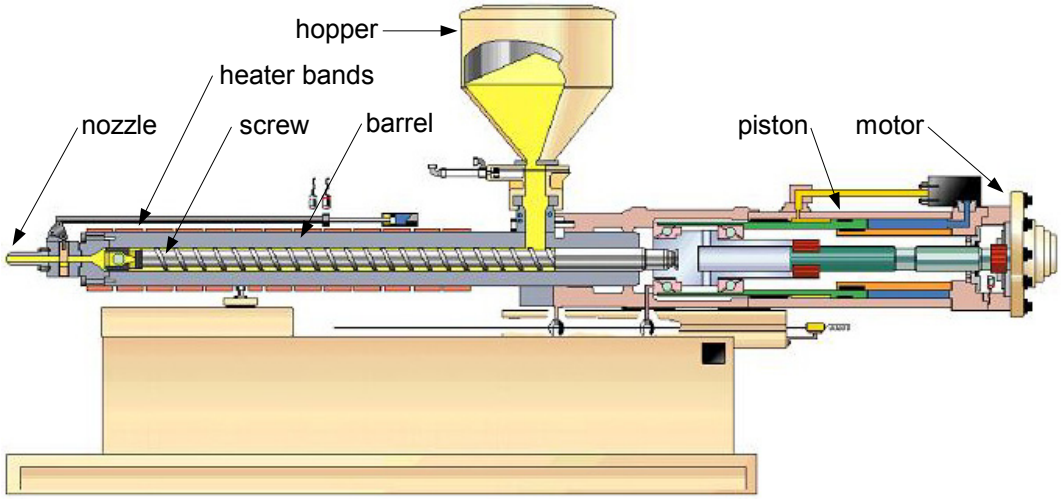

Figure 1-3: Injection unit

This very general description should only give a brief overview to the reader, for more details please refer to [5].

1.2.2 Quadloc™ Clamp Unit

Next to the PET systems and the Hylectric™, Husky offers the Quadloc™ clamp unit which is dedicated to large tonnage molding operations like for example in the automotive industry. It is available from the size Q1350 to Q5400 with a clamping force reaching from 13500 kN to 54000 kN, respectively. The machine is entirely engineered and assembled in Luxembourg [8].

The Quadloc™ clamp unit (see figure 1-4) has a two-platen concept: a stationary platen and a moving platen. The stationary platen is fixed to the clamp base and the moving platen is sliding on the clamp base. It is guided by the latter one and by four columns. These columns, called tie bars, are fixed to the stationary platen via the tie bar nuts and the retaining plates. The moving platen stroke is realized with two hydraulic cylinders that are fixed between both platens. Once the mold is closed, the moving platen is locked mechanically to the tie bars through a bayonet system. In fact, four pistons, which are integrated in the moving platen, are rotated by 45° to engage the tie bar teeth. Mechanical linkages allow the simultaneous rotation of the clamp pistons by the use of a single hydraulic cylinder, called the clamp locking mechanism.

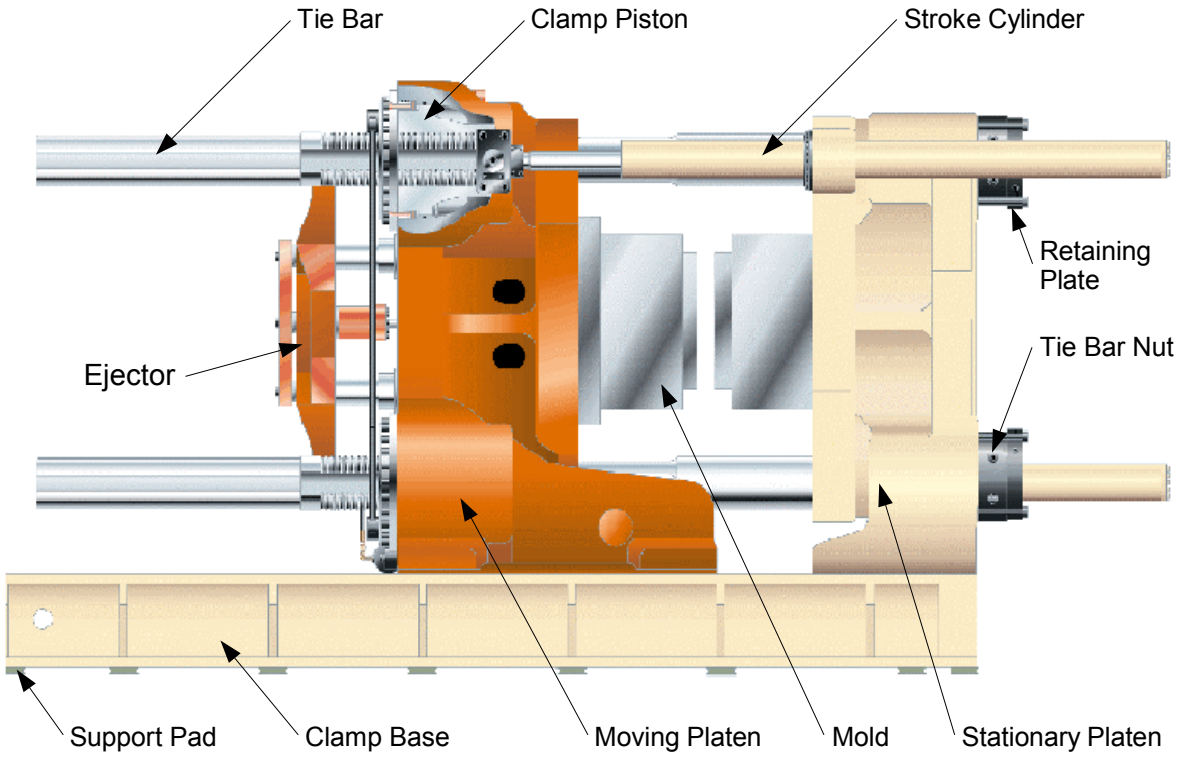

Figure 1-4: Quadloc™ clamp unit

Once the moving platen is locked, hydraulic oil is pumped in the cavity between the clamp piston and the moving platen in order to generate the necessary clamping force. After the cooling phase, the hydraulic pressure is released and the pistons are retracted and disengaged for the mold to open (see figure 1-5). Finally, the part is extracted with the ejector. The spacing of the tie bar teeth and the possible clamp piston stroke within the moving platen, allow an infinite adjustment of the shutheight.

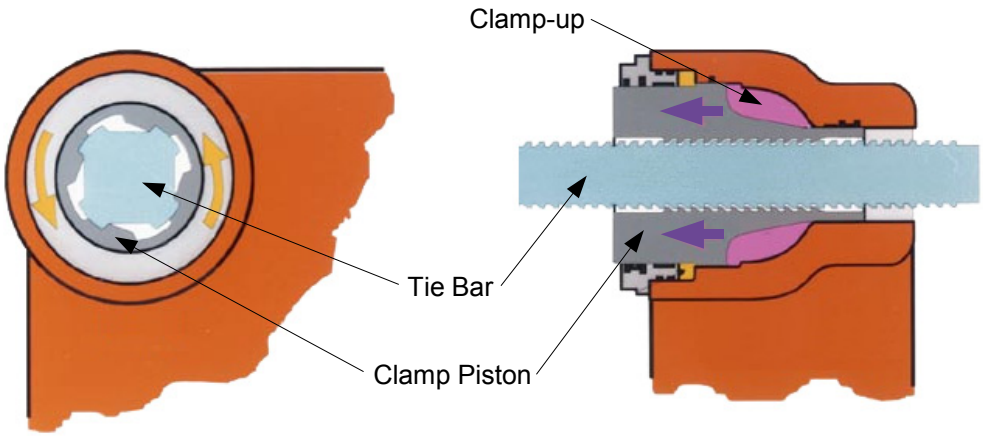

Figure 1-5: Quadloc™ locking and clamping function

As can be noticed all the main functions of the clamp unit are actuated hydraulically: the moving platen stroke, the clamping, the clamp piston rotation and the part ejection. Hydraulic systems present some clear advantages: their high power density, their compact design and their controllability. Furthermore, their power can be easily transformed in linear motion, they

allow a step-less adjustment of force and speed and are suitable for quick and for slow sequences of movement. Their main disadvantage is the total energy efficiency that is not always satisfying. Therefore, the hydraulic drive technology faces more and more the competition from electrical drive solution; generally having a better overall efficiency but being more expensive [9]. The Quadloc™ has an electrohydraulic drive unit that consists of an electric motor driving several variable displacement pumps. To control the flow rate, the flow direction and the pressure level, different types of valves are combined. They are actuated electromechanically by the controls system.

There were several issues with the clamp unit that Husky wanted to be investigated with the help of the mechatronic simulation. First, a cheaper solution for the clamp locking mechanism should be developed (see chapter 3). For the current design, the connecting bars (see figure 3-1) are manufactured from a single piece in order to accommodate the forces acting on the bars during locking and unlocking. This solution is however very expensive. The aim of the simulation is to find any means to reduce these forces and to replace the current design by a welding construction which should be much cheaper. Second, the moving platen stroke, and thus the overall cycle time of the machine, should be reduced (see chapter 4). Here, the focus is on the optimization of the control system in order to gain some time during the acceleration and deceleration phase of the moving platen. Third, possible root sources for machine creeping under operation should be found (see chapter 5). In fact, in order to prevent any displacement relative to the ground of the complete injection molding machine during operation, it is simply bolted to the ground at the clamp unit end. The interest is to determine under which conditions such a displacement becomes possible.

In order to investigate this three issues, the Quadloc™ clamp unit was modeled and analyzed with the interdisciplinary simulation tool presented in section 1.1. Several concrete improvements could be elaborated. During the analyses, the focus was on the Q2700 clamp unit as it is a mid-size machine that is relatively often sold and therefore should be normally available for measurements. The Q2700 has a maximum clamping force of 27000 kN. Its overall dimensions are approximately 6 m x 4 m x 4 m and its weight is about 130 tons - the moving platen having 65 tons. The machine has a mold shutheight of 1000 mm up to 1900 mm, and a maximum daylight of 3900 mm. The tie bar spacing is 2150 mm x 1700 mm. The Euromap-6 dry-cycle time[2] of the Q2700 is 8.0 seconds for an opening stroke of 1505 mm.

2 EUROMAP is the European committee of several national associations of plastics and rubber machinery manufacturers. It has elaborated some technical recommendations such as the EUROMAP 6 that defines the determination of the duration of the dry cycle for comparison reasons. During the dry cycle, the machine is operated without injection of plastic. The cycle time comprises mold closing, application of 70% of maximum clamping force, mold opening and all idle times such as locking and unlocking.

2 Simulation Software

In this chapter the three simulation tools mentioned in section *1.1* are presented in more details, with the focus lying on the multi-body system simulation software. At the end of the chapter, the set-up of the co-simulation for these particular programs is briefly explained.

2.1 MBS Software

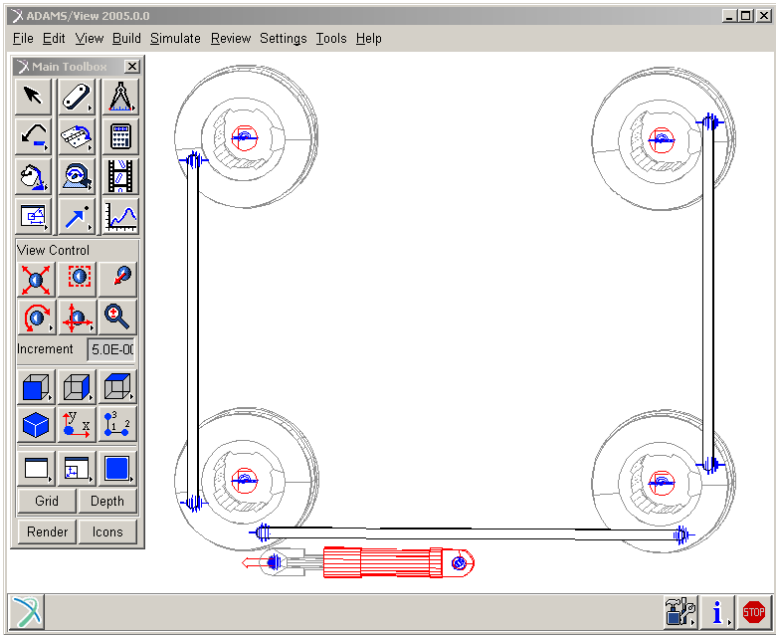

Figure 2-1: ADAMS

A MBS program allows the user to simulate the kinematics and dynamics of mechanical systems. Generally, the different components are modeled as rigid bodies - which means that their shape remains unchanged when forces are applied to them. Joints, gears or couplers connect the rigid bodies in order to define the motion of one component with respect to another one. Additionally, forces, motions and non-linear phenomena, such as contact or friction, can be added to the model. Afterwards, the user performs simulations to investigate the characteristics of the mechanical system. The program computes the forces and moments acting on the joints, the position, velocity and acceleration of the parts or any other user-defined parameters. Finally, the results are animated and plotted for analysis.

Furthermore, the employed software ADAMS gives the user the possibility to incorporate non-standard phenomena into the model by linking user-written subroutines to the solver.

Numerous plug-ins are also available that allow, for example, to model hydraulic, pneumatic and controls systems, or to perform modal, vibration and durability analyses. Other add-ons are tailored to the needs of specific fields of application such as the aerospace or the automobile industry. An interesting feature in this context is an add-on that allows to account for the flexibility of parts in the MBS model. The deformation is then written as a linear combination of mode shapes obtained from a finite element model. The underlying theories are exposed in the following sections where the development of the different formulas is mainly based on [10].

2.1.1 Rigid-Body Dynamics

2.1.1.1 Rigid-Body Kinematics

Figure 2-2 shows a rigid body in space. The coordinate system *XYZ* is fixed in time and serves as a reference for all bodies in the system. It is referred to as the global frame or the inertial frame of reference. The coordinate system *X'Y'Z'* is rigidly fixed to a point on the rigid body. It is referred to as the local frame or the body frame of reference. The configuration of a rigid body in space is completely defined by six independent coordinates: three coordinates that describe the location of the origin of the local coordinate system in the global coordinate system, and three coordinates that describe the orientation of the local coordinate system with respect to the global coordinate system.

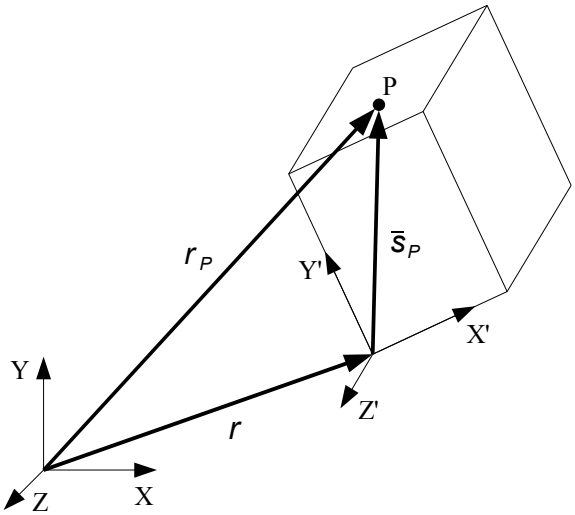

Figure 2-2: Rigid body positioning

The global position of an arbitrary point *P* on the rigid body can be written as

$$\boldsymbol{r}_P = \boldsymbol{r} + \boldsymbol{A} \cdot \bar{\boldsymbol{s}}_P \tag{2-1}$$

where $\boldsymbol{r}$ is the position of the origin of the selected body reference *X'Y'Z'*, $\boldsymbol{A}$ is the transformation matrix from the local coordinate system to the global coordinate system and $\bar{\boldsymbol{s}}_P$ is the vector of coordinates of point *P* in the body reference *X'Y'Z'*.

The transformation matrix $\boldsymbol{A}$, also called rotation matrix, can be represented in terms of

different parameters. One common way are the three Euler angles that involve three successive rotations about three axes. Again, these successive rotations are not unique and the most widely used set, commonly denoted (3-1-3) which stands for the rotation sequence, is shown in figure 2-3. For this particular set of Euler angles, the initial system of axes *xyz* is rotated by an angle ψ about the axis *z*. Then, the resultant axes *x′y′z′* are rotated about the axis *x′* by an angle θ. The new intermediate axes *x″y″z″* are finally rotated by an angle ϕ about the axis *z″* to get the *x‴y‴z‴* axes that correspond to the desired final system of axes.

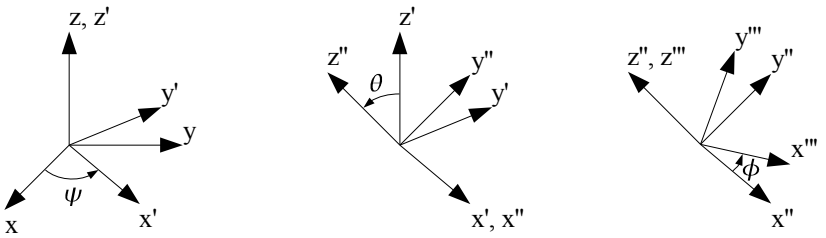

Figure 2-3: (3-1-3) Euler angles set

The transformation matrix $\boldsymbol{D}_1$ from the coordinate system *xyz* to *x′y′z′* is

$$\boldsymbol{D}_1=\begin{bmatrix}\cos\psi & \sin\psi & 0\\ -\sin\psi & \cos\psi & 0\\ 0 & 0 & 1\end{bmatrix} \tag{2-2}$$

It can be easily shown that $\boldsymbol{D}_1$ is orthogonal, which means that $\boldsymbol{D}_1\cdot\boldsymbol{D}_1^T=\boldsymbol{I}$ and $\boldsymbol{D}_1^{-1}=\boldsymbol{D}_1^T$. The same is true for the transformation matrices from *x′y′z′* to *x″y″z″* and *x″y″z″* to *x‴y‴z‴*, which are respectively

$$\boldsymbol{D}_2=\begin{bmatrix}1 & 0 & 0\\ 0 & \cos\theta & \sin\theta\\ 0 & -\sin\theta & \cos\theta\end{bmatrix} \tag{2-3}$$

$$\boldsymbol{D}_3=\begin{bmatrix}\cos\phi & \sin\phi & 0\\ -\sin\phi & \cos\phi & 0\\ 0 & 0 & 1\end{bmatrix} \tag{2-4}$$

As the transpose and the inverse of an orthogonal matrix and the product of two orthogonal matrices yield an orthogonal matrix, the transformation matrix $\boldsymbol{A}$ from the coordinate system *x‴y‴z‴* to *xyz* is also orthogonal. It can be derived from

$$\boldsymbol{A}=\boldsymbol{D}_1^T\cdot\boldsymbol{D}_2^T\cdot\boldsymbol{D}_3^T \tag{2-5}$$

Equations (2-2) through (2-5) lead to the expression of $\boldsymbol{A}$, that is

$$\boldsymbol{A}=\begin{bmatrix}\cos\psi\cdot\cos\phi-\sin\psi\cdot\sin\phi\cdot\cos\theta & -\cos\psi\cdot\sin\phi-\sin\psi\cdot\cos\phi\cdot\cos\theta & \sin\psi\cdot\sin\theta\\ \sin\psi\cdot\cos\phi+\cos\psi\cdot\sin\phi\cdot\cos\theta & -\sin\psi\cdot\sin\phi+\cos\psi\cdot\cos\phi\cdot\cos\theta & -\cos\psi\cdot\sin\theta\\ \sin\phi\cdot\sin\theta & \cos\phi\cdot\sin\theta & \cos\theta\end{bmatrix} \tag{2-6}$$

Thus

$$\boldsymbol{s}_P=\boldsymbol{A}\cdot\bar{\boldsymbol{s}}_P \quad\text{and}\quad \bar{\boldsymbol{s}}_P=\boldsymbol{A}^T\cdot\boldsymbol{s}_P \tag{2-7}$$

where $\boldsymbol{s}_P$ is the vector of coordinates of point *P* written in a reference frame whose origin is coincident with the one of the local reference frame of the body and whose axes are parallel to those of the global reference frame.

Differentiating equation (2-1) with respect to time yields

$$\dot{\boldsymbol{r}}_P = \dot{\boldsymbol{r}} + \dot{\boldsymbol{A}} \cdot \bar{\boldsymbol{s}}_P \tag{2-8}$$

where $\dot{\boldsymbol{r}}_P$ is the absolute velocity of *P* and $\dot{\boldsymbol{r}}$ the absolute velocity of the origin of the body reference frame. As the matrix $\boldsymbol{A}$ is orthogonal, it can be written that

$$\boldsymbol{A}^T \cdot \boldsymbol{A} = \boldsymbol{I} \tag{2-9}$$

The differentiation of equation (2-9) with respect to time yields

$$\dot{\boldsymbol{A}}^T \cdot \boldsymbol{A} + \boldsymbol{A}^T \cdot \dot{\boldsymbol{A}} = \boldsymbol{0} \tag{2-10}$$

which implies that

$$\boldsymbol{A}^T \cdot \dot{\boldsymbol{A}} = -(\boldsymbol{A}^T \cdot \dot{\boldsymbol{A}})^T \tag{2-11}$$

A matrix which is equal to the negative of its transpose is a skew-symmetric matrix[3], thus it can be written that

$$\boldsymbol{A}^T \cdot \dot{\boldsymbol{A}} = \tilde{\bar{\omega}} \tag{2-12}$$

which leads to

$$\dot{\boldsymbol{A}} = \boldsymbol{A} \cdot \tilde{\bar{\omega}} \tag{2-13}$$

$\bar{\omega}$ is defined as being the angular velocity vector of the body reference frame with respect to the global reference frame written in the body coordinate system. Substituting the expression of the transformation matrix $\boldsymbol{A}$ into equation (2-13), $\bar{\omega}$ can be identified as

$$\begin{gathered} \bar{\omega} = \begin{bmatrix} \sin\phi \cdot \sin\theta \cdot \dot{\psi} + \cos\phi \cdot \dot{\theta} \\ \cos\phi \cdot \sin\theta \cdot \dot{\psi} - \sin\phi \cdot \dot{\theta} \\ \cos\theta \cdot \dot{\psi} + \dot{\phi} \end{bmatrix} \Rightarrow \\ \bar{\omega} = \begin{bmatrix} \sin\phi \cdot \sin\theta & \cos\phi & 0 \\ \cos\phi \cdot \sin\theta & -\sin\phi & 0 \\ \cos\theta & 0 & 1 \end{bmatrix} \cdot \begin{bmatrix} \dot{\psi} \\ \dot{\theta} \\ \dot{\phi} \end{bmatrix} = \boldsymbol{B} \cdot \dot{\boldsymbol{\varepsilon}} \end{gathered} \tag{2-14}$$

Finally, substituting equation (2-13) into equation (2-8) yields the expression for the absolute velocity vector of *P*, which is

$$\dot{\boldsymbol{r}}_P = \dot{\boldsymbol{r}} + \boldsymbol{A} \cdot \tilde{\bar{\omega}} \cdot \bar{\boldsymbol{s}}_P \quad \text{or} \quad \dot{\boldsymbol{r}}_P = \dot{\boldsymbol{r}} + \boldsymbol{A} \cdot (\bar{\omega} \times \bar{\boldsymbol{s}}_P) \tag{2-15}$$

Differentiating equation (2-15) with respect to time yields the absolute acceleration of *P*, that is

$$\ddot{\boldsymbol{r}}_P = \ddot{\boldsymbol{r}} + \dot{\boldsymbol{A}} \cdot \tilde{\bar{\omega}} \cdot \bar{\boldsymbol{s}}_P + \boldsymbol{A} \cdot \dot{\tilde{\bar{\omega}}} \cdot \bar{\boldsymbol{s}}_P \tag{2-16}$$

Using equation (2-13), equation (2-16) becomes

3 It can be shown that

$$\vec{a} \times \vec{b} = \begin{bmatrix} 0 & -a_z & a_y \\ a_z & 0 & -a_x \\ -a_y & a_x & 0 \end{bmatrix} \cdot \vec{b} = \tilde{\boldsymbol{a}} \cdot \vec{b} = -\tilde{\boldsymbol{b}} \cdot \vec{a}$$

where $\tilde{\boldsymbol{a}}$ and $\tilde{\boldsymbol{b}}$ are called skew-symmetric matrices and $\sim$ is the skew-symmetric operator.

$$\ddot{\boldsymbol{r}}_P=\ddot{\boldsymbol{r}}+\boldsymbol{A}\cdot\tilde{\bar{\boldsymbol{\omega}}}\cdot\tilde{\bar{\boldsymbol{\omega}}}\cdot\bar{\boldsymbol{s}}_P+\boldsymbol{A}\cdot\tilde{\bar{\boldsymbol{\alpha}}}\cdot\bar{\boldsymbol{s}}_P \quad \text{or} \quad \ddot{\boldsymbol{r}}_P=\ddot{\boldsymbol{r}}+\boldsymbol{A}(\bar{\boldsymbol{\omega}}\times(\bar{\boldsymbol{\omega}}\times\bar{\boldsymbol{s}}_P))+\boldsymbol{A}\cdot(\bar{\boldsymbol{\alpha}}\times\bar{\boldsymbol{s}}_P) \tag{2-17}$$

where $\ddot{\boldsymbol{r}}_P$ is the absolute acceleration vector of *P*, $\ddot{\boldsymbol{r}}$ the absolute acceleration of the origin of the body reference frame and $\bar{\boldsymbol{\alpha}}$ the angular acceleration vector of the body reference frame with respect to the global reference frame.

Equation (2-14) shows that the matrix ***B*** becomes singular if $\theta=0$ or $\theta=\pi$. This means that singularities may occur at certain orientations of the body in space when Euler angles are used. Thus, special provisions must be made within the program to avoid these configurations. Another possibility would be to choose another set of parameters to define the transformation matrix ***A***. In fact, there exist different possible representations, as for example the Euler parameters as shown in [10], that do not present this disadvantage. The relationship between the Euler angles (ψ,θ,ϕ) and the Euler parameters ($\theta_0,\theta_1,\theta_2,\theta_3$) is

$$\begin{aligned}\theta_0&=\cos\frac{\theta}{2}\cdot\cos\frac{\phi+\psi}{2}, & \theta_1&=\sin\frac{\theta}{2}\cdot\cos\frac{\psi-\phi}{2}\\ \theta_2&=\sin\frac{\theta}{2}\cdot\sin\frac{\psi-\phi}{2}, & \theta_3&=\cos\frac{\theta}{2}\cdot\sin\frac{\psi+\phi}{2}\end{aligned} \tag{2-18}$$

In the case of Euler parameters, the configuration of a rigid body in space is defined by seven coordinates: three coordinates that describe the location of the origin of the local coordinate system and four coordinates that describe the orientation of the local coordinate system. However, these seven coordinates are not independent anymore as the Euler parameters have to satisfy the additional relationship

$$\theta_0^2+\theta_1^2+\theta_2^2+\theta_3^2=1 \tag{2-19}$$

The previous equations and the properties of the transformation matrix are irrespective of the set of rotational coordinates used. As the Euler angles are implemented in ADAMS, they will be used in the following. Henceforth, the set of generalized rigid-body coordinates that describes the configuration of a rigid body *i* in space is defined by the vector $\boldsymbol{q}^i$, which is

$$\boldsymbol{q}^i=\left[\boldsymbol{r}^{iT}\quad\boldsymbol{\varepsilon}^{iT}\right]^T=\left[x^i\quad y^i\quad z^i\quad\psi^i\quad\theta^i\quad\phi^i\right]^T \tag{2-20}$$

2.1.1.2 Constraint Equations

Each MBS software has an exhaustive library of constraints that define the absolute position and orientation of bodies in space or the relative position and orientation between two bodies in order to describe the motion of the complete mechanical system.

The multi-body system shown in figure 2-4 consists of 2 rigid bodies. To each body, with its local reference frame *X'Y'Z'*, is attached a second joint definition frame *X''Y''Z''* at point *P*. Additionally, the unit vectors ***a***, ***b*** and ***c*** are defined along the axes of *X''*, *Y''* and *Z''*, respectively, and expressed in the global coordinate system. The superscripts *i* and *j* are used to distinguish between the two bodies and their respective local frame, joint frame and unit vectors. In this example, it is assumed that P^i and P^j and $X''^iY''^iZ''^i$ and $X''^jY''^jZ''^j$ are

initially coincident.

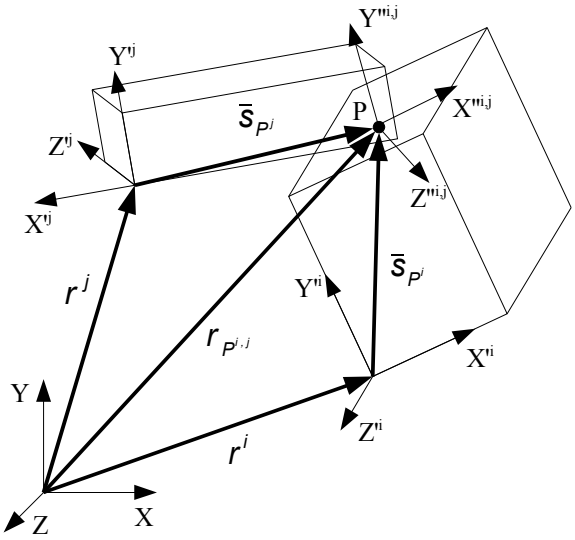

Figure 2-4: Multi-body system

A necessary and sufficient condition that two vectors on body *i* and *j* are orthogonal is that their scalar product is zero. For example if axes *X''ⁱ* and *Y''ʲ* should remain orthogonal then the constraint C_{orth} can be defined as

$$C_{orth}(\boldsymbol{a}^i, \boldsymbol{b}^j) \equiv \boldsymbol{a}^{iT} \cdot \boldsymbol{b}^j = 0 \tag{2-21}$$

C denotes a constraint and may be made up of one or several algebraic constraint equations that depend on the generalized coordinates of the rigid bodies. If the axes *Z''ⁱ* and *Z''ʲ* should remain parallel, i.e. $\boldsymbol{c}^i$ and $\boldsymbol{c}^j$ parallel, then $\boldsymbol{c}^i$ has to be orthogonal to $\boldsymbol{a}^i$ and $\boldsymbol{b}^i$, which leads to the constraint

$$C_{para}(\boldsymbol{c}^i, \boldsymbol{c}^j) \equiv \begin{cases} \boldsymbol{a}^{iT} \cdot \boldsymbol{c}^j = 0 \\ \boldsymbol{b}^{iT} \cdot \boldsymbol{c}^j = 0 \end{cases} \tag{2-22}$$

If it is required that the two bodies coincide at P^i and P^j, then

$$C_{coin}(P^i, P^j) \equiv (\boldsymbol{r}^i + \boldsymbol{A}^i \cdot \bar{\boldsymbol{s}}_{P^i}) - (\boldsymbol{r}^j + \boldsymbol{A}^j \cdot \bar{\boldsymbol{s}}_{P^j}) = \boldsymbol{0} \tag{2-23}$$

With equation (2-23) the relative rotation of both bodies is still possible. In fact, this constraint represents a spherical joint.

These three primitive constraint equations can also be combined to describe more complex constraints, as for example the revolute joint in figure 2-5. This joint allows the relative rotation between two bodies about one common axis but prohibits any relative translation. In figure 2-5, the center of the joint is located at P^i and P^j and the rotation is about the respective *Y''* axis. The analytical formulation of the joint specifies that P^i and P^j are coincident and that $\boldsymbol{b}^i$ and $\boldsymbol{b}^j$ are parallel. Thus the revolute joint is defined by the constraints

$$C_{coin}(P^i, P^j) \quad \text{and} \quad C_{para}(\boldsymbol{b}^i, \boldsymbol{b}^j) \tag{2-24}$$

Equation (2-24) gives rise to five scalar constraint equations. This means that a revolute joint

has only one degree of freedom (DOF), i.e. the rotation along the *Y''* axis.

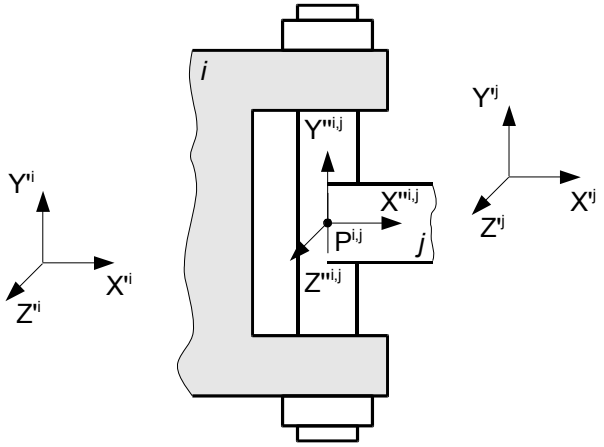

Figure 2-5: Revolute joint

Similar to the revolute joint is the cylindrical joint, except that a relative translation along the rotation axis is allowed. The parallelism condition of $\boldsymbol{b}^i$ and $\boldsymbol{b}^j$ remains, but P^i and P^j do not have to be coincident anymore. If $\boldsymbol{d}^{ij}$ is the distance between P^i and P^j then $\boldsymbol{d}^{ij}$ has to be collinear with $\boldsymbol{b}^i$, which means that

$$C_{para}(\boldsymbol{b}^i, \boldsymbol{b}^j) \quad \text{and} \quad C_{para}(\boldsymbol{b}^i, \boldsymbol{d}^{ij}) \tag{2-25}$$

where $\boldsymbol{d}^{ij}$ is defined as

$$\boldsymbol{d}^{ij} = (\boldsymbol{r}^j + \boldsymbol{A}^j \cdot \bar{\boldsymbol{s}}_{P^j}) - (\boldsymbol{r}^i + \boldsymbol{A}^i \cdot \bar{\boldsymbol{s}}_{P^i}) \tag{2-26}$$

A cylindrical joint has four constraint equations, thus two DOF: a translation and a rotation.

The translational joint can be derived from the cylindrical joint. In this case, the relative rotation is not allowed anymore. An orthogonality condition between $\boldsymbol{a}^i$ and $\boldsymbol{c}^j$ is needed in addition to the constraints of equation (2-25), i.e. the joint is defined by

$$C_{para}(\boldsymbol{b}^i, \boldsymbol{b}^j), \quad C_{para}(\boldsymbol{b}^i, \boldsymbol{d}^{ij}) \quad \text{and} \quad C_{orth}(\boldsymbol{a}^i, \boldsymbol{c}^j) \tag{2-27}$$

The translational joint has again five scalar constraint equations and thus only one DOF.

For the previous constraints, time does not appear explicitly in the equations. It is of course possible to specify a position or an orientation of a body that depends on time. For example, a relative driving constraint may be expressed for the translational joint defined above. It is assumed that the translation occurs along the axis $Y'''^{i,j}$ and that D, which is the distance between P^i and P^j, is time-dependent. In this case, additionally to equation (2-27) is defined the constraint

$$C_{trans} \equiv \boldsymbol{d}^{ij} - D(t) = 0 \tag{2-28}$$

The constraints defined by equations (2-21) through (2-28), are expressed as algebraic equations in terms of generalized coordinates and time and can be written as

$$C(\boldsymbol{q}, t) = \boldsymbol{0} \tag{2-29}$$

Constraints of this form are called holonomic or geometric constraints. Other constraint equations may be defined that contain relations between velocity components that cannot be

integrated and put in the form of equation (2-29). They are called nonholonomic or kinematic constraints and can be written as

$$C(\boldsymbol{q}, \dot{\boldsymbol{q}}, t) = \boldsymbol{0} \tag{2-30}$$

If the constraints of equation (2-29) and (2-30) depend explicitly on time then they are called rheonomic, otherwise they are denoted as scleronomic. Finally, the collection of all the constraints present in a multi-body model is denoted by $\boldsymbol{C}$. In the case of an holonomic system, $\boldsymbol{C}$ assumes the general expression

$$\boldsymbol{C}(\boldsymbol{q}, t) = \begin{bmatrix} C_1(\boldsymbol{q}, t) \\ C_2(\boldsymbol{q}, t) \\ \vdots \\ C_{n_c}(\boldsymbol{q}, t) \end{bmatrix} = \begin{bmatrix} c_1(\boldsymbol{q}, t) \\ c_2(\boldsymbol{q}, t) \\ \vdots \\ c_{n_{ce}}(\boldsymbol{q}, t) \end{bmatrix} = \boldsymbol{0} \tag{2-31}$$

where n_c is the number of constraints, i.e. joints or drivers, in the model and n_{ce} the total number of algebraic constraint equations. Generally, the number of generalized coordinates is larger or equal to the number of algebraic constraint equations. Because of the presence of constraint equations, the generalized coordinates are not independent. For holonomic systems, each constraint equation eliminates one generalized coordinate by writing this coordinate in terms of the others. Therefore, a system with n generalized coordinates has n-n_{ce} independent generalized coordinates, which is also referred to as the number of degrees of freedom of the multi-body system.

However, it is possible to define constraints that cannot be physically satisfied or that are automatically satisfied if the others constraints equations are satisfied. If such constraints exist, then one talks about an inconsistent redundancy or a consistent redundancy respectively. In that case, the constraint Jacobian, defined further below in equation (2-60) and which plays an important role in the numerical solution, becomes singular and no solution exists. Now when modeling complex mechanism, it is easy to implement constraints which seem to be proper but which include redundancies. Therefore, MBS programs include numerical strategies to identify, and if possible to “eliminate”, redundant constraint equations [53].

Prior to a dynamic analysis, a kinematic analysis can be done provided that no unconstrained generalized coordinates remain in the system. The aim of the kinematic analysis is to study only the motion, i.e. position, velocity and acceleration, of the individual components. Forces are not considered as they do not affect the motion. However, reaction forces as a consequence of the motion can be calculated. For holonomic MBS models, the system of equations to solve in a kinematic analysis is

$$\boldsymbol{C}(\boldsymbol{q}, t) = \boldsymbol{0} \tag{2-32}$$

For a complete system, the number of constraint equations must be equal to the number of generalized coordinates. By solving equation (2-32), the positions of the system are

known. Differentiating equation (2-32) with respect to time gives the velocities

$$\frac{\partial \boldsymbol{C}}{\partial q}\dot{\boldsymbol{q}}+\frac{\partial \boldsymbol{C}}{\partial t}=\boldsymbol{0} \tag{2-33}$$

and differentiating equation (2-33) with respect to time gives the accelerations

$$\frac{\partial \boldsymbol{C}}{\partial q}\ddot{\boldsymbol{q}}+\frac{\partial}{\partial t}\left(\frac{\partial \boldsymbol{C}}{\partial q}\right)\dot{\boldsymbol{q}}+\frac{\partial}{\partial t}\left(\frac{\partial \boldsymbol{C}}{\partial t}\right)=\boldsymbol{0} \tag{2-34}$$

Equation (2-32) is generally highly non-linear so that no analytical result can be found. An iterative method is needed to solve for the positions. For this purpose the Newton-Raphson method is used to compute $\boldsymbol{q}$. When the positions are known, the velocities and the accelerations are deduced.

2.1.1.3 Equation of Motion for Rigid Bodies

Lagrange's equation is used to formulate the equation of motion of a multi-body system. For this purpose, the principle of virtual displacements is used and needs to be introduced. In fact, a virtual displacement is defined as an infinitesimal imaginary change of the configuration of a system while time is held fixed. However, this virtual displacement has to be consistent with the boundaries and constraints of the system. Considering first of all a system of n_i particles then, if the configuration of a particle i is defined by the position vector $\boldsymbol{r}^i$, the vector of virtual displacements is denoted by $\delta \boldsymbol{r}^i$. Additionally, $\boldsymbol{F}^i$ is the total effective force vector acting on particle i. Now the principle of virtual displacement states that a system is in equilibrium if the sum of the virtual work of all the forces vanishes, that is if

$$\sum_{i=1}^{n_i}(\boldsymbol{F}^i)^T\cdot\delta\,\boldsymbol{r}^i=0 \tag{2-35}$$

This can also be extended to the dynamic case. As Newton's second law states that the sum of the forces acting on a particle i is equal to the rate of change of momentum of this particle, it can be written that

$$\boldsymbol{F}^i=\dot{\boldsymbol{P}}^i \tag{2-36}$$

where $\boldsymbol{P}^i$ is the momentum of the particle i. Considering the virtual displacement $\delta \boldsymbol{r}^i$ of the particle i, then equation (2-36) can be written as

$$(\dot{\boldsymbol{P}}^i-\boldsymbol{F}^i)^T\cdot\delta\,\boldsymbol{r}^i=0 \tag{2-37}$$

which gives, similar to the principle of virtual displacements, for a system of particles that

$$\sum_{i=1}^{n_i}(\dot{\boldsymbol{P}}^i-\boldsymbol{F}^i)^T\cdot\delta\,\boldsymbol{r}^i=0 \tag{2-38}$$

Equation (2-38) is called D'Alembert's principle. It states that any position of a system in motion can be regarded as an equilibrium position if to the effective forces acting on the system are added the inertia forces. The system can also be regarded to be in a dynamic equilibrium.

If the system has to satisfy a set of constraint equations, then the effective force $\boldsymbol{F}^i$

acting on a particle *i* can be divided into a vector of external forces $\boldsymbol{F}_e^i$ and a vector of constraint forces $\boldsymbol{F}_c^i$. Substituting into equation (2-38) yields

$$\sum_{i=1}^{n_i} (\dot{\boldsymbol{P}}^i - \boldsymbol{F}_e^i)^T \cdot \delta \boldsymbol{r}^i - \sum_{i=1}^{n_i} (\boldsymbol{F}_c^i)^T \cdot \delta \boldsymbol{r}^i = 0 \tag{2-39}$$

Considering that the constraints are workless, for example frictionless joints, then the term with $\boldsymbol{F}_c^i$ in equation (2-39) vanishes. The reasons are that, either the constraint forces do not work as they are perpendicular to the virtual displacements, or they are couples of forces that act along a vector connecting two particles and, according to Newton's third law, these forces are opposite in sign, thus the corresponding virtual work is canceled. Therefore, equation (2-39) becomes

$$\sum_{i=1}^{n_i} (\dot{\boldsymbol{P}}^i - \boldsymbol{F}_e^i)^T \cdot \delta \boldsymbol{r}^i = 0 \tag{2-40}$$

In equation (2-40), the virtual displacements are generally not independent because of the constraint equations. Therefore, it is not possible to write that each coefficient of $(\dot{\boldsymbol{P}}^i - \boldsymbol{F}_e^i)$ equals zero. In order to apply such a reasoning, equation (2-40) is first of all transformed into an expression that involves the virtual displacements of the generalized coordinates.

It is assumed that a displacement $\boldsymbol{r}^i$ depends on the *n* generalized coordinates of the system. Thus, by differentiating $\boldsymbol{r}^i$ with respect to time yields

$$\dot{\boldsymbol{r}}^i = \sum_{k=1}^{n} \frac{\partial \boldsymbol{r}^i}{\partial \boldsymbol{q}_k} \cdot \dot{\boldsymbol{q}}_k + \frac{\partial \boldsymbol{r}^i}{\partial \boldsymbol{t}} \tag{2-41}$$

which leads to the expression of $\delta \boldsymbol{r}^i$, that is

$$\delta \boldsymbol{r}^i = \sum_{k=1}^{n} \frac{\partial \boldsymbol{r}^i}{\partial \boldsymbol{q}_k} \cdot \delta \boldsymbol{q}_k \tag{2-42}$$

The total virtual work of the external forces δW_e can be written as

$$\begin{aligned} \delta W_e = \sum_{i=1}^{n_i} (\boldsymbol{F}_e^i)^T \cdot \delta \boldsymbol{r}^i &= \sum_{i=1}^{n_i} \sum_{k=1}^{n} (\boldsymbol{F}_e^i)^T \cdot \frac{\partial \boldsymbol{r}^i}{\partial \boldsymbol{q}_k} \cdot \delta \boldsymbol{q}_k \\ &= \sum_{k=1}^{n} \sum_{i=1}^{n_i} (\boldsymbol{F}_e^i)^T \cdot \frac{\partial \boldsymbol{r}^i}{\partial \boldsymbol{q}_k} \cdot \delta \boldsymbol{q}_k \end{aligned} \tag{2-43}$$

From equation (2-43), Q_k can be defined as

$$Q_k = \sum_{i=1}^{n_i} (\boldsymbol{F}_e^i)^T \cdot \frac{\partial \boldsymbol{r}^i}{\partial \boldsymbol{q}_k} \tag{2-44}$$

where Q_k is the component of the generalized force associated with the generalized coordinate q_k. The virtual work of the generalized external forces can be written in the compact form

$$\delta W_e = \sum_{k=1}^{n} Q_k \cdot \delta q_k \tag{2-45}$$

The total virtual work of the inertia forces δW_i in a system can be written with the help of equation (2-42) as

$$\delta W_i = \sum_{i=1}^{n_i} m^i \cdot (\ddot{\boldsymbol{r}}^i)^T \cdot \delta \boldsymbol{r}^i = \sum_{i=1}^{n_{ip}} \sum_{k=1}^{n} m^i \cdot (\ddot{\boldsymbol{r}}^i)^T \cdot \frac{\partial \boldsymbol{r}^i}{\partial q_k} \cdot \delta q_k \tag{2-46}$$

where m^i is the mass and $\ddot{\boldsymbol{r}}^i$ is the acceleration vector of particle *i*.

The following useful identity can be written [10]

$$\sum_{i=1}^{n_i} \frac{d}{dt}\left(m^i \cdot (\dot{\boldsymbol{r}}^i)^T \cdot \frac{\partial \boldsymbol{r}^i}{\partial q_k} \right) = \sum_{i=1}^{n_i} m^i \cdot (\ddot{\boldsymbol{r}}^i)^T \cdot \frac{\partial \boldsymbol{r}^i}{\partial q_k} + \sum_i m^i \cdot (\dot{\boldsymbol{r}}^i)^T \cdot \frac{d}{dt}\left(\frac{\partial \boldsymbol{r}^i}{\partial q_k} \right) \tag{2-47}$$

which leads to

$$\sum_{i=1}^{n_i} m^i \cdot (\ddot{\boldsymbol{r}}^i)^T \cdot \frac{\partial \boldsymbol{r}^i}{\partial q_k} = \sum_{i=1}^{n_i} \left[\frac{d}{dt}\left(m^i \cdot (\dot{\boldsymbol{r}}^i)^T \cdot \frac{\partial \boldsymbol{r}^i}{\partial q_k} \right) - m^i \cdot (\dot{\boldsymbol{r}}^i)^T \cdot \frac{d}{dt}\left(\frac{\partial \boldsymbol{r}^i}{\partial q_k} \right) \right] \tag{2-48}$$

Additionally, according to equation (2-41) the partial derivative of $\dot{\boldsymbol{r}}^i$ with respect to $\dot{q}_k$ gives

$$\frac{\partial \dot{\boldsymbol{r}}^i}{\partial \dot{q}_k} = \frac{\partial \boldsymbol{r}^i}{\partial q_k} \tag{2-49}$$

Furthermore, derivating $\frac{\partial \boldsymbol{r}^i}{\partial q_k}$ with respect to time and identifying with equation (2-41) yields

$$\frac{d}{dt}\left(\frac{\partial \boldsymbol{r}^i}{\partial q_k} \right) = \sum_{l=1}^{n} \frac{\partial^2 \boldsymbol{r}^i}{\partial q_k \cdot \partial q_l} \cdot \dot{q}_l + \frac{\partial^2 \boldsymbol{r}^i}{\partial q_k \cdot \partial t} = \frac{\partial \dot{\boldsymbol{r}}^i}{\partial q_k} \tag{2-50}$$

Substituting equation (2-49) and (2-50) into equation (2-48) yields

$$\sum_{i=1}^{n_i} m^i \cdot (\ddot{\boldsymbol{r}}^i)^T \cdot \frac{\partial \boldsymbol{r}^i}{\partial q_k} = \sum_{i=1}^{n_i} \left[\frac{d}{dt}\left(m^i \cdot (\dot{\boldsymbol{r}}^i)^T \cdot \frac{\partial \dot{\boldsymbol{r}}^i}{\partial \dot{q}_k} \right) - m^i \cdot (\dot{\boldsymbol{r}}^i)^T \cdot \frac{\partial \dot{\boldsymbol{r}}^i}{\partial q_k} \right] \tag{2-51}$$

which can be rewritten as

$$\sum_{i=1}^{n_i} m^i \cdot (\ddot{\boldsymbol{r}}^i)^T \cdot \frac{\partial \boldsymbol{r}^i}{\partial q_k} = \sum_{i=1}^{n_i} \left\{ \frac{d}{dt}\left[\frac{\partial}{\partial \dot{q}_k}\left(\frac{1}{2} \cdot m^i \cdot (\dot{\boldsymbol{r}}^i)^T \cdot \dot{\boldsymbol{r}}^i \right) \right] - \frac{\partial}{\partial q_k}\left(\frac{1}{2} \cdot m^i \cdot (\dot{\boldsymbol{r}}^i)^T \cdot \dot{\boldsymbol{r}}^i \right) \right\} \tag{2-52}$$

Defining the total kinetic energy *T* of the system as

$$T = \sum_{i=1}^{n_i} T^i = \sum_{i=1}^{n_i} \frac{1}{2} \cdot m^i \cdot (\dot{\boldsymbol{r}}^i)^T \cdot \dot{\boldsymbol{r}}^i \tag{2-53}$$

where T^i is the kinetic energy of particle *i*, equation (2-52) can be put in the more simple form

$$\begin{aligned} \sum_{i=1}^{n_i} m^i \cdot (\ddot{\boldsymbol{r}}^i)^T \cdot \frac{\partial \boldsymbol{r}^i}{\partial q_k} &= \sum_{i=1}^{n_i} \left\{ \frac{d}{dt}\left(\frac{\partial T^i}{\partial \dot{q}_k} \right) - \frac{\partial T^i}{\partial q_k} \right\} \\ &= \frac{d}{dt}\left(\frac{\partial T}{\partial \dot{q}_k} \right) - \frac{\partial T}{\partial q_k} \end{aligned} \tag{2-54}$$

Equation (2-45) and equation (2-46) with (2-54) are substituted into D'Alembert's principle expressed by equation (2-40) to yield

$$\sum_{k=1}^{n}\left[\frac{d}{dt}\left(\frac{\partial T}{\partial \dot{q}_k}\right)-\frac{\partial T}{\partial q_k}-Q_k\right]\cdot\delta q_k=0 \tag{2-55}$$

Using a matrix formulation, equation (2-55) can be put in the more convenient form of

$$\left[\frac{d}{dt}\left(\frac{\partial T}{\partial \dot{\boldsymbol{q}}}\right)-\frac{\partial T}{\partial \boldsymbol{q}}-\boldsymbol{Q}^T\right]\cdot\delta \boldsymbol{q}=0 \tag{2-56}$$

Equation (2-55) or (2-56) are called D'Alembert-Lagrange's equation.

The preceding development was done for a system consisting of particles. Considering that a body consists of particles, each representing a infinitesimal volume of the body, this development can also be applied to a system of bodies. In that case, the virtual work of the inertia forces of a body *i* can be written as the sum of the virtual work of the infinitesimal volumes.

$$\delta W_i^i=\sum(\rho^i\cdot dV^i)\cdot(\ddot{\boldsymbol{r}}^i)^T\cdot\delta\boldsymbol{r}^i=\int_{V^i}\rho^i\cdot(\ddot{\boldsymbol{r}}^i)^T\cdot\delta\boldsymbol{r}^i\cdot dV^i \tag{2-57}$$

Similarly, the kinetic energy can be written as

$$T^i=\frac{1}{2}\int_{V^i}\rho^i\cdot\dot{\boldsymbol{r}}_{P^i}^T\cdot\dot{\boldsymbol{r}}_{P^i}\cdot dV^i \tag{2-58}$$

where V^i is the volume and ρ^i is the mass density of body *i*.

Now, if the set of generalized coordinates is linearly independent then each coefficient of δq_k in equation (2-55) can be set to zero which leads to Lagrange's equation given by

$$\frac{d}{dt}\left(\frac{\partial T}{\partial \dot{q}_k}\right)-\frac{\partial T}{\partial q_k}-Q_k=0 \tag{2-59}$$

However, in multi-body systems the generalized coordinates are generally not independent due to the combined set of constraint equations. Therefore, one cannot pass directly from equation (2-55) to equation (2-59).

The collection of all the constraints present in a multi-body model is denoted by ***C***. In the case of an holonomic system, ***C*** assumes the general expression of equation (2-31). As the virtual displacements are considered to occur with time being fixed, the condition for a kinematically admissible virtual displacement is realized by taking the differential of the set of constraints ***C***, that is

$$\boldsymbol{C}_{\boldsymbol{q}}\cdot\delta\boldsymbol{q}=\begin{bmatrix}\frac{\partial \boldsymbol{c}_1}{\partial q_1} & \frac{\partial \boldsymbol{c}_1}{\partial q_2} & \cdots & \frac{\partial \boldsymbol{c}_1}{\partial q_n}\\ \frac{\partial \boldsymbol{c}_2}{\partial q_1} & \frac{\partial \boldsymbol{c}_2}{\partial q_2} & \cdots & \frac{\partial \boldsymbol{c}_2}{\partial q_n}\\ \vdots & \vdots & \ddots & \vdots\\ \frac{\partial \boldsymbol{c}_{n_{ce}}}{\partial q_1} & \frac{\partial \boldsymbol{c}_{n_{ce}}}{\partial q_2} & \cdots & \frac{\partial \boldsymbol{c}_{n_{ce}}}{\partial q_n}\end{bmatrix}\cdot\delta\boldsymbol{q}=\boldsymbol{0} \tag{2-60}$$

where n is the number of generalized coordinates and n_{ce} is the number of algebraic constraints equations. $\boldsymbol{C_q}$ is called the Jacobian matrix of the system. In other words, any virtual displacement that satisfies equation (2-60), i.e. this virtual displacement is consistent with the constraints of the system, satisfies equation (2-56). If the constraint equations are linearly independent, i.e. no redundancies exist, then the matrix $\boldsymbol{C_q}$ has a full row rank and is thus nonsingular.

If equation (2-60) holds, then it can also be written that

$$\boldsymbol{\lambda}^T \cdot \boldsymbol{C_q} \cdot \delta \boldsymbol{q} = 0 \tag{2-61}$$

where $\boldsymbol{\lambda}$ is a vector containing n_{ce} Lagrange multipliers. Equation (2-61) and (2-56) can be combined to give

$$\delta \boldsymbol{q}^T \cdot \left[\frac{d}{dt} \left(\frac{\partial T}{\partial \dot{\boldsymbol{q}}} \right)^T - \left(\frac{\partial T}{\partial \boldsymbol{q}} \right)^T - \boldsymbol{Q} + \boldsymbol{C_q}^T \cdot \boldsymbol{\lambda} \right] = 0 \tag{2-62}$$

as the Lagrange multiplier theorem guarantees the existence of a vector $\boldsymbol{\lambda}$ such that equation (2-62) holds for any arbitrary $\delta \boldsymbol{q}$ that satisfies equation (2-60). In that case, each coefficient of $\delta \boldsymbol{q}$ can be set to zero which leads to the Lagrange multiplier form of the equation of motion

$$\frac{d}{dt} \left(\frac{\partial T}{\partial \dot{\boldsymbol{q}}} \right)^T - \left(\frac{\partial T}{\partial \boldsymbol{q}} \right)^T + \boldsymbol{C_q}^T \cdot \boldsymbol{\lambda} - \boldsymbol{Q} = \boldsymbol{0} \tag{2-63}$$

Another approach to derive equation (2-63) is to say that if the generalized coordinates $\boldsymbol{q}$ are linearly dependent, then they can be divided into dependent and independent generalized coordinates, i.e. $\boldsymbol{q}_d$ and $\boldsymbol{q}_i$ respectively. It is then possible to choose $\boldsymbol{\lambda}$ such that

$$\frac{d}{dt} \left(\frac{\partial T}{\partial \dot{\boldsymbol{q}}_d} \right)^T - \left(\frac{\partial T}{\partial \boldsymbol{q}_d} \right)^T + \boldsymbol{C_{q_d}}^T \cdot \boldsymbol{\lambda} - \boldsymbol{Q}_d = \boldsymbol{0} \tag{2-64}$$

The same equation can of course be written for $\boldsymbol{q}_i$ as they are independent. Combining both equations finally leads again to equation (2-63).

Instead of deriving Lagrange's equation from D'Alembert's principle, Hamilton's principle can be used. If the Lagrangian L of a system is defined by

$$L = T - V \tag{2-65}$$

where T and V are the kinetic and potential energy, respectively, then Hamilton's principle states that the motion of a system from time t_1 to time t_2 is such that the variation of the Lagrangian plus the line integral of the virtual work done by the nonconservative forces must be equal to zero, that is

$$\int_{t_1}^{t_2} \delta L \cdot dt + \int_{t_1}^{t_2} \delta W_{nc} \cdot dt = 0 \tag{2-66}$$

With the techniques of calculus of variations equation, (2-66) finally leads to the very common form of Lagrange's equation [10], that is

$$\frac{d}{dt}\left(\frac{\partial L}{\partial \dot{\boldsymbol{q}}}\right)^T - \left(\frac{\partial L}{\partial \boldsymbol{q}}\right)^T + \boldsymbol{C_q}^T \cdot \boldsymbol{\lambda} - \boldsymbol{Q}_{nc} = \boldsymbol{0} \tag{2-67}$$

In fact, it can be shown that equation (2-63) and (2-67) are identical, as $\boldsymbol{Q}$ in equation (2-63) includes both, conservative and nonconservative external forces.

As stated above, Lagrange's equation (2-63) can also be applied to a system of rigid bodies where the kinetic energy of a body *i* is written as

$$T^i = \frac{1}{2}\int_{V^i} \rho^i \cdot \dot{\boldsymbol{r}}_{P^i}^T \cdot \dot{\boldsymbol{r}}_{P^i} \cdot dV^i \tag{2-68}$$

For a rigid body *i*, substituting equation (2-14) into equation (2-15) yields

$$\begin{aligned} &\dot{\boldsymbol{r}}_{P^i} = \dot{\boldsymbol{r}}^i + \boldsymbol{A}^i \cdot \tilde{\boldsymbol{\omega}}^i \cdot \bar{\boldsymbol{s}}_{P_i} = \dot{\boldsymbol{r}}^i - \boldsymbol{A}^i \cdot \tilde{\bar{\boldsymbol{s}}}_{P^i} \cdot \boldsymbol{\omega}^i \;\Leftrightarrow \\ &\dot{\boldsymbol{r}}_{P^i} = \dot{\boldsymbol{r}}^i - \boldsymbol{A}^i \cdot \tilde{\bar{\boldsymbol{s}}}_{P^i} \cdot \boldsymbol{B}^i \cdot \dot{\boldsymbol{\varepsilon}}^i = [\boldsymbol{I} \;\; -\boldsymbol{A}^i \cdot \tilde{\bar{\boldsymbol{s}}}_{P^i} \cdot \boldsymbol{B}^i] \cdot \begin{bmatrix} \dot{\boldsymbol{r}}^i \\ \dot{\boldsymbol{\varepsilon}}^i \end{bmatrix} \;\Leftrightarrow \\ &\dot{\boldsymbol{r}}_{P^i} = [\boldsymbol{I} \;\; -\boldsymbol{A}^i \cdot \tilde{\bar{\boldsymbol{s}}}_{P^i} \cdot \boldsymbol{B}^i] \cdot \dot{\boldsymbol{q}}^i \end{aligned} \tag{2-69}$$

Substituting equation (2-69) into equation (2-68) leads to

$$T^i = \frac{1}{2} \cdot \dot{\boldsymbol{q}}^{iT} \cdot \boldsymbol{M}^i \cdot \dot{\boldsymbol{q}}^i \tag{2-70}$$

where the mass matrix $\boldsymbol{M}^i$ of the rigid body is defined as

$$\boldsymbol{M}^i = \int_{V^i} \rho^i \begin{bmatrix} \boldsymbol{I} & -\boldsymbol{A}^i \cdot \tilde{\bar{\boldsymbol{s}}}_{P^i} \cdot \boldsymbol{B}^i \\ symmetric & \boldsymbol{B}^{iT} \cdot \tilde{\bar{\boldsymbol{s}}}_{P^i}^T \cdot \tilde{\bar{\boldsymbol{s}}}_{P^i} \cdot \boldsymbol{B}^i \end{bmatrix} dV^i = \begin{bmatrix} \boldsymbol{m}_{rr}^i & \boldsymbol{m}_{r\varepsilon}^i \\ \left(\boldsymbol{m}_{r\varepsilon}^i\right)^T & \boldsymbol{m}_{\varepsilon\varepsilon}^i \end{bmatrix} \tag{2-71}$$

The matrix $\boldsymbol{m}_{rr}^i$ is related to the translation of the rigid body. It is a constant diagonal matrix

$$\boldsymbol{m}_{rr}^i = \int_{V^i} \rho^i \cdot dV^i \cdot \boldsymbol{I} = m^i \cdot \boldsymbol{I} \tag{2-72}$$

where $\boldsymbol{I}$ is a 3*x*3 identity matrix and m^i is the total mass of the body. The matrix $\boldsymbol{m}_{r\varepsilon}^i$ represents the inertia coupling of the translation and rotation of a body. It can be written as

$$\boldsymbol{m}_{r\varepsilon}^i = -\boldsymbol{A}^i \cdot \int_{V^i} \rho^i \cdot \tilde{\bar{\boldsymbol{s}}}_{P^i} \cdot dV^i \cdot \boldsymbol{B}^i \tag{2-73}$$

where the integral becomes the null matrix if the origin of the body reference is taken at the center of mass of the body. Finally, the matrix $\boldsymbol{m}_{\varepsilon\varepsilon}^i$ is related to the rotation of the rigid body

$$\boldsymbol{m}_{\varepsilon\varepsilon}^i = \boldsymbol{B}^{iT} \cdot \int_{V^i} \rho^i \cdot \tilde{\bar{\boldsymbol{s}}}_{P^i}^T \cdot \tilde{\bar{\boldsymbol{s}}}_{P^i} \cdot dV^i \cdot \boldsymbol{B}^i = \boldsymbol{B}^{iT} \cdot \boldsymbol{J}_{\varepsilon\varepsilon}^i \cdot \boldsymbol{B}^i \tag{2-74}$$

The matrix $\boldsymbol{J}_{\varepsilon\varepsilon}^i$ is called the inertia tensor of body *i*, which is constant for a rigid body.

Equation (2-70) leads to the expressions

$$\frac{d}{dt}\left(\frac{\partial T^i}{\partial \dot{\boldsymbol{q}}^i}\right)^T = \frac{d}{dt}\left(\dot{\boldsymbol{q}}^{iT} \cdot \boldsymbol{M}^i\right)^T = \frac{d}{dt}\left(\boldsymbol{M}^i \cdot \dot{\boldsymbol{q}}^i\right) = \boldsymbol{M}^i \cdot \ddot{\boldsymbol{q}}^i + \dot{\boldsymbol{M}}^i \cdot \dot{\boldsymbol{q}}^i \tag{2-75}$$

and

$$\left(\frac{\partial T^i}{\partial \boldsymbol{q}^i}\right)^T = \frac{1}{2}\cdot\left(\frac{\partial \boldsymbol{M}^i}{\partial \boldsymbol{q}^i}\cdot\dot{\boldsymbol{q}}^i\right)^T\cdot\dot{\boldsymbol{q}}^i \tag{2-76}$$

which, substituted into equation (2-63), give the equation of motion of a rigid body *i*, that is

$$\boldsymbol{M}^i\cdot\ddot{\boldsymbol{q}}^i + \dot{\boldsymbol{M}}^i\cdot\dot{\boldsymbol{q}}^i - \frac{1}{2}\cdot\left(\frac{\partial \boldsymbol{M}^i}{\partial \boldsymbol{q}^i}\cdot\dot{\boldsymbol{q}}^i\right)^T\cdot\dot{\boldsymbol{q}}^i + \boldsymbol{C}_{q^i}^T\cdot\lambda - \boldsymbol{Q}^i = \boldsymbol{0} \tag{2-77}$$

The equation of motion of a complete multi-body system takes the same form as presented in equation (2-77). This set of differential equations is then combined with the set of algebraic constraint equations, for example (2-31), in order to determine the Lagrange multipliers. The combined set represents the dynamic equations of a constrained multi-body system. The solution of this set of nonlinear differential and algebraic equations (DAE) is very challenging from a numerical point of view. Several numerical procedures exist for solving such systems. They will not be presented here but can be looked up for example in [10, 11, 12]. The complete set of equations to solve for a system of n_i bodies and the meaning of the different variables is summed up below.

$$\boldsymbol{M}\cdot\ddot{\boldsymbol{q}} + \dot{\boldsymbol{M}}\cdot\dot{\boldsymbol{q}} - \frac{1}{2}\cdot\left(\frac{\partial \boldsymbol{M}}{\partial \boldsymbol{q}}\cdot\dot{\boldsymbol{q}}\right)^T\cdot\dot{\boldsymbol{q}} + \boldsymbol{C}_{\boldsymbol{q}}^T\cdot\lambda - \boldsymbol{Q} = \boldsymbol{0}$$

$$\boldsymbol{C}(\boldsymbol{q},t) = \left[c_1(\boldsymbol{q},t) \quad c_2(\boldsymbol{q},t) \quad \cdots \quad c_{n_{ce}}(\boldsymbol{q},t)\right]^T = \boldsymbol{0}$$

$\boldsymbol{q}, \dot{\boldsymbol{q}}, \ddot{\boldsymbol{q}}$ are vectors containing the *n* generalized coordinates of the system and their time derivatives,
where, for a body *i* $\boldsymbol{q}_i = \left[\boldsymbol{r}^{iT} \quad \boldsymbol{\varepsilon}^{iT}\right]^T = \left[x_i \quad y_i \quad z_i \quad \psi_i \quad \theta_i \quad \phi_i\right]^T$.

$\boldsymbol{M}$ is an (*n x n)* matrix containing the mass matrices $\boldsymbol{M}^i$ of each body *i*
where $\boldsymbol{M}^i = \begin{bmatrix} m^i\cdot\boldsymbol{I} & \boldsymbol{0} \\ \boldsymbol{0} & \boldsymbol{B}^{iT}\cdot\boldsymbol{J}^i_{\varepsilon\varepsilon}\cdot\boldsymbol{B}^i \end{bmatrix}$ if the origin of the body reference frame is taken at the center of gravity of body *i*. (2-78)

$\dot{\boldsymbol{M}}$ is the time derivative of the mass matrix.

$\frac{\partial \boldsymbol{M}}{\partial \boldsymbol{q}}$ is an (*n x n x n)* matrix containing the partial derivative of the mass matrix with respect to the generalized coordinates.

$\boldsymbol{C}_{\boldsymbol{q}}$ is an (n_{ce} *x n)* matrix called the system Jacobian, where $C_{ij} = \partial C_i / \partial q_i$.

λ is a vector containing the n_{ce} Lagrange multipliers.

$\boldsymbol{Q}$ is a vector containing the *n* generalized forces associated with each generalized coordinate q_k that are determined form the conservative and non-conservative external forces applied to each body *i*.

$\boldsymbol{C}$ is an (n_{ce} *x n)* matrix containing the n_{ce} algebraic constraint equations.

2.1.2 Flexible-Body Dynamics

Nonlinear dynamic problems of complex mechanisms which are represented with rigid bodies are simulated and analyzed efficiently with MBS programs. For the nonlinear dynamic simulation of flexible structures, the code has to handle additionally the flexibility of bodies. Today, most of the commercial MBS programs including flexible bodies are based on a formulation that assumes the large overall motion of the body superimposed by small linear deformations. These deformations are generally represented by a modal approach, which means that the deformation is written as a linear combination of mode shapes. In general, these mode shapes are not only made up of eigenvectors of the structure but may include static deformation modes as will be shown in the following.

2.1.2.1 Reduction Methods

To model the flexibility of a body which has an arbitrary geometry, the finite element method is used as a general systematic approach. However, a reasonable fine mesh is usually needed in order to obtain accurate results. Therefore, FE models often have a large number of degrees of freedom. Now using this full FE model with its large number of nodal DOF directly in a MBS model is unnecessary and often not feasible from a computational point of view. The model has to be reduced before being included in a multi-body dynamic simulation. The need for reduced FE models is also shared by other fields of mechanical analysis. For this reason, several reduction methods were developed. The general formalism of a reduction method can be expressed by

$$\boldsymbol{u} = \boldsymbol{T} \cdot \boldsymbol{v} \tag{2-79}$$

where $\boldsymbol{u}$ is the vector that contains the physical coordinates of the FE model, $\boldsymbol{v}$ is the vector with the generalized coordinates obtained by the reduction and $\boldsymbol{T}$ is the coordinate transformation matrix [13]. If n_p physical coordinates should be reduced to n generalized coordinates, then the transformation matrix $\boldsymbol{T}$ has the dimension n_p x n, i.e.

$$\begin{Bmatrix} u_1 \\ u_2 \\ \vdots \\ u_{n_p} \end{Bmatrix} = \begin{bmatrix} & & 1 \\ & & \\ & T & \\ & & \\ & & n_p \end{bmatrix} \begin{bmatrix} & & n \\ & & \\ \begin{Bmatrix} v_1 \\ v_2 \\ \vdots \\ v_n \end{Bmatrix} & & \\ & & \end{bmatrix} \tag{2-80}$$

It is assumed that $\boldsymbol{T}$ is time-independent therefore

$$\dot{\boldsymbol{u}} = \boldsymbol{T} \cdot \dot{\boldsymbol{v}} \quad \text{and} \quad \ddot{\boldsymbol{u}} = \boldsymbol{T} \cdot \ddot{\boldsymbol{v}} \tag{2-81}$$

The linear equation of motion of an undamped structure with the mass matrix $\boldsymbol{M}$ and the stiffness matrix $\boldsymbol{K}$ can be written as

$$\boldsymbol{M}\cdot\ddot{\boldsymbol{u}}+\boldsymbol{K}\cdot\boldsymbol{u}=\boldsymbol{F} \tag{2-82}$$

Substituting equation (2-79) and (2-81) into equation (2-82) and multiplying from the left with the transpose of matrix $\boldsymbol{T}$ yields the reduced linear equation of motion, that is

$$\begin{aligned}\boldsymbol{T}^T\cdot\boldsymbol{M}\cdot\boldsymbol{T}\cdot\ddot{\boldsymbol{v}}+\boldsymbol{T}^T\cdot\boldsymbol{K}\cdot\boldsymbol{T}\cdot\boldsymbol{v}&=\boldsymbol{T}^T\cdot\boldsymbol{F}\\ \Leftrightarrow\ \boldsymbol{M}_T\cdot\ddot{\boldsymbol{v}}+\boldsymbol{K}_T\cdot\boldsymbol{v}&=\boldsymbol{F}_T\end{aligned} \tag{2-83}$$

The resultant set of equations has now only n degrees of freedom. $\boldsymbol{M}_T$ and $\boldsymbol{K}_T$ are the reduced mass and stiffness matrix, respectively and $\boldsymbol{F}_T$ is the reduced force vector. The problem is to adequately choose the transformation matrix $\boldsymbol{T}$. Several possibilities are presented in the following sections.

a) Guyan Reduction

The physical coordinates $\boldsymbol{u}$ can be partitioned into two groups: the coordinates that should be retained - they are called master DOF and denoted by the subscript m - and the coordinates that should be eliminated by the reduction - they are called slave DOF and denoted by the subscript s. Thus equation (2-82) can be written in the partitioned form

$$\begin{bmatrix}\boldsymbol{M}_{ss} & \boldsymbol{M}_{sm}\\ \boldsymbol{M}_{ms} & \boldsymbol{M}_{mm}\end{bmatrix}\cdot\begin{bmatrix}\ddot{\boldsymbol{u}}_s\\ \ddot{\boldsymbol{u}}_m\end{bmatrix}+\begin{bmatrix}\boldsymbol{K}_{ss} & \boldsymbol{K}_{sm}\\ \boldsymbol{K}_{ms} & \boldsymbol{K}_{mm}\end{bmatrix}\cdot\begin{bmatrix}\boldsymbol{u}_s\\ \boldsymbol{u}_m\end{bmatrix}=\begin{bmatrix}\boldsymbol{F}_s\\ \boldsymbol{F}_m\end{bmatrix} \tag{2-84}$$

The Guyan reduction is based on a solution method used in static structural analysis. In this case, the coordinates to which no forces are applied, can be eliminated [14] without introducing an error according to the following process. The structural equations are arranged so that after partitioning the forces $\boldsymbol{F}_s$ are zero, i.e.

$$\begin{bmatrix}\boldsymbol{K}_{ss} & \boldsymbol{K}_{sm}\\ \boldsymbol{K}_{ms} & \boldsymbol{K}_{mm}\end{bmatrix}\cdot\begin{bmatrix}\boldsymbol{u}_s\\ \boldsymbol{u}_m\end{bmatrix}=\begin{bmatrix}\boldsymbol{0}\\ \boldsymbol{F}_m\end{bmatrix} \tag{2-85}$$

The upper partition of equation (2-85) gives the static constraint equations

$$\boldsymbol{K}_{ss}\cdot\boldsymbol{u}_s+\boldsymbol{K}_{sm}\cdot\boldsymbol{u}_m=\boldsymbol{0} \tag{2-86}$$

From equation (2-86) the transformation matrix $\boldsymbol{T}$ can be identified as having the form

$$\boldsymbol{T}=\begin{bmatrix}-\boldsymbol{K}_{ss}^{-1}\cdot\boldsymbol{K}_{sm}\\ \boldsymbol{I}\end{bmatrix} \tag{2-87}$$

so that finally

$$\boldsymbol{u}=\boldsymbol{T}\cdot\boldsymbol{v}\quad\Rightarrow\quad\begin{bmatrix}\boldsymbol{u}_s\\ \boldsymbol{u}_m\end{bmatrix}=\begin{bmatrix}-\boldsymbol{K}_{ss}^{-1}\cdot\boldsymbol{K}_{sm}\\ \boldsymbol{I}\end{bmatrix}\cdot\boldsymbol{u}_m \tag{2-88}$$

Although the transformation matrix $\boldsymbol{T}$ resulted from a static analysis approach, it is also applied in dynamic analysis for the mass matrix [14]. The advantage of the Guyan reduction is that the physical DOF of interest are kept. However, the fundamental idea of the Guyan reduction is that the mass of the structure can be concentrated at a limited number of degrees of freedom without significantly affecting the natural frequencies of interest. For an arbitrary structure, the master DOF must therefore be chosen judiciously. They should not only include the DOF of the nodes that connect to other structures but also DOF throughout

the rest of the structure in order to respect the mass distribution within the structure. Thus, this technique introduces errors in the inertia terms while the reduced stiffness matrix is exact with respect to the full FE model.

b) Modal Reduction

The equation of motion in (2-82) is considered without external forces, i.e.

$$\boldsymbol{M}\cdot\ddot{\boldsymbol{u}}+\boldsymbol{K}\cdot\boldsymbol{u}=\boldsymbol{0} \tag{2-89}$$

A solution for equation (2-89) can be put in the form of

$$\boldsymbol{u}=\boldsymbol{U}\cdot e^{(i\cdot\omega\cdot t)} \tag{2-90}$$

Substituting (2-90) into (2-89) yields the eigenvalue problem

$$\boldsymbol{K}\cdot\boldsymbol{U}=\omega^2\cdot\boldsymbol{M}\cdot\boldsymbol{U} \tag{2-91}$$

This problem has n_p solutions. To each ω_j, which is called an eigenvalue or natural frequency, corresponds a vector $\boldsymbol{U}_j$, which is commonly denoted as $\boldsymbol{\varphi}_j$, called an eigenvector or mode shape. When all $\boldsymbol{\varphi}_j$ have been determined, they can be grouped in the modal matrix $\boldsymbol{\Phi}$ such that

$$\boldsymbol{\Phi}=\overset{1}{\underset{n_p}{\left[\boldsymbol{\varphi}_1\ \ \boldsymbol{\varphi}_2\ \ \dots\ \ \boldsymbol{\varphi}_{n_p}\right]}}\overset{n_p}{} \tag{2-92}$$

and it can be written that

$$\boldsymbol{u}=\boldsymbol{\Phi}\cdot\boldsymbol{v} \tag{2-93}$$

Substituting equation (2-93) into equation (2-82) and multiplying from the left with the transpose of matrix $\boldsymbol{\Phi}$ yields the equation of motion

$$\boldsymbol{\Phi}^T\cdot\boldsymbol{M}\cdot\boldsymbol{\Phi}\cdot\ddot{\boldsymbol{v}}+\boldsymbol{\Phi}^T\cdot\boldsymbol{K}\cdot\boldsymbol{\Phi}\cdot\boldsymbol{v}=\boldsymbol{\Phi}^T\cdot\boldsymbol{F} \tag{2-94}$$

A fundamental property of the eigenvectors is that

$$\boldsymbol{\Phi}^T\cdot\boldsymbol{M}\cdot\boldsymbol{\Phi}=diag\,(m_j)\quad\text{and}\quad\boldsymbol{\Phi}^T\cdot\boldsymbol{K}\cdot\boldsymbol{\Phi}=diag\,(k_j) \tag{2-95}$$

with $\omega_j^2=k_j\,/\,m_j$. Thus the equation of motion (2-94) is uncoupled and can be rewritten as

$$diag\,(m_j)\cdot\ddot{\boldsymbol{v}}+diag\,(k_j)\cdot\boldsymbol{v}=\boldsymbol{\Phi}^T\cdot\boldsymbol{F} \tag{2-96}$$

Equation (2-96) is now made up of n_p independent algebraic equations that can be easily solved and used to determine $\boldsymbol{u}$ with

$$\boldsymbol{u}=\boldsymbol{\Phi}\cdot\boldsymbol{v}=\sum_{i=1}^{n_p}\boldsymbol{\varphi}_i\cdot v_i \tag{2-97}$$

In order to reduce the number of DOF, the eigenvectors corresponding to the highest eigenvalues are generally discarded, such that

$$\boldsymbol{u}\approx\sum_{i=1}^{n}\boldsymbol{\varphi}_i\cdot v_i \tag{2-98}$$

where $n\ll n_p$. These retained eigenvectors are used to fill the transformation matrix $\boldsymbol{T}$ with

$$\boldsymbol{T}=\overset{1}{\underset{n_p}{\left[\boldsymbol{\varphi}_1\ \ \boldsymbol{\varphi}_2\ \ \dots\ \ \boldsymbol{\varphi}_n\right]}}\overset{n}{} \tag{2-99}$$

This reduction method allows very high reduction degrees without significantly affecting the accuracy of the lower natural frequencies. However, the disadvantage of the modal

reduction is that the system is "frozen" in its state at which the eigenvalue problem is solved, i.e. the boundary conditions cannot be changed anymore.

c) Component Mode Synthesis

First component mode synthesis (CMS) techniques were developed in the sixties. The original idea, is to partition a structure into several components where each component is represented by a set of suitable defined component modes. These sets are then coupled to get a reduced order problem of the entire assembly for the dynamic analysis. Since then, CMS is used extensively in the dynamic analysis of structures and various formulations have been developed. First intended for undamped or lightly damped structures, the formulation has been extended for heavily damped and gyroscopic systems and for use with experimentally determined CMS parameters. References [15, 16, 17] provide a review on the different techniques with an exhaustive list of available literature. In this work, only the basic formulation is presented [18].

The principle of the CMS technique is that each substructure is projected from the physical space onto a mode subspace composed by normal modes, i.e eigenvectors of the substructure, and supplementary modes which are constraint modes, rigid body modes and attachment modes.

The following partitioned form of an undamped linear equation of motion is used.

$$\begin{bmatrix} \boldsymbol{M}_{ii} & \boldsymbol{M}_{ib} \\ \boldsymbol{M}_{bi} & \boldsymbol{M}_{bb} \end{bmatrix} \cdot \begin{bmatrix} \ddot{\boldsymbol{u}}_i \\ \ddot{\boldsymbol{u}}_b \end{bmatrix} + \begin{bmatrix} \boldsymbol{K}_{ii} & \boldsymbol{K}_{ib} \\ \boldsymbol{K}_{bi} & \boldsymbol{K}_{bb} \end{bmatrix} \cdot \begin{bmatrix} \boldsymbol{u}_i \\ \boldsymbol{u}_b \end{bmatrix} = \begin{bmatrix} \boldsymbol{F}_i \\ \boldsymbol{F}_b \end{bmatrix} \tag{2-100}$$

This partition is identical to the partition in (2-84) used for the Guyan reduction. However, instead of master and slave DOF, the terms of boundary and interior DOF are generally retained for CMS methods; thus the subscripts *b* and *i*, respectively.

Normal Modes

Normal modes are obtained by the solution of the eigenvalue problem

$$\left(\boldsymbol{K} - \omega_j^2 \cdot \boldsymbol{M}\right) \boldsymbol{\varphi}_j = \boldsymbol{0} \tag{2-101}$$

Different normal modes can be computed depending on whether all, none or part of the boundary coordinates are restrained so that they are classified as fixed-interface, free-interface or hybrid-interface normal modes, respectively. The $\boldsymbol{\varphi}_j$ are grouped in the normal mode matrix $\breve{\boldsymbol{\Phi}}_N$. The complete mode set is usually truncated to a set denoted hereafter as $\boldsymbol{\Phi}_N$.

If all the boundary DOF are fixed, then the eigenvalue problem to solve is

$$\left(\boldsymbol{K}_{ii} - \omega_j^2 \cdot \boldsymbol{M}_{ii}\right) \boldsymbol{\varphi}_{ij} = \boldsymbol{0} \tag{2-102}$$

and the reduced normal mode matrix $\boldsymbol{\Phi}_N$ can be written as

$$\boldsymbol{\Phi}_N \equiv \begin{bmatrix} \boldsymbol{\Phi}_{iN} \\ \boldsymbol{0}_b \end{bmatrix} = \begin{bmatrix} \boldsymbol{\varphi}_{i1} & \boldsymbol{\varphi}_{i2} & \boldsymbol{\varphi}_{i3} & \cdots \\ \boldsymbol{0}_{b1} & \boldsymbol{0}_{b2} & \boldsymbol{0}_{b3} & \cdots \end{bmatrix} \tag{2-103}$$

$\boldsymbol{\Phi}_{iN}$ represents the reduced set of eigenvectors while the coefficients related to the boundary DOF are zero.

Constraint Modes and Rigid-Body Modes

Constraint modes are static deformation shapes and can be interpreted as giving each coordinate of the set of boundary coordinates a unit displacement while holding the remaining coordinates of that set fixed; the remaining DOF of the structure are free. This set must prevent any rigid-body motion of the component. The constraint modes are defined by

$$\begin{bmatrix} \boldsymbol{K}_{ii} & \boldsymbol{K}_{ib} \\ \boldsymbol{K}_{bi} & \boldsymbol{K}_{bb} \end{bmatrix} \cdot \begin{bmatrix} \boldsymbol{\Psi}_{ib} \\ \boldsymbol{I} \end{bmatrix} = \begin{bmatrix} \boldsymbol{0} \\ \boldsymbol{R}_{bb} \end{bmatrix} \tag{2-104}$$

where $\boldsymbol{R}_{bb}$ are the reaction forces at the boundary DOF and $\boldsymbol{I}$ is an identity matrix. The upper row partition gives the constraint mode matrix $\boldsymbol{\Psi}_C$, which is then defined as

$$\boldsymbol{\Psi}_C \equiv \begin{bmatrix} \boldsymbol{\Psi}_{ib} \\ \boldsymbol{I} \end{bmatrix} = \begin{bmatrix} -\boldsymbol{K}_{ii}^{-1} \cdot \boldsymbol{K}_{ib} \\ \boldsymbol{I} \end{bmatrix} \tag{2-105}$$

One clearly notices the similarity to equation (2-87) of the Guyan reduction.

Rigid-body modes can be considered as a special case of constraint modes. From the set of boundary coordinates, a minimal set of coordinates is chosen that prevents rigid-body motion of the component, they are denoted by the subscript *r*. The remaining boundary coordinates are denoted by the subscript *e*, for excess (redundant) boundary coordinates. The rigid-body modes are then defined by

$$\begin{bmatrix} \boldsymbol{K}_{ii} & \boldsymbol{K}_{ie} & \boldsymbol{K}_{ir} \\ \boldsymbol{K}_{ei} & \boldsymbol{K}_{ee} & \boldsymbol{K}_{er} \\ \boldsymbol{K}_{ri} & \boldsymbol{K}_{re} & \boldsymbol{K}_{rr} \end{bmatrix} \cdot \begin{bmatrix} \boldsymbol{\Psi}_{ir} \\ \boldsymbol{\Psi}_{er} \\ \boldsymbol{I} \end{bmatrix} = \begin{bmatrix} \boldsymbol{0} \\ \boldsymbol{0} \\ \boldsymbol{0} \end{bmatrix} \tag{2-106}$$

$\boldsymbol{R}_{rr}$ is zero as there are no reaction forces acting on this particular set of boundary DOF. Thus, the rigid-body mode matrix $\boldsymbol{\Psi}_R$ is defined by

$$\boldsymbol{\Psi}_R \equiv \begin{bmatrix} \boldsymbol{\Psi}_{ir} \\ \boldsymbol{\Psi}_{er} \\ \boldsymbol{I} \end{bmatrix} = \begin{bmatrix} -\begin{bmatrix} \boldsymbol{K}_{ii} & \boldsymbol{K}_{ie} \\ \boldsymbol{K}_{ei} & \boldsymbol{K}_{ee} \end{bmatrix}^{-1} \cdot \begin{bmatrix} \boldsymbol{K}_{ir} \\ \boldsymbol{K}_{er} \end{bmatrix} \\ \boldsymbol{I} \end{bmatrix} \tag{2-107}$$

From the remaining set of boundary coordinates, a set of redundant-interface constraint modes can be defined similar to the constraint modes, while the "rigid-body" coordinates are fixed. Thus,

$$\begin{bmatrix} \boldsymbol{K}_{ii} & \boldsymbol{K}_{ie} & \boldsymbol{K}_{ir} \\ \boldsymbol{K}_{ei} & \boldsymbol{K}_{ee} & \boldsymbol{K}_{er} \\ \boldsymbol{K}_{ri} & \boldsymbol{K}_{re} & \boldsymbol{K}_{rr} \end{bmatrix} \cdot \begin{bmatrix} \boldsymbol{\Psi}_{ie} \\ \boldsymbol{I} \\ \boldsymbol{0} \end{bmatrix} = \begin{bmatrix} \boldsymbol{0} \\ \boldsymbol{R}_{ee} \\ \boldsymbol{R}_{re} \end{bmatrix} \tag{2-108}$$

The redundant-interface constraint mode matrix $\boldsymbol{\Psi}_E$ is then defined as

$$\boldsymbol{\Psi}_E \equiv \begin{bmatrix} \boldsymbol{\Psi}_{ie} \\ \boldsymbol{I} \\ \boldsymbol{0} \end{bmatrix} = \begin{bmatrix} -\boldsymbol{K}_{ii}^{-1} \cdot \boldsymbol{K}_{ie} \\ \boldsymbol{I} \\ \boldsymbol{0} \end{bmatrix} \tag{2-109}$$

Attachment Modes

Attachment modes are defined as static deflections which result when a unit force is applied to each coordinate of a specified set while the remaining coordinates of that set are force free. The difficulty when computing attachment modes is that the component may have one or more rigid-body DOF. In this configuration, it is impossible to apply directly to the unrestrained component the necessary unit forces. One solution to circumvent the problem is to select from the set of boundary coordinates, a minimal set of coordinates, denoted by the subscript *r*, that prevents rigid-body motion. The remaining boundary coordinates are chosen as "attachment" coordinates, they are denoted by the subscript *a*. Thus, the attachment modes are computed from

$$\begin{bmatrix} \boldsymbol{K}_{ii} & \boldsymbol{K}_{ia} & \boldsymbol{K}_{ir} \\ \boldsymbol{K}_{ai} & \boldsymbol{K}_{aa} & \boldsymbol{K}_{ar} \\ \boldsymbol{K}_{ri} & \boldsymbol{K}_{ra} & \boldsymbol{K}_{rr} \end{bmatrix} \cdot \begin{bmatrix} \boldsymbol{\Psi}_{ia} \\ \boldsymbol{\Psi}_{aa} \\ \boldsymbol{0} \end{bmatrix} = \begin{bmatrix} \boldsymbol{0} \\ \boldsymbol{I} \\ \boldsymbol{R}_{ra} \end{bmatrix} \tag{2-110}$$

and the attachment mode matrix $\boldsymbol{\Psi}_A$ is defined by

$$\boldsymbol{\Psi}_A \equiv \begin{bmatrix} \boldsymbol{\Psi}_{ia} \\ \boldsymbol{\Psi}_{aa} \\ \boldsymbol{0} \end{bmatrix} = \begin{bmatrix} -\begin{bmatrix} \boldsymbol{K}_{ii} & \boldsymbol{K}_{ia} \\ \boldsymbol{K}_{ai} & \boldsymbol{K}_{aa} \end{bmatrix}^{-1} \cdot \begin{bmatrix} \boldsymbol{0} \\ \boldsymbol{I} \end{bmatrix} \\ \boldsymbol{0} \end{bmatrix} \tag{2-111}$$

Another possibility to determine attachment modes leads to the so-called inertia-relief attachment modes. They are also defined by applying unit forces $\boldsymbol{f}$ at the "attachment" coordinates. However, instead of fixing some DOF to prevent rigid-body motion, a rigid-body D'Alembert force vector $\boldsymbol{M} \cdot \ddot{\boldsymbol{u}}_r$, where $\boldsymbol{u}_r$ is the rigid-body motion due to $\boldsymbol{f}$, is added to $\boldsymbol{f}$ in order to have an equilibrated load system $\boldsymbol{f}_e$ that is [18]

$$\boldsymbol{f}_e = \boldsymbol{f} - \boldsymbol{M} \cdot \ddot{\boldsymbol{u}}_r = \boldsymbol{P} \cdot \boldsymbol{f} \tag{2-112}$$

where $\boldsymbol{P}$ is called the inertia-relief projection matrix with

$$\boldsymbol{P} = \boldsymbol{I} - \boldsymbol{M} \cdot \boldsymbol{\Psi}_r \cdot \boldsymbol{\Psi}_r^T \tag{2-113}$$

$\boldsymbol{\Psi}_r$ are the rigid-body modes that have been normalized with respect to the mass matrix $\boldsymbol{M}$. The set of attachment modes $\boldsymbol{\Psi}_A$ measured relative to the "rigid-body" coordinates is defined by

$$\begin{bmatrix} \boldsymbol{K}_{ii} & \boldsymbol{K}_{ia} & \boldsymbol{K}_{ir} \\ \boldsymbol{K}_{ai} & \boldsymbol{K}_{aa} & \boldsymbol{K}_{ar} \\ \boldsymbol{K}_{ri} & \boldsymbol{K}_{ra} & \boldsymbol{K}_{rr} \end{bmatrix} \cdot \begin{bmatrix} \bar{\boldsymbol{\Psi}}_{ia} \\ \bar{\boldsymbol{\Psi}}_{aa} \\ \boldsymbol{0} \end{bmatrix} = \begin{bmatrix} \boldsymbol{P}_{ii} & \boldsymbol{P}_{ia} & \boldsymbol{P}_{ir} \\ \boldsymbol{P}_{ai} & \boldsymbol{P}_{aa} & \boldsymbol{P}_{ar} \\ \boldsymbol{P}_{ri} & \boldsymbol{P}_{ra} & \boldsymbol{P}_{rr} \end{bmatrix} \cdot \begin{bmatrix} \boldsymbol{0} \\ \boldsymbol{I} \\ \boldsymbol{0} \end{bmatrix} \tag{2-114}$$

In this case, there are no reaction forces at the "rigid-body" coordinates as the loads are

self-equilibrated. The attachment mode matrix $\bar{\Psi}_A$ is

$$\Psi_A \equiv \begin{bmatrix} \bar{\Psi}_{ia} \\ \bar{\Psi}_{aa} \\ \mathbf{0} \end{bmatrix} = \left[-\begin{bmatrix} \boldsymbol{K}_{ii} & \boldsymbol{K}_{ia} \\ \boldsymbol{K}_{ai} & \boldsymbol{K}_{aa} \end{bmatrix}^{-1} \begin{bmatrix} \mathbf{0} \\ \mathbf{0} \end{bmatrix} \cdot \begin{bmatrix} \boldsymbol{P}_{ii} & \boldsymbol{P}_{ia} & \boldsymbol{P}_{ir} \\ \boldsymbol{P}_{ai} & \boldsymbol{P}_{aa} & \boldsymbol{P}_{ar} \\ \boldsymbol{P}_{ri} & \boldsymbol{P}_{ra} & \boldsymbol{P}_{rr} \end{bmatrix} \cdot \begin{bmatrix} \mathbf{0} \\ \boldsymbol{I} \\ \mathbf{0} \end{bmatrix} = \boldsymbol{G} \cdot \boldsymbol{P} \cdot \boldsymbol{f} \tag{2-115}$$

This mode set is now made orthogonal to the rigid-body modes Ψ_r and it can be shown [18] that the resulting inertia-relief attachment mode set Ψ_A is

$$\Psi_A = \left(\boldsymbol{P}^T \boldsymbol{G} \boldsymbol{P} \right) \cdot \boldsymbol{f} \tag{2-116}$$

Basically, CMS can be divided into two different approaches: constraint-mode methods or attachment-mode methods. The latter ones employ attachment modes and free-interface normal modes, as presented by Mac-Neal [19] and Rubin [20]. They produce very good results, generally with a higher accuracy then constraint-mode methods, and are widely used in the context of experimental verification of finite element models [21]. The constraint-mode methods use fixed-interface normal modes that are supplemented by constraint modes. In reference [22], Hurty used fixed-interface normal modes with rigid-body modes and redundant-interface constraint modes. Instead of differentiating between rigid-body and redundant DOF, Craig and Bampton [23] simplified Hurty's method by using constraint modes and fixed-interface modes. The coordinate transformation matrix $\boldsymbol{T}$ for the Craig-Bampton method employs a combination of equations (2-103) and (2-105) and takes the form

$$\boldsymbol{T} = \begin{bmatrix} \Phi_{iN} & \Psi_{ib} \\ \mathbf{0} & \boldsymbol{I} \end{bmatrix} \tag{2-117}$$

Therefore, the set of physical FE coordinates $\boldsymbol{u}$ reduces to the set of generalized coordinates $\boldsymbol{v}$, with

$$\begin{bmatrix} \boldsymbol{u}_i \\ \boldsymbol{u}_b \end{bmatrix} = \begin{bmatrix} \Phi_{iN} & \Psi_{ib} \\ \mathbf{0} & \boldsymbol{I} \end{bmatrix} \cdot \begin{bmatrix} \boldsymbol{v}_N \\ \boldsymbol{v}_b \end{bmatrix} \tag{2-118}$$

where $\boldsymbol{v}_b$ are the physical boundary coordinates and $\boldsymbol{v}_N$ are modal coordinates. The resulting generalized mass and stiffness matrices are defined by equation (2-83) and can be written as

$$\begin{aligned} \boldsymbol{M}_T &= \begin{bmatrix} \boldsymbol{M}_{NN} & \boldsymbol{M}_{Nb} \\ \boldsymbol{M}_{bN} & \boldsymbol{M}_{bb} \end{bmatrix} \\ \boldsymbol{K}_T &= \begin{bmatrix} \boldsymbol{K}_{NN} & \mathbf{0} \\ \mathbf{0} & \boldsymbol{K}_{bb} \end{bmatrix} \end{aligned} \tag{2-119}$$

where $\boldsymbol{M}_{NN}$ and $\boldsymbol{K}_{NN}$ are diagonal as they are associated with eigenvectors. $\boldsymbol{M}_{Nb}$ and $\boldsymbol{M}_{bN}$ are not null matrices, which highlights that there is inertia coupling between the constraint modes and the fixed-interface normal modes.

The Craig-Bampton method combines the advantages of the two reduction methods

presented in the previous sections *a)* and *b)* - in fact, they can be regarded as special cases of CMS. On the one hand, the normal modes are truncated and allow a very high reduction of the interior (or slave) DOF while the dynamic properties of interest, i.e. natural frequencies and mode shapes, are still represented accurately. On the other hand, the use of constraint modes preserves the boundary (or master) DOF and allows the definition of arbitrary boundary conditions after the reduction, which greatly facilitates component coupling. Because of its very simple and straightforward formulation, the Craig-Bampton method is widely used in dynamic analysis. Therefore, it is also proposed as CMS technique in ANSYS and ADAMS for the generation of flexible bodies. The implementation of the generalized coordinates $\boldsymbol{v}$ into an MBS code is presented in the next section.

2.1.2.2 Equation of Motion for Flexible Bodies

The equation of motion for a flexible body *i* is derived from similar equations as presented in section *2.1.1*. In order to apply Lagrange's equation, the kinetic energy has to be determined. Therefore, the position and velocity of an arbitrary point on a flexible body are needed. From figure 2-6, the position in the global reference frame of a point P^i on a flexible body *i* is defined by

$$\boldsymbol{r}_{P^i} = \boldsymbol{r}^i + \boldsymbol{A}^i(\bar{\boldsymbol{s}}_{P^i} + \bar{\boldsymbol{u}}_{P^i}) \tag{2-120}$$

where $\boldsymbol{r}^i$ is the position of the origin of the selected body reference *X'Y'Z'*, $\boldsymbol{A}^i$ is the transformation matrix from the local coordinate system to the global coordinate system, $\bar{\boldsymbol{s}}_{P^i}$ is the position vector of point *P* with respect to the body reference *X'Y'Z'* in the undeformed state and $\bar{\boldsymbol{u}}_{P^i}$ is the deformation vector from the undeformed to the deformed position of P^i.

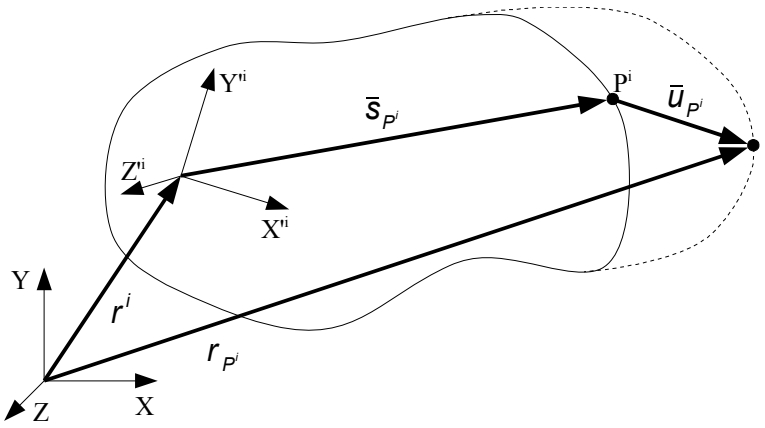

Figure 2-6: Flexible body positioning

This means, that the motion of a flexible body is defined by the motion of the local reference frame plus the motion of the material points on the body with respect to the local reference frame. For the following development, it is first of all assumed that the deformation of the body can be described by an approximation method such that the translational deformation of an arbitrary point P^i on a flexible body can be expressed as

$$\bar{\boldsymbol{u}}_{P^i} \approx \sum_k \boldsymbol{S}_{P^i}^k \cdot \boldsymbol{q}_f^{ik} = \boldsymbol{S}_{P^i} \cdot \boldsymbol{q}_f^i \tag{2-121}$$

where $\boldsymbol{S}_{P^i}$ is a matrix corresponding to point P^i that reflects the stiffness of the deformable body and $\boldsymbol{q}_f^i$ are the corresponding elastic coordinates of the body i that are time-dependent. According to equation (2-121), equation (2-120) can be written as

$$\boldsymbol{r}_{P^i} = \boldsymbol{r}^i + \boldsymbol{A}^i (\bar{\boldsymbol{s}}_{P^i} + \boldsymbol{S}_P^i \cdot \boldsymbol{q}_f^i) \tag{2-122}$$

And the generalized coordinates set for a flexible body i can be defined as

$$\boldsymbol{\xi}^i = \left\{ \boldsymbol{q}^{iT} \ \boldsymbol{q}_f^{iT} \right\}^T = \left\{ \boldsymbol{r}^{iT} \ \boldsymbol{\varepsilon}^{iT} \ \boldsymbol{q}_f^{iT} \right\}^T = \left\{ x^i \ y^i \ z^i \ \psi^i \ \theta^i \ \phi^i \ \boldsymbol{q}_f^{iT} \right\}^T \tag{2-123}$$

where $x^i \ y^i \ z^i \ \psi^i \ \theta^i \ \phi^i$, are the coordinates of the local reference frame that describe the rigid-body displacement and $\boldsymbol{q}_f^i$ are the elastic coordinates of the deformable body i.

The absolute velocity of a point P^i on a flexible body is obtained by taking the first time derivative of equation (2-122), that is

$$\dot{\boldsymbol{r}}_{P^i} = \dot{\boldsymbol{r}}^i + \dot{\boldsymbol{A}}^i \cdot (\bar{\boldsymbol{s}}_{P^i} + \boldsymbol{S}_{P^i} \cdot \boldsymbol{q}_f^i) + \boldsymbol{A}^i \cdot \boldsymbol{S}_{P^i} \cdot \dot{\boldsymbol{q}}_f^i \tag{2-124}$$

Substituting equation (2-13) and (2-14) into equation (2-124) yields

$$\begin{aligned} \dot{\boldsymbol{r}}_{P^i} &= \dot{\boldsymbol{r}}^i + \boldsymbol{A}^i \cdot \tilde{\bar{\boldsymbol{\omega}}}^i \cdot (\bar{\boldsymbol{s}}_{P^i} + \boldsymbol{S}_{P^i} \cdot \boldsymbol{q}_f^i) + \boldsymbol{A}^i \cdot \boldsymbol{S}_{P^i} \cdot \dot{\boldsymbol{q}}_f^i \\ &= \dot{\boldsymbol{r}}^i - \boldsymbol{A}^i \cdot \left(\tilde{\bar{\boldsymbol{s}}}_{P^i} + \widetilde{\boldsymbol{S}_{P^i} \cdot \boldsymbol{q}_f^i} \right) \cdot \bar{\boldsymbol{\omega}}^i + \boldsymbol{A}^i \cdot \boldsymbol{S}_{P^i} \cdot \dot{\boldsymbol{q}}_f^i \\ &= \dot{\boldsymbol{r}}^i - \boldsymbol{A}^i \cdot \left(\tilde{\bar{\boldsymbol{s}}}_{P^i} + \widetilde{\boldsymbol{S}_{P^i} \cdot \boldsymbol{q}_f^i} \right) \cdot \boldsymbol{B}^i \cdot \dot{\boldsymbol{\varepsilon}}^i + \boldsymbol{A}^i \cdot \boldsymbol{S}_{P^i} \cdot \dot{\boldsymbol{q}}_f^i \end{aligned} \tag{2-125}$$

In partitioned form, the absolute velocity can be written as

$$\dot{\boldsymbol{r}}_{P^i} = \begin{bmatrix} \boldsymbol{I} \\ -\boldsymbol{A}^i \cdot \left(\tilde{\bar{\boldsymbol{s}}}_{P^i} + \widetilde{\boldsymbol{S}_{P^i} \cdot \boldsymbol{q}_f^i} \right) \cdot \boldsymbol{B}^i \\ \boldsymbol{A}^i \cdot \boldsymbol{S}_{P^i} \end{bmatrix} \cdot \dot{\boldsymbol{\xi}}^i \tag{2-126}$$

Lagrange's equation is now used to derive the equation of motion of a flexible body i,

$$\frac{d}{dt} \left(\frac{\partial T^i}{\partial \dot{\boldsymbol{\xi}}^i} \right)^T - \left(\frac{\partial T^i}{\partial \boldsymbol{\xi}^i} \right)^T + \boldsymbol{C}_{\boldsymbol{\xi}^i}^T \cdot \boldsymbol{\lambda} - \boldsymbol{Q}^i = \boldsymbol{0} \tag{2-127}$$

where the kinetic energy T^i of a flexible body is defined by

$$T^i = \frac{1}{2} \int_{V^i} \rho^i \ \dot{\boldsymbol{r}}_{P^i}^T \ \dot{\boldsymbol{r}}_{P^i} \ dV^i \tag{2-128}$$

Substituting equation (2-126) into (2-128), the kinetic energy can be written as

$$\begin{aligned} T^i &= \frac{1}{2} \dot{\boldsymbol{\xi}}^{iT} \int_{V^i} \rho^i \cdot \begin{bmatrix} \boldsymbol{I} \\ -\boldsymbol{B}^{iT} \cdot \left(\tilde{\bar{\boldsymbol{s}}}_{P^i} + \widetilde{\boldsymbol{S}_{P^i} \cdot \boldsymbol{q}_f^i} \right)^T \cdot \boldsymbol{A}^{iT} \\ \boldsymbol{S}_{P^i}^T \cdot \boldsymbol{A}^{iT} \end{bmatrix} \cdot \left[\boldsymbol{I} \ \ -\boldsymbol{A}^i \cdot \left(\tilde{\bar{\boldsymbol{s}}}_{P^i} + \widetilde{\boldsymbol{S}_{P^i} \cdot \boldsymbol{q}_f^i} \right) \cdot \boldsymbol{B}^i \ \ \boldsymbol{A}^i \cdot \boldsymbol{S}_{P^i} \right] dV^i \ \dot{\boldsymbol{\xi}}^i \\ &= \frac{1}{2} \dot{\boldsymbol{\xi}}^{iT} \ \boldsymbol{M}^i \ \dot{\boldsymbol{\xi}}^i \end{aligned} \tag{2-129}$$

$\boldsymbol{M}^i$ is called the generalized mass matrix of the flexible body. It can be divided into sub-matrices and put in the symbolic form of

$$\boldsymbol{M}^i = \begin{bmatrix} \boldsymbol{M}^i_{rr} & \boldsymbol{M}^i_{r\varepsilon} & \boldsymbol{M}^i_{rq_f} \\ & \boldsymbol{M}^i_{\varepsilon\varepsilon} & \boldsymbol{M}^i_{\varepsilon q_f} \\ sym. & & \boldsymbol{M}^i_{q_f q_f} \end{bmatrix} \tag{2-130}$$

where

$$\begin{aligned}
\boldsymbol{M}^i_{rr} &= \int_{V^i} \rho^i \cdot \boldsymbol{I}\, dV^i \\
\boldsymbol{M}^i_{r\varepsilon} &= -\int_{V^i} \rho^i \cdot \boldsymbol{A}^i \cdot \left(\tilde{\tilde{\boldsymbol{s}}}_{P^i} + \widetilde{\boldsymbol{S}_{P^i} \cdot \boldsymbol{q}^i_f} \right) \cdot \boldsymbol{B}^i\, dV^i \\
\boldsymbol{M}^i_{rq_f} &= \int_{V^i} \rho^i \cdot \boldsymbol{A}^i \cdot \boldsymbol{S}_{P^i}\, dV^i \\
\boldsymbol{M}^i_{\varepsilon\varepsilon} &= \int_{V^i} \rho^i \cdot \boldsymbol{B}^{iT} \cdot \left(\tilde{\tilde{\boldsymbol{s}}}_{P^i} + \widetilde{\boldsymbol{S}_{P^i} \cdot \boldsymbol{q}^i_f} \right)^T \cdot \left(\tilde{\tilde{\boldsymbol{s}}}_{P^i} + \widetilde{\boldsymbol{S}_{P^i} \cdot \boldsymbol{q}^i_f} \right) \cdot \boldsymbol{B}^i\, dV^i \\
\boldsymbol{M}^i_{\varepsilon q_f} &= -\int_{V^i} \rho^i \cdot \boldsymbol{B}^{iT} \cdot \left(\tilde{\tilde{\boldsymbol{s}}}_{P^i} + \widetilde{\boldsymbol{S}_{P^i} \cdot \boldsymbol{q}^i_f} \right)^T \cdot \boldsymbol{S}_{P^i}\, dV^i \\
\boldsymbol{M}^i_{q_f q_f} &= \int_{V^i} \rho^i \cdot \boldsymbol{S}^T_{P^i} \cdot \boldsymbol{S}_{P^i}\, dV^i
\end{aligned} \tag{2-131}$$

Equation (2-131) shows that the solution of a flexible multi-body system needs a much higher computational effort than the solution of a rigid multi-body system. This results from the inertia coupling between the reference motion and the elastic deformation of the body. It is possible to determine several inertia terms in advance such as $\boldsymbol{M}^i_{rr}$ or parts of $\boldsymbol{M}^i_{r\varepsilon}$ and $\boldsymbol{M}^i_{\varepsilon\varepsilon}$. Nevertheless, the rest of the mass matrix has to be updated for each time-step as they depend on the orientation and motion of the body reference and the elastic coordinates.

It can be noticed from equation (2-131) that if the body is rigid, then the elastic deformations vanish and $\boldsymbol{M}^i_{rq_f}$, $\boldsymbol{M}^i_{\varepsilon q_f}$, $\boldsymbol{M}^i_{q_f q_f}$ are null matrices. The resulting mass matrix is identical to the one formulated in equation (2-71) for a rigid body. On the other hand, if no reference motion is allowed then the only remaining matrix is $\boldsymbol{M}^i_{q_f q_f}$, which is equivalent to the generalized mass matrix used in a linear structural analysis.

Equations (2-129) is used with Lagrange's equation (2-127) to finally give the equation of motion for a system of flexible bodies, similar as for rigid bodies (see equation (2-78)).

$$\boldsymbol{M}\cdot\ddot{\boldsymbol{\xi}}+\dot{\boldsymbol{M}}\cdot\dot{\boldsymbol{\xi}}-\frac{1}{2}\cdot\left(\frac{\partial \boldsymbol{M}}{\partial \boldsymbol{\xi}}\cdot\dot{\boldsymbol{\xi}}\right)^{T}\cdot\dot{\boldsymbol{\xi}}+\boldsymbol{D}\cdot\dot{\boldsymbol{\xi}}+\boldsymbol{K}\cdot\boldsymbol{\xi}+\boldsymbol{C}_{\xi}^{T}\cdot\boldsymbol{\lambda}-\boldsymbol{Q}=\boldsymbol{0}$$

$$\boldsymbol{C}(\boldsymbol{q},t)=\left[c_1(\boldsymbol{q},t)\quad c_2(\boldsymbol{q},t)\quad\cdots\quad c_{n_{ce}}(\boldsymbol{q},t)\right]^{T}=\boldsymbol{0}$$

$\boldsymbol{\xi},\dot{\boldsymbol{\xi}},\ddot{\boldsymbol{\xi}}$ are vectors containing the *n* generalized coordinates of the system and their time derivatives; for a flexible body *i* $\boldsymbol{\xi}^i=\left(x^i\ y^i\ z^i\ \psi^i\ \theta^i\ \phi^i\ \boldsymbol{q}_f^{iT}\right)^T$.

$\boldsymbol{M}$ is a *(n x n)* matrix containing the mass matrices $\boldsymbol{M}^i$ of each body *i* defined in equation (2-130) and (2-131).

$\dot{\boldsymbol{M}}$ is the time derivative of the mass matrix.

$\frac{\partial \boldsymbol{M}}{\partial \boldsymbol{\xi}}$ is a *(n x n x n)* matrix containing the partial derivative of the mass matrix with respect to the generalized coordinates.

$\boldsymbol{D}$ is the *(n x n)* damping matrix and is defined at the end of section 2.1.2.3.

$\boldsymbol{K}$ is a *(n x n)* matrix containing the stiffness matrices $\boldsymbol{K}^i$ of each body *i* defined in equation (2-138).

$\boldsymbol{C_q}$ is a (n_{ce} *x n)* matrix called the system Jacobian.

$\boldsymbol{\lambda}$ is a vector containing the n_{ce} Lagrange multipliers.

$\boldsymbol{Q}$ is a vector containing the *n* generalized forces.

$\boldsymbol{C}$ is an (n_{ce} *x n)* matrix containing the n_{ce} algebraic constraint equations.

(2-132)

A generalized force that is exclusively present in a system with flexible bodies is the elastic force due to the deformation of the bodies. Therefore, its expression is briefly developed in the following lines. According to [10, 25], the virtual work due to the elastic forces for a flexible body *i* can be written as

$$\delta W_e^i=-\int_{V^i}\boldsymbol{\sigma}^{iT}\cdot\delta\boldsymbol{\varepsilon}^i\,dV^i \tag{2-133}$$

where $\boldsymbol{\varepsilon}^i$ and $\boldsymbol{\sigma}^i$ are the strain and stress vectors, respectively. For a linear material and geometry, they are defined as

$$\boldsymbol{\varepsilon}^i=\boldsymbol{D}^i\cdot\bar{\boldsymbol{u}}^i\quad\text{and}\quad\boldsymbol{\sigma}^i=\boldsymbol{E}^i\cdot\boldsymbol{\varepsilon}^i \tag{2-134}$$

where $\boldsymbol{D}^i$ is the strain-displacement matrix and $\boldsymbol{E}^i$ is the stress-strain matrix. Based on equation (2-121), the deformation vector for the complete body can be written as

$$\bar{\boldsymbol{u}}^i=\boldsymbol{S}^i\cdot\boldsymbol{q}_f^i \tag{2-135}$$

Substituting into (2-134) leads to

$$\boldsymbol{\varepsilon}^i=\boldsymbol{D}^i\cdot\boldsymbol{S}^i\cdot\boldsymbol{q}_f^i\quad\text{and}\quad\boldsymbol{\sigma}^i=\boldsymbol{E}^i\cdot\boldsymbol{D}^i\cdot\boldsymbol{S}^i\cdot\boldsymbol{q}_f^i \tag{2-136}$$

Equation (2-133) can finally be written as

$$\begin{aligned}\delta W_e^i &= -\boldsymbol{q}_f^{iT}\cdot\left[\int_{V^i}\boldsymbol{S}^{iT}\cdot(\boldsymbol{D}^{iT}\cdot\boldsymbol{E}^i\cdot\boldsymbol{D}^i)\cdot\boldsymbol{S}^i\,dV^i\right]\cdot\delta\boldsymbol{q}_f^i \\ &= -\boldsymbol{q}_f^{iT}\cdot\boldsymbol{K}_{q_f q_f}^i\cdot\delta\boldsymbol{q}_f^i\end{aligned} \tag{2-137}$$

where $\boldsymbol{K}_{q_f q_f}^i$ is the stiffness matrix related to the elastic coordinates $\boldsymbol{q}_f^i$ of the flexible body *i*. Therefore, the generalized stiffness matrix $\boldsymbol{K}^i$ of a flexible body *i* has the form

$$\boldsymbol{K}^i = \begin{bmatrix} \mathbf{0} & \mathbf{0} & \mathbf{0} \\ & \mathbf{0} & \mathbf{0} \\ sym. & & \boldsymbol{K}_{q_f q_f}^i \end{bmatrix} \tag{2-138}$$

According to equation (2-45), the generalized elastic force $\boldsymbol{Q}^e$ for a system of flexible bodies is expressed as

$$\boldsymbol{Q}^e = -\boldsymbol{K}\cdot\xi \tag{2-139}$$

which can be added to equation (2-132).

2.1.2.3 Implementation of Flexible Bodies in ADAMS

The problem is to choose the appropriate matrix $\boldsymbol{S}$ to model the elastic deformation of a body. As indicated in section *2.1.2.1.*, the finite element method is generally used to model the flexibility of a body with an arbitrary geometry. As these FE models often present a large number of DOF, they have to be reduced before being included in a multi-body dynamic simulation. The reduction technique implemented by default in ADAMS is based on the Craig-Bampton method that uses normal modes and constraint modes. As explained at the end of section 2.1.2.1, the truncated set of normal modes allows a very high reduction of the number of interior DOF while the natural frequencies and mode shapes are still represented accurately. On the other hand, the constraint modes preserve the boundary DOF and allow the definition of arbitrary boundary conditions.

However, the original Craig-Bampton modal basis has a disadvantage that makes it inappropriate for a direct use in the multi-body formulation presented in the previous section. In fact, the set of constraint modes contains six rigid-body modes, or in other words, the rigid-body modes are represented by a linear combination of the constraint modes. However, as the large displacement of the flexible body is defined by the coordinates of the body reference frame, the rigid-body modes have to be removed. Besides, these linear rigid-body modes are generally not sufficient to describe the non-linear motion in space of a component. Deleting some constraint modes in order to disable the rigid-body modes is correct but not a feasible solution as the omission of a constraint mode is equivalent to restraining the corresponding boundary DOF.[4]

This problem is resolved by transforming the original Craig-Bampton basis with the solution of the eigenvalue problem [24]

$$\boldsymbol{K}_T\cdot\boldsymbol{v} = \lambda\cdot\boldsymbol{M}_T\cdot\boldsymbol{v} \tag{2-140}$$

4 In the following, the superscript *i*, which was used to identify a body *i*, is intentionally omitted to lighten up the formulas.

where $\boldsymbol{M}_T$ is the reduced mass matrix and $\boldsymbol{K}_T$ is the reduced stiffness matrix. The manipulation results in a modal basis where $\boldsymbol{v} = \boldsymbol{N} \cdot \check{\boldsymbol{q}}_f$. Finally, the reduction of the physical FE DOF $\boldsymbol{u}$ can be written as

$$\boldsymbol{u} = \boldsymbol{T} \cdot \boldsymbol{v} = \boldsymbol{T} \cdot \boldsymbol{N} \cdot \check{\boldsymbol{q}}_f \tag{2-141}$$

where $\boldsymbol{T}$ is defined by equation (2-117) which is recalled below

$$\boldsymbol{T} = \begin{bmatrix} \boldsymbol{\Phi}_{iN} & \boldsymbol{\Psi}_{ib} \\ \boldsymbol{0} & \boldsymbol{I} \end{bmatrix} \tag{2-142}$$

$\boldsymbol{N}$ contains the eigenvectors from equation (2-140) and $\check{\boldsymbol{q}}_f$ are the elastic coordinates of the flexible body. Comparing equation (2-141) with equation (2-121), matrix $\boldsymbol{S}$ of equation (2-121), denoted here by $\check{\boldsymbol{S}}$, can be identified as being

$$\check{\boldsymbol{S}} = \boldsymbol{T} \cdot \boldsymbol{N} \tag{2-143}$$

This is a purely mathematical approach and does not further reduce the number of DOF. The new modal basis has no direct physical meaning, but synthesized from the fixed-boundary normal modes and the constraint modes are two families of mode shapes: the first one approximates the mode shapes of the unconstrained structure and the second one defies any clear physical classification. However, the most important effect of this additional transformation is that it addresses the problem mentioned above. In fact, the mode shapes of the first family include the six rigid-body modes that can now be clearly identified. They are disabled by ADAMS by removing the corresponding coordinates and columns of $\check{\boldsymbol{q}}_f$ and matrix $\check{\boldsymbol{S}}$, respectively. The elimination of the rigid-body modes for the MBS formulation is henceforth underlined by using the denotation $\boldsymbol{q}_f$ and $\boldsymbol{S}$.

When relying on a FE model to describe a flexible body, the concept of infinitesimal volumes, implemented in the previous section, has to be replaced by a discrete approach using finite volumes. In that case, to each node of the FE mesh corresponds a finite volume. Thus, the volume integrals are replaced by sums and the total kinetic energy of a flexible body that is made up of n_p nodes can be written as

$$T = \frac{1}{2} \int_V \rho \, \dot{\boldsymbol{r}}_P^T \, \dot{\boldsymbol{r}}_P \, dV \approx \frac{1}{2} \cdot \sum_{p=1}^{n_P} \left(m_p \cdot \dot{\boldsymbol{r}}_p^T \cdot \dot{\boldsymbol{r}}_p + \boldsymbol{\omega}_p^T \cdot \boldsymbol{J}_p \cdot \boldsymbol{\omega}_p \right) \tag{2-144}$$

where m_p is the mass and $\boldsymbol{J}_p$ is the inertia tensor of the volume attached to node p. Generally, the inertia tensor $\boldsymbol{J}_p$ is a negligible quantity if the mesh is not too coarse [24].

The translational position $\boldsymbol{r}_p$ of a node p is expressed in the global reference frame, similar to equation (2-122), as

$$\boldsymbol{r}_p = \boldsymbol{r} + \boldsymbol{A} (\bar{\boldsymbol{s}}_p + \boldsymbol{S}_p \cdot \boldsymbol{q}_f) \tag{2-145}$$

where $\boldsymbol{r}$ is the position of the origin of the body reference expressed in the global reference frame. $\bar{\boldsymbol{s}}_p$ is the position vector of node p with respect to the body reference frame in the undeformed state of the FE model. $\boldsymbol{A}$ is the transformation matrix from the body reference

frame to a frame whose origin is coincident with the one of the local reference frame of the body and whose axes are parallel to those of the global reference frame. $\boldsymbol{S}_p$ is a matrix that contains the three rows of matrix $\boldsymbol{S}$, defined in equation (2-143), that correspond to the three translational degrees of freedom of node *p*. and $\boldsymbol{q}_f$ are the elastic coordinates of the flexible body.

Similar to equation (2-124), the velocity $\dot{\boldsymbol{r}}_p$ of a node *p* can be written as

$$\dot{\boldsymbol{r}}_p = \dot{\boldsymbol{r}} - \boldsymbol{A}\cdot\left(\tilde{\tilde{\boldsymbol{s}}}_p + \widetilde{\boldsymbol{S}_p\cdot\boldsymbol{q}_f}\right)\cdot\boldsymbol{B}\cdot\dot{\boldsymbol{\xi}} + \boldsymbol{A}\cdot\boldsymbol{S}_p\cdot\dot{\boldsymbol{q}}_f \tag{2-146}$$

Equation (2-146) can finally be transformed into

$$\dot{\boldsymbol{r}}_p = \left[\boldsymbol{I} \quad -\boldsymbol{A}\cdot\left(\tilde{\tilde{\boldsymbol{s}}}_p + \widetilde{\boldsymbol{S}_p\cdot\boldsymbol{q}_f}\right)\cdot\boldsymbol{B} \quad \boldsymbol{A}\cdot\boldsymbol{S}_p\right]\cdot\dot{\boldsymbol{\xi}} \tag{2-147}$$

In order to respect any angular constraints defined in the MBS at a node *p*, the orientation of a frame rigidly attached to that node must be known. This frame is called in the following nodal reference frame and it is assumed that it is initially parallel to the body reference frame[5]. In the next paragraph, the expression for the orientation of the nodal reference frame with respect to the global reference frame using $\boldsymbol{q}_f$ and $\boldsymbol{S}$ is developed.

As the deformations of the flexible bodies are supposed to be very small, the rotation of a nodal reference frame with respect to the body reference frame can be expressed as

$$\boldsymbol{\theta}_p = \hat{\boldsymbol{S}}_p\cdot\boldsymbol{q}_f \tag{2-148}$$

where $\hat{\boldsymbol{S}}_p$ contains only the three rows of matrix $\boldsymbol{S}$ that correspond to the three rotational degrees of freedom of node *p*. The orientation of a nodal reference frame relative to the global reference frame is defined by the transformation matrix $\boldsymbol{A}^p$, where

$$\boldsymbol{A}^p = \boldsymbol{A}\cdot{}^B\boldsymbol{A}^p \tag{2-149}$$

${}^B\boldsymbol{A}^p$ is the transformation matrix that takes into account the deformation at node *p*. Using the direction cosines and considering small rotations, ${}^B\boldsymbol{A}^p$ can be expressed as

$${}^B\boldsymbol{A}^p = \begin{bmatrix} 1 & -\theta_{pz} & \theta_{py} \\ \theta_{pz} & 1 & -\theta_{px} \\ -\theta_{py} & \theta_{px} & 1 \end{bmatrix} = \boldsymbol{I} + \tilde{\boldsymbol{\theta}}_p \tag{2-150}$$

where $\boldsymbol{\theta}_p$ is defined in equation (2-148) and $\sim$ is the skew-symmetric operator. Finally, the transformation matrix $\boldsymbol{A}^p$ is defined by

$$\boldsymbol{A}^p = \boldsymbol{A}\cdot\left(\boldsymbol{I} + \tilde{\boldsymbol{\theta}}_p\right) \tag{2-151}$$

Still remains the definition of the angular velocity of a nodal reference frame $\boldsymbol{\omega}_p$. In fact, it can be expressed as the sum of the angular velocity of the body reference frame and the angular velocity due to the deformation. According to equation (2-14) and (2-148), $\boldsymbol{\omega}_p$ can be written as

5 This is not imperative but allows to simplify the formulation of the following equations.

$$\omega_p = \boldsymbol{B}\cdot\dot{\varepsilon} + \hat{\boldsymbol{S}}_p\cdot\dot{\boldsymbol{q}}_f \tag{2-152}$$

which can be put in the partitioned form

$$\omega_p = \begin{bmatrix}\boldsymbol{0} & \boldsymbol{B} & \hat{\boldsymbol{S}}_p\end{bmatrix}\cdot\dot{\xi} \tag{2-153}$$

Now, substituting equations (2-147) and (2-153) into equation (2-144) yields

$$\begin{aligned} T = \frac{1}{2}\cdot\sum_{p=1}^{n_P}\left(m_p\cdot\dot{\xi}^T\cdot\begin{bmatrix}\boldsymbol{I} & -\boldsymbol{B}^T\cdot\left(\tilde{\tilde{\boldsymbol{s}}}_p+\widetilde{\boldsymbol{S}_p\cdot\boldsymbol{q}_f}\right)^T\cdot\boldsymbol{A}^T & \boldsymbol{S}_p^T\cdot\boldsymbol{A}^T\end{bmatrix}\cdot\begin{bmatrix}\boldsymbol{I} & -\boldsymbol{A}\cdot\left(\tilde{\tilde{\boldsymbol{s}}}_p+\widetilde{\boldsymbol{S}_p\cdot\boldsymbol{q}_f}\right)\cdot\boldsymbol{B} & \boldsymbol{A}\cdot\boldsymbol{S}_p\end{bmatrix}\cdot\dot{\xi}\right) \\ + \frac{1}{2}\cdot\sum_{p=1}^{n_P}\left(\dot{\xi}^T\cdot\begin{bmatrix}\boldsymbol{0} & \boldsymbol{B}^T\hat{\boldsymbol{S}}_p^T\end{bmatrix}\cdot\boldsymbol{J}_p\cdot\begin{bmatrix}\boldsymbol{0} & \boldsymbol{B} & \hat{\boldsymbol{S}}_p\end{bmatrix}\cdot\dot{\xi}\right)\end{aligned} \tag{2-154}$$

which can be put in the simplified form

$$T = \frac{1}{2}\cdot\dot{\xi}^T\cdot\boldsymbol{M}\cdot\dot{\xi} \tag{2-155}$$

where $\boldsymbol{M}$ is the generalized mass matrix of the flexible body and

$$\boldsymbol{M} = \begin{bmatrix}\boldsymbol{M}_{rr} & \boldsymbol{M}_{r\varepsilon} & \boldsymbol{M}_{rq_f} \\ & \boldsymbol{M}_{\varepsilon\varepsilon} & \boldsymbol{M}_{\varepsilon q_f} \\ sym. & & \boldsymbol{M}_{q_f q_f}\end{bmatrix} \tag{2-156}$$

with[6]

$$\boldsymbol{M}_{rr} = \bar{I}^1\boldsymbol{I} \qquad (3\ x\ 3) \tag{2-157}$$

$$\boldsymbol{M}_{r\varepsilon} = -\boldsymbol{A}\cdot\left[\tilde{\tilde{\bar{\boldsymbol{I}}}}^2+\widetilde{\bar{\boldsymbol{I}}^3\cdot\boldsymbol{q}_f}\right]\cdot\boldsymbol{B} \qquad (3\ x\ 3) \tag{2-158}$$

$$\boldsymbol{M}_{rq_f} = \boldsymbol{A}\cdot\bar{\boldsymbol{I}}^3 \qquad (3\ x\ k) \tag{2-159}$$

$$\boldsymbol{M}_{\varepsilon\varepsilon} = \boldsymbol{B}^T\cdot\left[\bar{\boldsymbol{I}}^7+\bar{\boldsymbol{I}}^8+(\bar{\boldsymbol{I}}^8)^T+\bar{\boldsymbol{I}}^9\right]\cdot\boldsymbol{B} \qquad (3\ x\ 3) \tag{2-160}$$

$$\boldsymbol{M}_{\varepsilon q_f} = -\boldsymbol{B}^T\cdot\left[\bar{\boldsymbol{I}}^4+\bar{\boldsymbol{I}}^5\right] \qquad (3\ x\ k) \tag{2-161}$$

$$\boldsymbol{M}_{q_f q_f} = \bar{\boldsymbol{I}}^6 \qquad (k\ x\ k) \tag{2-162}$$

k is the number of elastic coordinates $\boldsymbol{q}_f$ and $\boldsymbol{I}$ is the identity matrix. $\bar{\boldsymbol{I}}$ are terms, defined in equation (2-163) through (2-171), that depend on the elastic coordinates $\boldsymbol{q}_f$, the nodal masses m_p, the nodal inertia tensors $\boldsymbol{J}_p$, the nodal positions in the undeformed state $\bar{\boldsymbol{s}}_p$ and the shape vectors $\boldsymbol{S}_p$ and $\hat{\boldsymbol{S}}_p$. In fact, all these terms are time-invariant, except for $\bar{\boldsymbol{I}}^5$, $\bar{\boldsymbol{I}}^8$ and $\bar{\boldsymbol{I}}^9$ that depend on $\boldsymbol{q}_f$. However, they could also be further stripped down and expressed by time-invariant expressions as in [10] and [24].

$$\bar{I}^1 = \sum_{i=1}^{n_p} m_p \qquad (\text{scalar}) \tag{2-163}$$

$$\bar{\boldsymbol{I}}^2 = \sum_{i=1}^{n_p} m_p\cdot\bar{\boldsymbol{s}}_p \qquad (3\ x\ 1) \tag{2-164}$$

6 A more detailed development of the following expressions is found in appendix A.

$$\bar{\boldsymbol{l}}^3 = \sum_{i=1}^{n_p} m_p \cdot \boldsymbol{S}_p \qquad (3\ x\ k) \qquad (2\text{-}165)$$

$$\bar{\boldsymbol{l}}^4 = \sum_{i=1}^{n_p} m_p \cdot \tilde{\boldsymbol{s}}_p^T \cdot \boldsymbol{S}_p + \boldsymbol{J}_p \cdot \hat{\boldsymbol{S}}_p \qquad (3\ x\ k) \qquad (2\text{-}166)$$

$$\bar{\boldsymbol{l}}^5 = \sum_{i=1}^{n_p} m_p \cdot (\widetilde{\boldsymbol{S}_p \cdot \boldsymbol{q}_f})^T \cdot \boldsymbol{S}_p \qquad (3\ x\ k) \qquad (2\text{-}167)$$

$$\bar{\boldsymbol{l}}^6 = \sum_{i=1}^{n_p} m_p \cdot \boldsymbol{S}_p^T \cdot \boldsymbol{S}_p + \hat{\boldsymbol{S}}_p^T \cdot \boldsymbol{J}_p \cdot \hat{\boldsymbol{S}}_p \qquad (k\ x\ k) \qquad (2\text{-}168)$$

$$\bar{\boldsymbol{l}}^7 = \sum_{i=1}^{n_p} m_p \cdot \tilde{\boldsymbol{s}}_p^T \cdot \tilde{\boldsymbol{s}}_p + \boldsymbol{J}_p \qquad (3\ x\ 3) \qquad (2\text{-}169)$$

$$\bar{\boldsymbol{l}}^8 = \sum_{i=1}^{n_p} m_p \cdot \tilde{\boldsymbol{s}}_p^T \cdot \widetilde{\boldsymbol{S}_p \cdot \boldsymbol{q}_f} \qquad (3\ x\ 3) \qquad (2\text{-}170)$$

$$\bar{\boldsymbol{l}}^9 = \sum_{i=1}^{n_p} m_p \cdot (\widetilde{\boldsymbol{S}_p \cdot \boldsymbol{q}_f})^T \cdot (\widetilde{\boldsymbol{S}_p \cdot \boldsymbol{q}_f}) \qquad (3\ x\ 3) \qquad (2\text{-}171)$$

Finally, one remark concerning damping of flexible bodies in ADAMS. Damping of any kind is not considered by the Craig-Bampton reduction. This means that material damping or structural damping is not taken into account by the reduced FE model. Of course on the other hand, damping can be included in the MBS model through, for example, spring-damper elements or friction within joints. These elements add damping to the flexible body and affect the dying away of vibrations of the flexible body. Additionally, ADAMS allows the user to directly specify to the flexible body a damping ratio. Assuming that the damping forces only depend on the elastic coordinates $\boldsymbol{q}_f$, they can be derived from the Rayleigh dissipation function [24]

$$R = \frac{1}{2} \cdot \dot{\boldsymbol{q}}_f^T \cdot \boldsymbol{D} \cdot \dot{\boldsymbol{q}}_f \qquad (2\text{-}172)$$

Generally, the damping matrix $\boldsymbol{D}$ has non-zero coefficients. However, the eigenvectors of the modified Craig-Bampton basis are orthogonal and several of these eigenvectors approximate the mode shapes of the unconstrained structure. Thus, it comes in very handy to arbitrarily define the damping matrix $\boldsymbol{D}$ to be diagonal and to work with modal damping factors as used in the dynamic analysis of linear structures. In fact, a damping ratio η_i relative to the critical damping coefficient c_i^{cr} is defined, where

$$c_i = \eta_i c_i^{cr} = \eta_i 2\sqrt{k_i m_i} \qquad (2\text{-}173)$$

If such damping is specified by the user, then the term $\boldsymbol{D} \cdot \dot{\xi}$ is added to equation (2-132).

During this work, flexible bodies were derived from FE models that were generated with ANSYS. These FE models have to be detailed enough to correctly represent the frequencies and mode shapes of interest. Impact-hammer modal analysis measurements were

performed to verify the computed natural frequencies and mode shapes. The Craig-Bampton reduction and the following orthonormalization is also done within ANSYS. The necessary information is written to a file that is then imported into ADAMS. Adding flexible bodies to an ADAMS model is quite straightforward. Nevertheless, there are still some limitations regarding forces and joints that can be defined to them. Especially the problem of a moving force on a flexible body, i.e. moving platen sliding on clamp base, is still an open issue. However, there are "standard" workarounds which work well and which have proved their usefulness. A more detailed presentation of the generation of FE models in ANSYS and the solution implemented to model a moving force on a flexible body can be found in chapter 5.

2.1.3 Slider Crank Mechanism

The classical slider crank mechanism of figure 2-7 is chosen to illustrate the formulas derived in the previous sections. It consists of three bodies: body 1, which is the slider block, body 2, the crankshaft and body 3, the link. The mechanism is assumed to be planar, i.e. motion is only allowed in the *XY* plane. Furthermore, gravity is neglected. Body 1 slides on the ground. It is modeled as a rigid body and its center of mass is located at *B*. Body 2 is fixed to the ground but can rotate at *O* about the *Z* axis; it is also modeled as a rigid body. Body 3 is fixed to body 1 and body 2 at *B* and *A*, respectively, with the rotation about the *Z* axis being possible. However, body 3 is modeled as a flexible body. Finally, in order to actuate the slider crank mechanism, a driving moment *M* is applied to body 2.

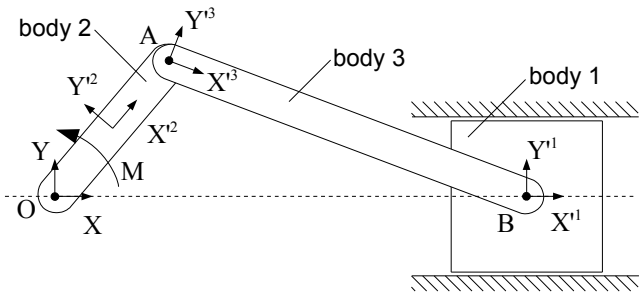

Figure 2-7: Slider crank mechanism

2.1.3.1 Kinematics and Kinetic Energy of the Rigid Bodies 1 & 2

The global reference frame *XYZ* has its origin at *O*. The local reference frame *X'Y'Z'* for body 1 and 2 is rigidly attached to the center of mass of the respective body as shown in figure 2-7. The global position and velocity of an arbitrary point P^i on the rigid body *i* is defined by equation (2-1) and (2-15) as

$$\boldsymbol{r}_{P^i} = \boldsymbol{r}^i + \boldsymbol{A}^i \cdot \bar{\boldsymbol{s}}_{P^i} \quad \text{and} \quad \dot{\boldsymbol{r}}_{P^i} = \dot{\boldsymbol{r}}^i + \boldsymbol{A}^i \cdot \tilde{\bar{\boldsymbol{\omega}}}^i \cdot \bar{\boldsymbol{s}}_{P^i} \tag{2-174}$$

$\bar{\boldsymbol{s}}_{P^i}$ is the vector of coordinates of point P^i in the local reference and $\bar{\omega}^i$ is

$$\bar{\boldsymbol{\omega}}^i = \boldsymbol{B}^i \cdot \dot{\boldsymbol{\varepsilon}}^i \tag{2-175}$$

As the motion is planar, the coordinates $\boldsymbol{z}^i$ and the Euler angles θ^i and ϕ^i are zero, i.e.

$$z^i = \theta^i = \phi^i = 0 \tag{2-176}$$

These expressions are in fact constraint equations and could only be taken into account during the formulation of the constraints. However, to simplify the equations already at this state, they are implemented immediately. Thus, substituting equation (2-176) into equation (2-6), (2-14) and (2-20), the set of generalized coordinates $\boldsymbol{q}^i$, the transformation matrix $\boldsymbol{A}^i$, the matrix $\boldsymbol{B}^i$ and the angular velocity of the local frame $\bar{\omega}^i$ for body 1 and 2 are

$$\boldsymbol{q}^i = \begin{bmatrix} x^i \\ y^i \\ 0 \\ \psi^i \\ 0 \\ 0 \end{bmatrix},\ \boldsymbol{A}^i = \begin{bmatrix} \cos\psi^i & -\sin\psi^i & 0 \\ \sin\psi^i & \cos\psi^i & 0 \\ 0 & 0 & 1 \end{bmatrix},\ \boldsymbol{B}^i = \begin{bmatrix} 0 & 1 & 0 \\ 0 & 0 & 0 \\ 1 & 0 & 1 \end{bmatrix} \text{ and } \bar{\omega}^i = \begin{bmatrix} 0 \\ 0 \\ \dot{\psi}^i \end{bmatrix} \tag{2-177}$$

And substituting equation (2-177) into equation (2-174), the global position and velocity of an arbitrary point P^i can be written as

$$\begin{cases} x_{P^i} = x^i + \bar{x}_{P^i} \cdot \cos\psi^i - \bar{y}_{P^i} \cdot \sin\psi^i \\ y_{P^i} = y^i + \bar{x}_{P^i} \cdot \sin\psi^i + \bar{y}_{P^i} \cdot \cos\psi^i \\ z_{P^i} = 0 \end{cases} \text{ and } \begin{cases} \dot{x}_{P^i} = \dot{x}^i - (\bar{x}_{P^i} \cdot \sin\psi^i - \bar{y}_{P^i} \cdot \cos\psi^i) \cdot \dot{\psi}^i \\ \dot{y}_{P^i} = \dot{y}^i + (\bar{x}_{P^i} \cdot \cos\psi^i - \bar{y}_{P^i} \cdot \sin\psi^i) \cdot \dot{\psi}^i \\ \dot{z}_{P^i} = 0 \end{cases} \tag{2-178}$$

The kinetic energy of body 1 and 2 is defined as

$$T^i = \frac{1}{2} \int_{V^i} \rho^i \cdot \dot{\boldsymbol{r}}_{P^i}^T \cdot \dot{\boldsymbol{r}}_{P^i} \cdot dV^i \tag{2-179}$$

where V^i is the volume and ρ^i is the mass density. Substituting (2-174) into (2-179) yields

$$T^i = \frac{1}{2} \cdot \dot{\boldsymbol{q}}^{iT} \cdot \begin{bmatrix} \int_{V^i} \rho^i \cdot dV^i \cdot \boldsymbol{I} & -\boldsymbol{A}^i \cdot \int_{V^i} \rho^i \cdot \tilde{\tilde{\boldsymbol{s}}}_{P^i} \cdot dV^i \cdot \boldsymbol{B}^i \\ sym & \boldsymbol{B}^{iT} \cdot \int_{V^i} \rho^i \cdot \tilde{\tilde{\boldsymbol{s}}}_{P^i}^T \cdot \tilde{\tilde{\boldsymbol{s}}}_{P^i} \cdot dV^i \cdot \boldsymbol{B}^i \end{bmatrix} \cdot \dot{\boldsymbol{q}}^i \tag{2-180}$$

It can be written that

$$\int_{V^i} \rho^i \cdot dV^i = m^i \tag{2-181}$$

where m^i is the total mass of body *i*, furthermore

$$\int_{V^i} \rho^i \cdot \tilde{\tilde{\boldsymbol{s}}}_{P^i} \cdot dV^i = \boldsymbol{0} \tag{2-182}$$

as the origin of the local reference frame is defined at the center of mass, and

$$\int_{V^i} \rho^i \cdot \tilde{\tilde{\boldsymbol{s}}}_{P^i}^T \cdot \tilde{\tilde{\boldsymbol{s}}}_{P^i} \cdot dV^i = \boldsymbol{J}^i \tag{2-183}$$

where $\boldsymbol{J}^i$ is the inertia tensor of body *i*.

Substituting equation (2-177), (2-181), (2-182) and (2-183) into equation (2-180) leads to

$$T^i = \frac{1}{2}\cdot[\dot{x}^i \quad \dot{y}^i \quad 0 \quad \dot{\psi}^i \quad 0 \quad 0]\cdot\begin{bmatrix} m^i & 0 & 0 & 0 & 0 & 0 \\ 0 & m^i & 0 & 0 & 0 & 0 \\ 0 & 0 & m^i & 0 & 0 & 0 \\ 0 & 0 & 0 & J^i_{zz} & J^i_{zx} & J^i_{zz} \\ 0 & 0 & 0 & J^i_{xz} & J^i_{xx} & J^i_{xz} \\ 0 & 0 & 0 & J^i_{zz} & J^i_{zx} & J^i_{zz} \end{bmatrix}\cdot\begin{bmatrix} \dot{x}^i \\ \dot{y}^i \\ 0 \\ \dot{\psi}^i \\ 0 \\ 0 \end{bmatrix} \tag{2-184}$$

Equation (2-184) finally simplifies to

$$T^i = \frac{1}{2}\cdot\left[m^i\cdot\left(\dot{x}^i\right)^2 + m^i\cdot\left(\dot{y}^i\right)^2 + J^i_{zz}\cdot\left(\dot{\psi}^i\right)^2\right] \tag{2-185}$$

which is, as expected, the general expression of the kinetic energy of a rigid body for a planar motion.

2.1.3.2 Kinematics and Kinetic Energy of the Flexible Body

In order to account for the flexibility of the link, the component is modeled with five beam elements as shown in figure 2-8. The FE model has six equidistant nodes with each node having two translational and one rotational DOF.

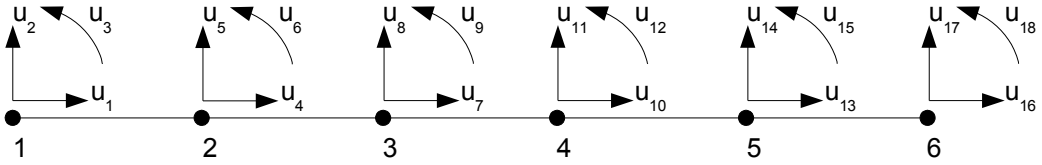

Figure 2-8: Finite element model

The full FE model of figure 2-8 has eighteen physical DOF and is reduced according to the Craig-Bampton method as described in section *2.1.2.1*. Therefore, node 1 and node 6 are chosen as interface nodes for the MBS model as they are attached to body 2 at *A* and to body 1 at *B*, respectively. Each node having three DOF, a total of six constraint modes are computed. Additionally, the first three normal modes of the structure, with node 1 and node 6 being fully restrained, are computed for the reduction. ANSYS is used to determine the nine component modes. For this purpose, the link has the following properties: overall length 0.5 m, section area 0.0004 m^2, density 7850 kg/m^3 and E-module $2.1\cdot10^{11}$ Pa. It is modeled with the element BEAM3, a 2-D Euler-Bernoulli beam element with three DOF at each node. The element has tension, compression and bending capabilities and the results are summarized in table 2-1.

These modes are used to fill the transformation matrix ***T***. If the physical DOF are arranged according to interior and boundary DOF as in equation (2-100), then ***T*** takes the form

$$\boldsymbol{T} = {}^{1}_{18}\left[\boldsymbol{\Phi}^1_N \quad \boldsymbol{\Phi}^2_N \quad \boldsymbol{\Phi}^3_N \quad \boldsymbol{\Psi}^{u_1}_C \quad \boldsymbol{\Psi}^{u_2}_C \quad \boldsymbol{\Psi}^{u_3}_C \quad \boldsymbol{\Psi}^{u_{16}}_C \quad \boldsymbol{\Psi}^{u_{17}}_C \quad \boldsymbol{\Psi}^{u_{18}}_C\right]^{9} \tag{2-186}$$

and

$$\left\{u_4 \cdots u_{15}\ u_1\ u_2\ u_3\ u_{16}\ u_{17}\ u_{18}\right\}^T = \boldsymbol{T}\cdot\left\{v_1\ v_2\ v_3\ u_1\ u_2\ u_3\ u_{16}\ u_{17}\ u_{18}\right\}^T \tag{2-187}$$

where v_1, v_2, v_3 are modal coordinates.

Normal Modes	*Mode Shape*	*Comment*
$\boldsymbol{\Phi}_N^1$: 451.6 Hz	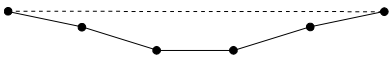	1st bending shape
$\boldsymbol{\Phi}_N^2$: 1357 Hz		2nd bending shape
$\boldsymbol{\Phi}_N^3$: 3044 Hz	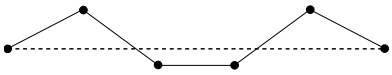	3rd bending shape

Constraint Modes	*Static Shape*	*Comment*
$\boldsymbol{\Psi}_C^{u_1}$		u_2, u_3, u_{16}, u_{17}, u_{18} fixed
$\boldsymbol{\Psi}_C^{u_2}$		u_1, u_3, u_{16}, u_{17}, u_{18} fixed
$\boldsymbol{\Psi}_C^{u_3}$		u_1, u_2, u_{16}, u_{17}, u_{18} fixed
$\boldsymbol{\Psi}_C^{u_{16}}$		u_1, u_2, u_3, u_{17}, u_{18} fixed
$\boldsymbol{\Psi}_C^{u_{17}}$	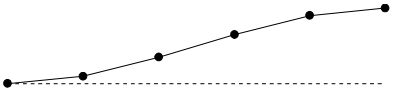	u_1, u_2, u_3, u_{16}, u_{18} fixed
$\boldsymbol{\Psi}_C^{u_{18}}$	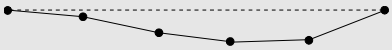	u_1, u_2, u_3, u_{16}, u_{17} fixed

Table 2-1: Craig-Bampton Modes

This Craig-Bampton basis is then transformed, again within ANSYS, by solving the eigenvalue problem as described in section *2.1.2.3* such that

$$\left\{v_1\ v_2\ v_3\ u_1\ u_2\ u_3\ u_{16}\ u_{17}\ u_{18}\right\}^T = \boldsymbol{N}\cdot\left\{q_f^1\ q_f^2\ q_f^3\ q_f^4\ q_f^5\ q_f^6\ q_f^7\ q_f^8\ q_f^9\right\}^T \tag{2-188}$$

The final reduction matrix reduces the eighteen physical DOF $\boldsymbol{u}$ to nine coordinates $\check{\boldsymbol{q}}_f$ according to

$$\boldsymbol{u} = \boldsymbol{T}\cdot\boldsymbol{N}\cdot\check{\boldsymbol{q}}_f = \check{\boldsymbol{S}}\cdot\check{\boldsymbol{q}}_f \tag{2-189}$$

Synthesized from the fixed-boundary normal modes and the constraint modes are eigenvectors that approximate the normal modes of the unconstrained structure, including the three rigid-body modes that must be disabled for ADAMS. It was previously said that these rigid-body modes are a linear combination of the constraint modes. In fact, it can be clearly seen from table 2-1 that the horizontal and vertical rigid-body mode is described by the sum of $\boldsymbol{\Psi}_C^{u_1}$ and $\boldsymbol{\Psi}_C^{u_{16}}$ and the sum of $\boldsymbol{\Psi}_C^{u_2}$ and $\boldsymbol{\Psi}_C^{u_{17}}$, respectively. Furthermore, it can be shown that the rotational rigid-body mode is described by $-0.5\cdot\boldsymbol{\Psi}_C^{u_2}+0.5\cdot\boldsymbol{\Psi}_C^{u_{17}}+\boldsymbol{\Psi}_C^{u_3}+\boldsymbol{\Psi}_C^{u_{18}}$. As the non-linear motion of the flexible body is represented by the coordinates of the body reference frame, the rigid-body modes of the reduced FE model must be disabled. This can now be easily done by removing the coordinates q_f^1, q_f^2 and q_f^3 and the corresponding

columns of matrix $\check{\boldsymbol{S}}$. Finally, the set of elastic coordinates of the flexible body is denoted as $\boldsymbol{q}_f$ and the transformation matrix is denoted as $\boldsymbol{S}$, with

$$\boldsymbol{q}_f = \begin{bmatrix} q_f^4 & q_f^5 & q_f^6 & q_f^7 & q_f^8 & q_f^9 \end{bmatrix} \tag{2-190}$$

Table 2-2 regroups the eigenvalues of the modified Craig-Bampton basis and compares them to the natural frequencies of the unrestrained FE model. As stated earlier, some eigenvectors of the modified Craig-Bampton basis approximate the first mode shapes of the unrestrained FE model, while for the remaining eigenvectors, no clear physical interpretation can be given.

modified Craig-Bampton		***full unrestrained FE model***	***Comment***
q_f^1	0 Hz	0 Hz	rigid-body mode
q_f^2	0 Hz	0 Hz	rigid-body mode
q_f^3	0 Hz	0 Hz	rigid-body mode
q_f^4	383.6 Hz	383.6 Hz	1st bending shape
q_f^5	1031.6 Hz	1031.6 Hz	2nd bending shape
q_f^6	2109.2 Hz	2109.2 Hz	3rd bending shape
q_f^7	5487.9 Hz		no physical meaning
q_f^8	5556.0 Hz		no physical meaning
q_f^9	20056.6 Hz		no physical meaning

Table 2-2: Comparison of eigenfrequencies

The local reference frame of body 3 is attached at *A* as shown in figure 2-7. The absolute position and velocity vector of a node *i*, $\boldsymbol{r}_i$ and $\dot{\boldsymbol{r}}_i$ respectively, is

$$\boldsymbol{r}_i = \boldsymbol{r}^3 + \boldsymbol{A}^3 \left(\bar{\boldsymbol{s}}_i + \boldsymbol{S}_i \cdot \boldsymbol{q}_f \right) \text{ and } \dot{\boldsymbol{r}}_i = \dot{\boldsymbol{r}}^3 - \boldsymbol{A}^3 \cdot \left(\tilde{\bar{\boldsymbol{s}}}_i + \widetilde{\boldsymbol{S}_i \cdot \boldsymbol{q}_f} \right) \cdot \boldsymbol{B}^3 \cdot \dot{\boldsymbol{\varepsilon}}^3 + \boldsymbol{A}^3 \cdot \boldsymbol{S}_i \cdot \dot{\boldsymbol{q}}_f \tag{2-191}$$

The transformation matrix $\boldsymbol{A}^3$, the matrix $\boldsymbol{B}^3$ and the angular velocity of the local frame $\bar{\omega}^3$ of body 3 are identical to the rigid-body ones defined in equation (2-177). $\bar{\boldsymbol{s}}_i$ is the position vector of node *i* with respect to the body reference frame in the undeformed state of the FE model and $\boldsymbol{S}_i$ is a matrix that contains the two rows of the transformation matrix $\boldsymbol{S}$ that correspond to the two translational degrees of freedom of node *i*. Considering that $\boldsymbol{z}^3$, θ^3 and ϕ^3 are zero, the set of generalized coordinates of body 3 is

$$\xi = \begin{bmatrix} \boldsymbol{r}^{3\,T} & \boldsymbol{\varepsilon}^{3\,T} & \boldsymbol{q}_f^T \end{bmatrix}^T = \begin{bmatrix} x^3 & y^3 & \psi^3 & \boldsymbol{q}_f^T \end{bmatrix}^T \tag{2-192}$$

The position vector in the undeformed state $\bar{\boldsymbol{s}}_i$ and the mass m_i of node *i* given by ANSYS are listed in table 2-3; the inertia tensor $\boldsymbol{J}_i$ being zero. In fact, the Craig-Bampton reduction in ANSYS is done with lumped element mass matrices. This means that the mass and inertia terms for a particular node are found on the main diagonal of the mass matrix; and for this particular element the inertia tensor is zero.

node	$\bar{s}$	m
1	$[0 \quad 0 \quad 0]^T$	0.157
2	$[0.1 \quad 0 \quad 0]^T$	0.314
3	$[0.2 \quad 0 \quad 0]^T$	0.314
4	$[0.3 \quad 0 \quad 0]^T$	0.314
5	$[0.4 \quad 0 \quad 0]^T$	0.314
6	$[0.5 \quad 0 \quad 0]^T$	0.157

Table 2-3: Node properties

Finally, the total kinetic energy of body 3 can be written as

$$T^3 = \frac{1}{2}\,\dot{\xi}^T \cdot \boldsymbol{M}^3 \cdot \dot{\xi} \quad =>$$

$$T^3 = \frac{1}{2}\begin{bmatrix} x^3 & y^3 & \psi^3 & q_f^4 & \dots & q_f^9 \end{bmatrix} \cdot \begin{bmatrix} \boldsymbol{M}_{rr} & \boldsymbol{M}_{r\varepsilon} & \boldsymbol{M}_{rq_f} \\ & \boldsymbol{M}_{\varepsilon\varepsilon} & \boldsymbol{M}_{\varepsilon q_f} \\ sym. & & \boldsymbol{M}_{q_f q_f} \end{bmatrix} \cdot \begin{bmatrix} x^3 \\ y^3 \\ \psi^3 \\ q_f^4 \\ \vdots \\ q_f^9 \end{bmatrix} \tag{2-193}$$

where $\boldsymbol{M}^3$ is the generalized mass matrix defined by equations (2-156) through (2-162). In this particular case, $\boldsymbol{M}_{rr}$ is a (2*x*2) matrix, $\boldsymbol{M}_{r\varepsilon}$ is a (2*x*1) matrix, $\boldsymbol{M}_{rq_f}$ is a (2*x*6) matrix, $\boldsymbol{M}_{\varepsilon\varepsilon}$ is a scalar, $\boldsymbol{M}_{\varepsilon q_f}$ is a (2*x*6) matrix and $\boldsymbol{M}_{q_f q_f}$ is a (6*x*6) matrix; the rows and columns corresponding to z^3, θ^3 and ϕ^3, which are zero, have been intentionally omitted. The terms defined by equations equations (2-163) through (2-171) are for example $\bar{l}^1 = 1.57$ kg and $\bar{\boldsymbol{l}}^2 = [0.3925 \;\; 0 \;\; 0]^T$. Except for $\boldsymbol{M}_{rr}$ and $\boldsymbol{M}_{q_f q_f}$, the coefficients of the mass matrix $\boldsymbol{M}^3$ must be computed for each time-step as they depend on $\boldsymbol{A}^3$ or $\boldsymbol{q}_f$ in this particular case.

2.1.3.3 Constraint Equations

Constraints define the absolute position and orientation of bodies in space or the relative position and orientation between two bodies in order to describe the motion of the complete mechanical system. The planar slider crank mechanism of figure 2-7 yields the following constraint equations. (In the following lines, the equations have been simplified by considering that z^i, θ^i and ϕ^i are zero for all three bodies.

Body 1, can only translate along the *X* axis which gives rise to two constraint equations

$$\begin{cases} y^1 = 0 \\ \psi^1 = 0 \end{cases} \tag{2-194}$$

Body 2 can only rotate about the *Z* axis at *O* which leads to

$$\boldsymbol{r}_0=\boldsymbol{0} \;\Leftrightarrow\; \boldsymbol{r}^2+\boldsymbol{A}^2\cdot\left[-\frac{l^2}{2}\quad 0\quad 0\right]^T=\boldsymbol{0}$$

$$\Rightarrow\begin{cases} x^2-\frac{l^2}{2}\cdot\cos\psi^2=0 \\ y^2-\frac{l^2}{2}\cdot\sin\psi^2=0 \end{cases} \tag{2-195}$$

where l^2 is the distance between *0* and *A*.

Body 3 is attached to body 2 at *A*, while the rotation about the *Z* axis is allowed, i.e

$$\boldsymbol{r}_{A^2}=\boldsymbol{r}_{A^3} \;\Leftrightarrow\; \boldsymbol{r}^2+\boldsymbol{A}^2\cdot\left[\frac{l^2}{2}\quad 0\quad 0\right]^T=\boldsymbol{r}^3+\boldsymbol{A}^3\cdot\left(\begin{bmatrix}0\\0\\0\end{bmatrix}+\boldsymbol{S}^1\cdot\boldsymbol{q}_f\right)$$

$$\Rightarrow\begin{cases} x^2-x^3+\frac{l^2}{2}\cdot\cos\psi^2-\cos\psi^3\cdot\sum_{k=4}^{9}S_{u_1}^k\cdot q_f^k+\sin\psi^3\cdot\sum_{k=4}^{9}S_{u_2}^k\cdot q_f^k=0 \\ y^2-y^3+\frac{l^2}{2}\cdot\sin\psi^2-\sin\psi^3\cdot\sum_{k=4}^{9}S_{u_1}^k\cdot q_f^k-\cos\psi^3\cdot\sum_{k=4}^{9}S_{u_2}^k\cdot q_f^k=0 \end{cases} \tag{2-196}$$

where $\boldsymbol{S}^1$ contains the rows that correspond to the translational DOF of node 1.
Finally, body 3 is also attached to body 1 at *B* which leads to

$$\boldsymbol{r}_{B^1}=\boldsymbol{r}_{B^3} \;\Leftrightarrow\; \boldsymbol{r}^1+\boldsymbol{A}^1\cdot\left[0\quad 0\quad 0\right]^T=\boldsymbol{r}^3+\boldsymbol{A}^3\cdot\left(\begin{bmatrix}l^3\\0\\0\end{bmatrix}+\boldsymbol{S}_6\cdot\boldsymbol{q}_f\right)$$

$$\Rightarrow\begin{cases} x^1-x^3-\cos\psi^3\cdot l^3-\cos\psi^3\cdot\sum_{k=4}^{9}S_{u_{16}}^k\cdot q_f^k+\sin\psi^3\cdot\sum_{k=4}^{9}S_{u_{17}}^k\cdot q_f^k=0 \\ y^1-y^3-\sin\psi^3\cdot l^3-\sin\psi^3\cdot\sum_{k=4}^{9}S_{u_{16}}^k\cdot q_f^k-\cos\psi^3\cdot\sum_{k=4}^{9}S_{u_{17}}^k\cdot q_f^k=0 \end{cases} \tag{2-197}$$

where l^3 is the total length of the flexible body and $\boldsymbol{S}^6$ contains the rows that correspond to the translational DOF of node 6.

The eight independent holonomic constraints equations, that are defined in equation (2-194) through (2-197), form the set of constraints $\boldsymbol{C}$. This set depends on the fifteen generalized coordinates $\boldsymbol{q}_{sc}$ of the slider crank mechanism which are

$$\boldsymbol{q}_{sc}=\left[x^1\quad y^1\quad \psi^1\quad x^2\quad y^2\quad \psi^2\quad x^3\quad y^3\quad \psi^3\quad q_f^4\quad q_f^5\quad q_f^6\quad q_f^7\quad q_f^8\quad q_f^9\right]^T \tag{2-198}$$

Thus the flexible multi-body system has seven DOF, one rigid and six flexible DOF.

The Jacobian matrix $\boldsymbol{C}_{\boldsymbol{q}_{sc}}$ of the system, which is needed for the Lagrange multiplier form of the equation of motion can now be determined according to equation (2-60).

2.1.3.4 Equation of Motion of the Multi-body System

The only external forces acting on the mechanism are the elastic forces of the flexible body and the driving moment. The generalized elastic force is defined in equation (2-139)

and takes the form

$$\boldsymbol{Q}^e = -\boldsymbol{K}\cdot\boldsymbol{q}_{sc} \tag{2-199}$$

The virtual work of the driving moment is $M\cdot\delta\psi^2$, thus according to equation (2-44) the generalized force is

$$Q_{\psi^2} = M \quad \Leftrightarrow \quad \boldsymbol{Q}^M = \begin{bmatrix} 0 & 0 & 0 & 0 & 0 & M & 0 & \dots & 0 \end{bmatrix}^T \tag{2-200}$$

The total kinetic energy T of the system, with

$$T = T^1 + T^2 + T^3 \quad \Leftrightarrow$$

$$T = \frac{1}{2}\cdot\left[m^1\cdot\left(\dot{x}^1\right)^2 + m^1\cdot\left(\dot{y}^1\right)^2 + J^1_{zz}\cdot\left(\dot{\psi}^1\right)^2 + m^2\cdot\left(\dot{x}^2\right)^2 + m^2\cdot\left(\dot{y}^2\right)^2 + J^2_{zz}\cdot\left(\dot{\psi}^2\right)^2 + \dot{\boldsymbol{\xi}}^T\cdot\boldsymbol{M}^3\cdot\dot{\boldsymbol{\xi}}\right] \tag{2-201}$$

is substituted into Lagrange's equation of the slider crank mechanism, that is

$$\frac{d}{dt}\left(\frac{\partial T}{\partial \dot{\boldsymbol{q}}_{sc}}\right)^T - \left(\frac{\partial T}{\partial \boldsymbol{q}_{sc}}\right)^T + \boldsymbol{C}_{\boldsymbol{q}_{sc}}{}^T\cdot\boldsymbol{\lambda} + \boldsymbol{K}\cdot\boldsymbol{q}_{sc} = \boldsymbol{Q}^M \tag{2-202}$$

in order to get the governing equations of motion in terms of the generalized coordinates of the system. This set of fifteen differential equations is associated with the eight algebraic constraint equations defined in equations (2-194) through (2-197) and solved numerically for the position, velocity and acceleration of the generalized coordinates.

2.2 FPS Software

Fluid power simulation tools were developed for the dynamic simulation of complex fluid-technical systems, such as pneumatic or hydraulic units. The mathematical formulation of these programs is based on the one-dimensional flow theory supplemented by empirical considerations. This means that FPS software cannot model, for example, the unsteady non-uniform flow through a valve. Despite the simplifications, they give however very good results for the dynamic simulation of complete hydraulic systems in common engineering applications. (They are not comparable to computational fluid dynamics (CFD) codes. In fact, comparing fluid power simulation to computational fluid dynamics is like comparing multi-body simulation to finite element analysis.)

The program used for the simulations is DSHplus. It has different libraries containing hydraulic, thermo-hydraulic and pneumatic components. In addition, controls and mechanical libraries exist to complete the simulation tool. An interesting feature is the open mathematical description in C++. The user can take a look at the mathematical description of each component and can edit the existing or include his own code. A graphical interface allows the user to quickly and easily generate the simulation model and to access and visualize the results (see figure 2-9). Finally, interfaces to several other simulation tools are available.

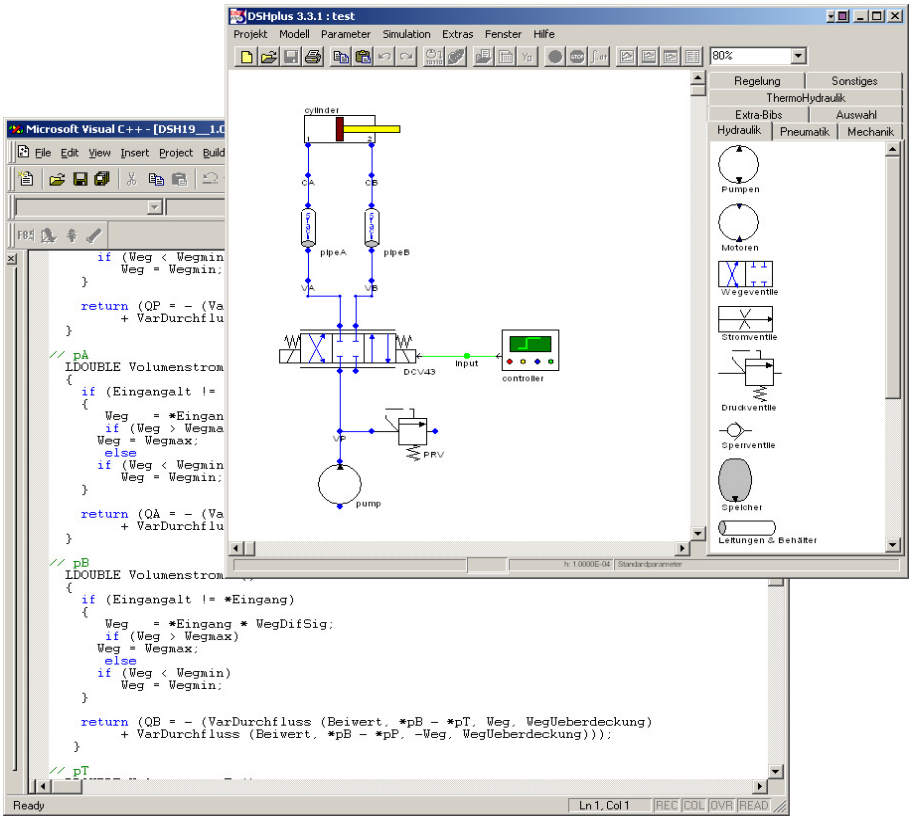

Figure 2-9: DSHplus

2.2.1.1 Fluid Mechanics

In the following, the very basic concepts of fluid mechanics implemented in the FPS program are briefly presented.

2.2.1.2 Pascal's Law

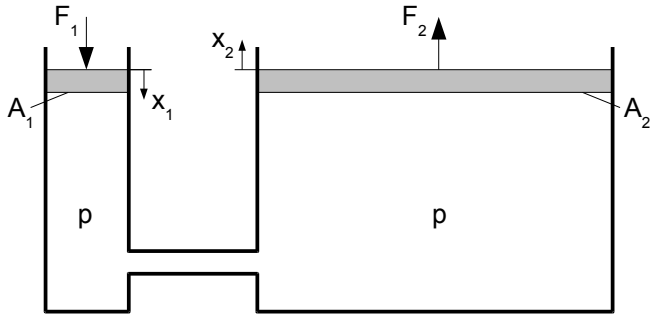

Figure 2-10: Hydraulic press

Pascal's law states that in a fluid at rest in a closed container, a pressure change in one part is transmitted without loss to every portion of the fluid and to the walls of the container. The pressure always acts at right angles to the walls. A direct application of Pascal's law is the hydraulic press as shown in figure 2-10 where

$$p = \frac{F_1}{A_1} = \frac{F_2}{A_2} \tag{2-203}$$

2.2.1.3 Conservation of Mass / Equation of Continuity

The law of conservation of mass states that mass can neither be created nor destroyed. For hydrodynamics this means that the inflows, outflows and change in storage of mass in a system must be in balance. This can be written as

$$\dot{m}_1 - \dot{m}_2 = \frac{d}{dt}\int_V \rho dV \tag{2-204}$$

$\dot{m}$ is called the mass flow rate and is expressed as

$$\dot{m} = \rho \cdot v \cdot A \tag{2-205}$$

where ρ is in general not constant.

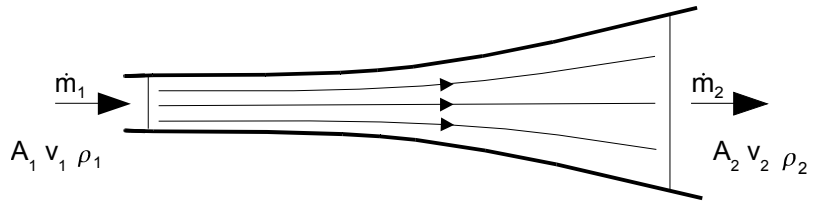

Figure 2-11: Equation of continuity

For a steady flow, i.e. conditions such as velocity, pressure and cross-section may differ from one point to another but do not change with time, and an incompressible fluid, i.e. density ρ is constant, then equation (2-204) becomes

$$A_1 \cdot v_1 = A_2 \cdot v_2 = Q \tag{2-206}$$

where A is the section area, v is the mean flow velocity[7] and Q is the discharge, also called volume flow rate. A standard assumption in hydraulics is that the flow and fluid may be regarded as steady and incompressible, respectively. Therefore equation (2-206) is commonly used for calculations in hydrodynamics.

2.2.1.4 Bernoulli's Equation

When a fluid is in motion, inertia and friction must be considered. If inviscid steady flow and incompressible fluid is assumed, then the application of Newton's second law to a fluid volume brings forth Bernoulli's equation.

$$\frac{\rho}{2} \cdot v^2 + p + \rho \cdot g \cdot h = constant \tag{2-207}$$

As the altitude difference in hydraulic systems is generally small, the pressure due to gravity is often neglected compared to the relatively high pressures in the system. For a component with a variable sections, e.g. figure 2-11, Bernoulli's equation allows to determine the pressure difference between two sections, that is

7 In practice, every fluid that flows near a solid boundary will take the speed of the boundary, which is usually zero. Therefore, the velocity through a component, e.g. a pipe, is not constant across the cross section: its is minimum at the walls and increases to a maximum at the centre of the cross section. This variation is known as the velocity profile.

$$p_1 - p_2 = \frac{\rho}{2} \cdot \left(v_2^2 - v_1^2 \right) = \frac{\rho}{2} \cdot \left(\frac{Q_2^2}{A_2^2} - \frac{Q_1^2}{A_1^2} \right) \tag{2-208}$$

2.2.1.5 Pressure Loss in Components

Hydraulic energy cannot be transferred through components without losses. Because of friction within the fluid and friction between fluid and components, energy is transformed to heat which results in a pressure loss. For example, if the pressure loss is taken into account for the component in figure 2-11, the equation (2-208) becomes

$$p_1 - p_2 = \frac{\rho}{2} \cdot \left(v_2^2 - v_1^2 \right) + \Delta p_{loss} \tag{2-209}$$

This pressure loss can be expressed as a function of the dynamic pressure [26] and the resistance coefficient ξ. The hydraulic resistance of a component can then be written as

$$\Delta p_{loss} = \xi \cdot \frac{\rho}{2} \cdot \frac{Q^2}{A^2} \quad \Leftrightarrow \quad Q = \sqrt{\frac{1}{\xi}} \cdot A \cdot \sqrt{\frac{2}{\rho}} \cdot \sqrt{\Delta p_{loss}} \tag{2-210}$$

ξ depends on the viscosity ν and the flow rate *Q* or the flow velocity *v*. Generally, ξ is expressed as a function of the Reynolds number *R*, that is

$$\xi = \frac{K_1}{R} + K_2 \tag{2-211}$$

The Reynolds number is defined as

$$R = \frac{v \cdot d_h}{\nu} \tag{2-212}$$

where d_h is called the hydraulic diameter. For circular sections d_h equals the diameter, otherwise it is defined as

$$d_h = \frac{4 \cdot A}{U} \tag{2-213}$$

A being the cross-section area and *U* the section circumference.

Substituting equations (2-211) through (2-213) into equation (2-210) yields

$$\Delta p_{loss} = \frac{K_1 \cdot U}{8 \cdot A^2} \cdot \rho \cdot \nu \cdot Q + \frac{K_2}{2 \cdot A^2} \cdot \rho \cdot Q^2 \tag{2-214}$$

Thus, the pressure loss of a component can be expressed by two terms, the first one is linearly dependent on discharge and viscosity and the second one is square dependent on discharge and independent of viscosity. Generally, K_1 and K_2 can only be determined experimentally; only for some components they may be derived theoretically.

The pressure loss for an orifice constriction as shown in figure 2-12 can be derived using Bernoulli's equation. Assuming that the fluid is incompressible and that the pressure due to gravity is negligible leads to

$$Q = \frac{A_3}{\sqrt{1-\left(\frac{A_1}{A_2}\right)^2}} \cdot \sqrt{\frac{2}{\rho}} \cdot \sqrt{\Delta p_{loss}} \tag{2-215}$$

A_3 is lying slightly behind the orifice and is smaller than the actual orifice area due to a jet contraction. This point of minimum area is called the *vena contracta*.

$$A_3 / A_0 = \alpha_c \tag{2-216}$$

where α_c is called the coefficient of contraction. For a sharp orifice α_c is about 0.62, for an orifice that resembles to a short tube α_c is nearly 1. Of course, there are also losses due to turbulences and friction. Therefore, the velocity over A_3 is corrected with the coefficient of velocity α_v. However, this coefficient is usually very high, between 0.95 and 0.99. Finally, the commonly known coefficient of discharge α_D is introduced. It accounts for both effects and equation (2-215) can be written with respect to A_0 as

$$Q = \alpha_D \cdot A_0 \cdot \sqrt{\frac{2}{\rho}} \cdot \sqrt{\Delta p_{loss}} \tag{2-217}$$

α_D is again determined experimentally, it ranges from 0.6 to 0.9 for most orifices.

Comparing equation (2-217) to equation (2-214) one can say that the pressure loss of an orifice is independent of the viscosity of the fluid. Generally, all kind of valves can be regarded as orifices and equation (2-217) is commonly used to calculate the flow rate at a given pressure difference with α_D and ρ constant; which is acceptable for most applications.

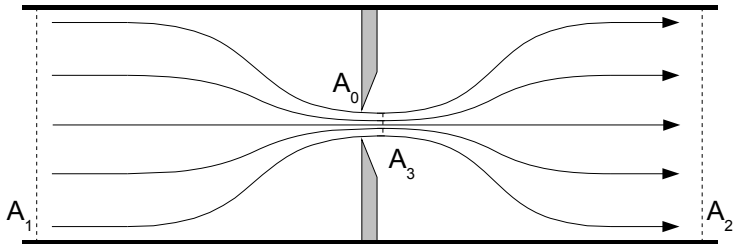

Figure 2-12: Orifice

In contrast to an orifice, the pressure loss in a straight pipe depends mainly on the Reynolds number, i.e. flow velocity and viscosity. The resistance coefficient for a pipe is commonly defined as

$$\xi = \lambda \cdot \frac{l}{d_h} \tag{2-218}$$

where l is the length of the pipe, d_h the hydraulic diameter and λ the dimensionless friction coefficient that is depending on the Reynolds number and the wall roughness of the pipe. This friction coefficient is encoded in the Moody chart. Similar charts can also be found for other standard components in the literature [26, 28, 29].

Until now, the case of steady flow has been assumed, but in reality, flow and pressure

vary in time. This is, for example, happening during start-up and brake operations of cylinders or during switching operations of valves. Under these conditions, pressure peaks or oscillations are possible that may damage the system. In order to account for these effects in the simulation, compressibility and inertia of the fluid have to be included. The respective formulas are developed in the following.

2.2.1.6 Compressibility of Fluid

If a pressure is applied to a fluid then the fluid is compressed and its volume is reduced. Similar to steel, a bulk modulus can be defined for the fluid such that

$$\Delta V = \frac{V_0}{E_{oil}} \cdot \Delta p \tag{2-219}$$

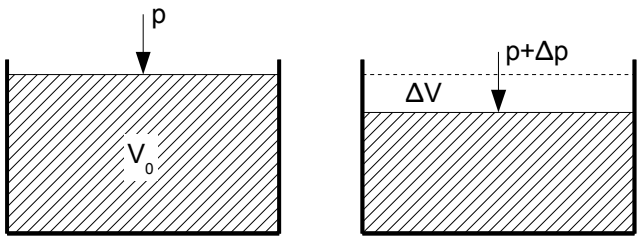

Figure 2-13: Fluid compressibility

Now applying equation (2-204) to a control volume *V* with the stored mass being *m* having a density ρ , then one can write that

$$\dot{m}_1 - \dot{m}_2 = \frac{d(\rho \cdot V)}{dt} = \rho \cdot \dot{V} + V \cdot \dot{\rho} \tag{2-220}$$

Considering that ρ is depending on the pressure *p*, then it can be expressed as (30)

$$\rho = \rho_i + \frac{\rho_i}{E_{oil}} \cdot p \tag{2-221}$$

where ρ_i is the mass at zero pressure.

Inserting equation (2-221) into (2-220) and dividing by ρ leads to

$$Q_1 - Q_2 = \dot{V} + \frac{V}{E_{oil}} \cdot \dot{p} \tag{2-222}$$

If the volume is fixed, equation (2-222) finally simplifies to

$$\dot{p} = \frac{E_{oil}}{V} \cdot (Q_1 - Q_2) \tag{2-223}$$

Equation (2-223) is fundamental for the description of the pressure dynamics in hydraulic systems.

The elastic modulus E_{oil} of mineral oil has the order of magnitude of $10^{\cdot 9}$ Pa, which, compared to the elastic modulus of steel, shows that the hydraulic system can represent a stiffness weak point. The effective bulk modulus in a hydraulic system depends on several parameters such as temperature, pressure, amount of undissolved air or flexibility of hoses. Therefore, an equivalent bulk modulus E'_{oil} is commonly defined and used for calculations.

The variation of E_{oil} against these parameters is generally described by empirical formulas. Figure 2-14 shows the influence of temperature, pressure and piping.

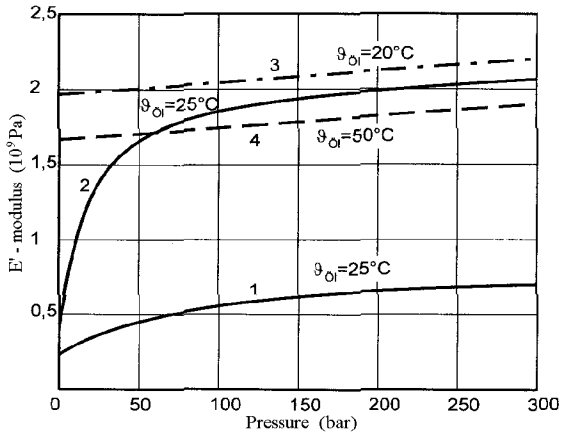

1 - high pressure hose NW30
2 - steel pipe dia.30 x 4
3, 4 - hydraulic oil

Figure 2-14: E-modulus of oil (taken from [26] p20)

2.2.1.7 Inertia of Fluid

When the flow rate changes, the mass of the fluid has to be accelerated or decelerated. Applying Newton's second law to a finite volume of fluid yields

$$\Delta p \cdot A = \rho \cdot V \cdot \ddot{x} \tag{2-224}$$

where $\ddot{x} = \dot{v} = \dot{Q}/A$, hence the hydraulic inertia can be defined as

$$\Delta p = \frac{\rho \cdot V}{A^2} \cdot \dot{Q} \tag{2-225}$$

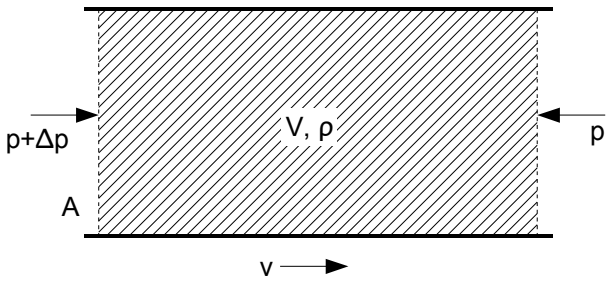

Figure 2-15: Fluid inertia

2.2.2 Hydraulic Modeling Components

It is possible to define an analogy between a fluid power system and an electrical circuit. The concept of resistance, capacitance and inductance can be defined [26, 27, 30], they are resumed in figure 2-16. DSHplus uses this analogy for the dynamic simulation. The basic modeling components are resistances of flow and volumes of fluid, they are combined to create simple or more elaborated models. In this section, the most important modeling components are briefly presented to give a better understanding of the possibilities and limitations of the simulation tool.

Resistance

$\Delta p = R_h \cdot Q^2$ with $R_h = \xi \cdot \frac{\rho}{2 \cdot A^2}$ all components responsible for a pressure loss: orifice, throttle, valve, pipe, etc

Capacitance

$p = \frac{1}{C_H} \cdot \int Q \cdot dt$ with $C_H = \frac{V_0}{E'_{oil}}$ compressibility of a fluid volume

Inductance

$\Delta p = L_H \cdot \frac{dQ}{dt}$ with $L_H = \frac{\rho \cdot V}{A^2}$ inertia of a fluid volume

Figure 2-16: Electrical-hydraulic analogy

2.2.2.1 Fluid

In the fluid options the user chooses the type of fluid that is characterized by its viscosity υ, its density ρ and its bulk modulus E_{oil}; all three depending in real systems on temperature, pressure and other parameters. In a standard simulation the temperature is supposed to remain constant; otherwise the thermo-hydraulic library must be used. Viscosity and density are also kept constant as they generally vary little under normal conditions. Only the bulk modulus changes with pressure. Additionally, it can also depend on the amount of undissolved air in the fluid and the pressure related change of volume of the recipient.

2.2.2.2 Hydraulic Node

All hydraulic components need to be connected via hydraulic nodes. The flow rates *Q* from the components are summed up at the node and the actual pressure Δ*p* in the node is calculated according to equation (2-226).

$$p = \frac{E'}{V} \cdot \int Q \cdot dt \tag{2-226}$$

The volume *V* consists of the volume of the connected components. This means that the volume of a node may change if components such as cylinders or accumulators are attached to it. The corrected bulk modulus *E'* depends on the actual pressure, the amount of undissolved air and the volume change of the recipient.

2.2.2.3 Valves

Directional control valves, proportional valves, pressure reducing valves or orifices are flow resistances. A flow of fluid through a resistance causes a pressure drop, or vice versa a pressure difference causes a flow. Depending on the component the user has to specify a flow rate and a pressure drop or a coefficient of discharge α_D and an area *A* according to

$$\Delta p = R_H \cdot Q^2 \tag{2-227}$$

Equation (2-227) can be written in the more common form of

$$Q = \alpha_D \cdot A \cdot \sqrt{\frac{2}{\rho}} \cdot \sqrt{\Delta p} \tag{2-228}$$

These components have no volume; if necessary it has to be specified "manually" at the

hydraulic node. For non-standard components, the user has the possibility to define look-up tables. For example, a proportional valve with a special spool-cut needs a look-up table that defines the flow section area versus the spool position. On the other hand. the dynamic behavior of a valve is modeled with a controls approach. The control path for the position of the spool against the input signal may be equivalent to a P-, PT1- or $PT2_S$-element.

2.2.2.4 Cylinder

The cylinder computes a force according to the actual pressure P_i and the area A_i of the cylinder chambers.

$$F_{cyl} = \sum P_i \cdot A_i \tag{2-229}$$

The compressibility of the fluid inside the cylinder is considered as its volume is added automatically to the volume of the hydraulic nodes. However it is massless, i.e. has no inertia. Generally, the inertia of the fluid in the cylinder chambers is negligible compared to the inertia of the mechanical parts attached to the cylinder. The velocity v_{cyl} of the cylinder rod is directly related to the discharge of a cylinder chamber by

$$Q_i = A_i \cdot v_{cyl} \tag{2-230}$$

2.2.2.5 Piping

The pipe is modeled as a hydraulic resistance and inductance. The capacitance of the pipe is taken into account at the hydraulic nodes. In order to model the continuous nature of the pipe, several pipe components have to be lined up. The number n of pipe elements depends on the highest frequency f of interest [31].

$$n > 10 \cdot L \cdot f \cdot \sqrt{\frac{\rho}{E'}} \tag{2-231}$$

The resistance coefficient of a pipe is calculated according to

$$\Delta p = \lambda \cdot \frac{L}{d_h} \cdot \frac{\rho}{2} \cdot \frac{Q^2}{A^2} \tag{2-232}$$

L is the length of the pipe, d_h the hydraulic diameter and λ the dimensionless friction coefficient that in DSHplus is only depending on the Reynolds number. Adding pipe components to the model drastically increases the computation effort.

Figure 2-17 shows the set of differential equations that needs to be integrated to simulate the cylinder extension for this particular hydraulic system. The user can choose among different integration methods with a variable or a fixed time-step. He can also set the simulation error and control the amount of solution output.

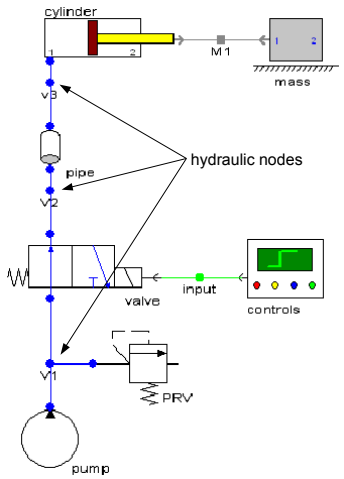

$$
\begin{cases}
\dot{p}_{V_1} = \dfrac{E_{oil}(p_{V_1})}{V_1} \cdot \left(Q_{pump} - Q_{PRV}(p_{V_1}) - Q_{valve}(p_{V_1}, p_{V_2}) \right) \\
\dot{p}_{V_2} = \dfrac{E_{oil}(p_{V_2})}{V_2 + \dfrac{V_{pipe}}{2}} \cdot \left(Q_{valve}(p_{V_1}, p_{V_2}) - Q_{pipe} \right) \\
\dot{p}_{V_3} = \dfrac{E_{oil}(p_{V_3})}{V_3 + \dfrac{V_{pipe}}{2} + V_{cyl}(x_{cyl})} \cdot \left(Q_{pipe} - v_{cyl} \cdot A_{cyl} \right) \\
\dot{Q}_{pipe} = \dfrac{A_{pipe}^2}{\rho \cdot V_{pipe}} \cdot \left(p_{V_2} - p_{V_3} - p_{loss}(Q_{pipe}) \right) \\
\dot{v}_{cyl} = \dfrac{1}{m} \cdot \left(p_{V_2} \cdot A_{cyl} + F_{friction} \right) \\
\dot{x}_{cyl} = v_{cyl}
\end{cases}
$$

Figure 2-17: DSHplus formulation

Generally the problem in such hydraulic simulations is not the generation of the model itself, but the definition of the input parameters for the different components. Most of the time the only information available is the one found in the manufacturer catalogues. However, this data has been determined experimentally at specific conditions, so that it may have to be adapted to the required simulation input. It is also possible that it is not complete. In that case, extensive measurements on the hydraulic system are necessary.

2.3 Controls Software

Simulink is used to model the controller. It is a software package developed for simulating and analyzing time-varying systems. It can model linear and non-linear phenomena and plug-ins extend the program with tools for specific modeling tasks. A graphical user interface serves for generating the models that are built from block diagrams which are connected among each other. The program includes a large library of various blocks, and, of course, customized blocks may also be created. After a model has been generated, it can be simulated with different integration methods. The results may be displayed while the simulation is running and they can also be exported to the MATLAB workspace for further processing and visualization.

Simulink can be used in a wide range of applications, including signal processing, financial or electrical circuits modeling; actually all kind of time-varying systems may be modeled. But the tool is very popular for controls system modeling and analyzing. Furthermore, as Simulink is integrated with MATLAB, the user has access to the Control System Toolbox. This add-on provides additional means for designing and analyzing closed-loop control systems such as root locus, pole placement and frequency response

analyses or state-space model representations.

The controller logic of the moving platen positioning has been translated into a Simulink block diagram. This was not imperative as the displacement of the platen is controlled through an open-loop system. However, it comes in handy when simulating different machine setups and it can be extended to a closed-loop system.

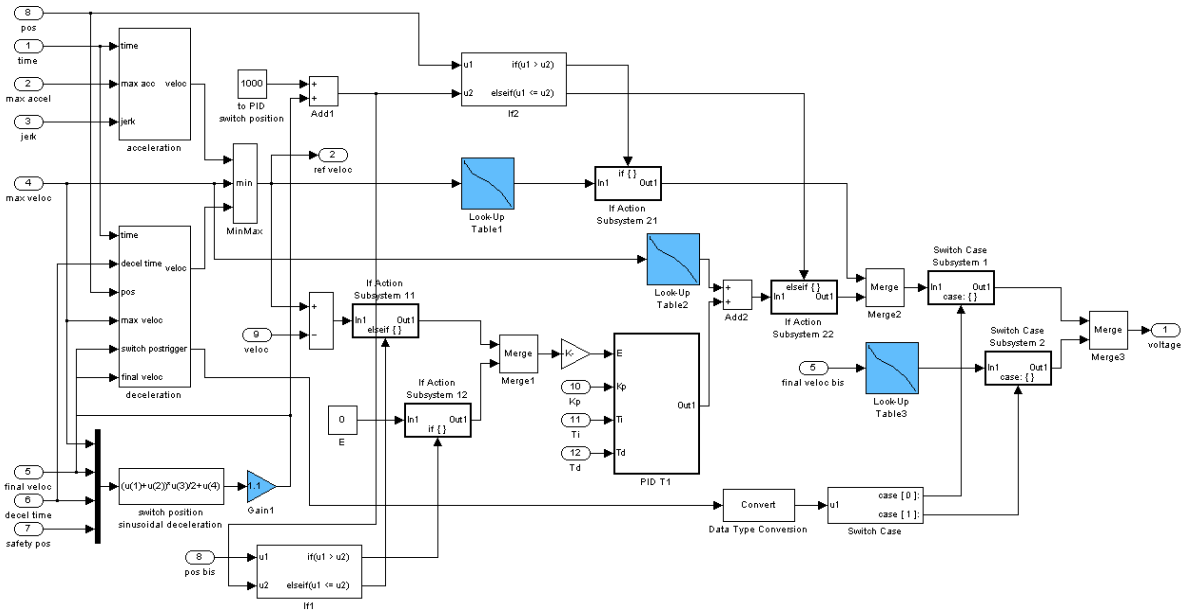

Figure 2-18: Simulink block diagram model

2.4 Co-simulation

The co-simulation is possible as the software companies offer add-ons to their products developed especially for this purpose. The models have only to be generated accordingly. The different set-ups for these particular programs are presented in the following.

2.4.1 MBS-FPS

The user can include own written subroutines in ADAMS if he wants to model specialized phenomena that are not part of the standard simulation package. The subroutines are programmed in FORTRAN or C. Afterwards they are compiled in order to work with the solver. These functions are then evaluated as part of the solution process. DSHplus-STC (Simulation-Tool-Chain) makes use of this feature to link the hydraulic model with the MBS tool. The STC-module generates an interface between the FPS model and the user-subroutine.

In order to illustrate the coupling procedure, a simple example of a hydraulic cylinder actuating a clamp piston is used. The MBS model computes the position and velocity of the clamp piston and cylinder, and the hydraulic model computes the cylinder force.

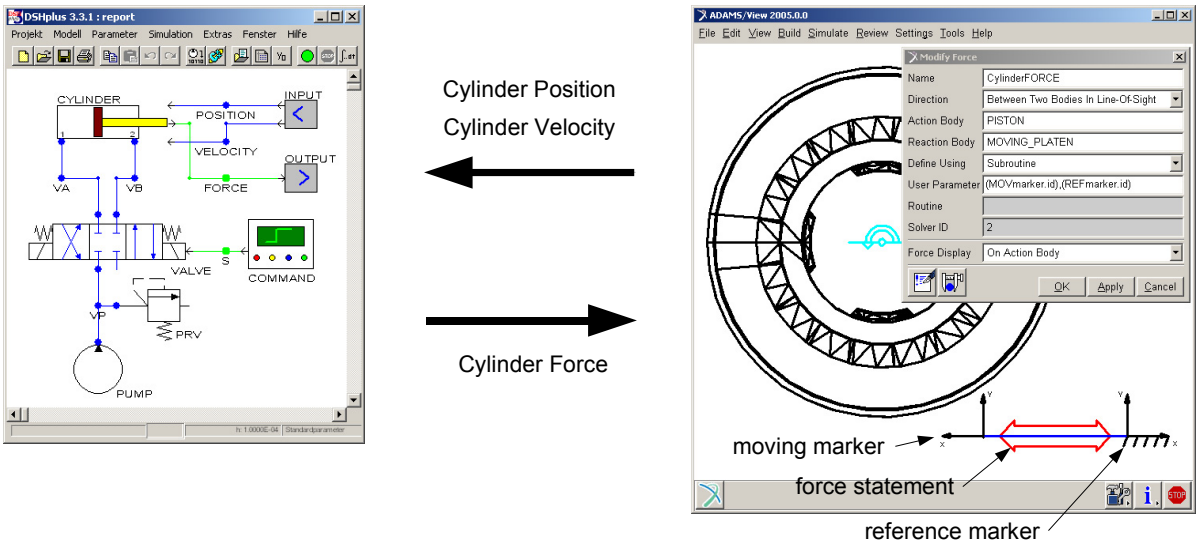

Figure 2-19: ADAMS - DSHplus co-simulation

In DSHplus, special input- and output-components need to be defined so that the STC-module recognizes the data exchanged during the simulation. In ADAMS, the model is generated as usually except for the force statement. The user-subroutine and its input parameters have to be specified here; in this example the input parameters are the id's of the moving marker and reference marker. Finally, the FORTRAN subroutine must be programmed. It computes the actual relative position and velocity of the moving marker with respect to the reference marker and calls the STC-module.

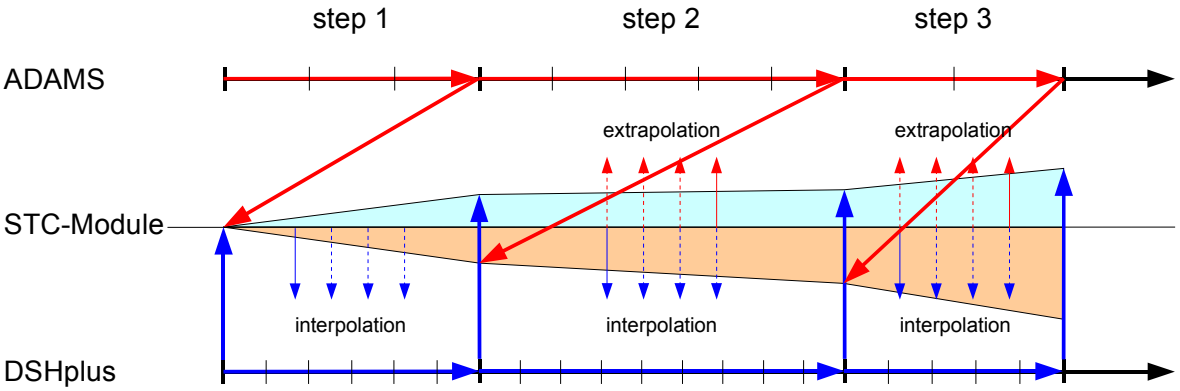

Figure 2-20: Inter- and extrapolation of exchanged values

When the simulation is started, both programs are first of all initialized. ADAMS then gets the initial values of DSHplus from the STC-module and computes the first time-step. At the end of every successful simulation step in ADAMS, the new position and velocity values and the duration of the time-step are transferred to the STC-module. The module then triggers the calculation of the same time period in DSHplus with the new position and velocity values of the cylinder. When DSHplus has computed its time-step, the new force value is passed back to ADAMS which then starts to compute the next time-step. The STC-module also manages the interpolation or extrapolation of the input- and output-parameters in order to

smooth out the computation process [32]. The detailed FORTRAN code can be found in appendix B.

DSHplus distinguishes between the *co-simulation* mode and the *embedded* mode. The only difference is that for the embedded mode the DSHplus online plots and graphical user interface are not available. This has two advantages: first, less memory and CPU time is required and second, no DSHplus version is necessary on the processing computer. The drawback is that the user has only access to the DSHplus results that have been defined as import or export parameter of the MBS model. The configuration of the STC-module allows a very flexible mode of operation. The user can switch between different hydraulic or mechanical models as long as the import- and output-parameters do not change.

2.4.2 MBS-Controls

The ADAMS/Controls plug-in provides the possibility to integrate a controls system into the MBS model or to link it to a block diagrams model developed with controls applications such as Simulink. For this purpose, inputs and outputs have to be specified in the mechanical model. The inputs describe the variables that are transferred from the controls application to the MBS software and the outputs are the variables that are exported from the mechanical to the controls model. The final step consists of linking both programs. Several procedures exist depending on the chosen simulation method: *discrete*, *continuous* or *C-code import*.

In the discrete or co-simulation mode, ADAMS solves the mechanical system equations and Simulink solves the controls system equations; identical to the ADAMS-DSHplus coupling. In the continuous mode, the controls application solves both, the mechanical and controls system equations. This mode is also called the *function evaluation* mode. As the system of differential and algebraic equations (DAE) cannot be solved by Simulink, ADAMS simplifies the DAE system and transforms it into a set of ordinary differential equations (ODE). This ODE set is transferred to Simulink and combined with the controls equations set. The combined set is then integrated by Simulink [33]. For most analyzes, the discrete mode is generally the more efficient simulation method because of the optimized DAE solver algorithms in ADAMS. It is faster and can handle complex mechanical models better than the continuous mode. The latter one can be of interest when the equations solved in the controls system cause a large coupling effect on the mechanical model or when very small time-steps are required.

For both methods, a "Controls Plant Export" dialog box in ADAMS creates the appropriate files and Simulink variables from the specified input and output parameters and options. In the next step, the *ADAMS_SUB* block, that is created during the export, is integrated into the controls model. From the *ADAMS_SUB* block, additional parameters such as discrete or continuous mode, with or without animation or communication step size can

be specified.

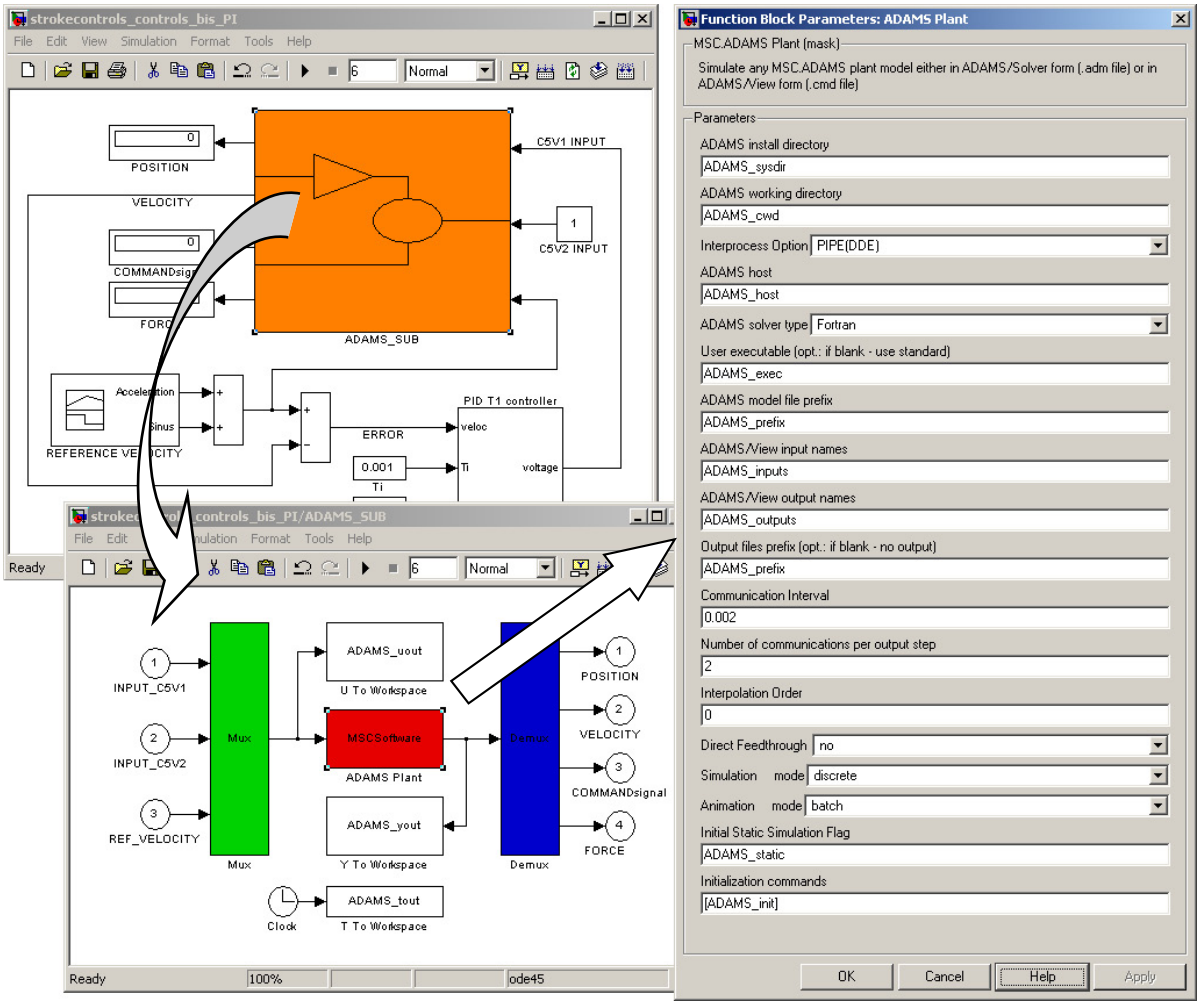

Figure 2-21: ADAMS - Simulink co-simulation

In the C-code import mode, ADAMS solves the combined sets of DAE and ODE. For this purpose a C-code representation of the controls system is exported using the Real-Time Workshop plug-in of Simulink. ADAMS/Controls can then automatically create a general state equation element and connect it to the inputs and outputs of the mechanical system. The combined model is simulated within ADAMS.

2.4.3 MBS-FPS-Controls

With the licenses available at the University of Luxembourg only the co-simulation, or discrete simulation mode, is possible. Linking the three programs is straightforward and does not request any additional operations than those presented in the two preceding paragraphs. The setup of the co-simulation proves to be very flexible. The user can for example replace a rigid-body model by a flexible-body model, add an orifice to the hydraulic model or simply change the gain of the controller without having to reconfigure the co-simulation. Of course this is only possible as long as the input- and output-parameters do not change.

Figure 2-22 shows the configuration of the moving platen stroke simulation. The

computation time for this hybrid model depends on various parameters like the complexity of the model, the solvers used for the computation or the settings of the solvers. To give an idea, the computation of a complete stroke of the moving platen takes about ten minutes for a rigid-body model, whereas at least ten hours are needed for a flexible-body model.

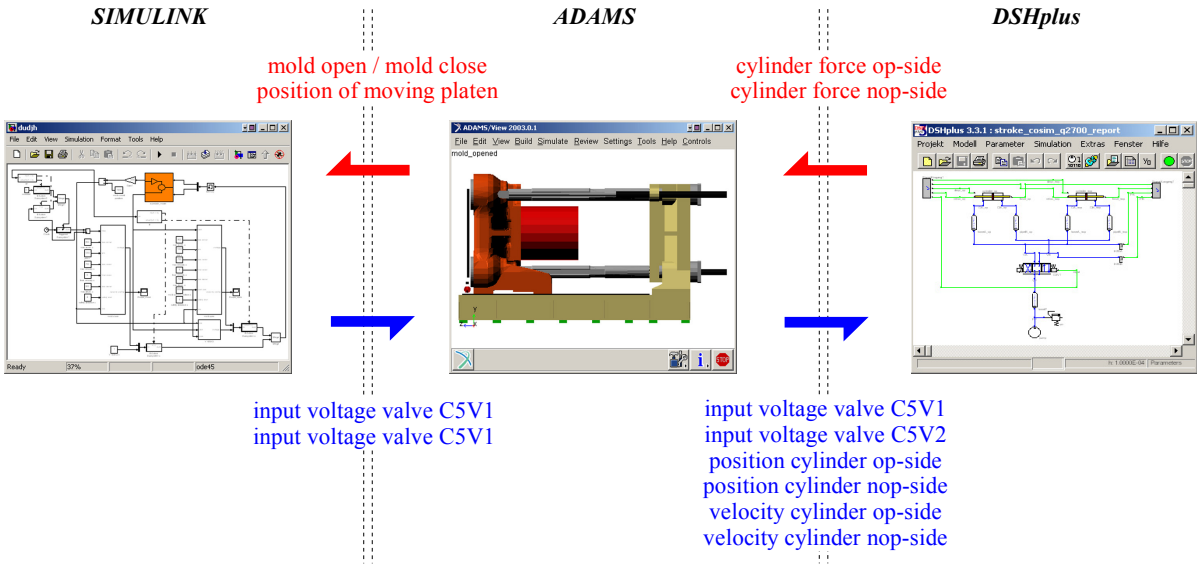

Figure 2-22: ADAMS - DSHplus - Simulink co-simulation

In the following three chapters, the different simulations tools were used to investigate the clamp unit and to work out improvements. In chapter 3, a cheaper solution for the clamp locking mechanism is proposed. Therefore, the mechanism was modeled with a flexible MBS model while the force of the hydraulic cylinder was computed with the FPS program (34). In chapter 4, different possibilities to reduce the machine cycle time are analyzed. In this case, the focus was on the complex hydraulic system and on the implementation of a PID controller for the moving platen positioning, as the mechanical system was only modeled as rigid bodies (35). Finally in chapter 5, possible root causes for machine creeping during operation are investigated. For this purpose, the rigid clamp base, stationary platen and tie bars in the MBS model of chapter 4 were replaced by flexible bodies.

3 Clamp Locking Mechanism

3.1 Introduction

The four clamp pistons mechanically lock the moving platen to the tie bars through a bayonet coupling (see section 1.2.2). The pistons are rotated with the help of the so-called clamp locking mechanism. This mechanism is made up of a hydraulic cylinder, three connecting bars and several fixation parts such as clevises, screws, pins or washers. A flow directional valve controls the hydraulic cylinder and thereby the direction of rotation of the clamp pistons. The end positions of the cylinder determine the "locked" and "unlocked" positions of the clamp pistons. As the valve only controls the direction of flow, and not the flow rate, the cylinder always operates at maximum possible velocity. When reaching an end position, the cylinder is decelerated by its built-in cushion, which basically works by throttling the fluid flow [34].

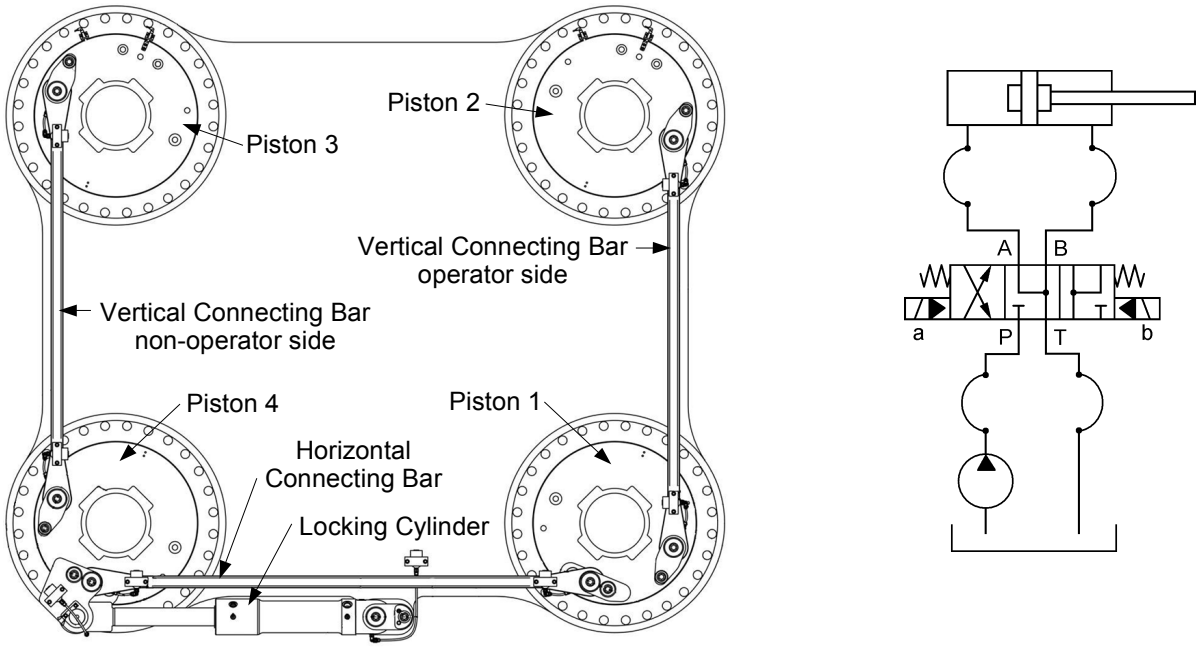

Figure 3-1: Clamp locking mechanism

For a Q2700, each clamp piston weights 1400 kg and the connecting bars are about 2.5 m long. The hydraulic cylinder has a stroke of 390 mm and can generate a maximum force at 180 bar system pressure of 221 kN for pushing and 106 kN for pulling. The locking

or un-locking time is under 1 second.

At valve opening and cylinder cushioning, the connecting bars are exposed to force peaks. Therefore, the initial design, which was a welded construction, was replaced by connecting bars that are manufactured from a single piece (see figure 3-2). If this design is far more robust, it is also more expensive. The aim of the simulation is to quantify the forces acting on the bars and to give an additional understanding of the locking mechanism. The idea is to change the system accordingly so that the acting forces are reduced and a cheaper welded construction can be installed. Thus, in a first step the simulation model is used to determine the parameter that influences the most the level of the acting forces; the opening velocity of the directional valve is identified to have by far the biggest influence. In a next step, the directional valve is replaced by a proportional valve. This allowed to reduce the force peak in the simulation by 40% and to use much cheaper welded connecting bars, but at the expense of more expensive hydraulic components.

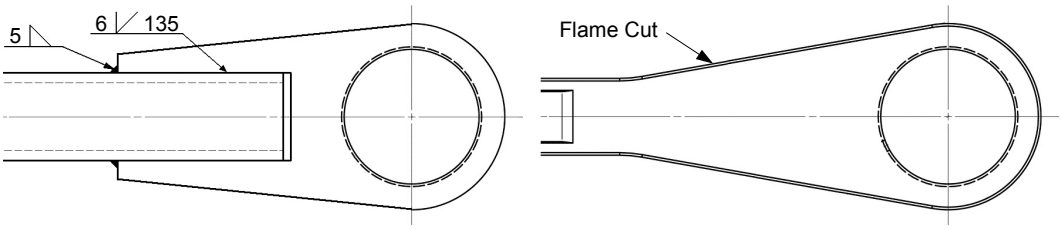

Figure 3-2: Connecting bar designs

3.2 Simulation Model

The mechanical and hydraulic system are simulated with the multi-body and the fluid-power simulation software, respectively; a controls model is not necessary. The clamp pistons are modeled as rigid bodies and the connecting bars are represented by flexible bodies in order to account for their flexibility. The hydraulic system is needed to include the effects of valve opening and cushioning.

3.2.1 Mechanical System

3.2.1.1 Rigid-Body Model

The model includes 9 moving parts: the 4 clamp pistons, the cylinder rod and the cylinder body, which were created from simplified CAD geometries, and the 3 connecting bars (see figure 3-3). The mass and inertia properties of the different parts are computed by the CAD program from the detailed geometry and are entered manually in the MBS model. In order to describe the motion of the complete mechanical system, 4 revolute joints define the rotation of the clamp pistons relative to the moving platen (ground part), 6 spherical joints model the spherical bearings by which the connecting bars are fixed to the pistons and a spherical, translational and cylindrical joint model the mechanism of the hydraulic cylinder that is connected between the moving platen and piston 4. For the purpose of preventing the free

rotation of each connecting bar along its longitudinal axis, additional rotational-joint motions are applied to some spherical joints in order to lock the respective degree of freedom.

The following survey of the degrees of freedom of the moving parts and joints shows that the system has 1 degree of freedom, which of course corresponds to the overall motion of the locking mechanism.

9 moving parts	:	9 x 6 degrees of freedom	=	54
4 revolute joints	:	- 4 x 5 constraint equations	=	-20
7 spherical joints	:	- 7 x 3 constraint equations	=	-21
1 cylindrical joint	:	- 1 x 4 constraint equations	=	-4
1 translational joint	:	- 1 x 5 constraint equations	=	-5
3 motion joints	:	- 3 x 1 constraint equation	=	-3
remaining degrees of freedom				1

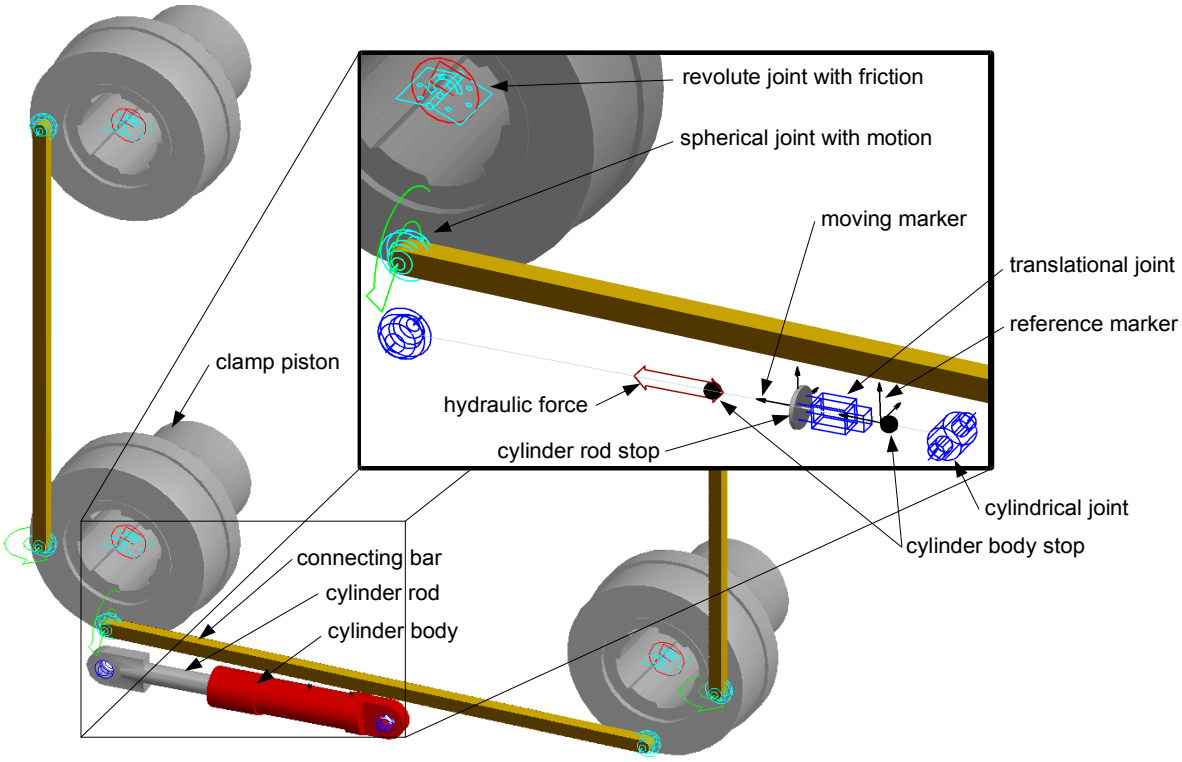

Figure 3-3: Clamp Locking Mechanism

The hydraulic force driving the MBS model is computed by the hydraulic model and acts between the moving platen and clamp piston 4. For this purpose, a user-subroutine determines the actual position and velocity of the cylinder with the help of the moving and reference marker as explained in section 2.4.1. Contact statements are also defined between the cylinder rod and cylinder body in order to add a mechanical stop in addition to

the hydraulic stop that is the cylinder cushion.[8]

Friction occurs everywhere in the system, e.g. between the clamp pistons and seals, in the spherical bearings or in the hydraulic cylinder. As it is not negligible, it has to be included in the model. However for the sake of simplicity, the overall friction is only specified in the clamp piston revolute joints. The friction algorithm implemented in the MBS tool is capable of modeling stiction, Stribeck and Coulomb friction. It computes the instantaneous friction forces from the forces and moments applied to the joint, the geometric properties of the joint and the actual friction coefficient. This instantaneous friction coefficient depends on the joint velocity: if it exceeds 1.5 times the user-defined transition velocity then the joint is in dynamic friction, if it is below the transition velocity then the joint is in static friction, otherwise the joint is considered to be transitioning between static and dynamic friction and the coefficient is estimated from a cubic interpolation as shown in figure 3-4 [12].

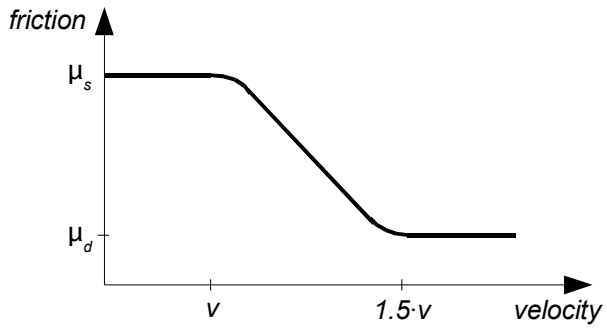

Figure 3-4: Friction model

Both friction coefficients are not known and are estimated from measurements. The dynamic friction coefficient is selected so that the computed hydraulic pressures correspond to the measured ones during the constant velocity phase. It is assumed that at this moment the hydraulic cylinder has only to overcome the friction forces within the system. A dynamic friction coefficient of $\mu_d = 0.42$ and a static friction coefficient of $\mu_s = 0.5$ are retained for the following simulations.

3.2.1.2 Flexible Connecting Bars

The connecting bars are modeled as flexible bodies as they are relatively slender in relation to the mass of the clamp pistons that they have to actuate. That way, the effect of their stiffness on the behavior of the overall system can be investigated. Additionally, stress/time histories, that may be useful for fatigue analyses, can be obtained with a special add-on. For this purpose, a modal stress matrix has to be computed during the flexible-body generation which relates the stress components to the component generalized coordinates. Thus, it is possible to get a stress distribution directly within the MBS tool. Of course, there is

8 Basically, the contact statement is a nonlinear spring-damper element where the force is proportional to the penetration depth and velocity. If there is no penetration, then no force is applied, otherwise a force acting between both parts is computed. More details on the contact statement can be found in chapter 4.

also the possibility to export the results and to calculate the stresses within a finite element software.

A quarter of the connecting bar model is shown in figure 3-5. A simplified CAD geometry is imported in the FE code and meshed automatically with tetrahedral elements. Afterwards, beam elements with a very high stiffness and a low density are added manually. They connect the solid elements to a node representing the center of the spherical bearing. The two boundary nodes, each having 6 DOF, serve as attachment for the flexible body in the MBS model. Additionally to the 12 static modes, 13 fixed normal modes are calculated (see section 2.1.2.1.c). Finally, the FE model with 40000 physical DOF is reduced to 25 modal coordinates. Despite the very high degree of reduction, the method gives very good results for the lowest natural frequencies as can be seen in table 3-1 and 3-2.

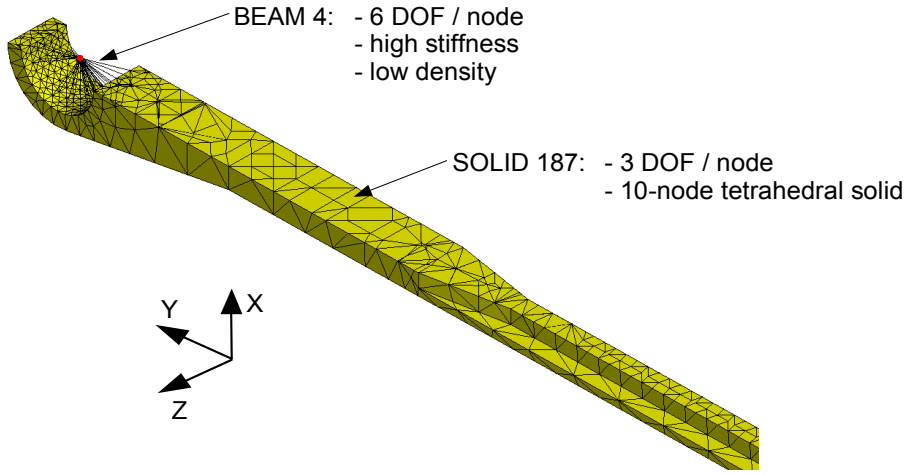

Figure 3-5: Finite element model of connecting bar

FE model	Craig-Bampton	comment	FE model	Craig-Bampton	comment
0.0 Hz	0.0 Hz	6 rigid-body modes	652.4 Hz	652.9 Hz	4th bending mode x
44.2 Hz	44.2 Hz	1st bending mode z	771.6 Hz	771.4 Hz	5th bendingmode z
65.4 Hz	65.4 Hz	1st bending mode x	896.1 Hz	923.5 Hz	1st long. mode
138.1 Hz	138.0 Hz	2nd bending mode z	990.6 Hz	991.1 Hz	5th bending mode x
158.1 Hz	154.3 Hz	1st torsion mode	996.7 Hz	966.4 Hz	local mode
197.3 Hz	197.2 Hz	2nd bending mode x	1085 Hz	1085 Hz	6th bendingmode z
288.6 Hz	288.4 Hz	3rd bending mode z	/	2074 Hz	no phys. classific.
392.0 Hz	391.7 Hz	3rd bending mode x	/	2141 Hz	no phys. classific.
500.6 Hz	500.3 Hz	4th bending mode z	/	2685 Hz	no phys. classific.
528.5 Hz	512.1 Hz	local mode	/	3074 Hz	no phys. classific.

Table 3-1: Eigenfrequencies of a free-free vertical connecting bar

As mentioned in chapter 2, the orthonormalisation of the fixed-boundary normal modes and the constraint modes yields, first, mode shapes of the unconstrained structure, and, second, mode shapes with no physical meaning. This result can be found in table 3-1, where the eigenfrequencies of the unconstrained FE model are compared to the eigenfrequencies of the modified Craig-Bampton modal basis.

Furthermore, an experimental modal analysis is performed on an installed connecting bar, i.e. fixed at both ends by spherical bearings, in order to validate the FE model and the flexible MBS model. The impact-hammer modal testing allows to measure the natural frequencies and the corresponding mode shapes of the structure [see appendix C]. In table 3-2, the first eigenfrequencies of the constrained FE model and the flexible MBS [9] model are compared to the natural frequencies obtained from the measurements.

FE model		flexible MBS model		measured	comment
26.8 Hz	4.7 %	26.7 Hz	4.3 %	25.6 Hz	1st bending mode z
39.5 Hz	0.3 %	39.4 Hz	0.3 %	39.4 Hz	1st bending mode x
106.4 Hz	/	103.6 Hz	/	/	1st mode long. rotat.
106.5 Hz	6.0 %	106.5 Hz	6.0 %	100.5 Hz	2nd bending mode z
151.1 Hz	1.3 %	151.2 Hz	1.4 %	149.1 Hz	2nd bending mode x
244.7 Hz	/	244.7 Hz	/	?	3rd bending mode z
331.4 Hz	3.0 %	331.4 Hz	3.0 %	321.8 Hz	3rd bending mode x
447.5 Hz	/	447.5 Hz	/	?	4th bending mode z
589.5 Hz	4.8 %	591.8 Hz	5.2 %	562.3 Hz	4th bending mode x

Table 3-2: Eigenfrequencies of a constrained vertical connecting bar

As modal damping ratios can be specified for flexible bodies (see section 2.1.2.3), they are estimated from the impact modal analysis. The evaluation of the measurements gives modal damping parameters that lie between 1 % and 6 % [see appendix C]. Next to this approach, the damping parameters can also be derived from acceleration measurements of the connecting bars under operation. In this case, they are calculated from the logarithmic decrement of two successive maxima of response [35], that is

$$\ln\left(\frac{x_p}{x_{p+1}}\right) \simeq \ln\left(\frac{e^{-\alpha\omega t_p}}{e^{-\alpha\omega(t_p+T)}}\right) \tag{3-1}$$

where

$$\ln\left(\frac{e^{-\alpha\omega t_p}}{e^{-\alpha\omega(t_p+T)}}\right) = \ln\left(e^{(\alpha\omega T)}\right) = \alpha\omega T = \alpha 2\pi \tag{3-2}$$

For α small, which is usually the case for mechanical structures, equation (3-1) simplifies to

9 Natural frequencies and mode shapes can be computed with a special plug-in that linearizes the non-linear MBS model and expresses it by complex valued eigenvalues & mode shapes.

$$\alpha \simeq \frac{1}{2\pi} \ln\left(\frac{x_p}{x_{p+1}}\right) \tag{3-3}$$

The modal damping from the acceleration measurements is about 0.6 % for the first mode. Finally, a modal damping of 1 % is retained for the simulation and applied to all the modes of the flexible bodies.

3.2.2 Hydraulic System

3.2.2.1 Hydraulic model

The basic hydraulic schematic of the clamp locking mechanism is found in figure 3-1. It is made up of a cylinder, a directional control valve, a pump and some piping; the remaining hydraulic circuit of the machine is not considered. This schematic is translated into a fluid-power model where simplifications and adaptations are necessary with respect to the hydraulic components available and their limitations (see figure 3-6).

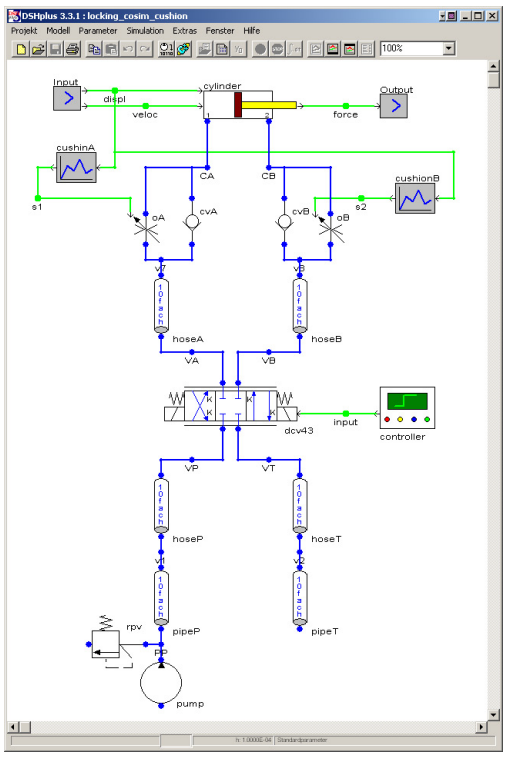

differential cylinder:
- displacement & velocity as input from MBS
- force as output to MBS

cushion model:
- check valve
- variable orifice dependent on cylinder position

flexible hoses

pilot operated directional control valve:
- special spool parameterized by look-up table

flexible hoses & pipes

pump & pressure relief valve

Figure 3-6: Hydraulic model

The fluid characteristics are those of HLP46: viscosity υ = 46 mm²/s at 40 °C, density ρ = 835.2 kg/m³ and E-modulus = 1.49·10⁹ Pa. The system pressure is at 185 bar. As the pump configuration of the machine is able to deliver an output flow that largely exceeds the flow rate needed by the locking cylinder, the pump system is modeled as an ideal pressure source, i.e. it can hold a specified pressure constant regardless of the flow needed in the system. In reality, fluctuations of the pressure occur as variable displacement pumps with pressure and/or flow controllers are installed on the machine. Piping is integrated in the

model in order to contribute to the effects of fluid inertia as these are not negligible due to the high dynamics of the clamp locking mechanism. Additionally, the volume change under pressure of the flexible hoses can also be represented by the piping.

The pilot operated directional control valve controls the start, stop and direction of flow of the fluid (see figure 3-7). If a controls signal is applied, the spool of the valve moves completely to either side; its position is not proportional to the input signal. As large actuating forces are needed due to the high flow through the valve, a small valve, called pilot valve, is needed to operate the main valve. The pilot valve is however directly operated by solenoids. This means that the electrical control signal is hydraulically amplified in order to actuate the main spool, which is centered again by springs. The main valve opening and closing time can be controlled by different means. In this case, orifices are mounted between the pilot valve and the main valve. They reduce the amount of flow from the pilot valve to the main valve and thus influence the total reaction time of the main spool.

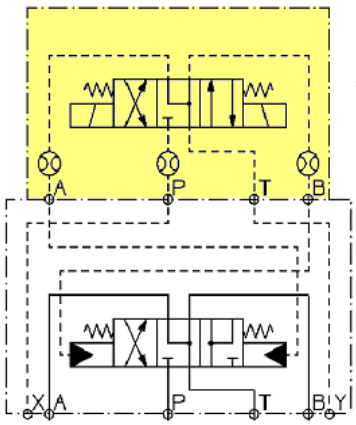

When the main spool is in central position then port *A* and port *B* are connected to port *T* .

When the main spool is moved to the right then port *B* is connected to port *P* and port *A* to port *T*.

When the main spool is moved to the left then port *A* and *B* are connected to port *P*.

Figure 3-7: Pilot operated directional control valve

The pilot operated valve is not modeled in detail, i.e. with main valve, pilot valve and orifices. The modeling component directly relates the stroke of the spool to the input signal by a first order delay. The total response time of the valve was determined by measurements and found to be 90 ms. In order to respect the non-standard spool of the main valve, look-up tables are defined that relate the relative opening area of one port to the position of the spool. The particularity of this valve is that it connects the bore and rod side during cylinder extension. Thus, the fluid in the rod chamber is not fed to the tank but directly to the bore chamber which reduces the flow that has to be delivered by the pump.

Another particularity of the hydraulic system is the cylinder cushion. It is a built-in device that decelerates the cylinder when reaching an end position. The basic principle of a cushion is to reduce the flow area so that a pressure build-up occurs in the cylinder. When the cylinder starts from an end position, a check valve, or similar device, is used to by-pass the

throttling point. The cushioning effect is modeled with a variable orifice and a check valve. A look-up table relates the orifice area to the cylinder position. The characteristic curve is determined from measured data. This is a very heavy simplification and only models approximatively what is happening in the cushion. However, it gives decent results compared to the modeling effort.

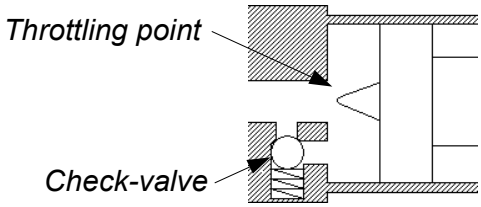

Figure 3-8: Cylinder cushion

3.2.2.2 Comparison with Measurements

As gauge ports are available on the hydraulic cylinder, the pressure in the cylinder chambers can be measured. In figure 3-9 they are compared to the pressure of node CA and CB of the hydraulic model. Although differences in the absolute values are found, the relative correlation of the results with the measured data is fairly good. The discrepancies mainly result from the simplified model of the spoolcut, of the pump and of the cylinder cushion. A further fine-tuning might improve the correlation of measured and computed data but is not really necessary for the further analyses.

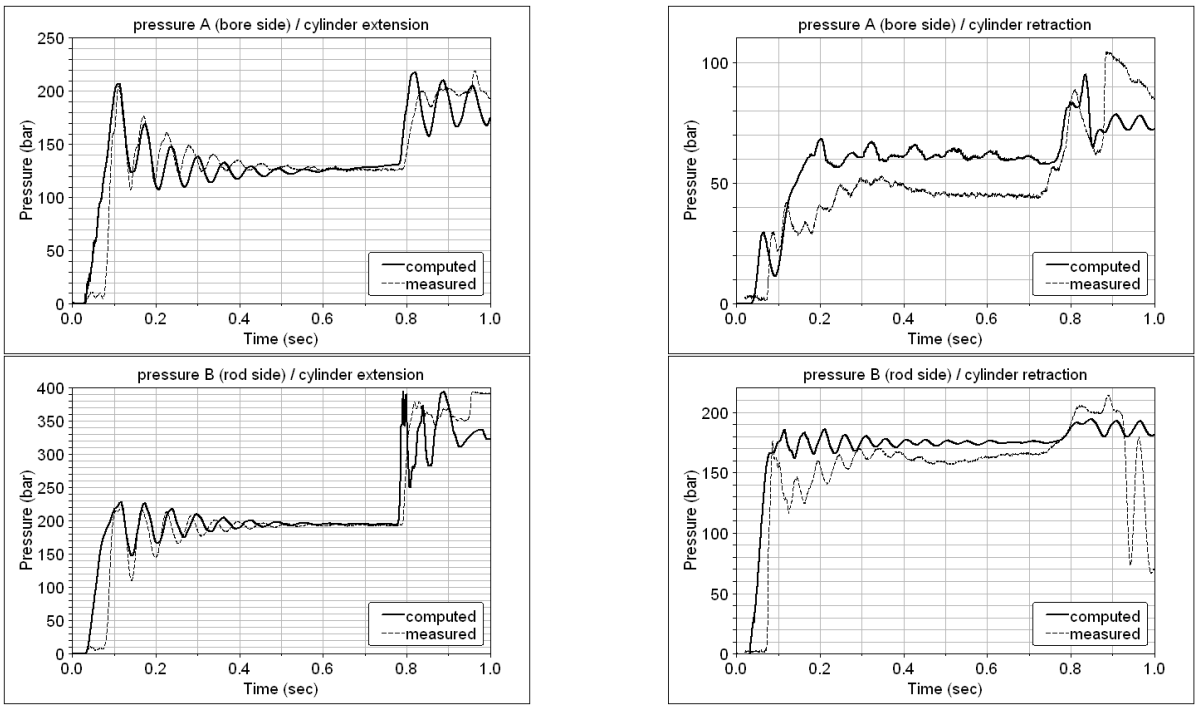

cylinder extension *cylinder retraction*

Figure 3-9: Hydraulic pressures in cylinder chambers

For the directional control valve, only the flow rate at maximum opening is available in

the technical data sheets. The exact spoolcut and the corresponding flow rate in relation to the spool position is not known. However, the spoolcut is optimized with fine control notches in order to reduce pressure peaks during valve opening. As this information is not available, it cannot be incorporated in the model. Furthermore, at valve opening, the variable displacement pumps have to react to the flow demand. The delay of the pumps causes first of all a pressure drop in the system. The adjustment of the discharge of the pumps by the controller system leads to fluctuations in the system pressure. Both effects are not included in the model and explain the differences at valve opening.

The oscillations in the cylinder pressures observed between 0.2 and 0.8 seconds are due to the overall stiffness of the hydraulic system, i.e. compressibility of oil volumes and elasticity of hoses, and mass of the mechanical system attached to the cylinder; the frequencies lie between 16 Hz and 21 Hz.

The pressure built-up at t = 0.8 s results from the cylinder cushioning. The discrepancy at cylinder extension is rather large but still acceptable when only considering the first pressure peak (see also figure 3-10).

3.3 Simulation Results

Once the model is validated by measurements, it is used to analyze and quantify the influence of different parameters on the behavior of the complete system. As explained in the introduction, the main interest lies in the forces acting on the connecting bars.

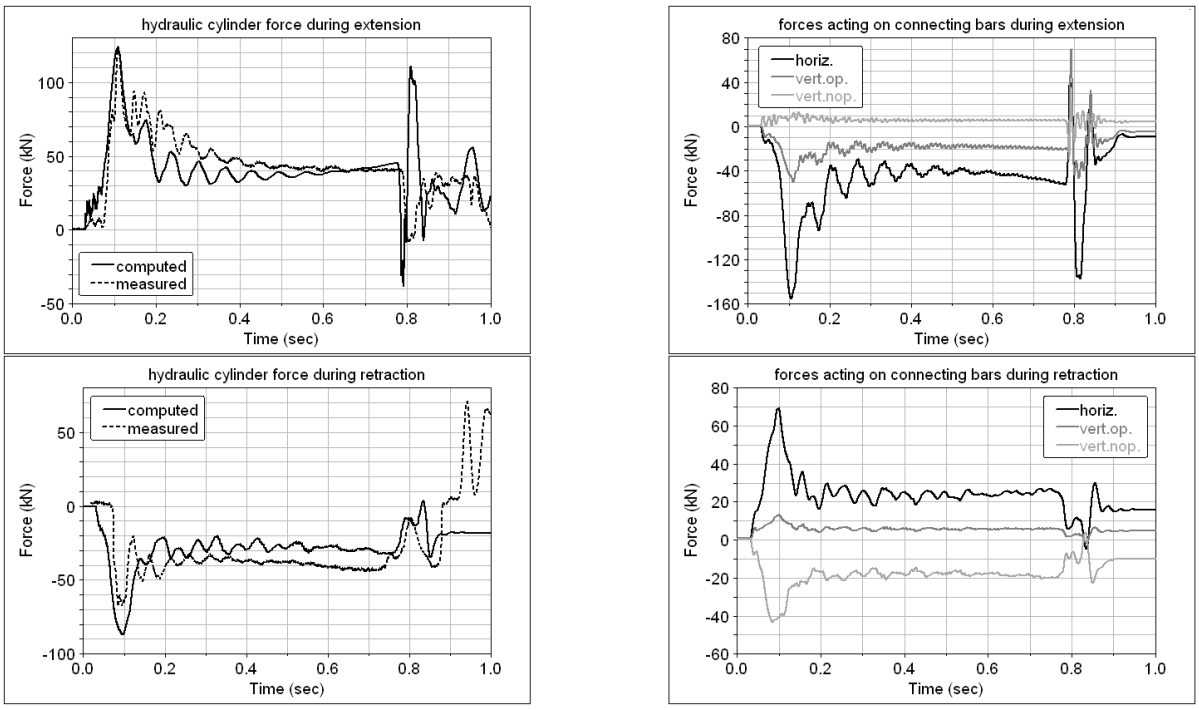

Figure 3-10: Comparison of cylinder force & computed connecting bar forces

A survey of the current model leads to the following conclusions:

- The force peaks are greater at valve opening than during cushioning, as they have not

only to cause acceleration but also have to overcome friction. Accelerations measurements also confirm this observation. (Besides, this is also the reason why the cushion model was not further improved.)

- The horizontal connecting bar is exposed to the highest forces. In fact it has to operate piston 1 and piston 2, whereas the vertical connecting bars only act on one clamp piston.
- The vertical connecting bars see the highest force when subjected to traction. The traction force adds to the weight of the clamp piston thus the friction force acting on piston 2 and piston 3 is higher during extension, respectively retraction. The opposite occurs when a compression force is applied.

A durability analysis of the current configuration shows the failure of the old welded design for an unlimited service life and the non-failure of the new manufactured design (see figure 3-2). The proof is done with the application of the German FKM-guideline [36, 37]. For this purpose, a flexible body of the welded connecting bars is generated. The time/stress history at node 3110 near a welding seam is plotted in figure 3-11 for a complete cycle. There exist several approaches for the durability check in the FKM guideline. One possibility is to use the local stress as computed by the MBS analysis and shown in the figure below. Another possibility is to compute the nominal stress in the welding seam, which is $\tau = 12.2 \pm 32.2\ MPa$ for the welded connecting bar over a complete cycle.

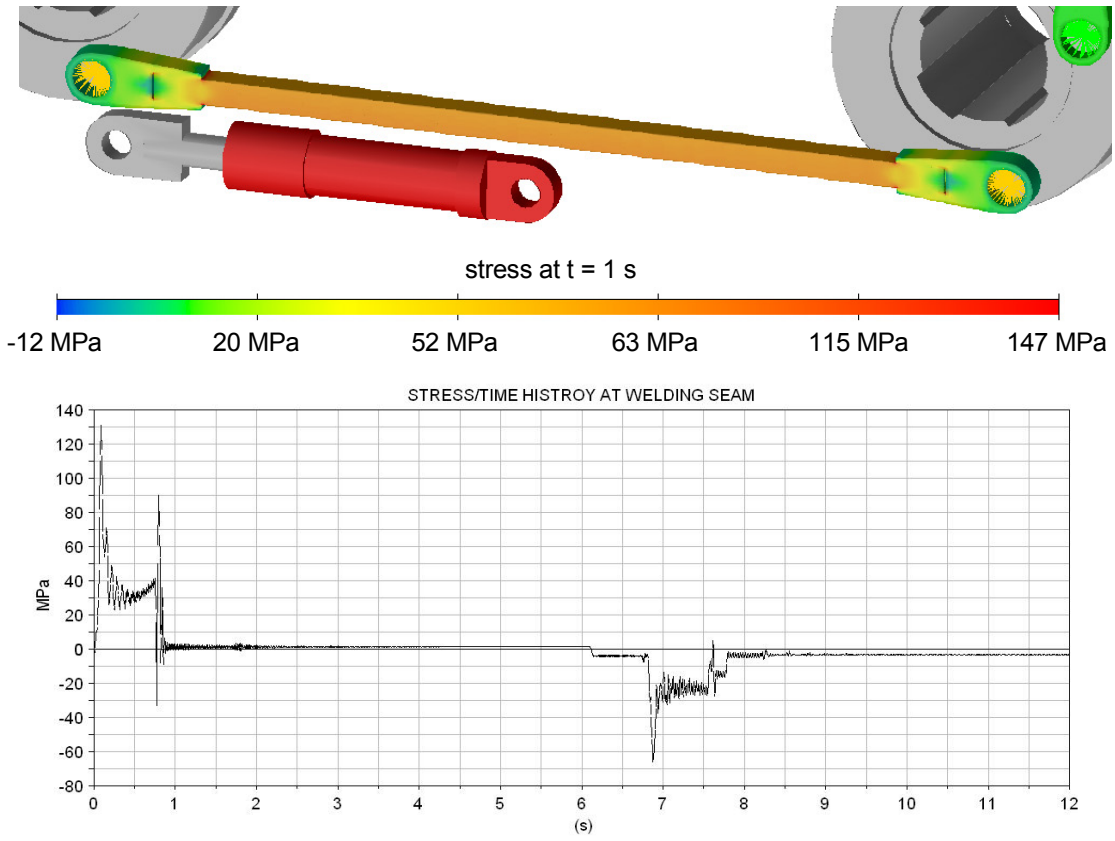

Figure 3-11: Stress/time history for welded connecting bar

Considering the nominal stress and parameters such as loading history, welding construction or security concerns, the conclusion from the FKM is that the old design has only a limited service life. Different welding designs were checked but only a welding according to construction Nr.221 (figure 3-12) and complying with the highest FAT class passes the durability test [FKM, table 5.4.1, page 198].

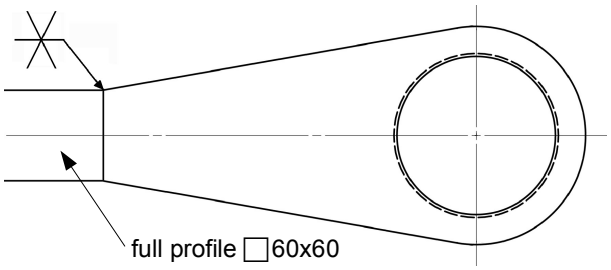

Figure 3-12: New welding design

However, the execution of this weld is technically challenging and probably no alternative to the new design from a costing point of view. The only possibility is to reduce the acting forces. Therefore, in a next step the influence of different parameters on the force amplitude is investigated.

3.3.1 Connecting Bar Stiffness

In order to reduce the force peaks at valve opening and during cushioning, the idea is to make the connecting bars as soft as possible. Therefore a hollow profile is used for the old welding design and a longitudinal slot is added to the profile for the single-piece construction. To quantify the impact of this solution, the influence of the stiffness is analyzed by changing the E-modulus. The results are partially surprising.

Indeed, a softer connecting bar reduces the force peak during deceleration. However, it unexpectedly has the opposite effect during acceleration. For example, when the stiffness is halved the force acting on the connecting bars increases by 10%. This effect results from the interaction of the mechanical and hydraulic system. First of all, a softer connecting bar reduces the hydraulic force by approximately 3%. In fact, as it is more flexible, the hydraulic cylinder starts moving earlier and thus the pressure built-up is reduced. But on the other hand, the connecting bar is more compressed and due to the interaction with the clamp piston inertia and friction, the effective forces acting finally on the connecting bars increase. These interactions could only hardly be assessed by simple calculations and the example shows the interest of such integrated dynamic simulations.

Reducing the stiffness by one half or one fifth is not really realistic. However, considering the results it is not advisable to reduce the stiffness of the connecting bar because, first, this is generally achieved by reducing the cross-section area of the structure which in return increases the stresses, second, this design constraint normally increases cost and limits the design possibilities and third, the influence of the mechanical stiffness on the force acting

during acceleration, which is crucial for the fatigue analysis, is marginal.

relative stiffness	horizontal bar		vertical bar op.-side		vertical bar non op.-side	
	acceleration	deceleration	acceleration	deceleration	acceleration	deceleration
1/5	171 kN	25 kN	63 kN	43 kN	15 kN	21 kN
1/2	170 kN	39 kN	57 kN	48 kN	14 kN	29 kN
1	155 kN	41 kN	50 kN	70 kN	13 kN	30 kN
2	147 kN	55 kN	47 kN	82 kN	13 kN	30 kN
5	145 kN	60 kN	46 kN	82 kN	12 kN	30 kN

Table 3-3: Forces vs. Stiffness during Cylinder extension

3.3.2 Different Mechanical Configurations

Figure 3-10 shows that the forces vary whether they act against or with the clamp piston weight. The question is, if the forces may be reduced by judiciously placing the connecting bars and the hydraulic cylinder. Thus, different configurations are simulated. As expected, the force repartition in the mechanical system changes completely. However, the difference between the maximum force value during extension and retraction remains the same. As this parameter is crucial for the durability analysis, changing the configuration is not a option.

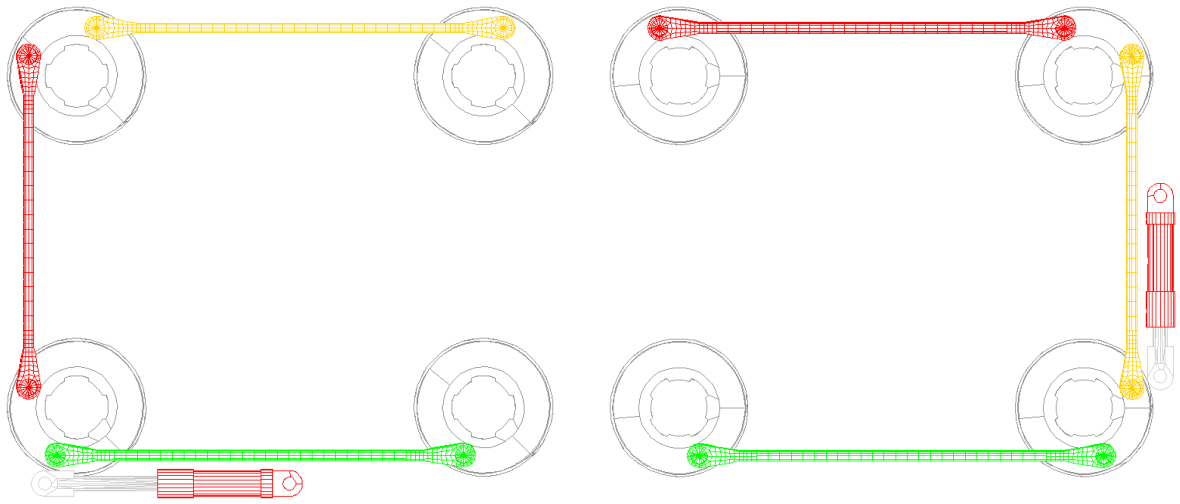

Figure 3-13: Different connecting bars and cylinder configurations

3.3.3 Valve Response Time

The opening time of the main valve can be altered by adding orifices in the control channels between the pilot and the main valve. By throttling the fluid flow the response time is lengthened. Actually, orifices of diameter 0.5 mm are used and the response time, taken from measurements, is about 90 ms. The directional valve is not modeled in detail but the opening time of the valve component can be changed. The effect of the opening time is recapitulated in table 3-4. It shows that changing the response time of the directional valve is a very effective way to reduce the force peaks without noticeably affecting the overall locking or unlocking time.

The simulation gives the evidence that the best results can be achieved by changing the hydraulic system. Unfortunately, the smallest orifices available are already fitted in the valve. Other means have to be found to reduce the pressure peaks at valve opening.

opening time of valve	horizontal bar		vertical bar op.-side		vertical bar non op.-side		(un)locking time
50 ms	214 kN	+ 38 %	72 kN	+ 44 %	56 kN	+ 30 %	- 22 ms
70 ms	182 kN	+ 17 %	59 kN	+ 18 %	47 kN	+ 9 %	- 12 ms
90 ms	155 kN	/	50 kN	/	43 kN	/	≈ 0.9 s
110 ms	150 kN	- 3 %	48 kN	- 4 %	45 kN	+ 5 %	+ 12 ms
130 ms	138 kN	-11,00%	44 kN	- 12 %	44 kN	+ 2 %	+ 25 ms

Table 3-4: Forces vs. Stiffness during Cylinder extension

3.3.4 Proportional Valve

As the spool velocity cannot be further influenced, the directional control valve is replaced by a proportional valve where the spool position is directly related to the command signal. The higher the input signal, the further the spool shift, and the greater the spool stroke, the greater the flow through the valve (see figure 3-14). The composition of the proportional valve is similar to the directional control valve except that it additionally has a positional transducer and a controller unit. When the solenoid of the pilot valve is energized, the main spool is actuated. The actual position of the spool is measured by the transducer and compared to the specified command value by the controller unit. If necessary, the controller corrects any deviations. By judiciously choosing the input signal the force peaks can be reduced without affecting the locking time.

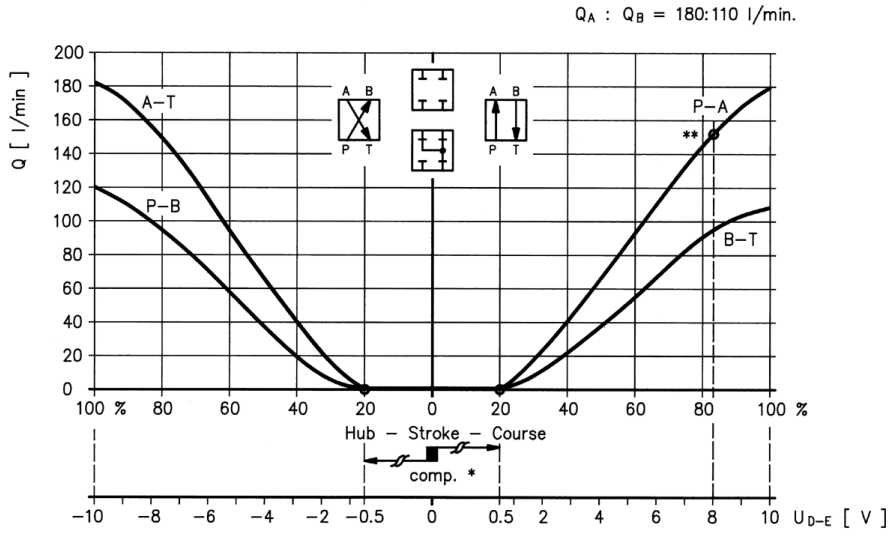

Figure 3-14: Performance curve at Δp = 5 bar

Using a proportional valve, the acting force at valve opening could be reduced by over 40 % (see figure 3-15). The input signal is slowly ramped up to the maximum input in order to reduce the pressure peaks to a minimum. To compensate for the time lost due to the

moderate acceleration, the maximum velocity of the cylinder is increased. Then, the velocity is again reduced to about 500 mm/s before cushioning as the current cushion is limited to this velocity for the deceleration of the clamp piston mass.

The old welded design still fails the FKM durability test, and a further reduction of the forces is only possible by considerably extending the locking time. However, the alternative welding design of figure 3-12 has no more to comply with the highest FAT class to pass the FKM check. A standard welding will do, which is an acceptable solution.

The disadvantage of the proportional valve solution is the increase of the maximum cylinder velocity. During retraction the velocity is raised from 500 mm/s to 600 mm/s and during extension, 1000 mm/s are reached. This probably means that another cylinder with special sealing is needed to accommodate these higher velocities; but this has to be discussed with the cylinder manufacturer. Additionally, the current piping might also be adapted due to the larger flow rates.

A preliminary price check yields that the welded connecting bar is about 30 % cheaper than the machined design. On the other hand, the proportional valve is nearly three times more expensive than the directional control valve, and the special cylinder about 15 % more expensive than the standard one. All in all, the cost reduction due to the welding design might be out weighted by the new hydraulic components that are necessary; but this has to be looked into more detail.

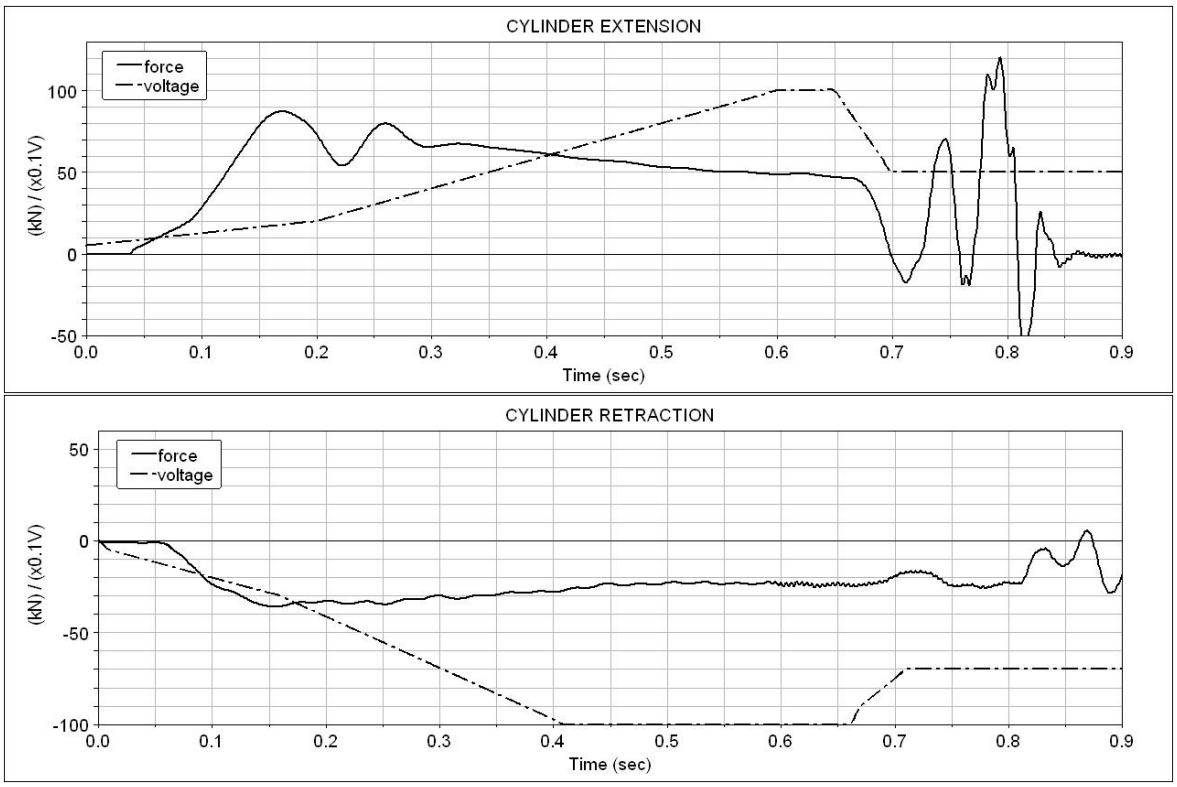

Figure 3-15: Command signal and cylinder force

3.4 Summary

This case study shows the interest of such integrated analyses. First of all, it gives a better understanding of the dynamic characteristics of the overall system. The tool also allows the user to easily evaluate different setups and parameters in order to optimize the design. But most striking is the possibility to investigate the interactions between quite different subsystems, which are generally difficult to assess. Additionally, as the MBS tool has the possibility to derive stress/time histories of a flexible body, the extra stress due to the dynamics of the system can also be computed.

The preceding analysis highlights the importance of the hydraulic system in the clamp locking mechanism. It is relevant for the force peaks in the mechanical system and dictates the design of the connecting bars. For the hydraulic system with the directional control valve only the new manufactured design passes the FKM durability test. By replacing the directional control valve with a proportional valve, it is possible to significantly reduce the forces peaks by 40 % without extending the locking time. The current design can then be replaced by a cheaper welding design. However, it still has to be checked if this solution is also a success from a costing point of view. Finally, an easy to implement cost reduction is possible by simply leaving out the longitudinal slot which is added to the current connecting bars. The simulations show that a reduction of the connecting bar stiffness is counter-productive as it does not reduce the force peaks as was expected, but in contrary increases them.

4 Moving Platen Stroke

4.1 Introduction

In order to extract the finished product, a mold consists of two parts. One half of the mold is fixed to the moving platen which is sliding on the clamp base while being guided by the latter one and by the four tie bars. The other half is attached to the stationary platen. The displacement of the moving platen is realized with the two stroke cylinders so that the mold can be opened after the injection phase for part extraction [38].

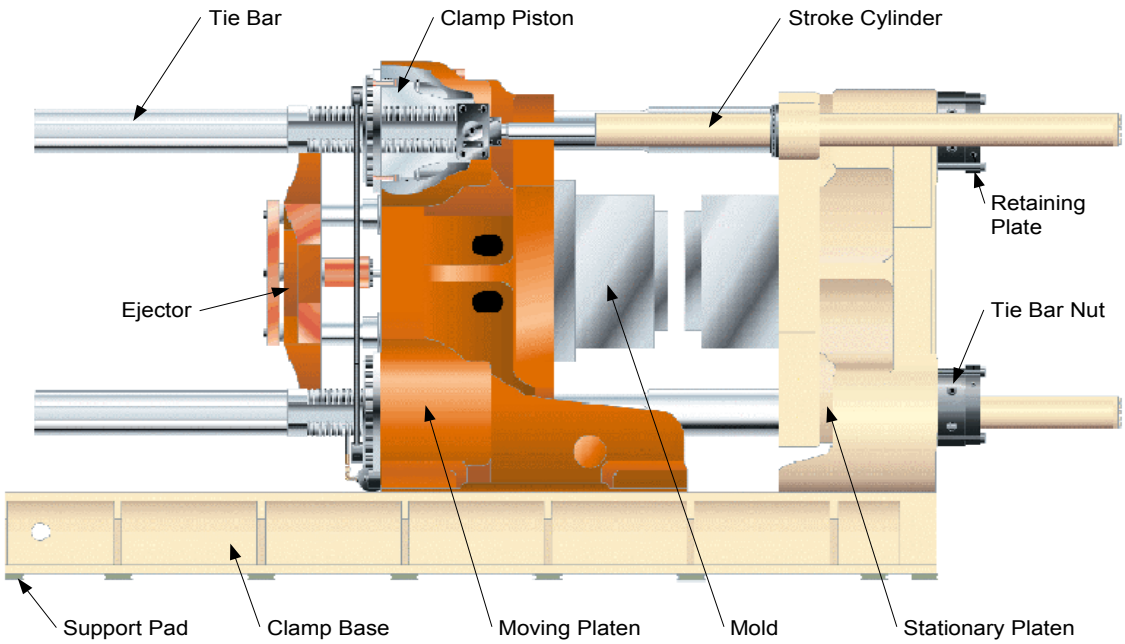

Figure 4-1: Quadloc™ clamp unit

The hydraulic cylinders are actuated by a pilot operated proportional valve. The flow through this valve, and thus the velocity of the moving platen, can be influenced as the position of the spool is directly related to the electrical input signal for the valve. Currently, the velocity, and indirectly the position, of the moving platen are controlled through an open-loop system. The aim of the simulation is to investigate the moving platen stroke in order to find any means to reduce the overall cycle time of the machine. As the mechanical configuration is difficult to change, potential improvements are possible with the hydraulic and controls systems.

4.2 Simulation Model

The moving platen stroking is analyzed with the simulation tool presented in section 1.1.1. The flexibility of the mechanical components is neglected as the influence on the moving platen stroke is marginal compared to the required modeling and computational efforts. The main focus is on the hydraulic and controls system.

4.2.1 Mechanical System

The rigid-body model of the Quadloc™ clamp unit consists only of two components: the moving platen and the stationary platen assembly that comprises the clamp base and tie bars (see figure 4-2). The 3D models are created from simplified CAD geometries. The mass and inertia properties of the different parts are computed by the CAD program from the detailed geometry and entered manually in the MBS program.

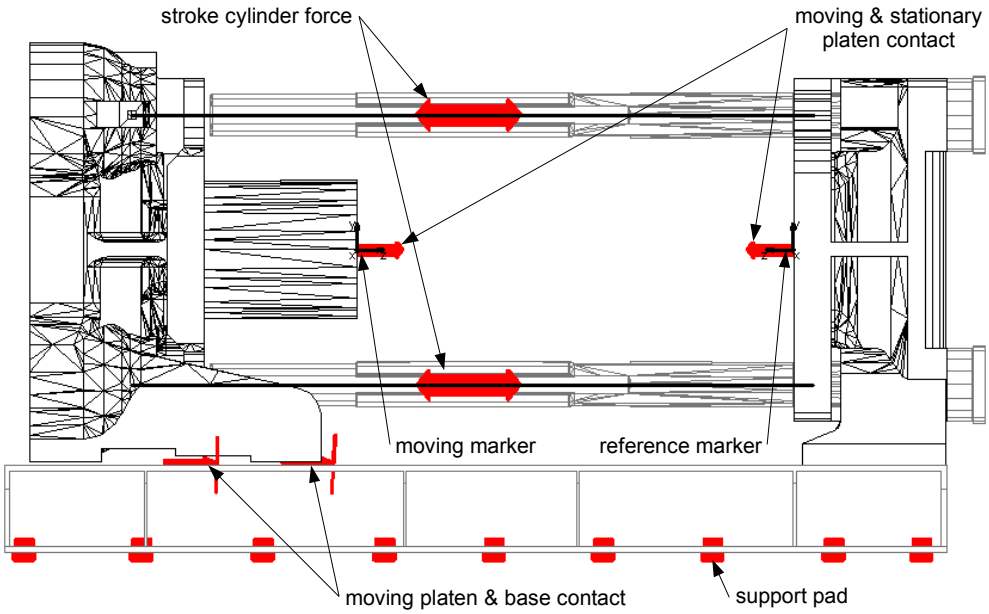

Figure 4-2: Rigid MBS model

The Q2700 clamp unit is standing on 18 support pads. They are height-adjustable to allow the leveling of the machine and are equipped with composite material to act as isolator and damper. In the model, the clamp base is simply fixed with linear spring-damper elements to the ground. Their stiffness and damping coefficients are deduced from catalog data and measurements (see section 5.1.3). Single-Force statements model the two stroke cylinders. Similar to the clamp locking model, their force is calculated by the hydraulic model. The actual position and velocity of the cylinders are computed by a user-subroutine from the moving marker and the reference marker (see section 2.4.1). The sliding of the moving platen is modeled with Contact statements. Basically, the Contact formulation is a nonlinear spring-damper element where the force is proportional to the penetration depth x and the penetration velocity $\dot{x}$. If there is no penetration then no force is applied to the

geometries. Otherwise the solver computes the location of the points of contact, the normals at the points of contact and the force acting between both parts based on equation (4-1), that is

$$\begin{aligned} F &= k \cdot x^e + d \cdot \dot{x} \quad for\ x < 0 \\ F &= 0 \qquad\qquad\ for\ x \geqslant 0 \end{aligned} \tag{4-1}$$

where *k* and *d* are the contact stiffness and damping coefficients, respectively, and *e* is an exponent that for numerical reasons should be chosen greater then 1. As the components are generally modeled as rigid bodies, the stiffness coefficient has to reflect the rigidity of the impacting area and of the overall structure. For some specific contact configurations, the stiffness may be determined from formulas based on the hertzian elastic contact theory [39]. Otherwise, it may be estimated from impact measurements or from finite element models. For the moving platen contact, the impact parameters are set to k = 1.6 10^{11} N/m, d = 1.6 10^{8} N/m and e = 1.2. Because of computational reasons, the Contact statements are not defined between the imported CAD geometries but between additional simplified geometries that represent the potentially contacting surfaces. 4 vertical and 4 lateral contacts are defined between the moving platen and clamp base to model the sliding and guiding respectively.

Friction can also be associated with the Contact statement. However, it uses a more simpler friction model than the one presented in the section 3.2.1.1. The formulation is based on the Coulomb friction model, that is

$$F_{friction} = \mu \cdot F_{contact} \tag{4-2}$$

However, μ depends on the relative sliding velocity *v* between the two colliding geometries and the specified static and dynamic friction coefficient, μ_s and μ_d. A typical representation of μ with respect to *v* can be found in figure 4-3. The plot shows that this friction formulation cannot model sticking as a minimum velocity is required to compute a friction force.

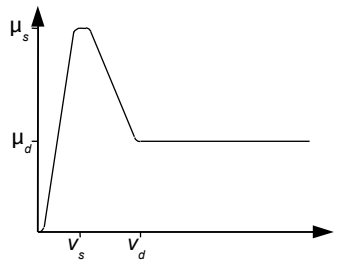

Figure 4-3: Contact friction coefficient

The friction coefficients are estimated from measurements. It is assumed that the stroke cylinders only have to overcome friction forces when the moving platen has a constant velocity. The cylinder force is calculated from the measured hydraulic pressures in the cylinder chambers. Knowing the overall weight of the moving platen, the dynamic friction

coefficient μ_d and the static friction coefficient μ_s are estimated to be 0.09 and 1.20 respectively.

Finally, a Contact statement is defined between the moving platen and the stationary platen. In this case, the stiffness coefficient is estimated from impact measurements on an operating machine. The coefficient is chosen so that the acceleration peak at impact from the model corresponds to the acceleration peak measured on the machine. The impact parameters are set to k = 6 10^9 N/m, d = 6 10^6 N/m and e = 1.2.

4.2.2 Hydraulic System

The hydraulic system for the moving platen stroke is quite complex and, as for the locking mechanism, the schematic is not translated one-to-one into a hydraulic model. Simplifications and adaptations are necessary with respect to the hydraulic components available and their limitations. Additionally, valves that only have a safety function and that are not active during normal operation are not included in the model. The simplified hydraulic model is presented in figure 4-4. Basically, the hydraulic system consists of the two hydraulic cylinders, the pump configuration and the stroke manifold block[10] which includes the proportional valve.

The fluid characteristics are those of HLP46: viscosity υ = 46 mm^2/s at 40 °C, density ρ = 835.2 kg/m^3 and E-modulus = 1.49·10^9 Pa. The system pressure is at 185 bar. As the pump configuration of the machine is able to deliver a flow that exceeds the flow rate needed by the stroke cylinders, the pump system is modeled as an ideal pressure source. In reality, pressure fluctuations occur as variable displacement pumps with pressure and flow regulators are used on the machine. Their influence is not taken into account by the model.

Hoses and pipes connect the manifold block with the pump system and the stroke cylinders. In the model they contribute to the effects of the fluid inertia and of the volume change under pressure of the flexible hoses. In contrary to the clamp locking model, their influence on the dynamic behavior of the system is although limited.

The stroke cylinders are actuated by a pilot operated proportional valve. As the high flow through the valve involves large actuating forces, a pilot valve controls the main valve. This valve is directly operated electrically by solenoids so that the control signal is hydraulically amplified in order to actuate the main spool. Again, the pilot operated valve is not modeled in detail, i.e. with main valve and pilot valve. The modeling component directly relates the stroke of the spool to the input signal by a second order delay; a natural frequency and damping coefficient need to be defined. Furthermore, look-up tables relate the relative opening area of one port to the position of the spool. For this purpose, the flow characteristic of the valve, similar to figure 3-14, is converted to a corresponding orifice area according to

10 A manifold block is a machined steel block on which different hydraulic components such as valves, or cartridges are mounted. This allows a compact construction by eliminating the use of subplates and piping.

$$Q = \alpha_D \cdot A \cdot \sqrt{\frac{2}{\rho}} \cdot \sqrt{\Delta p} \qquad (4\text{-}3)$$

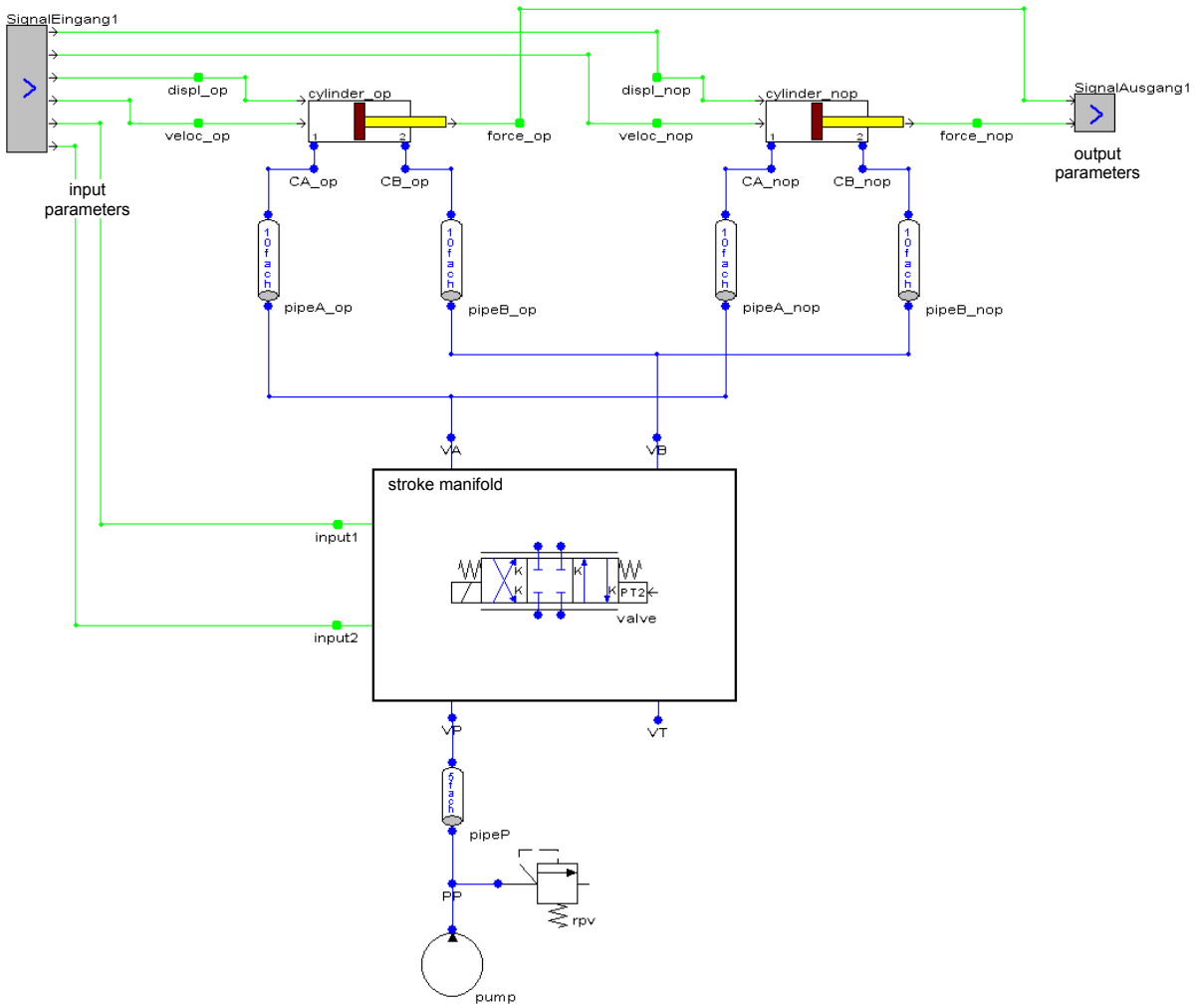

Figure 4-4: Hydraulic model

Finally, the input parameters for the hydraulic model are the position and velocity of the hydraulic cylinders, computed by the rigid-body model, and the command signal for the proportional valves and a directional valve, computed by the controls model. In return, the hydraulic model determines the stroke cylinder forces needed by the mechanical model.

In the beginning, the input parameters for the different hydraulic components were taken from the technical sheets available from the suppliers. Any unknown parameters were deduced from experience values. Unfortunately, first simulation results showed unacceptable deviations from the measured data. The discrepancies could be reduced by tuning specific parameters. However, these parameters had to be adapted each time that a different configuration, e.g. another maximum moving platen velocity, was simulated. This is not acceptable so that in the end, extensive measurements on the complete hydraulic system were necessary in order to adequately determine the input parameters.

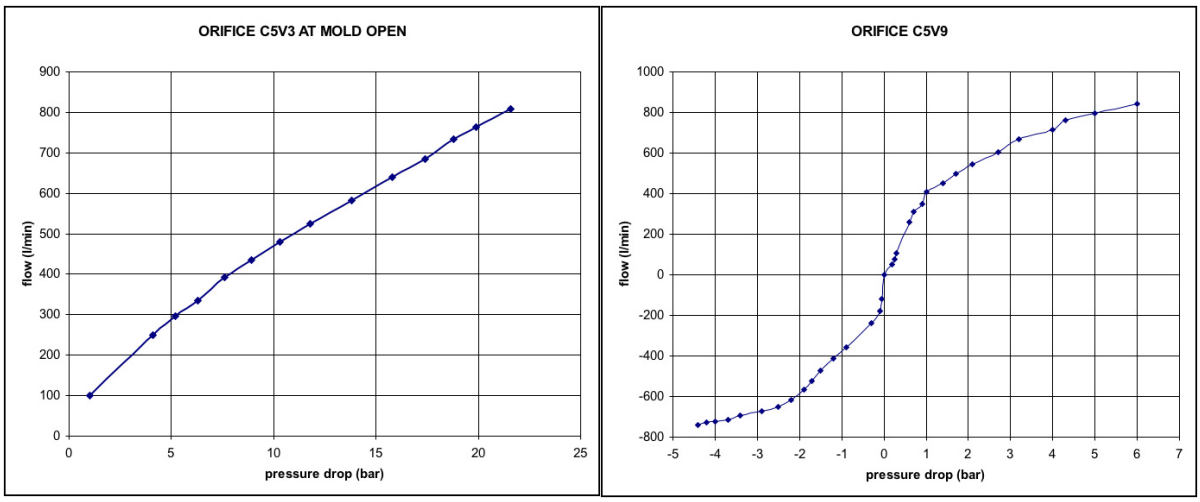

Figure 4-5: Measured pressure-flow characteristics

Therefore, pressures at specific locations of the stroke manifold were measured during a complete machine cycle. These measurements were repeated for different moving platen velocities. Deriving the oil flow in the system from the cylinder velocity and taking as reference the flow characteristic of the proportional valve, relevant input parameters for the main hydraulic components, such as pressure-flow characteristics, can be identified. After the complete analysis of the measurements and the implementation of the results, a very good correlation of the computed and measured data is finally achieved, and this for any machine setup (see figure 4-8 and 4-9). The measurements highlight two important points: first, the manifold block design has a big influence on the overall behavior of the hydraulic system, and second, the supplier data may not always be correct - in fact, a measured flow characteristic differed noticeably from what is specified by the supplier.

4.2.3 Controls System

The displacement of the moving platen is controlled through an open-loop system. A velocity profile for the moving platen is generated by the controller unit according to the input parameters specified by the operator. The accelerating phase is time dependent whereas the decelerating velocity profile depends on the actual moving platen position. From the velocity profile a command signal for the stroke valve is generated with the help of a look-up table (see figure 4-6). It relates the input voltage to the platen velocity. This means that the complete dynamic behavior of the machine, i.e. mechanic and hydraulic system, is approximated by the measured look-up table which in fact roughly reflects the stationary behavior of the system.

The controller logic is translated into a controls block diagram model. Unnecessary options are not included and any safety checks are bypassed. Of course, the model is not imperative as the platen position is controlled through an open-loop system. However, it comes in very handy when simulating different machine setups and it can be later on extended to a closed-loop system.

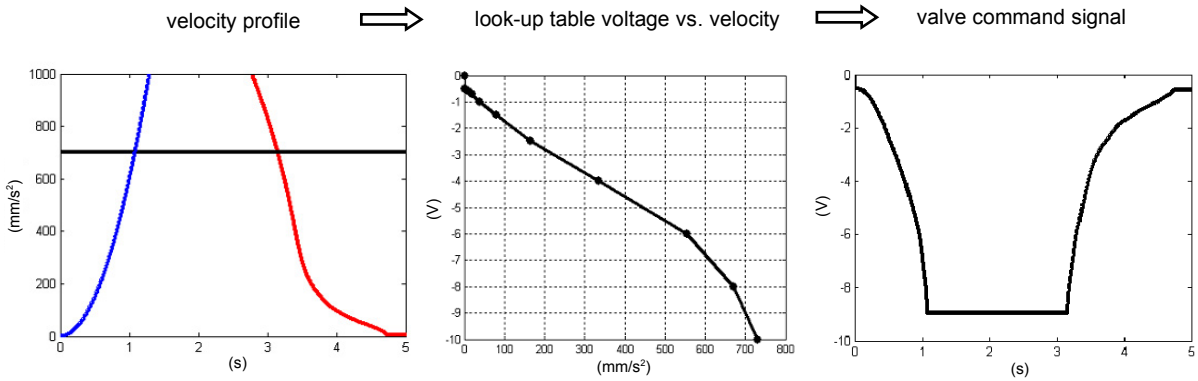

Figure 4-6: Mold close command signal for stroke valve

4.2.4 Co-Simulation

The three models are linked for the overall simulation as explained in chapter 2. Figure 4-7 shows the configuration for the simulation of the moving platen stroke. The computation of a complete stroke of the moving platen takes about ten minutes.

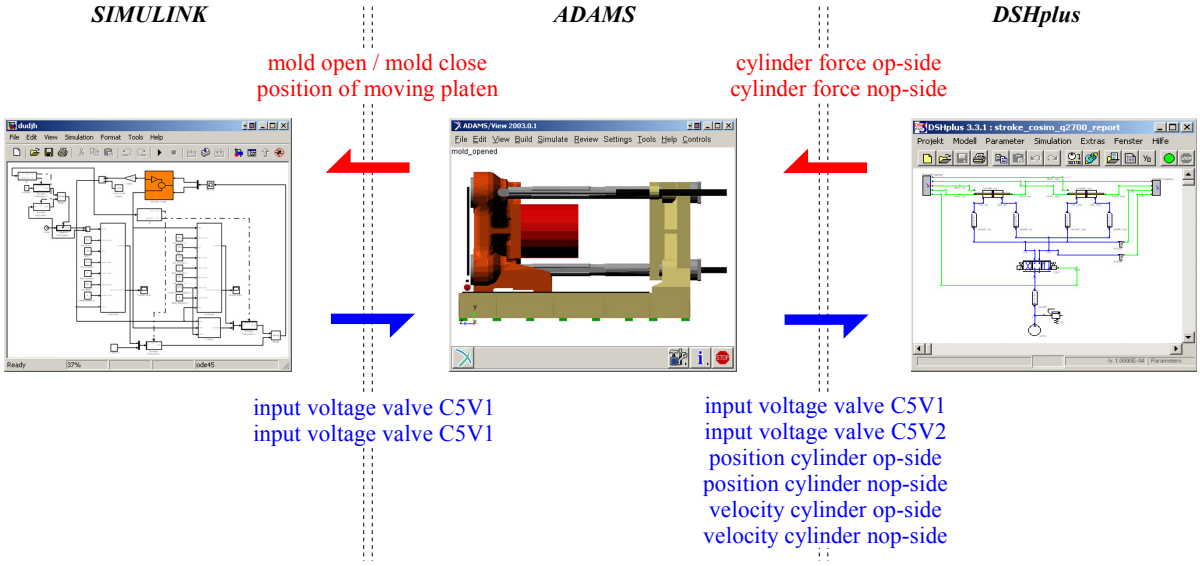

Figure 4-7: Hybrid simulation model

4.3 Simulation Results

The simulation results are now compared to measurements. Figures 4-8 and 4-9 show that, although differences in the absolute values are found, the relative correlation of both data is very good.

4.3.1 Comparison with Measurements

During the measurements, the machine is running in dry-cycle mode. This means that only the clamp unit is operated; no plastic is melted and injected. The overall moving platen stroke is 3300 mm, the maximum velocity is 760 mm/s for mold-close and 880 mm/s for mold open. The overall dry-cycle time, i.e. mold close, lock, clamp-up, unlock and mold open, for this specific configuration is 15.6 seconds. The complete moving platen stroke requires 9.8 seconds where 5.2 seconds are needed for mold-close and 4.6 seconds for mold-open.

The comparison shows that the simulation lacks an accurate modelization of the pump configuration. The variable displacement pumps installed on the machine deliver only as much flow as is required by the attached actuators. Their discharge is adjusted by either a pressure and/or flow controller. For example at valve opening, the pump controller has to react to the sudden demand of oil flow by the stroke cylinders. Due to the time delay of the pump configuration, the system pressure can momentarily drop as much as 20 bar. As the complete pump system is simply modeled by an ideal pressure source, these fluctuations cannot be represented. The discrepancies during the deceleration phase are due to the approximated pressure-flow characteristics of some components. A better correlation is not possible with the actual information and measurements available. However, the model is accurate enough for further analyses.

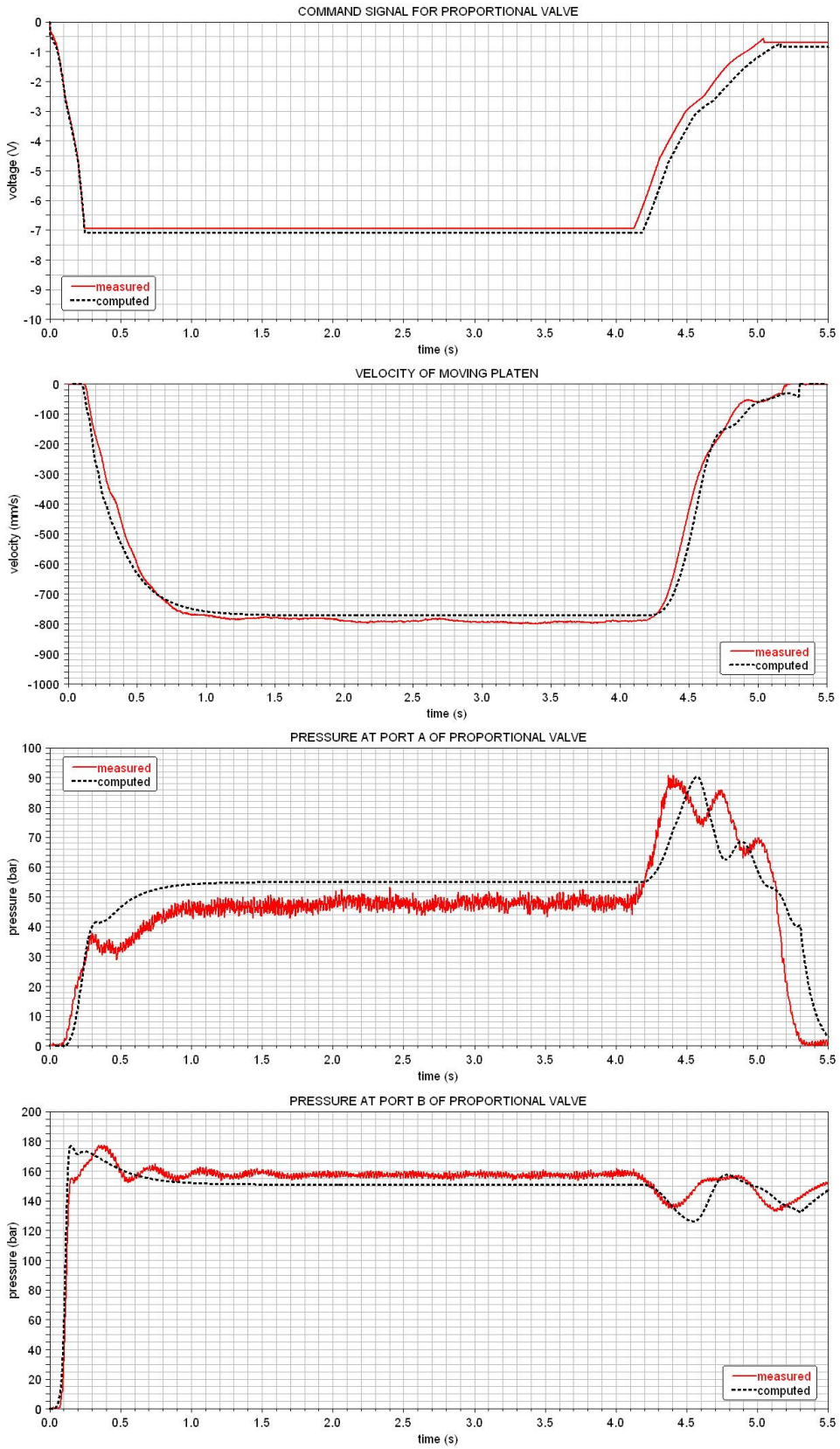

Figure 4-8: Mold closing

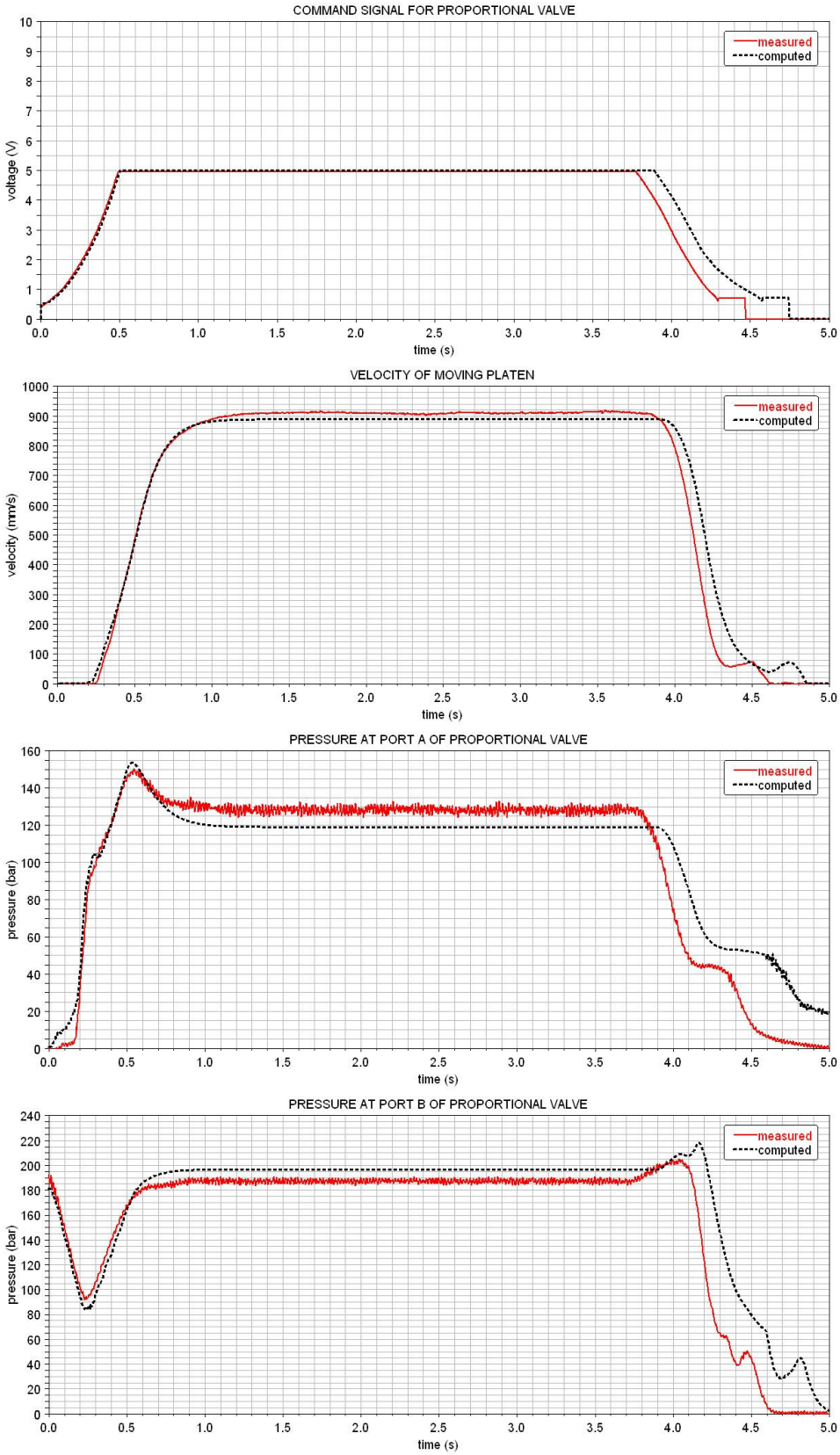

Figure 4-9: Mold opening

4.3.2 Remarks

The model allows to simulate various design parameters of the hydraulic system. The effect of different valve characteristics onto the system's dynamic or how the system performs under changing operating conditions can be investigated. The same is true for the controls. Different command signals of the proportional valve can be simulated in order to get some benchmark data that will help for the design of improved controllers.

The modifications presented in figure 4-10 and 4-11 should rather demonstrate the possibilities of the simulation model. In figure 4-10 b), the proportional valve is opened completely during acceleration in order to get the maximal possible flow. This allows to reach the set velocity earlier and to shorten the mold closing by 0.06 seconds, which are 1.2 %[11]. In figure 4-10 a), the acceleration profile is used for the deceleration of the moving platen. The moving platen is abruptly decelerated. Because of the fast closing of the proportional valve, the pressure rise at the bore side of the stroke cylinders is so important that the moving platen moves backwards for a brief moment. This in turn is responsible that the pressure at port A drops down to 0 bar. In a real hydraulic system this would lead to cavitation which is unacceptable as the hydraulic components could be damaged.

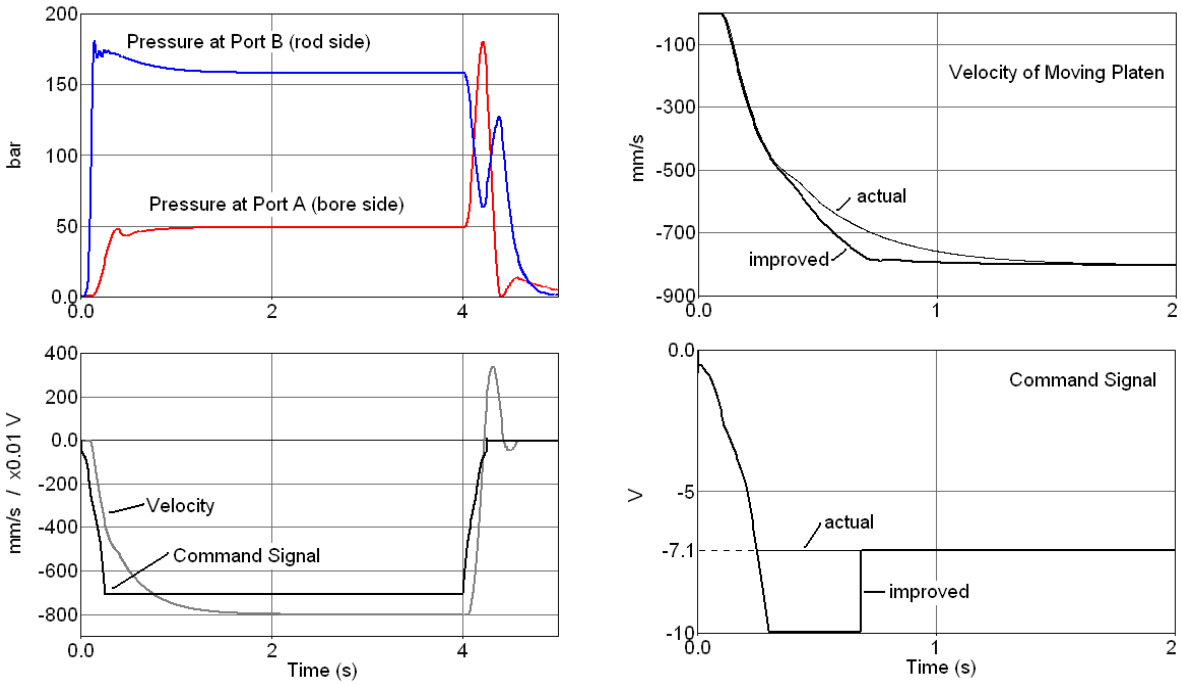

Figure 4-10: a) Modified deceleration profile, b) Modified acceleration profile

In figure 4-11, the proportional valve is completely opened during mold close in order to reach the maximum possible velocity, which is 882 mm/s. This velocity is specified to the controller model in order to generate the appropriate command signal for the proportional valve. The other parameters remain the same, i.e. deceleration 1200 mm/s^2, final velocity 25 mm/s safety distance 3.5 mm and mold stroke 3300 mm. The overall gain of time for

11 All the percentages refer to the corresponding displacement, i.e. mold close 5.2 s and mold open 4.6 s.

mold closing is 0.5 seconds, i.e. 9.6 %. For mold opening the maximum possible velocity is 1240 mm/s and the overall gain of time is 0.8 seconds, 17.4 %.

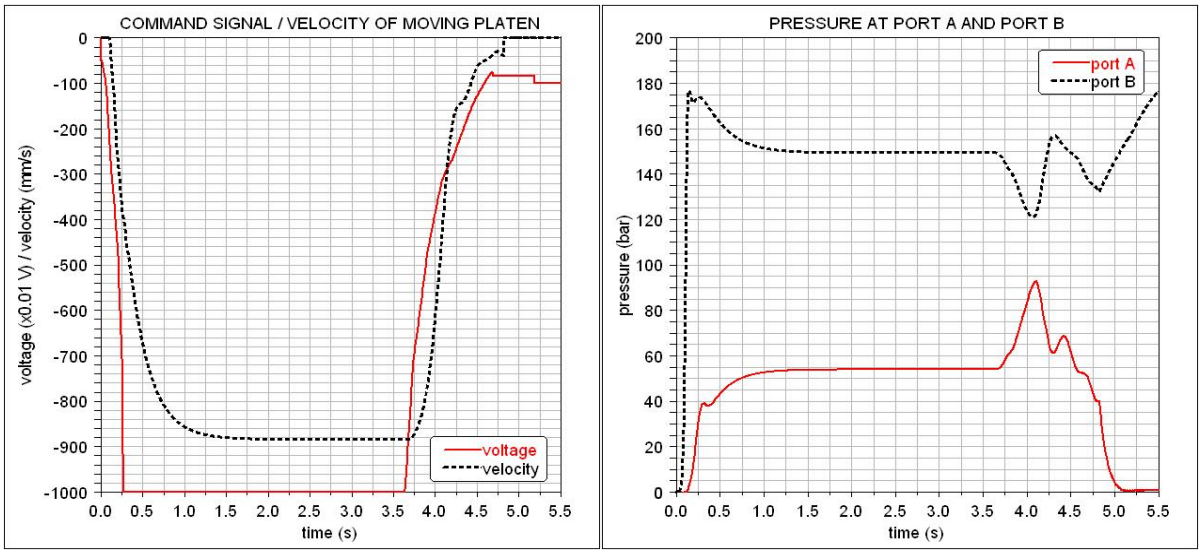

Figure 4-11: Maximum velocity at mold closing

Even though the simulation model does not always give exact absolute values, it helps to make qualitative and quantitative statements to the influence of different parameters on the dynamic behavior of the complete machine.

4.4 Closed-Loop Controls

Figure 4-8 and 4-9 show that the acceleration and deceleration of the moving platen take both about 1 second. As figure 4-10 b) brings forth, the acceleration cannot be significantly improved anymore. However, it should be possible to further reduce the deceleration time as the friction forces help to slow down the moving platen. Instead of finding an adequate command signal through a trial and error approach, a closed-loop model is developed according to figure 4-12.

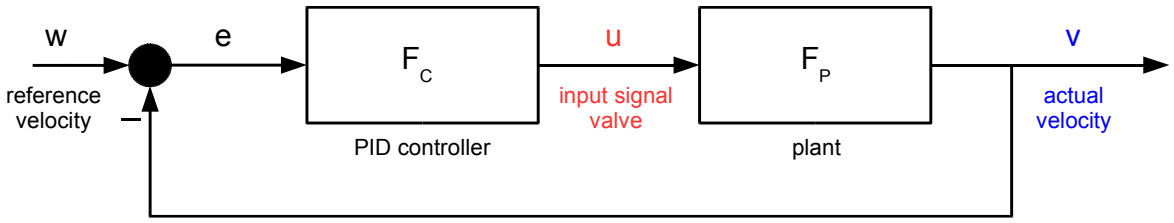

Figure 4-12: Closed-loop model

The feedback controller adjusts the input signal for the proportional valve so that the velocity of the moving platen follows a given velocity profile. For this purpose, a simplified linearized model of the moving platen stroke is created in order to get a first estimation of the PID parameters. Afterwards the controller is applied to the complete simulation model for further fine tuning.

4.4.1 Linearized Model

The dynamic of the complete system is highly nonlinear. Furthermore it is subjected to non-smooth and discontinuous nonlinearities due to control saturation, directional change of valves, friction and impact. For a preliminary analysis of the closed-loop model, the combined mechanical and hydraulic system is heavily simplified, linearized at a specific working point and reformulated as a transfer function model where the input is the valve command signal and the output is the moving platen velocity. In this form, the controller system can be analyzed using the tools available in MATLAB and Simulink, such as frequency response analysis, root locus or pole placement.

Figure 4-13 shows the equivalent simplified moving platen stroke model. It consists of a hydraulic cylinder, representing the two stroke cylinders, acting on a mass, the moving platen. The cylinder is actuated by two variable orifices that correspond to the complete stroke manifold block. The nominal flow rate of each orifice is directly related to the command signal *u* that is controlling the moving platen velocity *v*.

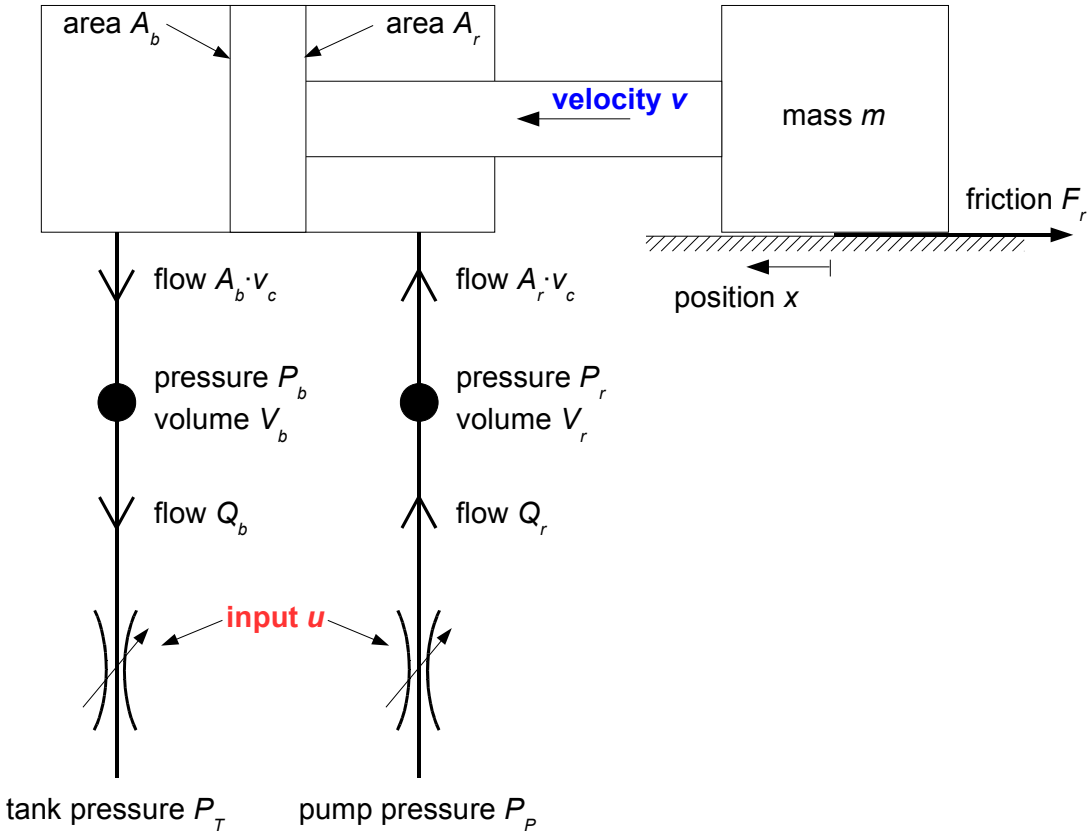

Figure 4-13: Simplified moving platen stroke model

The set of differential equations to solve is derived from the hydraulic equations presented in chapter 2. The equations describe the cylinder retraction, i.e. the mold close. *E* is the elastic modulus of the oil and α and β are the nominal flow rates of the equivalent valve, the other parameters are explained in figure 4-13.

$$\begin{cases} \dot{P}_r = \dfrac{E}{V_r + A_r \cdot x} \cdot \left[Q_r - A_r \cdot v \right] \\ \dot{P}_b = \dfrac{E}{V_b - A_b \cdot x} \cdot \left[A_b \cdot v - Q_b \right] \\ Q_r = \alpha \cdot \sqrt{P_P - P_r} \cdot u \\ Q_b = \beta \cdot \sqrt{P_b - P_T} \cdot u \\ \dot{x} = v \\ \dot{v} = \dfrac{1}{m} \cdot \left[P_r \cdot A_r - P_b \cdot A_b - F_r \right] \end{cases} \tag{4-4}$$

The set of equations (4-4) is now linearized around the working point. To make this possible several assumptions are made: first, the bulk modulus E of the oil is constant, second, the valve dynamics is infinitely fast, i.e. the control input u is porportional to the valve opening, third, the nominal flow rates depend linearly on the control input u.

At the working point, the velocity v and the pressures P_r and P_b are constant, which means that

$$\dot{v} = 0, \;\; \dot{P}_r = 0, \;\; \dot{P}_b = 0 \tag{4-5}$$

Additionally it is assumed that

$$u = u_0, \;\; V_r = V_{r_0}, \;\; V_b = V_{b_0}, \;\; x = x_0 = 0 \tag{4-6}$$

thus equations (4-4), (4-5) and (4-6) yield

$$v_0 = u_0 \cdot \alpha \cdot \beta \cdot \sqrt{\frac{P_P \cdot A_r - P_T \cdot A_b - F_r}{\beta^2 \cdot A_r^3 + \alpha^2 \cdot A_b^3}}$$

$$P_{k_0} = P_T + \frac{A_b^2}{\beta^2 \cdot u_0^2} \cdot v_0^2 \tag{4-7}$$

$$P_{r_0} = \frac{F_r}{A_r} + \frac{A_b}{A_r} \cdot P_b$$

The set of equations (4-4) is linearized by a first-order Taylor series expansion and reformulated into a set of algebraic equations using the Laplace transformation. This leads to the system of equations

$$s\cdot\boldsymbol{P}_r=\left[\frac{E}{V_{r_0}}\right]\cdot\boldsymbol{Q}_r-\left[\frac{E\cdot A_r}{V_{r_0}}\right]\cdot\boldsymbol{v}$$

$$s\cdot\boldsymbol{P}_b=-\left[\frac{E}{V_{b_0}}\right]\cdot\boldsymbol{Q}_b+\left[\frac{E\cdot A_b}{V_{b_0}}\right]\cdot\boldsymbol{v}$$

$$\boldsymbol{Q}_r=\left[\alpha\cdot\sqrt{P_P-P_{r_0}}\right]\cdot\boldsymbol{u}-\left[\frac{\alpha\cdot u_0}{2\cdot\sqrt{P_P-P_{r_0}}}\right]\cdot\boldsymbol{P}_r \tag{4-8}$$

$$\boldsymbol{Q}_b=\left[\beta\cdot\sqrt{P_{b_0}-P_T}\right]\cdot\boldsymbol{u}+\left[\frac{\beta\cdot u_0}{2\cdot\sqrt{P_{r_0}-P_T}}\right]\cdot\boldsymbol{P}_r$$

$$s\cdot\boldsymbol{v}=\left[\frac{A_r}{m}\right]\cdot\boldsymbol{P}_r-\left[\frac{A_b}{m}\right]\cdot\boldsymbol{P}_b$$

Finally, the transfer function between the input *u*, the valve command signal, and the output *v*, the moving platen velocity, is

$$\boldsymbol{v}=\frac{[a]\cdot s+[b]}{s^3+[c]\cdot s^2+[d]\cdot s+[e]}\cdot\boldsymbol{u} \tag{4-9}$$

with

$$\begin{aligned}
a &= \frac{E\cdot A_r}{V_{r_0}\cdot m}\cdot\alpha\cdot\sqrt{P_P-P_{r_0}}+\frac{E\cdot A_b}{V_{b_0}\cdot m}\cdot\beta\cdot\sqrt{P_{b_0}-P_T}\\
b &= u_0\cdot\alpha\cdot\beta\cdot\frac{E^2\cdot A_r}{2\cdot V_{r_0}\cdot V_{b_0}\cdot m}\cdot\sqrt{\frac{P_P-P_{r_0}}{P_{b_0}-P_T}}-u_0\cdot\alpha\cdot\beta\cdot\frac{E^2\cdot A_b}{2\cdot V_{r_0}\cdot V_{b_0}\cdot m}\cdot\sqrt{\frac{P_{b_0}-P_T}{P_P-P_{r_0}}}\\
c &= \frac{u_0\cdot\alpha\cdot E}{2\cdot V_{r_0}\cdot\sqrt{P_P-P_{r_0}}}+\frac{u_0\cdot\beta\cdot E}{2\cdot V_{b_0}\cdot\sqrt{P_{b_0}-P_T}}\\
d &= \frac{u_0\cdot\alpha\cdot\beta\cdot E^2}{4\cdot V_{r_0}\cdot V_{b_0}\cdot\sqrt{P_P-P_{r_0}}\cdot\sqrt{P_{b_0}-P_T}}+\frac{E\cdot A_r^2}{V_{r_0}\cdot m}+\frac{+E\cdot A_b^2}{V_{b_0}\cdot m}\\
e &= \frac{u_0\cdot\alpha\cdot E^2\cdot A_b^2}{2\cdot V_{r_0}\cdot V_{b_0}\cdot m\cdot\sqrt{P_P-P_{r_0}}}+\frac{u_0\cdot\beta\cdot E^2\cdot A_r^2}{2\cdot V_{r_0}\cdot V_{b_0}\cdot m\cdot\sqrt{P_{b_0}-P_T}}
\end{aligned} \tag{4-10}$$

The behavior of the system heavily depends on the selected working point. However, as the stability margins are worst at low velocity, a working point at the end of the deceleration process is selected, i.e. for u_0 = -1 V which corresponds to a velocity v_0 of 53.2 mm/s. The other parameters are:

E	= 1.4 x10^9 Pa	P_P	= 180 bar	P_T	= 0 bar
m	= 62400 kg	F_r	= 55.1 kN		
A_r	= 0.01508 m^2	A_b	= 0.03079 m^2		
V_{r0}	= 0.05978 m^3	V_{b0}	= 0.02208 m^3		
α	= -0.4394 x10^{-6} m^3/(sV√Pa)	β	= -0.7049 x10^{-6} m^3/(sV√Pa)		
P_{r0}	= 146.7 bar	P_{b0}	= 54.0 bar		

and equation (4-3) becomes

$$\frac{\boldsymbol{v}}{\boldsymbol{u}} = F_P = \frac{-55.76 \cdot s - 188.1}{s^3 + 12.44 \cdot s^2 + 1076 \cdot s + 3537} \tag{4-11}$$

Figure 4-14 shows the step and frequency response of the transfer function defined by equation (4-2). The zero of the transfer function is -3.37 and the poles are -4.53 ± j·32.0 (=> ω_0 = 32.3 rad/s = 5.1 Hz; D = 14 %) and -3.38 (=> T = 0.3 s).

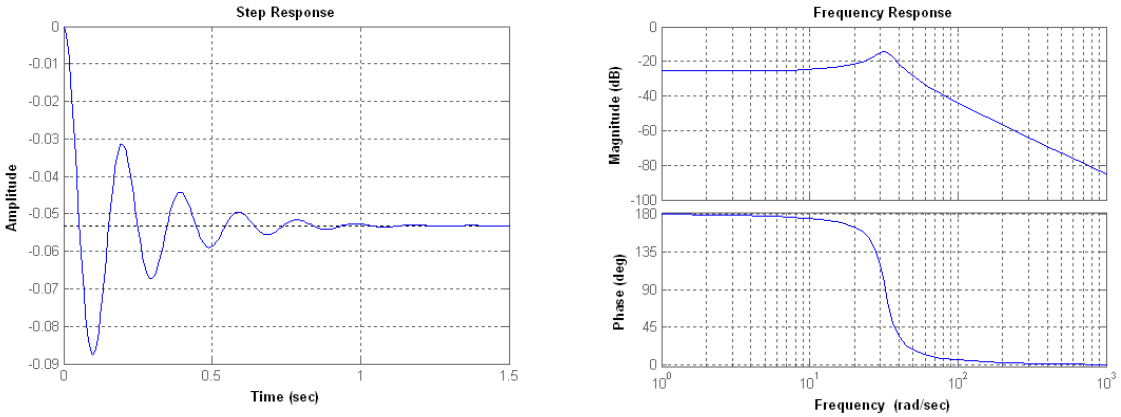

Figure 4-14: Step Response & Frequency Response of Plant

The results presented above correspond relatively good with the full simulation model when close to the working point. For example in figure 4-15 the frequency response of the linearized model is compared to the one of the full non-linear simulation model.

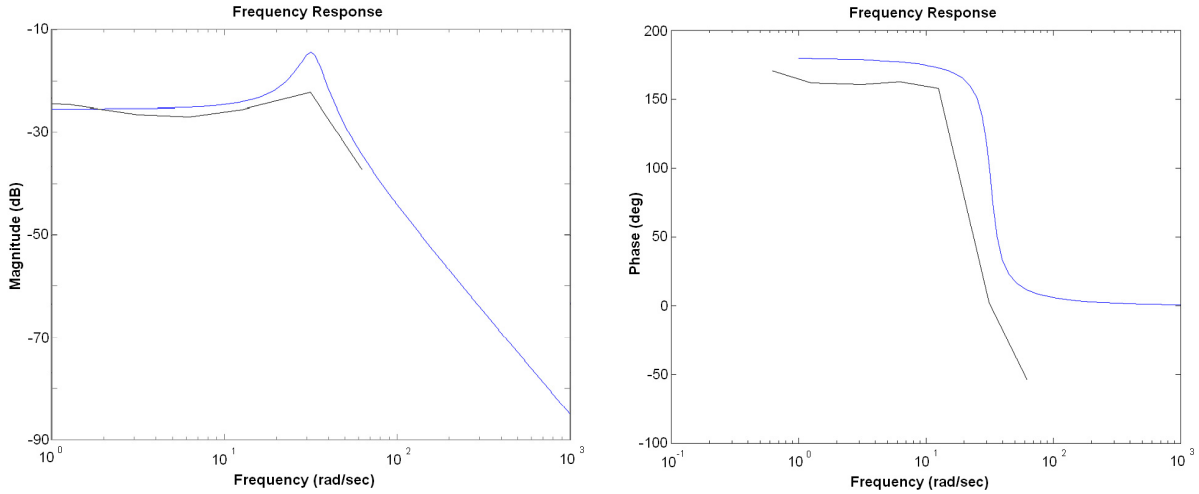

Figure 4-15: Frequency Response of linear (blue line) and non-linear model

However, a discrepancy is observed when leaving the working point. Furthermore, the behavior of the system strongly depends on the selected working point. The main reason for this is the assumed linear dependency of the control input on the nominal flow rates.

4.4.2 Controller Model

A PID algorithm is chosen for the closed-loop system as it is a very popular feedback controller with a robust and easy algorithm. The controller consists of three basic elements, a Proportional, an Integral and a Derivative element. The transfer function of the PID controller implemented in the model is

$$F_C = K_P \cdot \left(1 + \frac{1}{T_I \cdot s} + T_D \cdot \frac{s}{1 + T \cdot s}\right) \tag{4-12}$$

The different controller parameters need to be determined. For this purpose, various rules of thumb are found in the literature [40, 41]. To make a first guess, the Ziegler-Nichols method is applied to the step-response obtained from the full simulation model. The parameters retained are: K_P = -4, T_I = 0.07 and T_D = 0.015, T is set to 0.01.

Thus the open-loop and closed-loop transfer functions are:

open-loop system

$$F_0 = \frac{0.3903 \cdot s^3 + 19.16 \cdot s^2 + 283.2 \cdot s + 752.3}{0.0007 \cdot s^5 + 0.07871 \cdot s^4 + 1.624 \cdot s^3 + 77.77 \cdot s^2 + 247.6 \cdot s} \tag{4-13}$$

The zeros are: -3.37
-22.86 ± j·7.00

The poles are: -100
-4.53 ± j·32.0 (=> ω_0 = 32.3 rad/s = 5.1 Hz; D = 14.0 %)
-3.38
0

closed-loop system

$$F_w = \frac{0.3903 \cdot s^3 + 19.16 \cdot s^2 + 283.2 \cdot s + 752.3}{0.0007 \cdot s^5 + 0.07871 \cdot s^4 + 2.014 \cdot s^3 + 96.93 \cdot s^2 + 580.8 \cdot s + 752.3} \tag{4-14}$$

The zeros are: -3.37
-22.86 ± j·7.00

The poles are: -96.7
-4.91 ± j·35.5 (=> ω_0 = 35.8 rad/s = 5.7 Hz; D = 13.7 %)
-3.41
-2.54 (=> T = 0.4 s)

The root locus plot of the open-loop model in figure 4-18 a) shows that the controller is stable for the given T_I and T_D, and that the stability and damping of the system can be

improved by increasing the gain K_P of the controller. However, the gain cannot be infinitely raised due to the control saturation limit of the proportional valve. Furthermore, the controller has, unfortunately, no real influence on the pole at -2.54. This dominant pole dictates the overall time response of the system.

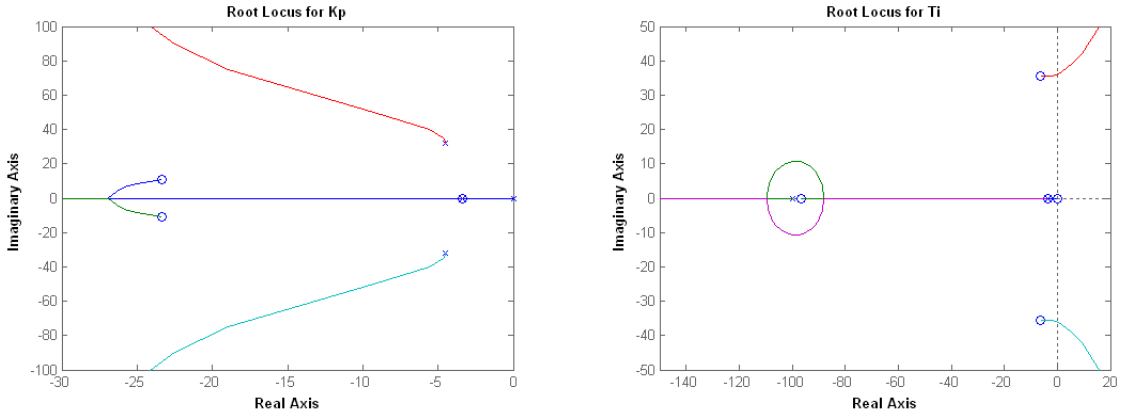

Figure 4-16: a) Root locus plot for K_P b) Root locus plot for T_i

The root locus of the open-loop model is also expressed as a function of the parameter T_I and plotted in figure 4-18 b). The diagram shows that for K_P = -4 and T_D = 0.07 the system becomes unstable for T_I < 0.0142.

For K_P = -4 and T_D = 0.015, an optimal T_I of 0.020 can be determined with the integrated squared error criterion [40, 42]. However, an absolute optimal PID setting cannot be estimated for this particular controller model. Therefore, in the next step the PID setting, K_P = -4, T_I = 0.02 and T_D = 0.015 is, as a start, applied to the full simulation model.

4.4.3 Full Simulation Model

The controller model in section 4.2.3 is extended with a PID controller. In practice, the original controller algorithm is used for the acceleration phase and the PID controller is only switched on during the constant-velocity phase. It controls the command signal with respect to the reference velocity. When the reference velocity reaches the final velocity, the controller is switched off again and a constant command signal is maintained until impact of the moving platen on the stationary platen (see figure 4-17).

The current deceleration time is about 1 second. In order to have any significant improvement, a deceleration time of half a second is targeted. Different controller gains and deceleration profiles are tested. Several individual test runs can be found in appendix D. Finally, the best results are obtained for a PID setting of K_P = -20, T_I = 0.048, T_D = 0.015, and a deceleration velocity profile based on a cubic spline as reference.

The overall gain of time, compared to the current controller, is 0.36 seconds, i.e. 6.9 %, for mold closing and 0.26 seconds, i.e. 5.7 % for mold opening. The controller handles the targeted deceleration time of 0.5 seconds without any saturation, i.e. no valve inputs above ±10 V and no cavitation. Of course, the sharper deceleration causes higher pressure peaks

in the hydraulic system, but they do not exceed the maximum specified pressure rise rate. An implementation of the proposed PID controller or of an optimized command signal on a real machine would be very interesting in order to test and validate these results.

4.5 Summary

The analysis of the moving platen stroke shows the potential of the simulation tools. Once the model is generated and validated, it allows to simulate various design parameters and to predict the influence of modifications on the performance of the overall system faster than proceeding experimentally. It also allows to simulate worst-case situations that are preferably not performed on real machines in a first step. The biggest modeling effort is needed for the hydraulic system. However, the generation of the model itself is not the problem, but the determination of the input parameters for the modeling components. The case study highlights the importance of measurements as the technical data from the suppliers is often insufficient.

In order to reduce the cycle time of the machine, the focus was on the controller system. Of course, the potential for improvements is probably greater by changing the mechanical or hydraulic system. However, any software changes are generally easier to implement than hardware modifications. Basically, two possibilities have been found to reduce the cycle-time of the clamp unit: first, to increase the moving platen velocity and second, to reduce the deceleration time. By opening the proportional valve completely during mold close and mold open, the model yields a maximum velocity of 882 mm/s and 1240 mm/s, respectively. The overall stroke time is reduced by 1.3 seconds, i.e. 13.3 %. No direct technical reasons have been identified not to run with higher velocities, except that probably other stroke cylinders and bigger piping are required in order to accommodate the much higher flow rates [43]. The PID controller implemented in the controls system allows to further reduce the overall stroke time by 0.6 seconds, i.e. 6.1 %.

The controller and optimization strategy used is well suited for linearized applications. Of course, there exist other solutions that are tailored to hydraulic systems, as for example presented in [30, 44, 45, 46], which probably yield better results. The comparison of the original controller with the PID controller basically shows that if the deceleration time should be reduced then the proportional valve must be closed faster. The limits are the intensity of the pressure peaks and the possibility of cavitation as shown in figure 4-12 a).

The great advantage of the optimization procedure presented in this chapter is that it can be done offline for a given machine configuration and load case, which means that some parameter tuning can be done upfront. The closed-loop controller can then afterwards be implemented directly on the injection molding machine or it can be used to generate an optimized command signal which is then used in an open-loop controller.

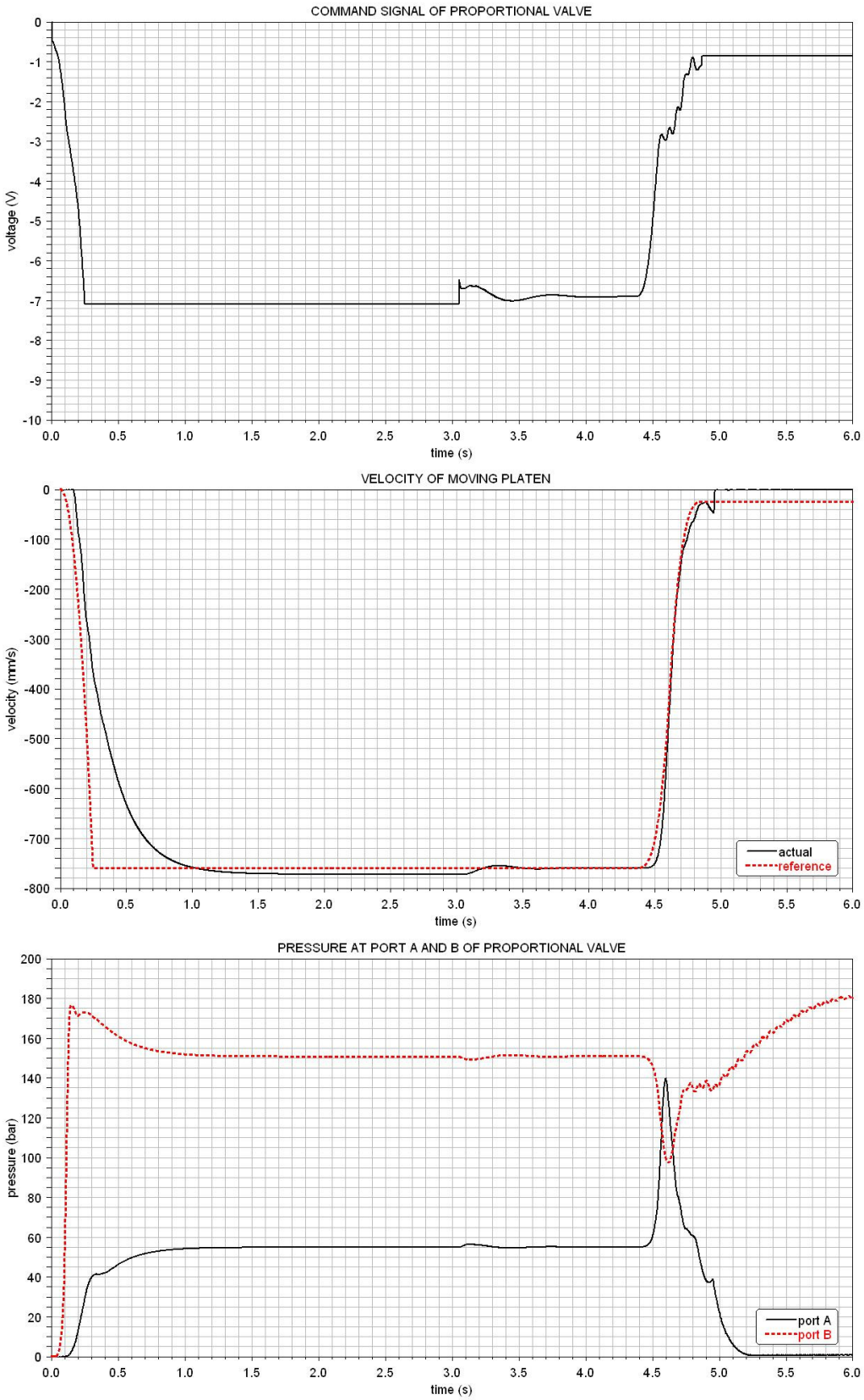

Figure 4-17: Mold closing with PID controller

5 Machine Creeping

In order to prevent any displacement relative to the ground of the complete injection molding machine during operation, it is simply bolted to the ground at the clamp unit end. The interest is now to determine under which conditions such a displacement becomes possible. With the simulation tools available, the root source of the phenomenon should be identified. It is expected that for some particular situations, such as acceleration, deceleration and/or impact of the moving platen, the lateral forces acting on the support pads are temporarily so important that the complete machine slides for a split second. The model is used to compute the lateral and vertical forces acting on the support pads during moving platen stroking and to see if at any moment the friction coefficient of the support pads is exceeded.

5.1 Flexible MBS Model

For this purpose, the clamp unit model of the previous chapter is changed to a flexible-body model in order to include mechanical vibrations and to have a more exact representation of the force distribution on the support pads. Furthermore, the model is extended with an injection unit to account for this additional mass. However, only the stationary platen, the tie bars and the clamp base are modeled as flexible bodies, the moving platen and the injection unit remain rigid bodies.

The modeling effort is much higher than for the clamp locking mechanism presented in chapter 3 because, first, the finite element models necessary for the stationary platen and the clamp base are more complex, and second, there are some limitations regarding forces and joints that can be defined to flexible bodies.

5.1.1 Moving Platen Sliding

Currently, several modeling elements such as translational joints or contact statements cannot be directly defined to flexible bodies. However, this can be overcome by attaching a dummy part to the node of a flexible body and defining the joints and forces to that dummy[12]. In fact, a moving force on a flexible body cannot be modeled with the standard constraints currently available. The point of contact must be defined to a node that is determined a

12 A dummy part is a part whose mass and inertia properties are set to zero. Furthermore it does not add any degrees of freedom to the model as it is completely attached to the flexible body with a fixed joint.

priori. This means that, when working with dummy parts for translational joints or contact statements, rather than modeling a point force sliding over the flexible surface, a varying point torque acting on the flexible surface at the location of the dummy part is modeled. This is an issue for the modeling of the moving platen sliding on the clamp base. Fortunately, this limitation can be avoided by different means - several approaches are presented in [47, 48]. The technique implemented in the flexible clamp unit model is based on the contact statement presented in chapter 4.

Basically the approach works as follows: for each of the selected nodes of the clamp base along the sliding path, a force *F* is computed according to equation (5-1). *DY* is the relative vertical position and *VY* the relative vertical velocity of the node to the moving platen. *K* and *D* are the contact stiffness and damping coefficients, respectively, and *E* is an exponent.

$$\begin{aligned} F &= K \cdot DY^{E} + D \cdot VY \quad && for\ DY < 0 \\ F &= 0 && for\ DY \geqslant 0 \end{aligned} \tag{5-1}$$

However, the force *F* is only activated when the node and the moving platen effectively overlap. In fact, it is weighted by a function that depends on the horizontal distance *DZ* between the node and the moving platen. The force is ramped up from zero or ramped down to zero in order to guarantee a smooth application and to minimize any discontinuities. The basic algorithm for the contact force computation can be found in figure 5-1.

```
CALL IMPACT(DY, VY, K, E, D, force)
IF ( (DZ < d1) OR (DZ > d2) ) THEN
    impactFORCE = 0.0
ENDIF
IF ( (DZ > d3) AND (DZ < d4) ) THEN
    impactFORCE = force
ENDIF
IF ( (DZ > d1) AND (DZ < d3) ) THEN
    CALL STEP(DZ, d1, 0, d3, 1, coeff)
    impactFORCE = coeff * force
ENDIF
IF ( (DZ > d4) AND (DZ < d2) ) THEN
    CALL STEP(DZ, d4, 1, d2, 0, coeff)
    impactFORCE = coeff * force
ENDIF
```

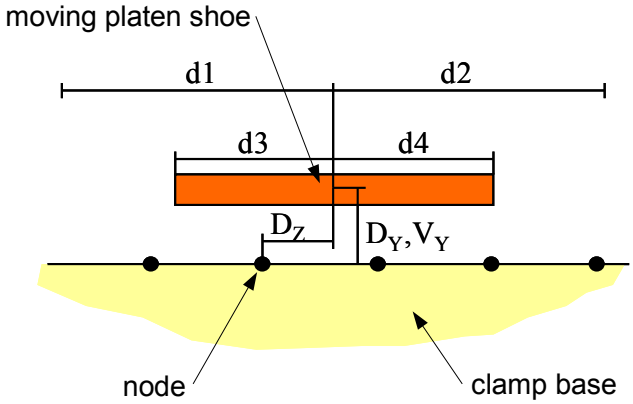

Figure 5-1: Sliding contact algorithm

IMPACT is an internal function of the MBS program that computes the contact force based on equation (5-1). *STEP* is an internal function that approximates the unit step with a cubic polynomial; it depends on *DZ* and varies between 0 and 1. Like in chapter 4, a friction force is also computed based on a Coulomb friction model according to equation (5-2).

$$F_{friction} = \mu \cdot F_{contact} \tag{5-2}$$

Where μ depends on the relative sliding velocity *VZ* between a node and the moving platen.

This very simple approach does not compute contact points and contact normals. The distance and velocity of a node relative to the moving platen are taken in the global coordinate system and the contact and friction forces are always collinear with the coordinate system unit vectors. However, as the deformation of the clamp base is very small, the rotation of the clamp base or the moving platen can be neglected. This approach adequately models the moving platen sliding with regard to the results needed and the modeling effort. The same technique is also implemented for the tie bar sliding. In fact, the tie bars are fixed at one end to the stationary platen while the other end is supported by the moving platen.

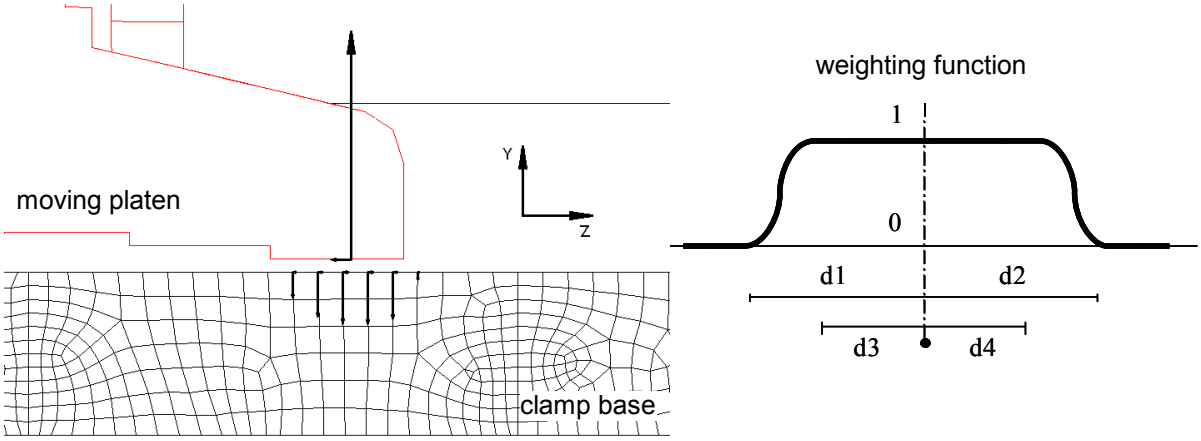

Figure 5-2: Moving platen sliding

The main disadvantage of this modeling approach is that a huge number of interface nodes are needed to have any sound representation of the moving contact forces. Unfortunately, this gives a huge number of flexible-body DOF in the MBS model and thus unacceptable computation times. Therefore, instead of defining these nodes as interface nodes, they remain interior nodes. The accuracy of the static deformation at the contact nodes is reduced when defining them as interior nodes instead of interface nodes. To compensate for the accuracy loss, additional normal modes are chosen during the computation of the Craig-Bampton basis. It is up to the user to find a compromise between computation time and accuracy. A comparison of a model using interior nodes for the moving platen sliding with a model using interface nodes shows a very good compliance of the results while having a much faster computation time. Therefore, in the following simulations, interior nodes are used for the contact sliding of the moving platen and the tie bars.

5.1.2 Flexible Body

The flexible body is created in the FE program by importing simplified CAD geometries of the stationary platen and the clamp base and meshing them automatically with 10-nodes

tetrahedral elements and 4-nodes shell elements, respectively. Afterwards, the tie bars are modeled manually with beam elements and the different components are connected via spring-damper elements. Additionally, beam elements with very high stiffness and low density are used to generate several interface nodes for the MBS model. The final FE model is composed of 14858 solid, 10061 shell, 280 beam and 44 spring-damper elements, and has a total number of 139287 finite element DOF.

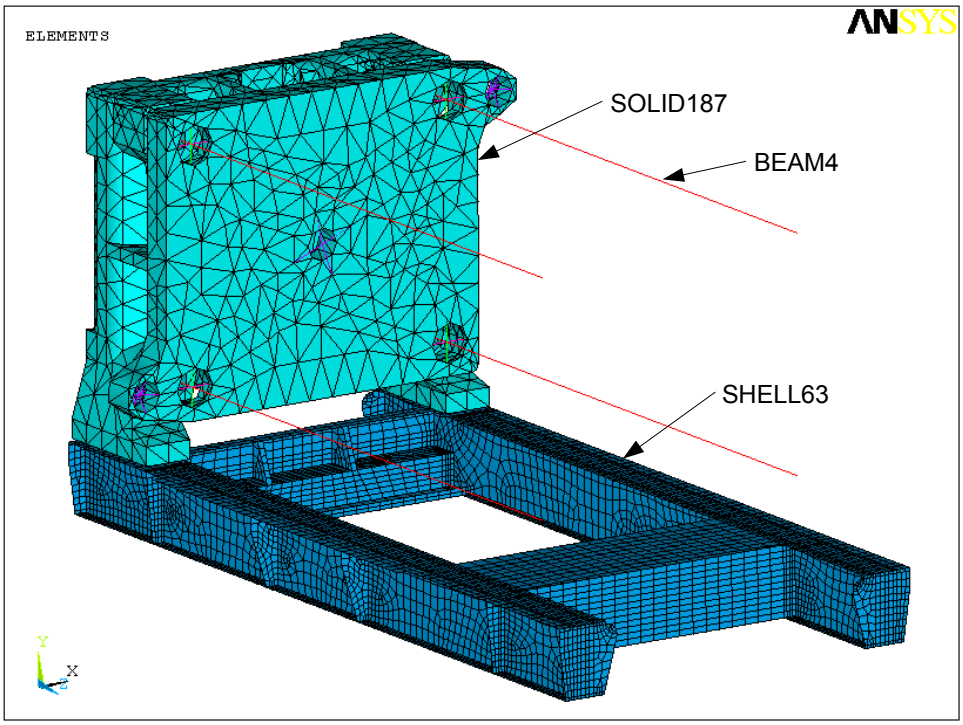

Figure 5-3: FE model

A predefined macro for the computation of the modified Craig-Brampton modal basis is available in the FE program. It allows the user to specify the interface nodes and the number of normal modes to consider. The resulting modal basis is written to a file that has to be imported into the MBS code. The macro automatically selects the six DOF of each interface node as master DOF. However, it is not imperative to select all the six DOF. For example, for a spherical joint defined at an interface node, only forces along the three translational DOF are transmitted, the three rotational DOF can be saved. This allows to furthermore reduce the number of static modes and thus the total number of flexible-body DOF. The macro has been changed accordingly to select only the effectively required DOF. Finally, the flexible body representing the stationary platen, clamp base and tie bars, has only 150 flexible-body DOF. Despite the very high reduction degree from nearly 140000 physical DOF to 150 modal DOF, the first free-free natural frequencies of interest are still met as can be seen in table 5-1.

full FE model	comment	modified Craig-Bampton	comment
0.0 Hz	rigid-body modes	0.0 Hz	rigid-body modes
4.7 Hz	injection interface modes	4.6 Hz	injection interface modes
8.5 Hz	tie bar modes	8.5 Hz	tie bar modes
9.0 Hz	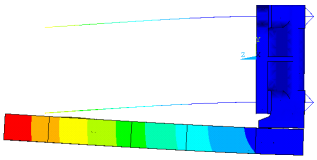	9.0 Hz	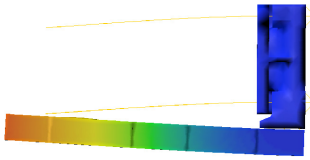
9.7 Hz	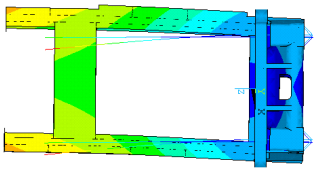	9.7 Hz	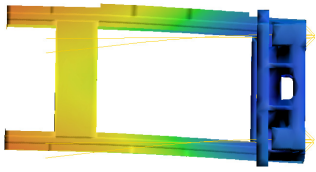
13.3 Hz	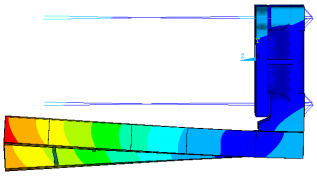	13.3 Hz	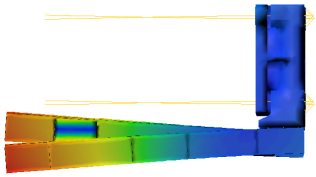
18.8 Hz	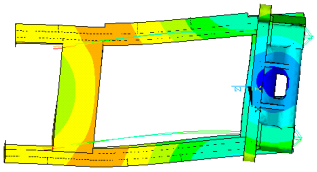	18.8 Hz	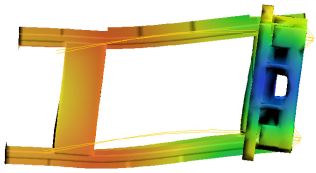
19.5 Hz	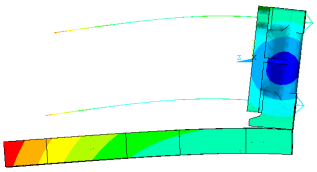	19.5 Hz	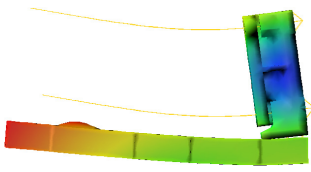
35.7 Hz	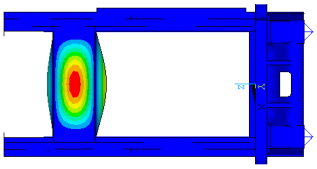	35.7 Hz	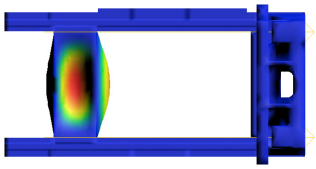
50.4 Hz	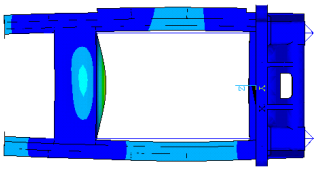	50.3 Hz	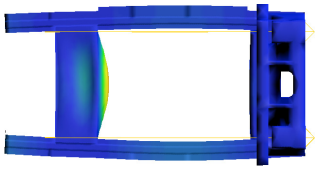

Table 5-1: First major eigenfrequencies of flexible body

Impact-hammer modal analyses of the different components are done in order to validate the FE model and the flexible MBS model. Unfortunately, measurements of the complete assembly as in figure 5-3 are not possible, only the individual parts are measured; the results can be found in appendix C. In fact, the characteristics of the joint elements that are connecting the different subassemblies have an influence on the natural frequencies of the complete assembly. They are deduced from catalog data and acceleration measurements

on an injection molding machine under operation. The concordance of the measured and computed data is satisfying as shown in section 5.2.

5.1.3 Overall Simulation Model

The composition of the flexible MBS model is similar to the rigid-body model of chapter 4. It consists of one flexible body that represents the stationary platen, the clamp base and the tie bars and of two rigid bodies that are the moving platen and the injection unit. The clamp base and the injection unit are fixed with linear spring-damper elements to the ground. Spherical joints connect the clamp base to the injection and the stroke cylinder forces and the contact statement for the moving platen impact are defined between both platens. Finally, the customized contact statements with friction for the moving platen and tie bar sliding are added.

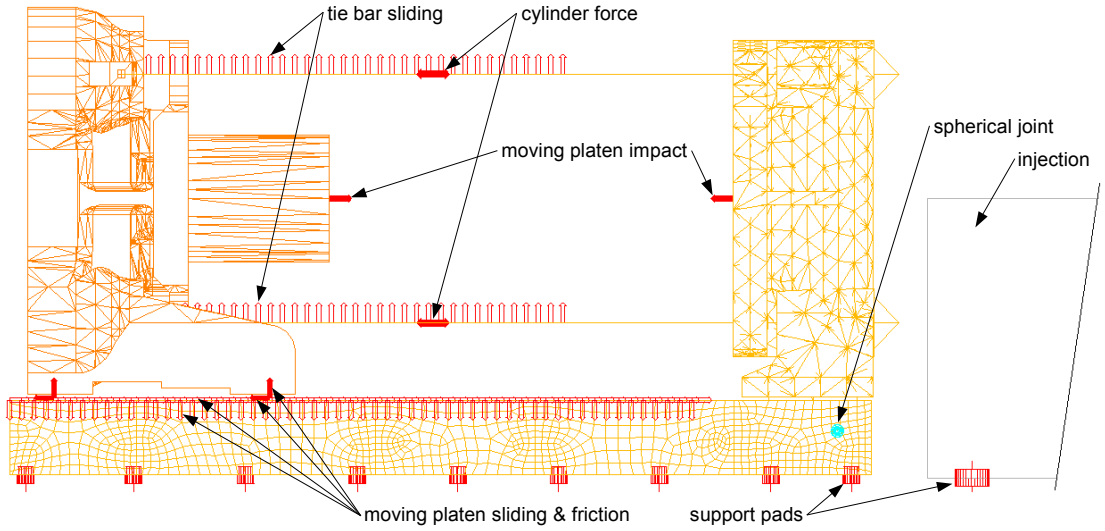

Figure 5-4: Flexible MBS model

The modal damping of the flexible body is difficult to assess. It mainly depends on the friction at the interconnections of the substructures and on the damping characteristic of the composite material of the support pads. These damping and stiffness parameters are estimated from acceleration measurements presented in the following section and from catalog data. A vertical stiffness and damping coefficient of respectively 6.3×10^8 N/m and 4.0×10^6 Ns/m and a lateral stiffness and damping coefficient of respectively 4.1×10^7 N/m and 8.0×10^5 Ns/m for the spring-damper elements are retained. A modal damping of 5 % is estimated for the flexible body and applied to all modes. In fact, the modal damping of some local modes, such as the one at 35.7 Hz in table 5-1, is generally much lower. But as these local modes are not of interest for this analysis, their damping is not specifically estimated by additional modal analysis measurements.

Finally, the hydraulic and controls model of chapter 4 are taken as they are and linked with the flexible mechanical model for the simulation of the injection molding machine. Due

to the flexible body and the sliding contact, the computation time is significantly increased; for example the calculation of the mold closing takes about 10 hours.

5.2 Acceleration Measurements

In the following, some simulation results are compared to acceleration measurements on an operating machine. The measurements are done on a machine available in the Technical Center in Luxembourg. During the measurements, the machine is running in dry-cycle mode. The maximum admissible velocity, acceleration and deceleration parameters are specified to the controller unit.

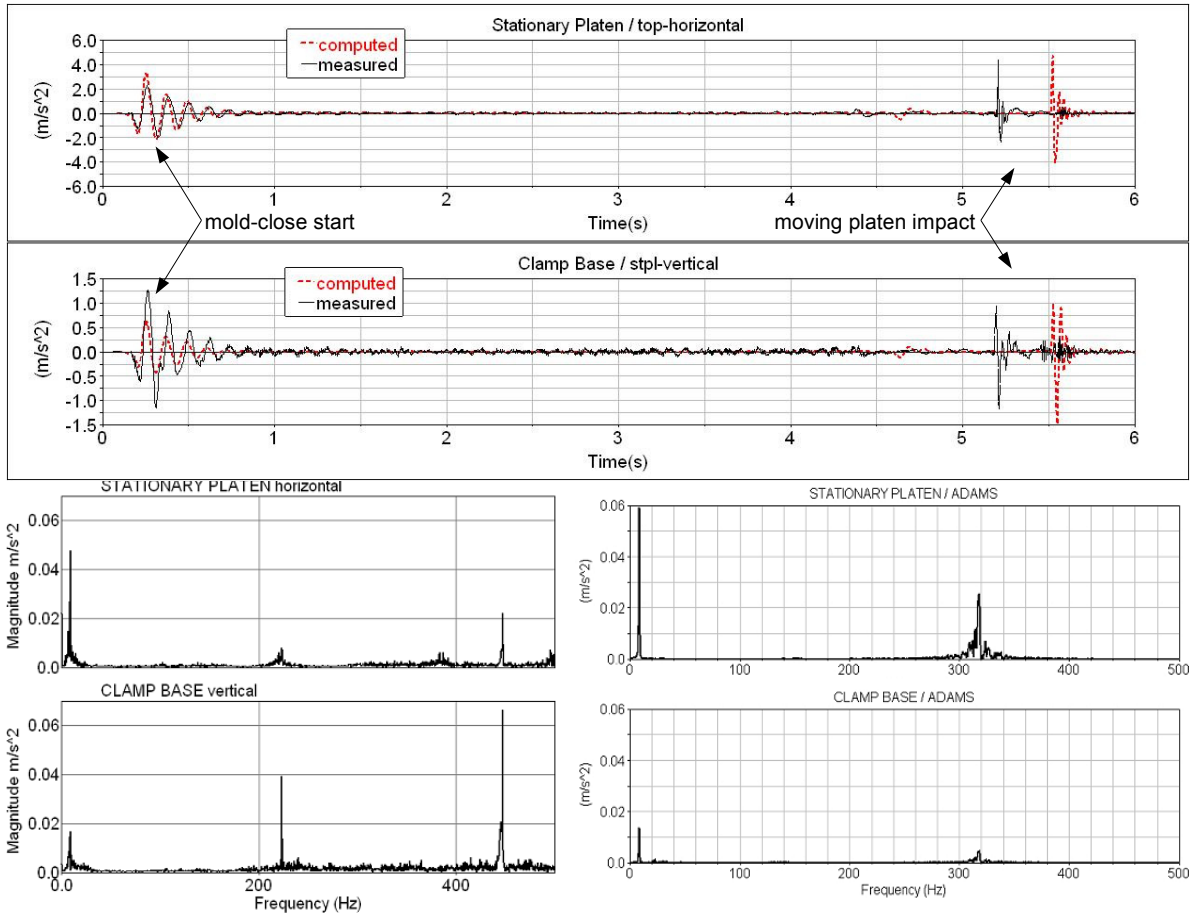

Figure 5-5: a) measured and computed accelerations b) FFT of measured and computed data

In a first step, simple accelerometer measurements are carried out on the clamp unit in order to determine the frequencies of interest. The accelerometers are fixed on both platens in the stroke direction and on the clamp base in the vertical direction. Three frequencies clearly appear in the spectrum of the time signals at 8.2 Hz, 223 Hz and 447 Hz. The two latter frequencies are due to the operating pumps. The frequency of 8.2 Hz corresponds to a deflection of the stationary platen and clamp base. The oscillation is particularly observed at mold-close start as can be seen in figure 5-5 a). The time delay between the computed and measured moving platen impact results from slightly different maximum velocities. The peak at 320 Hz in the ADAMS FFT is not found in the other spectrum. Probably the damping of

this mode is not properly defined.

Afterwards, more exhaustive measurements are carried out in order to generate operating deflection shapes (ODS). Several sets of measurements are necessary where vertical and horizontal accelerations from several locations along the clamp base and stationary platen are measured in reference to vertical and horizontal accelerations from fixed locations. The acquired data is evaluated with the algorithm implemented in ME'scopeVES. The ODS gives an information on the deformation under operation of the structure at a certain frequency [49, 50].

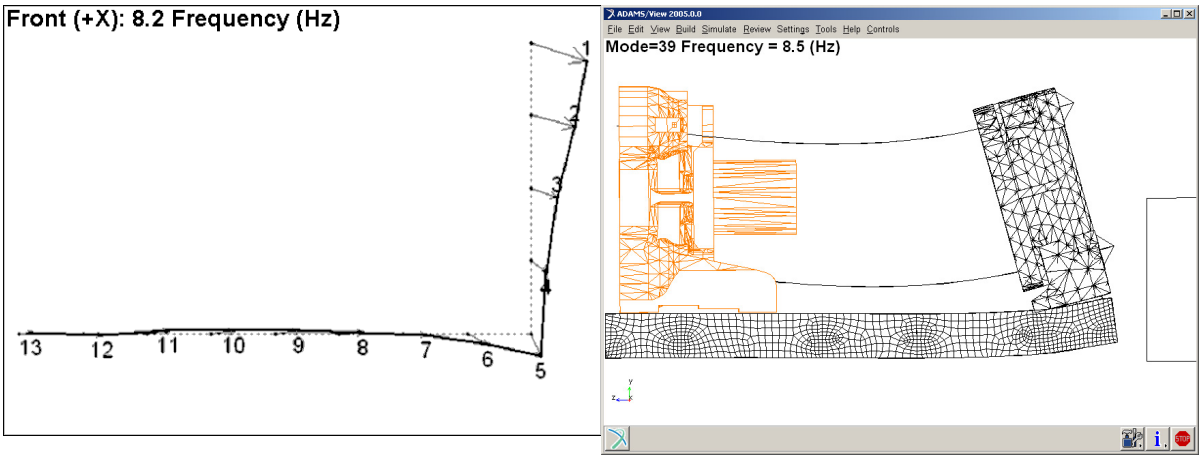

Figure 5-6: a) ODS measurement, b) ADAMS modal analysis

The MBS model is linearized and the eigenfrequencies of the complete clamp unit, with the corresponding mode shapes, are computed (see figure 5-6 b). Actually, figure 5-6 shows that the ODS at 8.2 Hz corresponds to a mode shape of the clamp unit. It is the force impulse from the stroke cylinders at mold-close start that excites this natural frequency. The same phenomenon is observed at mold-open start; however less pronounced and at a slightly higher frequency because the moving platen is nearby the stationary platen. Additionally, the measurement shows that the complete machine, i.e. clamp and injection unit, is oscillating at the same frequency in machine direction on the support pads.

5.3 Forces Acting on Support Pads

Preliminary to this investigation, the question arose if a vibrational problem could be the root source for the creeping. One can for example imagine that the complete machine is excited by the moving platen displacement, and therefore "bouncing" through the production hall. But neither the acceleration measurements nor any simulation results point to this possibility in the slightest sense. What seems more plausible is that the lateral forces acting on the support pads are temporarily so important that the complete machine slides for a split second, for example at moving platen impact.

The manufacturer of the pads indicates a friction coefficient of 0.8 on concrete with fine mortar as reference. With the simulation model it is possible to compute the lateral and

vertical forces acting on the support pads during the moving platen stroke. Thus, it is possible to determine if at any moment or for any particular situation, the lateral-force to vertical-force ratio exceeds the specified coefficient of adhesion. In figure 5-7 a), the vertical force of three pads is plotted for mold-close at maximum admissible velocity, acceleration and deceleration. In figure 5-7 b), the sum of all the lateral forces acting in machine direction (18 clamp unit and 4 injection unit support pads) is divided by the sum of all the vertical forces.

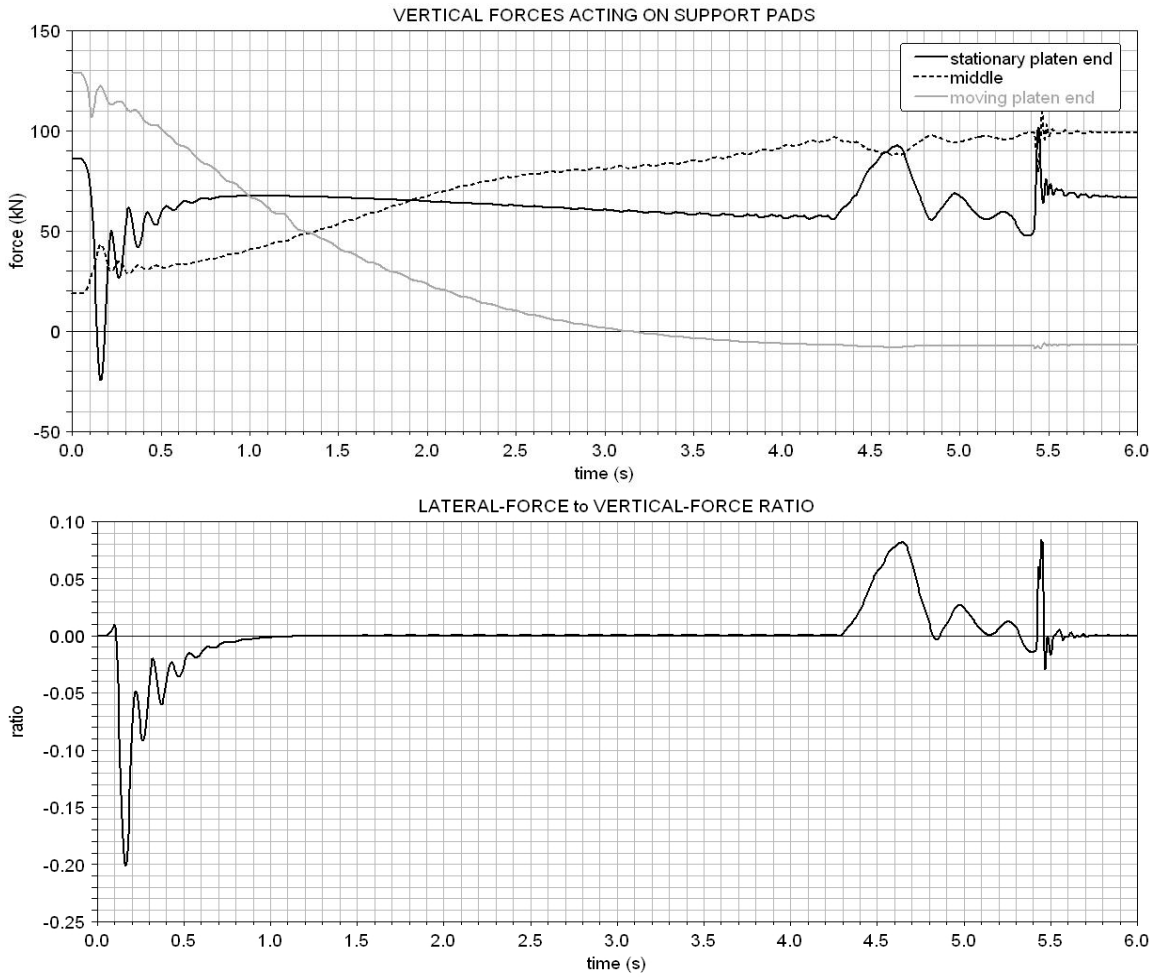

Figure 5-7: a) Vertical force, b) Force ratio

It can be noticed in figure 5-7 a) that the support pads at the extremities of the clamp base see negative forces. In reality, this would mean that the clamp base lifts of from those pads. At this particular moment, these pads cannot take up anymore lateral forces. Of course, the linear spring-damper elements cannot model this phenomenon. In order to simulate this, a more complex model is generated where the flexible clamp base is attached via spring-damper elements to support pads which in turn apply with contact-friction statements on the ground. However, the computation time becomes unrealistic (estimated to be at least one week) so that this model is finally abandoned. Therefore, the following results are all based upon the initial flexible MBS model.

Friction is a very complex phenomenon and there is a wide range of physical circumstances that cause friction. There exist a number of models of quite different nature to capture the essence of the different friction phenomena [52]. To get any notion if creeping might occur or not, the simple Coulomb friction model is considered. Figure 5-7 b) shows that for a standard cycle, the ratio between both forces does not exceed 0.2. It can be assumed that as long as the friction coefficient between the support pads and ground is much higher than 0.2, no creeping can occur. In fact, the injection molding machine of the Luxembourg Technical Center, which is now running for several months, is not bolted to the ground and no creeping can be noticed.

Figure 5-8: Emergency stop

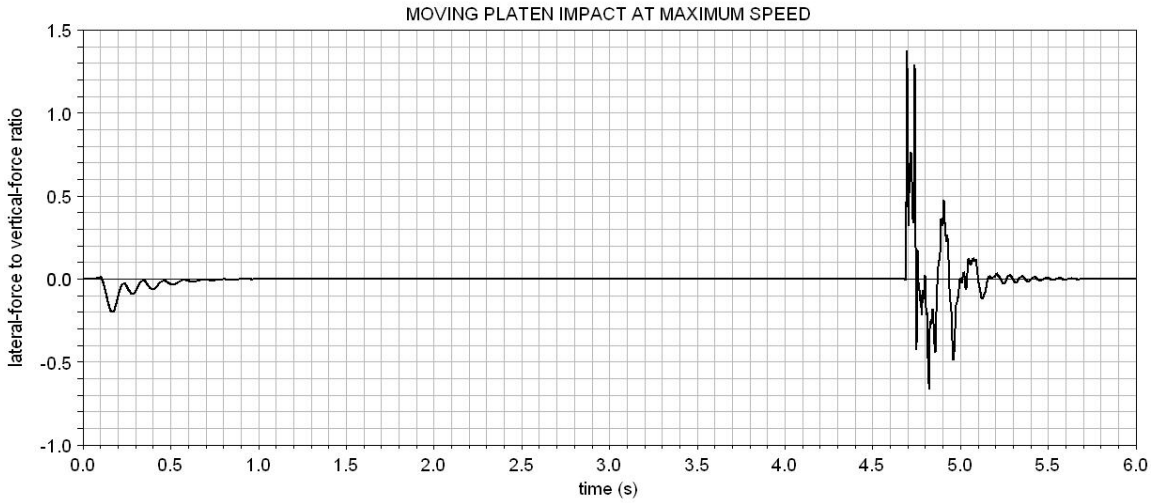

Figure 5-9: Moving platen impact at maximum speed

In a next step, different machine configurations and particular situations are investigated. The following worst case scenarios are considered: first, the moving platen impacts the stationary platen at maximum speed (this is technically possible if for example a wrong shutheight is specified by the operator) and second, an emergency stop is pressed while the

moving platen is traveling at maximum speed (in this case the proportional valve is instantly de-energized and the main spool is centered as fast as possible in order to stop the moving platen). The lateral-force to vertical-force ratio for both cases is plotted in figure 5-8 and 5-9. If the maximum ratio is nearly 0.5 for an emergency stop, it clearly exceeds the specified friction coefficient of 0.8 for a moving platen impact.

It is also interesting to have an idea of the potential displacement of the machine under these particular situations. As stated above, it is not feasible to apply contact statements between the flexible body and ground. However, it is very well possible for a rigid body. In this particular model, the complete injection molding machine is represented by a single rigid body. Contact statements with Coulomb friction are defined between the rigid body and the ground. Then, the computed lateral and vertical forces of the flexible MBS model are applied to the rigid body. The resulting displacement of the overall machine depends on the friction coefficient, the overall machine weight and the intensity of the lateral forces.

Table 5-2 lists the overall machine displacement in case of an emergency stop and a moving platen impact for different friction coefficients. The order of magnitude of the results in figure 5-8, figure 5-9 and table 5-2 appears to be reasonable in spite of the simplified simulation model. By intuition, the displacements seem however to be slightly too small. Unfortunately, there is actually no data available to compare the results with.

Friction Coefficient	Emergency Stop	Moving Platen Impact
0,8	0	0.4 mm
0,7	0	1.0 mm
0,6	0	3.0 mm
0,5	0	6.1 mm
0,4	0.9 mm	10.2 mm
0,3	7.0 mm	15.6 mm
0,2	17.2 mm	25.5 mm

Table 5-2: Machine displacement per cycle

5.4 Summary

The modeling and computation effort for the flexible clamp unit model is very high, but necessary in order to have a sound representation of the forces acting on the support pads during the moving platen stroke. The computation time can probably be reduced by more carefully generating the respective FE models. In fact, the stationary platen and the clamp base models are obtained from automatically meshed CAD geometries. A more regular meshing can be obtained by a "manual" mesh that would generally consist of less nodes. Furthermore, instead of 10-node tetrahedral elements, 4-node brick elements can be used that would further reducing the number of nodes. Thus, the size of the reduction matrix is reduced, speeding up the computation process. The drawback is that more time is needed to

manually generate adequate FE models; especially for the stationary platen. Additionally, the setting-up of the customized contacts in the MBS model is also quite time-consuming; the effort is reduced by working with macros. But the software companies are working on this issue and it can be expected that a "flexible" contact will soon be available in the standard constraint-library.

The results for the machine creeping are obtained from a relative simple simulation model, in the sense that it uses the Coulomb friction model and does not account for the contact loss of some support pads. However, the results are reasonable and give a very good qualitative information when creeping can occur. For a standard machine cycle, the lateral-force to vertical-force ratio for the support pads does not exceed 0.2. In case of an emergency stop, the ratio reaches already a maximum peak of 0.5, and in the case of a moving platen impact at maximum velocity, the maximum peak is 1.4. However, as the manufacturer of the support pads indicates a friction coefficient of 0.8 on concrete with fine mortar, creeping should normally not be an issue if the machine is properly operated and maintained, i.e for example no impacts at high speed level and no oil on the floor.

6 Synopsis

Today, the interest in integrated dynamic analysis of mechatronic systems increases [54, 55, 56, 57, 58, 59]. As already explained in the introduction, different approaches are possible depending on the nature of the system, on the required complexity of the model, or simply on the tools available to the engineer. During this work, the aim was to implement specialized commercial simulation software packages and to combine them in order to simulate the dynamic behavior of mechatronic systems as for example an injection molding machine [60, 61, 62].

The multi-body simulation software is the backbone of the current analysis as it inherently models large non-linear motions. Such analyses are only conditionally possible with an FE program and normally at the expense of very long computation times. But on the other hand, the FE formulation inherently includes the flexibility of the components. It is possible to account for the flexibility of components in the MBS model if necessary, but the use of flexible bodies has some restraints. They cannot for example account for non-linear material characteristics or model large deformations. Moreover, there are currently still some limitations regarding forces and joints that can be defined to them. Especially the problem of a moving force on a flexible body, like the sliding of the moving platen on the clamp base, is still an open issue in multi-body dynamics. However, there exist "standard" workarounds which work quite well. Additionally, stress-time histories of flexible bodies, which are necessary for durability analyses, are also directly accessible.

The flexible MBS components are created from FE models. They are reduced before being imported into ADAMS in order to limit the computation efforts. With the help of the component mode synthesis method, the generally huge number of FE DOF can be considerably reduced to a few DOF without significantly compromising the natural frequencies and the component stiffness of interest. To speed up the generation of the flexible bodies, simplified CAD geometries are imported into the FE tool and automatically meshed whenever possible. The finite-element and flexible-body models are validated by comparing the computed eigenfrequencies with measured natural frequencies. Generally, the agreement for single parts that are manufactured from solid metal and from casting is very good so that measurements are not really a necessity. For assembled parts or welding

constructions, it is more difficult to generate an appropriate FE model. In that case, measurements are advisable to confirm their accuracy.

Finally, another very interesting feature of the MBS program is that it can be linked with other simulation tools. For the analyses, other simulation codes were used to model the hydraulic and controls systems. It is important to mention that for hydraulic systems, the real modeling effort is not the generation of the model itself, but the determination of the input parameters for the different modeling components. Generally, the data found in the technical sheets is insufficient and often too optimistic - which highlights the importance of measurements.

The case studies show the interest and the potential of a combined analysis of mechatronic systems. Once the different sub-models, generated with the adequate simulation tool, have been successfully linked and, if possible, validated by measurements, various scenarios can be simulated and analyzed. The model provides the engineer with an additional insight into the overall system and thus with a better understanding of its dynamic characteristics. The interactions between the subsystems, which may be of very distinctive nature, can be investigated. Generally, it is difficult to predict such relations intuitively. Finally, the model allows to simulate with different design parameters and to asses the effect of modifications to these on the overall performance of the machine. This helps to identify the significant parameters that are crucial for an optimized functioning.

The simulation results presented in the preceding chapters show a very good correlation with the time-measurements done on an operating injection molding machine. There are in some cases small discrepancies in the absolute values that mainly result from a simplified model, for example the cylinder cushioning or the pump configuration. Nevertheless, it is always possible to make qualitative statements in order to give the direction to go. This is very helpful to work out improvements while being generally much faster and cheaper than proceeding experimentally. Such a simulation tool is also valuable in the early design stages as it serves as a fast method of evaluating different solutions in order to meet the specified objectives. Thereby, the need of costly prototypes can be significantly reduced. Furthermore, worst-case situations, which are preferably not performed on real machines, can be simulated without any concerns.

The simulation tools implemented at the university of Luxembourg are applied to the Q2700 clamp unit. Several issues were investigated: first, the clamp locking mechanism, second, the reduction of the moving platen cycle-time and third, the possible causes for machine creeping during operation. For this purpose, specific models are created to analyze the different problems in order to elaborate improvements.

Due to the high dynamics of the clamp locking mechanism and the installed hydraulic

system, the current connecting bars are manufactured from solid. This design is very robust but also very expensive. The aim of the investigation is to change the system accordingly so that the acting forces are reduced and a cheaper welded construction can be installed. The analysis in chapter 3 highlights the importance of the hydraulic system. The high force peaks responsible for the concerns occur at valve opening and are directly related to the opening speed of the flow directional valve. The only possibility to influence this parameter effectively is to install a proportional valve and to choose the command signal accordingly. With a very slow opening rate, the forces peaks are reduced by 40 %. The locking time remains the same as the maximum cylinder velocity is significantly increased in order to compensate for the time loss due to the moderate opening speed. With these changes in the hydraulic system, the current design can be replaced by a cheaper welding design. The drawback is that probably a special cylinder and bigger piping are needed to accommodate the higher flow rates. Furthermore, the proportional valve is also more expensive. All in all, the cost reduction obtained with the welding design may be abrogated by the cost of the special hydraulic components that are needed; but this still has to be looked into detail. Finally, an easy to implement cost reduction is possible by simply leaving out the longitudinal slot in the current connecting bars. The simulations shows that reducing the stiffness of the connecting bars is counterproductive and does not reduce the force peaks as hoped.

Another aim of the project was to simulate and analyze the moving platen stroke in order to reduce the overall cycle time of the machine. The mechanical design is frozen so that potential improvements are only expected by judiciously changing the hydraulic and/or controls systems. The model allows to easily test different extreme situations that would preferably not be done on a real machine. For example, the proportional valve is completely opened during mold close and mold open. The moving platen reaches then a maximum velocity of 882 mm/s and 1240 mm/s, respectively; the current acceleration and deceleration parameters are not changed. The overall cycle-time is reduce by 1.3 seconds, i.e. 13.3 %. In a next step, the acceleration and deceleration phase is investigated. The simulation shows that the acceleration cannot be improved anymore, whereas it is possible to further reduce the deceleration time. Instead of finding an adequate command signal through a trial and error approach, a closed-loop model is developed. A feedback controller adjusts the input signal for the proportional valve by comparing the actual velocity of the moving platen to a given velocity profile. The PID controller that is implemented in the controls system allows to further reduce the overall cycle-time by 0.6 seconds, i.e. 6,1 %. Basically, a shortening of the deceleration time is achieved by faster closing the proportional valve. This causes higher pressure peaks, and in the worst case can lead to cavitation, which limits the closing rate. A feedback controller is not indispensable as the same result can be obtained by changing the input parameters for the existing open-loop controller in order to generate a steeper deceleration profile. However, the advantage of this approach is that a command signal can

be automatically generated offline, whereas the current use of a look-up table relating the input voltage to the moving platen velocity is an oversimplified approximation of the system dynamics.

Finally, in the past the complete injection molding machine was sometimes creeping during operation. For this reason, it is nowadays bolted to the ground at the clamp unit end. With the simulation tools available, the possible causes of the phenomenon are investigated. In the beginning, the idea was that a vibrational problem could be responsible for the creeping, but such a phenomenon cannot be observed in the simulation runs, nor in the measurements. It seems more plausible that creeping is related to the friction between support pads and ground. It is assumed that for specific situations, the lateral forces acting on the support pads are temporarily very high so that the complete machine is sliding for a split second. For a standard machine cycle, the maximum lateral-force to vertical-force ratio is about 0.2, during an emergency stop the ratio reaches nearly 0.5, and for a moving platen impact at maximum velocity it is 1.4. The manufacturer of the support pads indicates a friction coefficient of 0.8 on concrete with fine mortar. Considering Coulomb friction, sliding is then only possible during an impact of the moving platen at maximum velocity. However, the effective friction coefficient is not really known and may vary from one machine to another. For example, it is not uncommon that the floor of the production halls is very dirty and oily, or that an operator regularly uses the emergency stop to interrupt a cycle. The simulation shows that creeping should normally not be an issue if the machine is properly operated and maintained.

APPENDIX A

Generalized Mass Matrix *M*

The kinetic energy of a flexible body can be written as

$$T=\frac{1}{2}\sum_{i=1}^{n_P}\left(m_p\cdot\dot{\boldsymbol{r}}_p^T\cdot\dot{\boldsymbol{r}}_p+\boldsymbol{\omega}_p^T\cdot\boldsymbol{J}_p\cdot\boldsymbol{\omega}_p\right)\equiv\frac{1}{2}\,\dot{\boldsymbol{\xi}}^T\boldsymbol{M}\,\dot{\boldsymbol{\xi}} \tag{A-1}$$

where n_P is the total number of FE nodes and m_p and $\boldsymbol{J}_p$ are the mass and inertia tensor of node p, respectively. The absolute translational velocity and the angular deformation velocity of a node p are defined by

$$\dot{\boldsymbol{r}}_p=\left[\boldsymbol{I}\quad-\boldsymbol{A}\cdot\left(\tilde{\tilde{\boldsymbol{s}}}_p+\widetilde{\boldsymbol{S}_p\cdot\boldsymbol{q}_f}\right)\cdot\boldsymbol{B}\quad\boldsymbol{A}\cdot\boldsymbol{S}_p\right]\cdot\dot{\boldsymbol{\xi}} \tag{A-2}$$

and

$$\boldsymbol{\omega}_p=\left[\boldsymbol{0}\quad\boldsymbol{B}\quad\hat{\boldsymbol{S}}_p\right]\cdot\dot{\boldsymbol{\xi}} \tag{A-3}$$

Therefore, the kinetic energy of a node p can expressed by

$$T_p=\underbrace{\frac{1}{2}\cdot m_p\cdot\dot{\boldsymbol{r}}_p^T\cdot\dot{\boldsymbol{r}}_p}_{(A)}+\underbrace{\frac{1}{2}\cdot\boldsymbol{\omega}_p^T\cdot\boldsymbol{J}_p\cdot\boldsymbol{\omega}_p}_{(B)} \tag{A-4}$$

where (A) is (recalling that $\boldsymbol{A}^T\cdot\boldsymbol{A}=\boldsymbol{I}$)

$$\frac{1}{2}\cdot m_p\cdot\dot{\boldsymbol{\xi}}^T\cdot\left[\boldsymbol{I}\quad-\boldsymbol{B}^T\cdot\left(\tilde{\tilde{\boldsymbol{s}}}_p+\widetilde{\boldsymbol{S}_p\cdot\boldsymbol{q}_f}\right)^T\cdot\boldsymbol{A}^T\quad\boldsymbol{S}_p^T\cdot\boldsymbol{A}^T\right]\cdot\left[\boldsymbol{I}\quad-\boldsymbol{A}\cdot\left(\tilde{\tilde{\boldsymbol{s}}}_p+\widetilde{\boldsymbol{S}_p\cdot\boldsymbol{q}_f}\right)\cdot\boldsymbol{B}\quad\boldsymbol{A}\cdot\boldsymbol{S}_p\right]\cdot\dot{\boldsymbol{\xi}}$$

$$\Rightarrow\ \frac{1}{2}\cdot m_p\cdot\dot{\boldsymbol{\xi}}^T\cdot\begin{bmatrix}\boldsymbol{I} & -\boldsymbol{A}\cdot\left(\tilde{\tilde{\boldsymbol{s}}}_p+\widetilde{\boldsymbol{S}_p\cdot\boldsymbol{q}_f}\right)\cdot\boldsymbol{B} & \boldsymbol{A}\cdot\boldsymbol{S}_p\\ & \boldsymbol{B}^T\cdot\left(\tilde{\tilde{\boldsymbol{s}}}_p+\widetilde{\boldsymbol{S}_p\cdot\boldsymbol{q}_f}\right)^T\cdot\left(\tilde{\tilde{\boldsymbol{s}}}_p+\widetilde{\boldsymbol{S}_p\cdot\boldsymbol{q}_f}\right)\cdot\boldsymbol{B} & -\boldsymbol{B}^T\cdot\left(\tilde{\tilde{\boldsymbol{s}}}_p+\widetilde{\boldsymbol{S}_p\cdot\boldsymbol{q}_f}\right)^T\cdot\boldsymbol{S}_p\\ sym & & \boldsymbol{S}_p^T\cdot\boldsymbol{S}_p\end{bmatrix}\cdot\dot{\boldsymbol{\xi}} \tag{A-5}$$

and (B) is

$$\frac{1}{2}\cdot\dot{\boldsymbol{\xi}}^T\cdot\left[\boldsymbol{0}\quad\boldsymbol{B}^{\,T}\,\hat{\boldsymbol{S}}_p{}^T\right]\cdot\boldsymbol{J}_p\cdot\left[\boldsymbol{0}\quad\boldsymbol{B}\quad\hat{\boldsymbol{S}}_p\right]\cdot\dot{\boldsymbol{\xi}}$$

$$\Rightarrow\ \frac{1}{2}\cdot\dot{\boldsymbol{\xi}}^T\cdot\begin{bmatrix}\boldsymbol{0} & \boldsymbol{0} & \boldsymbol{0}\\ & \boldsymbol{B}^T\cdot\boldsymbol{J}_{pi}\cdot\boldsymbol{B} & \boldsymbol{B}^T\cdot\boldsymbol{J}_p\cdot\hat{\boldsymbol{S}}_p\\ sym & & \hat{\boldsymbol{S}}_p^T\cdot\boldsymbol{J}_p\cdot\hat{\boldsymbol{S}}_p\end{bmatrix}\cdot\dot{\boldsymbol{\xi}} \tag{A-6}$$

From equations (A-4), (A-5) and (A-6), the generalized nodal mass matrix $\boldsymbol{M}^p$ is

$$\boldsymbol{M}^p = \begin{bmatrix} \boldsymbol{M}^p_{rr} & \boldsymbol{M}^p_{r\varepsilon} & \boldsymbol{M}^p_{rq_f} \\ & \boldsymbol{M}^p_{\varepsilon\varepsilon} & \boldsymbol{M}^p_{\varepsilon q_f} \\ sym. & & \boldsymbol{M}^p_{q_f q_f} \end{bmatrix} \tag{A-7}$$

where

$$\boldsymbol{M}^p_{rr} = m_p \cdot \boldsymbol{I} \qquad (3\ x\ 3) \tag{A-8}$$

$$\boldsymbol{M}^p_{r\varepsilon} = -m_p \cdot \boldsymbol{A} \cdot \left(\tilde{\bar{\boldsymbol{s}}}_p + \widetilde{\boldsymbol{S}_p \cdot \boldsymbol{q}_f} \right) \cdot \boldsymbol{B} \qquad (3\ x\ 3) \tag{A-9}$$

$$\boldsymbol{M}^p_{rq_f} = m_p \cdot \boldsymbol{A} \cdot \boldsymbol{S}_p \qquad (3\ x\ k) \tag{A-10}$$

$$\boldsymbol{M}^p_{\varepsilon\varepsilon} = m_p \cdot \boldsymbol{B}^T \cdot \left(\tilde{\bar{\boldsymbol{s}}}_p + \widetilde{\boldsymbol{S}_p \cdot \boldsymbol{q}_f} \right)^T \cdot \left(\tilde{\bar{\boldsymbol{s}}}_p + \widetilde{\boldsymbol{S}_p \cdot \boldsymbol{q}_f} \right) \cdot \boldsymbol{B} + \boldsymbol{B}^T \cdot \boldsymbol{J}_p \cdot \boldsymbol{B} \qquad (3\ x\ 3) \tag{A-11}$$

$$\boldsymbol{M}^p_{\varepsilon q_f} = -m_p \cdot \boldsymbol{B}^T \cdot \left(\tilde{\bar{\boldsymbol{s}}}_p + \widetilde{\boldsymbol{S}_p \cdot \boldsymbol{q}_f} \right)^T \cdot \boldsymbol{S}_p + \boldsymbol{B}^T \cdot \boldsymbol{J}_p \cdot \hat{\boldsymbol{S}}_p \qquad (3\ x\ k) \tag{A-12}$$

$$\boldsymbol{M}^p_{q_f q_f} = m_p \cdot \boldsymbol{S}_p^T \cdot \boldsymbol{S}_p + \hat{\boldsymbol{S}}_p^T \cdot \boldsymbol{J}_p \cdot \hat{\boldsymbol{S}}_p \qquad (k\ x\ k) \tag{A-13}$$

In the following, the different vectors and matrices are presented in their expanded form for a clearer understanding of the developed formulas. $\boldsymbol{\xi}$ is the generalized coordinates set for a flexible body with $\boldsymbol{\xi} = \left(\boldsymbol{r}^T\ \boldsymbol{\varepsilon}^T\ \boldsymbol{q}_f^T \right)^T = \left(x\ y\ z\ \psi\ \theta\ \phi\ \boldsymbol{q}_f^T \right)^T$, where x, y, z, ψ, θ, ϕ are the coordinates of the local reference frame of the flexible body and $\boldsymbol{q}_f$ are the modal coordinates of the modified Craig-Bampton basis with $\boldsymbol{q}_f = \left(q_f^1\ q_f^2\ q_f^3 \ldots q_f^k \right)^T$; k is the total number of modal coordinates. Generally, the first six modal coordinates are the rigid-body modes that are disabled in ADAMS.

$\boldsymbol{A}$ is the Euler transformation matrix from the local reference coordinates to the global reference coordinates and $\boldsymbol{B}$ is a matrix used in the description of the angular velocity of the local reference frame, [1]

$$\boldsymbol{A} = \begin{bmatrix} c\psi \cdot c\phi - s\psi \cdot s\phi \cdot c\theta & -c\psi \cdot s\phi - s\psi \cdot c\phi \cdot c\theta & s\psi \cdot s\theta \\ s\psi \cdot c\phi + c\psi \cdot s\phi \cdot c\theta & -s\psi \cdot s\phi + c\psi \cdot c\phi \cdot c\theta & -c\psi \cdot s\theta \\ s\phi \cdot s\theta & c\phi \cdot s\theta & c\theta \end{bmatrix} \text{ and } \boldsymbol{B} = \begin{bmatrix} s\phi \cdot s\theta & 0 & c\phi \\ c\phi \cdot s\theta & 0 & -s\phi \\ c\theta & 1 & 0 \end{bmatrix}.$$

$\bar{\boldsymbol{s}}_p$ is the position vector of node p of the undeformed flexible body defined in the local reference frame, with $\bar{\boldsymbol{s}}_p = \left(\bar{x}_p\ \bar{y}_p\ \bar{z}_p \right)^T$. m_p and $\boldsymbol{J}_p$ are respectively the mass and inertia tensor of the finite volume corresponding to node p. $\boldsymbol{S}_p$ and $\hat{\boldsymbol{S}}_p$ are the rows of the shape matrix corresponding to the translational and rotational DOF of node p, respectively, thus

1 $c \equiv$ cosinus; $s \equiv$ sinus

$$\boldsymbol{S}_p = \begin{bmatrix} q^1_{x_p} & q^2_{x_p} & q^3_{x_p} & \cdots & q^k_{x_p} \\ q^1_{y_p} & q^2_{y_p} & q^3_{y_p} & \cdots & q^k_{y_p} \\ q^1_{z_p} & q^2_{z_p} & q^3_{z_p} & \cdots & q^k_{z_p} \end{bmatrix} \text{ and } \hat{\boldsymbol{S}}_p = \begin{bmatrix} q^1_{rotx_p} & q^2_{rotx_p} & q^3_{rotx_p} & \cdots & q^k_{rotx_p} \\ q^1_{roty_p} & q^2_{roty_p} & q^3_{roty_p} & \cdots & q^k_{roty_p} \\ q^1_{rotz_p} & q^2_{rotz_p} & q^3_{rotz_p} & \cdots & q^k_{rotz_p} \end{bmatrix}.$$

Finally $\boldsymbol{I}$ is an (3 *x* 3) identity matrix and $\sim$ is the skew symmetric operator such that for

$\boldsymbol{a} = \begin{bmatrix} x_a \\ y_a \\ z_a \end{bmatrix}$ the operator yields $\tilde{\boldsymbol{a}} = \begin{bmatrix} 0 & -z_a & y_a \\ z_a & 0 & -x_a \\ -y_a & x_a & 0 \end{bmatrix}$

The total kinetic energy of a flexible body is written as

$$T = \sum_{i=1}^{n_p} T_p = \frac{1}{2} \cdot \dot{\boldsymbol{\xi}}^T \cdot \sum_{i=1}^{n_p} \boldsymbol{M}^p \cdot \dot{\boldsymbol{\xi}} = \frac{1}{2} \cdot \dot{\boldsymbol{\xi}}^T \cdot \boldsymbol{M} \cdot \dot{\boldsymbol{\xi}} \tag{A-14}$$

The summation of the sub-matrices defined in equations (A-8) to (A-13) yields

$$\begin{aligned} \boldsymbol{M}_{rr} &= \sum_{i=1}^{n_p} m_p \cdot \boldsymbol{I} \\ &= \bar{I}^1 \cdot \boldsymbol{I} \end{aligned} \tag{A-15}$$

$$\begin{aligned} \boldsymbol{M}_{r\varepsilon} &= \sum_{i=1}^{n_p} \left[-m_p \cdot \boldsymbol{A} \cdot \left(\tilde{\boldsymbol{s}}_p + \widetilde{\boldsymbol{S}_p \cdot \boldsymbol{q}_f} \right) \cdot \boldsymbol{B} \right] \\ &= -\boldsymbol{A} \cdot \left[\sum_{i=1}^{n_p} m_p \cdot \tilde{\boldsymbol{s}}_p + \sum_{i=1}^{n_p} m_p \cdot \widetilde{\boldsymbol{S}_p \cdot \boldsymbol{q}_f} \right] \cdot \boldsymbol{B} \\ &= -\boldsymbol{A} \cdot \left[\widetilde{\left(\sum_{i=1}^{n_p} m_p \cdot \bar{\boldsymbol{s}}_p \right)} + \widetilde{\left(\sum_{i=1}^{n_p} m_p \cdot \boldsymbol{S}_p \right) \cdot \boldsymbol{q}_f} \right] \cdot \boldsymbol{B} \\ &= -\boldsymbol{A} \cdot \left[\tilde{\bar{I}}^2 + \widetilde{\bar{I}^3 \cdot \boldsymbol{q}_f} \right] \cdot \boldsymbol{B} \end{aligned} \tag{A-16}$$

$$\begin{aligned} \boldsymbol{M}_{rq_f} &= \sum_{i=1}^{n_p} m_p \cdot \boldsymbol{A} \cdot \boldsymbol{S}_p \\ &= \boldsymbol{A} \cdot \sum_{i=1}^{n_p} m_p \cdot \boldsymbol{S}_p \\ &= \boldsymbol{A} \cdot \bar{\boldsymbol{I}}^3 \end{aligned} \tag{A-17}$$

$$\begin{aligned} \boldsymbol{M}_{\varepsilon\varepsilon} &= \sum_{i=1}^{n_p} m_p \cdot \boldsymbol{B}^T \cdot \left(\tilde{\boldsymbol{s}}_p + \widetilde{\boldsymbol{S}_p \cdot \boldsymbol{q}_f} \right)^T \cdot \left(\tilde{\boldsymbol{s}}_p + \widetilde{\boldsymbol{S}_p \cdot \boldsymbol{q}_f} \right) \cdot \boldsymbol{B} + \sum_{i=1}^{n_p} \boldsymbol{B}^T \cdot \boldsymbol{J}_p \cdot \boldsymbol{B} \\ &= \boldsymbol{B}^T \cdot \left[\sum_{i=1}^{n_p} m_p \cdot \left(\tilde{\boldsymbol{s}}_p^T \cdot \tilde{\boldsymbol{s}}_p + \tilde{\boldsymbol{s}}_p^T \cdot \widetilde{\boldsymbol{S}_p \cdot \boldsymbol{q}_f} + \left(\widetilde{\boldsymbol{S}_p \cdot \boldsymbol{q}_f} \right)^T \cdot \tilde{\boldsymbol{s}}_p + \left(\widetilde{\boldsymbol{S}_p \cdot \boldsymbol{q}_f} \right)^T \cdot \widetilde{\boldsymbol{S}_p \cdot \boldsymbol{q}_f} \right) + \sum_{i=1}^{n_p} \boldsymbol{J}_p \right] \cdot \boldsymbol{B} \\ &= \boldsymbol{B}^T \cdot \left[\sum_{i=1}^{n_p} \left(m_p \cdot \tilde{\boldsymbol{s}}_p^T \cdot \tilde{\boldsymbol{s}}_p + \boldsymbol{J}_p \right) + \sum_{i=1}^{n_p} m_p \cdot \tilde{\boldsymbol{s}}_p^T \cdot \widetilde{\boldsymbol{S}_p \cdot \boldsymbol{q}_f} + \sum_{i=1}^{n_p} m_p \cdot \left(\tilde{\boldsymbol{s}}_p^T \cdot \widetilde{\boldsymbol{S}_p \cdot \boldsymbol{q}_f} \right)^T \right. \\ &\qquad \left. \ldots + \sum_{i=1}^{n_p} m_p \cdot \left(\widetilde{\boldsymbol{S}_p \cdot \boldsymbol{q}_f} \right)^T \cdot \widetilde{\boldsymbol{S}_p \cdot \boldsymbol{q}_f} \right] \cdot \boldsymbol{B} \\ &= \boldsymbol{B}^T \cdot \left[\bar{\boldsymbol{I}}^7 + \bar{\boldsymbol{I}}^8 + (\bar{\boldsymbol{I}}^8)^T + \bar{\boldsymbol{I}}^9 \right] \cdot \boldsymbol{B} \end{aligned} \tag{A-18}$$

$$\begin{aligned}\boldsymbol{M}_{\varepsilon q_f} &= \sum_{i=1}^{n_p}\left[-m_p\cdot\boldsymbol{B}^T\cdot\left(\tilde{\boldsymbol{s}}_p+\widetilde{\boldsymbol{S}_p\cdot\boldsymbol{q}_f}\right)^T\cdot\boldsymbol{S}_p\right]+\sum_{i=1}^{n_p}\boldsymbol{B}^T\cdot\boldsymbol{J}_p\cdot\hat{\boldsymbol{S}}_p \\ &= -\boldsymbol{B}^T\cdot\left[\sum_{i=1}^{n_p}m_p\cdot\tilde{\boldsymbol{s}}_p^T\cdot\boldsymbol{S}_p+\boldsymbol{J}_p\cdot\hat{\boldsymbol{S}}_p+\sum_{i=1}^{n_p}m_p\cdot(\widetilde{\boldsymbol{S}_p\cdot\boldsymbol{q}_f})^T\cdot\boldsymbol{S}_p\right] \\ &= -\boldsymbol{B}^T\cdot\left[\bar{\boldsymbol{I}}^4+\bar{\boldsymbol{I}}^5\right]\end{aligned} \tag{A-19}$$

$$\begin{aligned}\boldsymbol{M}_{q_f q_f} &= \sum_{i=1}^{n_p}m_p\cdot\boldsymbol{S}_p^T\cdot\boldsymbol{S}_p+\sum_{i=1}^{n_p}\hat{\boldsymbol{S}}_p^T\cdot\boldsymbol{J}_p\cdot\hat{\boldsymbol{S}}_p \\ &= \bar{\boldsymbol{I}}^6\end{aligned} \tag{A-20}$$

The terms $\bar{\boldsymbol{I}}$ are recapitulated below

$$\bar{I}^1=\sum_{i=1}^{n_p}m_p \qquad \text{(scalar)} \tag{A-21}$$

$$\bar{\boldsymbol{I}}^2=\sum_{i=1}^{n_p}m_p\cdot\bar{\boldsymbol{s}}_p \qquad (3\ x\ 1) \tag{A-22}$$

$$\bar{\boldsymbol{I}}^3=\sum_{i=1}^{n_p}m_p\cdot\boldsymbol{S}_p \qquad (3\ x\ k) \tag{A-23}$$

$$\bar{\boldsymbol{I}}^4=\sum_{i=1}^{n_p}m_p\cdot\tilde{\boldsymbol{s}}_p^T\cdot\boldsymbol{S}_p+\boldsymbol{J}_p\cdot\hat{\boldsymbol{S}}_p \qquad (3\ x\ k) \tag{A-24}$$

$$\bar{\boldsymbol{I}}^5=\sum_{i=1}^{n_p}m_p\cdot(\widetilde{\boldsymbol{S}_p\cdot\boldsymbol{q}_f})^T\cdot\boldsymbol{S}_p \qquad (3\ x\ k) \tag{A-25}$$

$$\bar{\boldsymbol{I}}^6=\sum_{i=1}^{n_p}m_p\cdot\boldsymbol{S}_p^T\cdot\boldsymbol{S}_p+\hat{\boldsymbol{S}}_p^T\cdot\boldsymbol{J}_p\cdot\hat{\boldsymbol{S}}_p \qquad (k\ x\ k) \tag{A-26}$$

$$\bar{\boldsymbol{I}}^7=\sum_{i=1}^{n_p}m_p\cdot\tilde{\boldsymbol{s}}_p^T\cdot\tilde{\boldsymbol{s}}_p+\boldsymbol{J}_p \qquad (3\ x\ 3) \tag{A-27}$$

$$\bar{\boldsymbol{I}}^8=\sum_{i=1}^{n_p}m_p\cdot\tilde{\boldsymbol{s}}_p^T\cdot\widetilde{\boldsymbol{S}_p\cdot\boldsymbol{q}_f} \qquad (3\ x\ 3) \tag{A-28}$$

$$\bar{\boldsymbol{I}}^9=\sum_{i=1}^{n_p}m_p\cdot(\widetilde{\boldsymbol{S}_p\cdot\boldsymbol{q}_f})^T\cdot(\widetilde{\boldsymbol{S}_p\cdot\boldsymbol{q}_f}) \qquad (3\ x\ 3) \tag{A-29}$$

APPENDIX B

Co-Simulation

In the following, the detailed FORTRAN code for the ADAMS-DSHplus co-simulation model of figure B-1 is presented. For DSHplus the input parameters are the position and the velocity of the hydraulic cylinder and the output parameter is the cylinder force. For ADAMS the input parameter is the cylinder force and the output parameters are the moving and reference marker id's. The coupling of both models is done via the STC-module and the FORTRAN subroutine as explained in chapter 2. The code can of course be extended with additional exchange parameters or with more complex calculations, the basic structure remains the same.

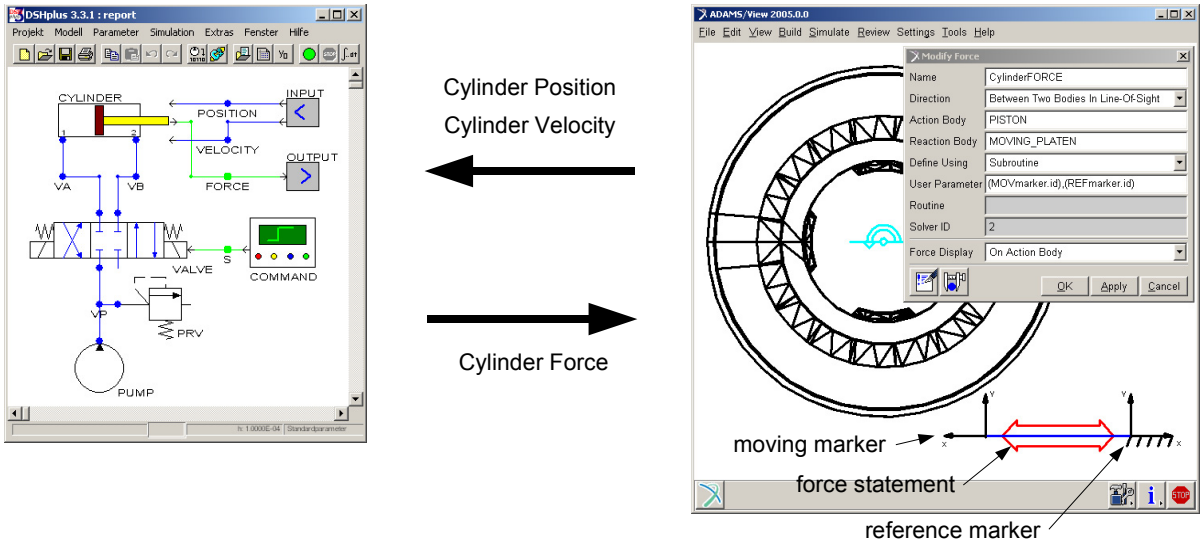

Figure B-1: ADAMS-DSHplus co-simulation

```
SUBROUTINE SFOSUB(ID, TIME, PAR, NPAR, DFLAG, IFLAG, RESULT)

------ External variable definitions

      INTEGER           ID        identifier of calling FORCE statement
      DOUBLE PRECISION  TIME      current time
      DOUBLE PRECISION  PAR( * )  array containing passed parameters
```

```
    INTEGER             NPAR        number of passed parameters
    LOGICAL             DFLAG       differencing flag
    LOGICAL             IFLAG       initial pass flag
    DOUBLE PRECISION    RESULT      computed force returned to ADAMS

------ Local variable and parameter definitions

    INTEGER             IPAR(3)     array of marker id's for SYSFNC evaluation
    INTEGER             movMARKER   ADAMS id of moving marker
    INTEGER             refMARKER   ADAMS id of reference marker
    DOUBLE PRECISION    DISPL       output of SYSFNC
    DOUBLE PRECISION    VELOC       output of SYSFNC
    LOGICAL             ERRFLG
    INTEGER             nDSHin      number of DSHplus inputs
    INTEGER             nDSHout     number of DSHplus outputs
    DOUBLE PRECISION    DSHin(2)    array of DSHplus inputs
    DOUBLE PRECISION    DSHout(1)   array of DSHplus outputs
    DOUBLE PRECISION    SIMENDTIME  simulation end
    INTEGER             FLAGS(2)
    INTEGER             nFLAGS
    DOUBLE PRECISION    H
    DOUBLE PRECISION    OLDTIME
    DOUBLE PRECISION    LASTSUCCSTEP

=== INITIALISATION ==========================================================

    movMARKER           = PAR(1)
    refMARKER           = PAR(2)

    IPAR(1)             = movMARKER
    IPAR(2)             = refMARKER
    IPAR(3)             = refMARKER

    nDSHin              = 2
    nDSHout             = 1

    FLAGS(1)            = 1         flag for embedded (0) or normal co-simulation (1)
    FLAGS(2)            = 1         flag for no extrapolation (0) or extrapolation (1)
    nFLAGS              = 2

    IF (IFLAG) THEN

------ Setting functional dependencies for SYSFNC in ADAMS

      CALL SYSFNC('DM', IPAR, 3, DISPL, ERRFLG)    evaluates the actual distance between both markers
      CALL ERRMES(ERRFLG, 'Error for DISPL', ID, 'STOP')
```

```
      CALL SYSFNC('VM', IPAR, 3, VELOC, ERRFLG)    evaluates the actual velocity between both markers
      CALL ERRMES(ERRFLG, 'Error for VELOC', ID, 'STOP')

      DSHin(1) = ABS(DISPL)
      DSHin(2) = VELOC

------ Initialisation of DSHplus interface

      CALL LOCKING_MAPMODULC(nDSHin, nDSHout, 'LOCKING.txt', 'LOCKING.ken.txt', FLAGS, nFLAGS)

------ Pass actual displacement and velocity to DSHplus

      CALL LOCKING_SETMODULDATAC(DSHin, TIME, H, FLAGS, nFLAGS)

    ELSE

=== NEW TIMESTEP ===================================================================

------ if ADAMS successfully computed a new timestep then the result is passed to DSHplus that in return
------ computes a new force. But if the ADAMS solver did not converge and has to step back to recompute
------ the timestep then no DSHplus computation occurs and the forces of the latest successful timestep are
------ kept.

      IF (TIME .GT. OLDTIME) THEN

        CALL TIMGET(LASTSUCCSTEP)
        H = TIME - LASTSUCCSTEP
        OLDTIME = TIME

        CALL SYSFNC('DX', IPAR, 3, DISPL, ERRFLG)
        CALL ERRMES(ERRFLG, 'Error for DISPL', ID, 'STOP')

        CALL SYSFNC('VX', IPAR, 3, VELOC, ERRFLG)
        CALL ERRMES(ERRFLG, 'Error for VELOC', ID, 'STOP')

        DSHin(1) = ABS(DISPL)
        DSHin(2) = VELOC

------ Pass actual displacement and velocity to DSHplus

        CALL LOCKING_SETMODULDATAC(DSHin, TIME, H, FLAGS, nFLAGS)

------ Get actual hydraulic force from DSHplus

        CALL LOCKING_GETMODULDATAC(DSHout, TIME, FLAGS, nFLAGS)
```

```
        RESULT = DSHout

      ELSE

        CALL TIMGET(LASTSUCCSTEP)
        H = TIME - LASTSUCCSTEP

        RESULT = DSHout

      ENDIF

    ENDIF

=== END CO-SIMULATION ================================================================

    IF (ABS (SIMENDTIME - TIME) .LT. 1.0E-09) THEN

------ Stop co-simulation with DSHplus

      CALL LOCKING_UNMAPMODULC(FLAGS, nFLAGS)

    ENDIF

    RETURN
    END
```

APPENDIX C

Experimental Modal Analysis

Impact testing is one of the most common methods used to identify the modal parameters. The advantage is that a minimum of equipment is needed to perform a modal analysis: a 2-channel FFT analyzer, a hammer with a load cell to produce a broad-banded excitation and measure the input force and an accelerometer to measure the response. The aim is to determine the Frequency Response Function (FRF) that describes the input-output relationship at one point or at two distinct points of a structure as a function of frequency. In other words, it is a measure of the displacement, velocity or acceleration a structure has at an output point when applying a unit of excitation force at an input point. In experimental modal analysis, the FRF is measured in order to estimate resonant frequencies, mode shapes and damping coefficients.

Theoretically, the FRF can be defined as the ratio of the Fourier Transform of the output at point *j* $X_j(\omega)$ divided by the Fourier Transform of the input force at point *k* of the structure $F_k(\omega)$.

$$H_{jk}(\omega)=\frac{X_j(\omega)}{F_k(\omega)} \tag{C-1}$$

Considering the equation of motion for an *n* degree-of-freedom system

$$[\boldsymbol{M}]\{\ddot{\boldsymbol{x}}\}+[\boldsymbol{C}]\{\dot{\boldsymbol{x}}\}+[\boldsymbol{K}]\{\boldsymbol{x}\}=\{\boldsymbol{F}(t)\} \tag{C-2}$$

The Fourier Transform of equation (C-2) becomes

$$[\boldsymbol{X}(\omega)]=\left[[\boldsymbol{K}]-\omega^2[\boldsymbol{M}]+i\,\omega[\boldsymbol{C}]\right]^{-1}[\boldsymbol{F}(\omega)] \tag{C-3}$$

By diagonalizing the matrices ***M***, ***C***, ***K***, equations (C-3) can be reformulated and the FRF, i.e. Matrix ***H*** can be expressed only in terms of modal parameters. The development can be looked-up in [51]. The individual element of the matrix ***H*** can be expressed as

$$H_{jk}(\omega)=\sum_{r=1}^{n}\left(\frac{{}_rA_{jk}}{\omega_r\alpha_r+i(\omega-\omega_r\sqrt{1-\alpha_r^2})}+\frac{{}_r\bar{A}_{jk}}{\omega_r\alpha_r+i(\omega+\omega_r\sqrt{1-\alpha_r^2})}\right) \tag{C-4}$$

In practice the FRF is calculated using the *auto-spectral density* (S_{ff}) and the *cross-spectral density* (S_{fx}) of the input and output signal such that

$$H_{jk}(\omega) = \frac{S_{f_k x_j}(\omega)}{S_{f_k f_k}(\omega)} \tag{C-5}$$

When a structure is tested, the measured set of FRF is typically used to estimate the modal parameters by a curve fitting method. This means that the data is matched to a parametric model of the FRF similar to equation (C-4). Multitudes of different methods were developed to estimate the natural frequencies with the associated mode shape and damping. They are more or less effective depending on how the FRF were obtained - e.g. by Impact Testing or Shaker -, how many FRF were measured and what the measured structure is like - e.g. lightly or highly damped. In the commercial modal analysis programm available at the University of Luxembourg two related methods that are based on a least-squares procedure - known as the Rational Fraction Polynomial method and Global Rational Fraction Polynomial method - are used to estimate the natural frequencies with their corresponding mode shape and modal damping coefficient.

Vertical Connecting Bar

A hammer-impact modal analysis of an assembled vertical connecting bar is done. For the measurement, the accelerometer is fixed with wax at position 4 in direction *x*. Then, the structure is excited in the same direction with the impact hammer at each measuring one after the other. Afterwards, the measurement is repeated for the *z*-direction (see figure C-1). Finally, the measured FRF are exported to the other software for modal parameter estimation. The natural frequencies with the corresponding mode shape and damping are estimated and the results are presented in figure C-2.

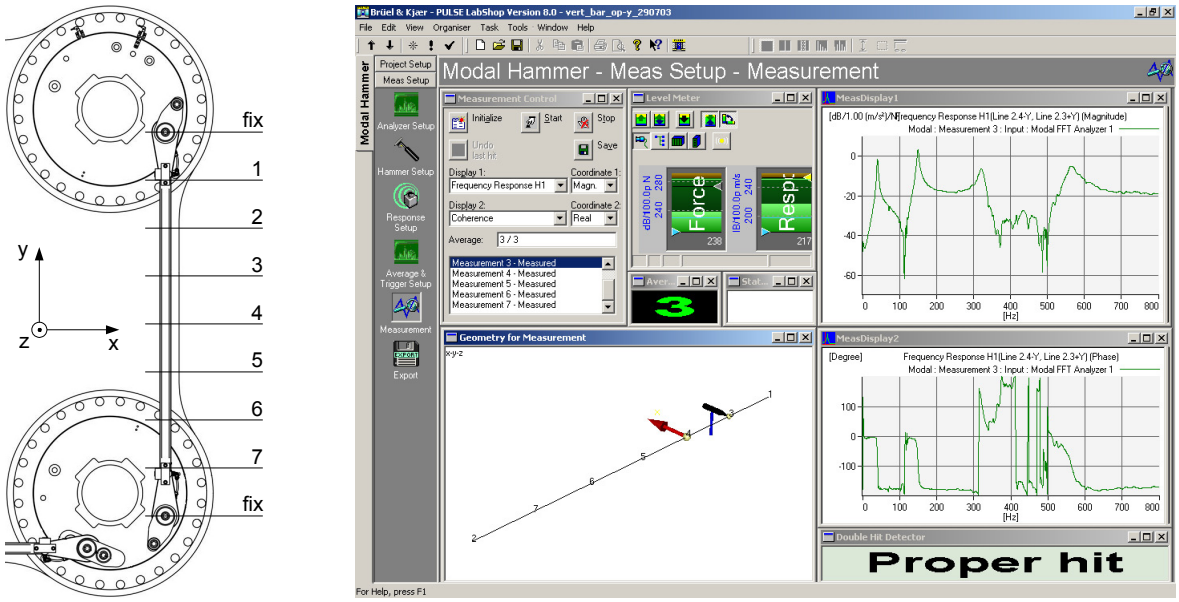

Figure C-1: Modal analysis measurement setup

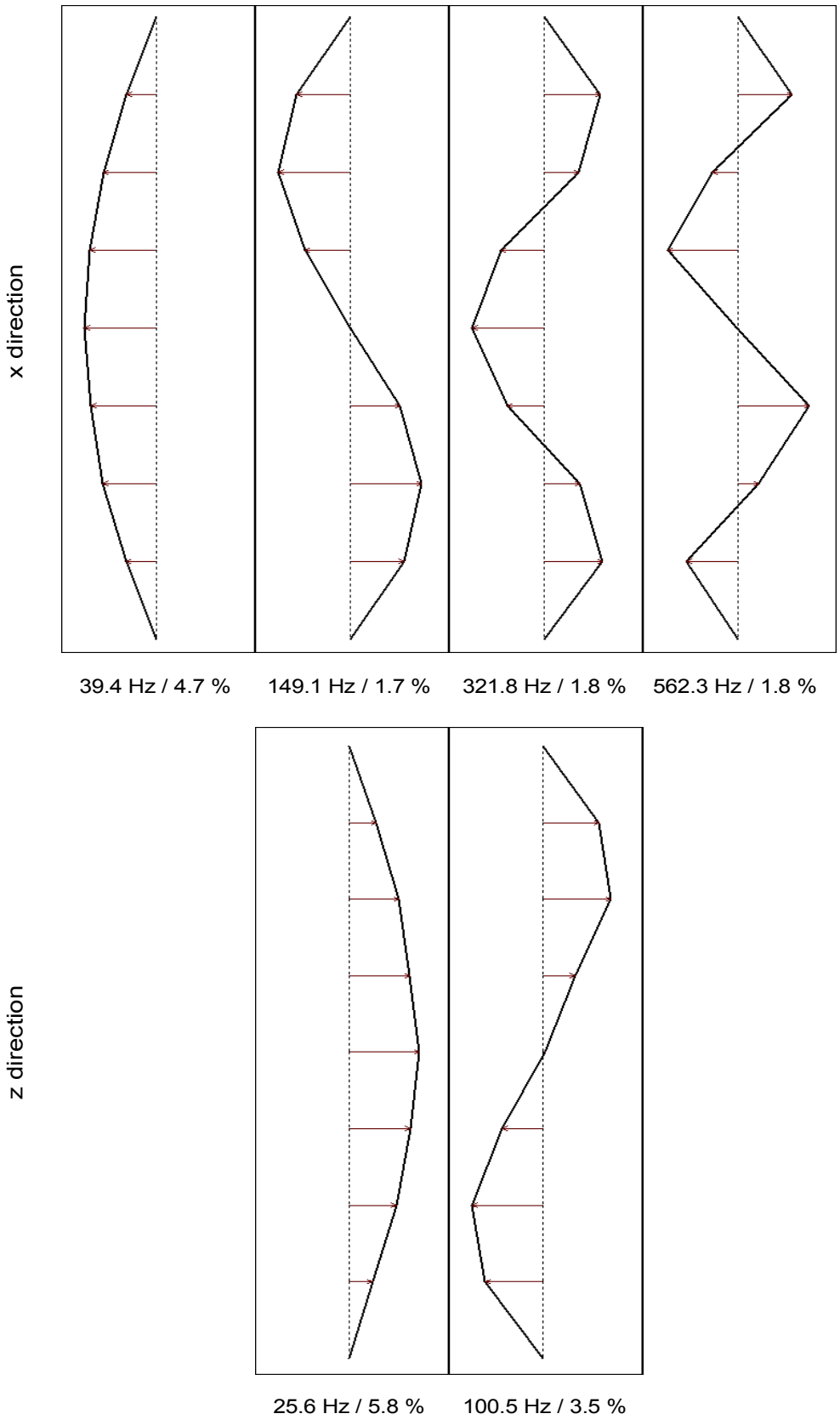

Figure C-2: Modal parameter estimation: mode shape / natural frequency / damping

Major Clamp Unit Parts

A stationary, a tie bar and a clamp base have been measured in order to validate the FE models of the flexible bodies in ADAMS. The FE models have not to be very detailed for the dynamic analysis. A correct overall mass distribution and structural stiffness are sufficient to represent the inertia effects, natural frequencies and mode shapes. A too fine mesh unnecessarily increases the computation efforts.

As the parts weigh several tons, they could only be suspended through lifting ropes to a crane. Impact measurements were done with a modal hammer and two accelerometers. A complete experimental modal analysis of the parts as for the vertical connecting bar has not been done due to time constraints in production. Generally, one accelerometer is enough to measure the natural frequencies. The second accelerometer is needed to get additional information about the relative phasing between two measuring points. Thus, it is easier to compare and allocate the measured and the calculated natural frequencies by having a rough idea of the mode shapes.

Stationary Platen

The overall dimensions of stationary platen are 3.5 x 3 x 1.2 meters and its weight is 36 tons. Two FE models are generated: one detailed and one coarse model. Both are created from 3D CAD models that are imported and automatically meshed with ANSYS/Workbench. For the detailed model, only the threaded holes, some pads and some grooves are removed, for the coarse model nearly all blends and some major features are suppressed. They are meshed using the 10-node tetrahedral element SOLID92 with 3 translational DOF per node. The detailed model has 252459 DOF whereas the coarse model has 53982 DOF. The material properties are: E-modulus 1.6×10^{11} Pa, Poisson's ratio 0.28 and density 7100 kg/m^3.

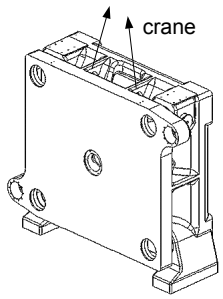

Figure C-3: Stationary platen

The natural frequencies of the detailed model differ from the measured frequencies by ± 4 %. As expected, the coarse model is not as good but still reproduces the same mode shapes and the corresponding natural frequencies with an error of under 10 %.

Measured Frequencies (Hz)	Detailed Model Frequencies (Hz)	%	Coarse Model Frequencies (Hz)	%
138.5	141.99	2.5	138.66	0.1
146.5	150.18	2.5	147.15	0.4
183.0	178.55	-2.4	168.22	-8.1
189.5	181.68	-4.1	178.96	-5.6
203.5	203.40	0.0	204.20	0.3
222.5	220.52	-0.9	220.81	-0.8
235.5	235.97	0.2	240.08	1.9
266.5	257.75	-3.3	254.65	-4.4
272.5	266.60	-2.2	258.39	-5.2
307.5	298.56	-2.9	292.92	-4.7
309.5	301.08	-2.7	290.78	-6.0
317.0	308.70	-2.6	302.07	-4.7
336.0	325.65	-3.1	321.36	-4.4
379.5	369.62	-2.6	356.58	-6.0

Table C-1: Eigenfrequencies of stationary platen

Tie Bar

The tie bar length is 5.8 meters and its weight is about 4.1 tons. The tie bar is suspended near its center of gravity to a crane. Again, two different FE models are generated: a detailed model that is created from a simplified 3D CAD geometry and automatically meshed with 18862 SOLID92 elements and a coarse model that is created manually with 54 BEAM4 elements. BEAM4 is a uniaxial element with tension, compression, torsion, and bending capabilities. The element has six DOF at each node: three translational and three rotational. The material properties are: E-modulus 2.05×10^{11} Pa, Poisson's ratio 0.3 and density 7830 kg/m^3.

For the first three natural frequencies, the BEAM4 element performs very well. Therefore, depending on the frequencies of interest, a coarse model is sufficient for a dynamic analysis.

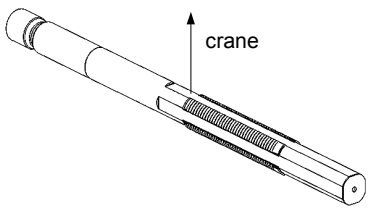

Figure C-4: Tie bar

Measured Frequencies (Hz)	Detailed Model Frequencies (Hz)	%	Coarse Model Frequencies (Hz)	%
46.5	47.39	1.9	46.35	-0.3
126.5	128.06	1.2	126.96	0.4
240.5	240.62	0.0	246.85	2.6
386.5	385.60	-0.2	403.98	4.5
555.0	552.42	-0.5	596.42	7.5
745.5	745.44	0.0	822.10	10.0

Table C-2: Eigenfrequencies of tie bar

Clamp Base

The clamp base is a welding-construction. Its overall dimensions are 6.5 x 3.5 x 0.7 meters and its weight is about 7.4 tons. One model is generated from a simplified 3D CAD model and has 23668 SOLID92 elements. Another model is created manually with 4532 SHELL63 elements. The material characteristics are: E-modulus 2.10×10^{11} Pa, Poisson's ratio 0.3 and material density 7850 kg/m^3.

The clamp base is not really clement regarding modal analysis. It is difficult to generate an accurate FE model and to include all possible things that might influence the frequencies and mode shapes. For example, the welding has certainly induced tensions in the structure that are difficult to determine. Furthermore, in contrary to stationary platen and tie bar, the influence of the lifting robes must also be taken into account.

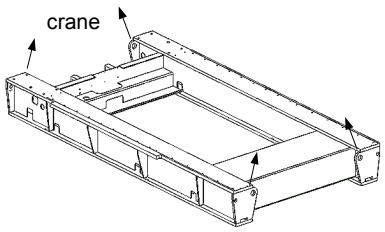

Figure C-5: Clamp base

Measured Frequencies (Hz)	Detailed Model Frequencies (Hz)	%	Coarse Model Frequencies (Hz)	%
30.0	31.13	3.8	28.75	-4.2
47.8	48.55	1.6	44.46	-7.0
68.3	75.09	9.9	67.78	-0.8

Table C-3: Eigenfrequencies of clamp base

APPENDIX D

As an absolute optimal PID setting cannot be estimated analytically for this particular closed-loop model, different parameter sets are tested. The value of K_P is gradually increased, starting with -4. T_I is determined for each K_P with the integrated squared error criterion [37, 39] and T_D is kept constant.

K_P = -4, T_I = 0.0200 and T_D = 0.015

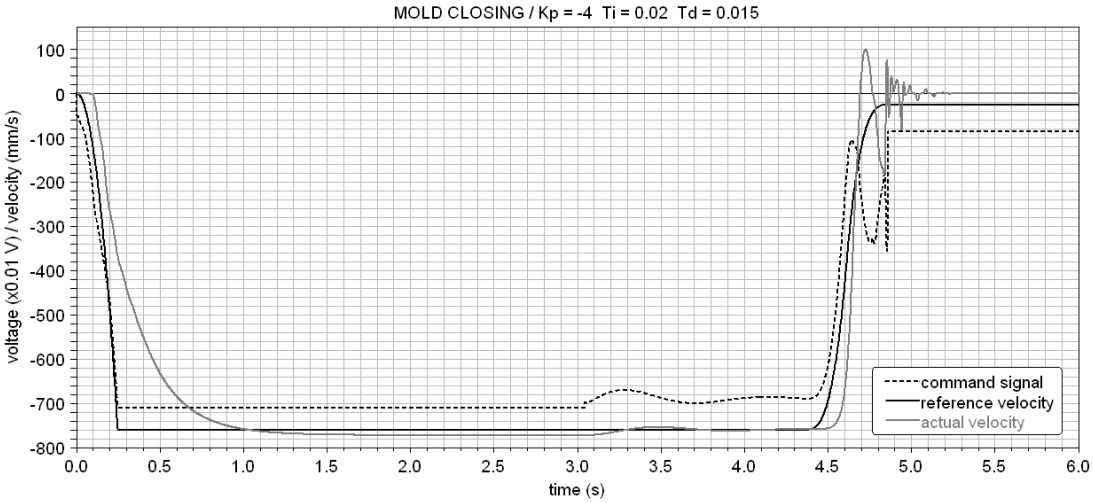

K_P = -10, T_I = 0.0347 and T_D = 0.015

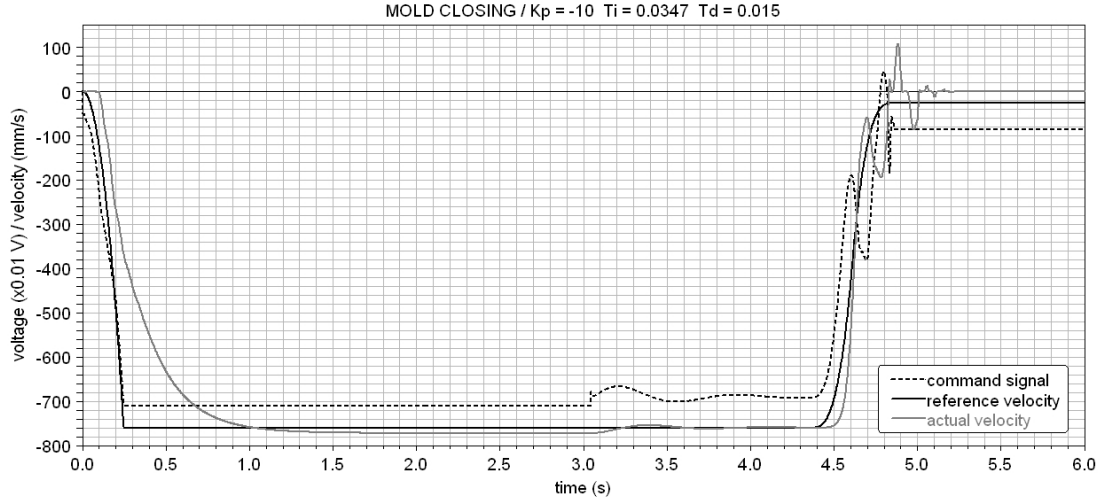

K_P = -20, T_I = 0.0484 and T_D = 0.015

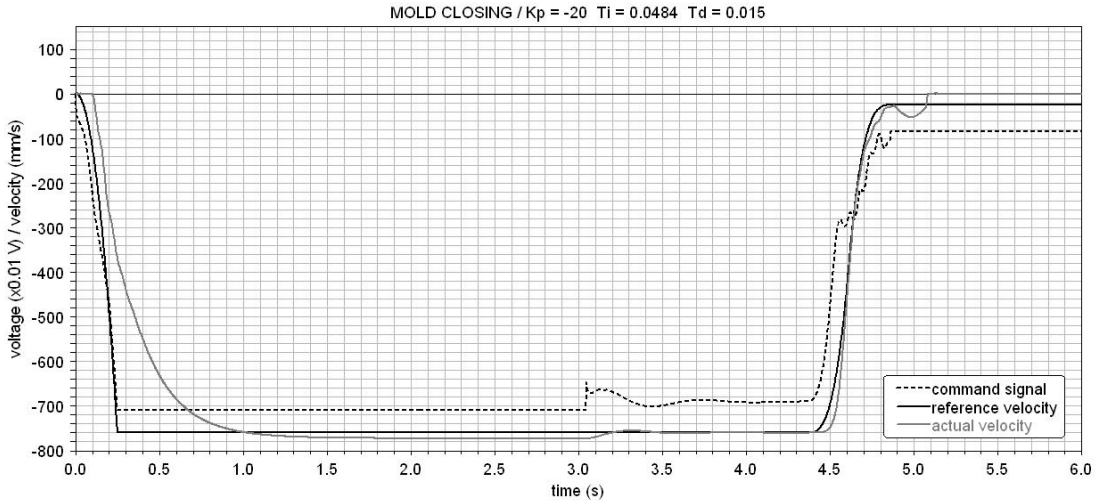

K_P = -30, T_I = 0.0573 and T_D = 0.015

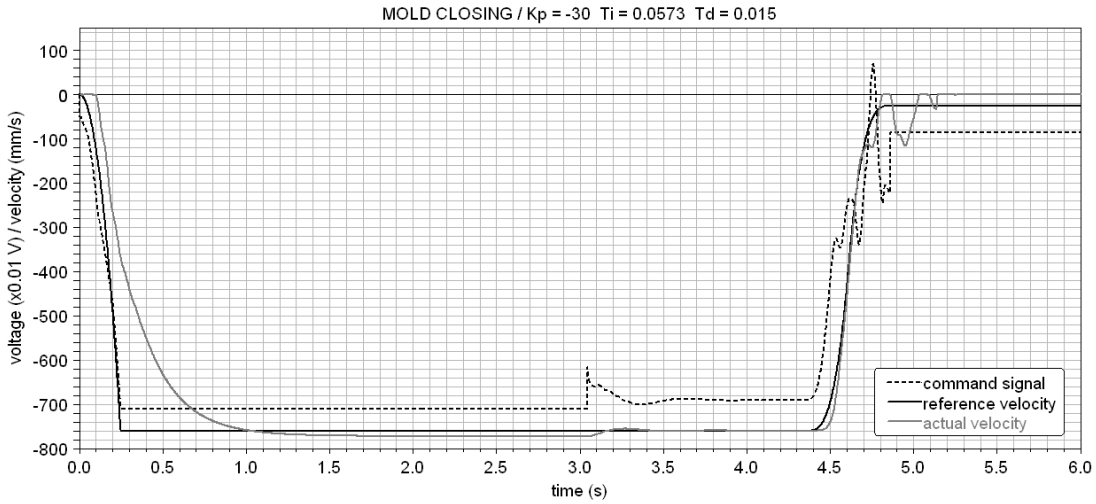

K_P = -40, T_I = 0.0644 and T_D = 0.015

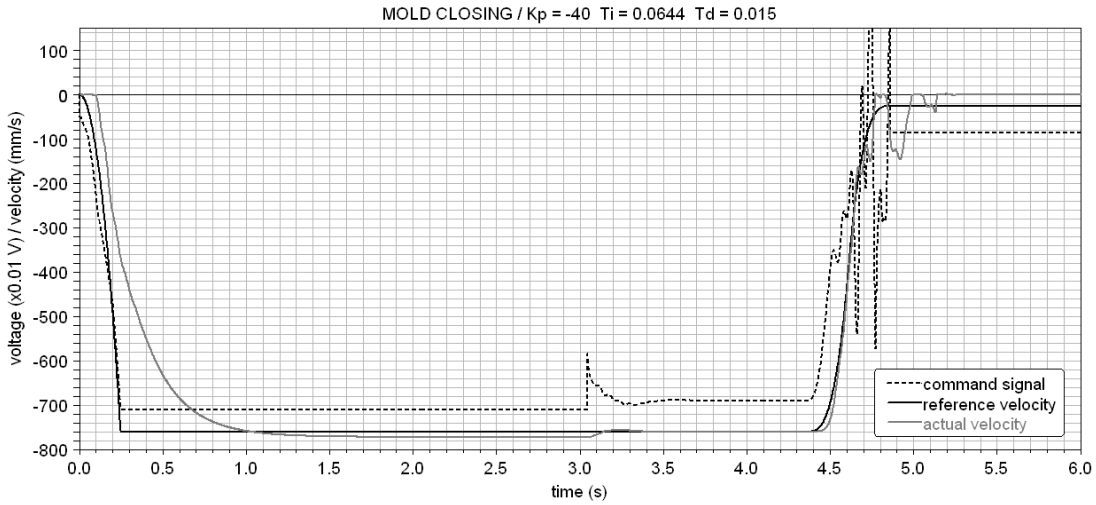

References

[1] Helduser S.: Simulation in der Fluidtechnik. *Olhydraulik und Pneumatik 46 Nr.1*, pp27-36, 2002.

[2] Schönhoff U., Eisenträger P., Nordmann R.: Reduction of finite element models of flexible structures for controller design and integrated modelling. *International Conference on Noise and Vibration Engineering*, *ISMA25*, September 2000, Leuven.

[3] Schönhoff U.: *Practical Robust Control of Mechatronic Systems with Structural Flexibilities*. Aachen: Shaker Verlag, 2003.

[4] Hatch M. R.: *Vibration Simulation using MATLAB and ANSYS.* Florida: Chapmann & Hall, 2001.

[5] Johannaber F.: *Injection Molding Machines, A User's Guide - 3rd Edition*. Munich; Vienna; New York: Hanser, 1994.

[6] *Plastics Europe* [Online]. 2005 [Accessed 9th July 2005]. Available from World Wide Web: <http://www.plasticseurope.org>.

[7] *Corporate Information* [Online]. 2005 [Accessed 7th May 2005]. Available from World Wide Web: <http://www.husky.ca/shareholders/corporate_info.html>.

[8] *Quadloc Machines* [Online]. 2005 [Accessed 7th May 2005]. Available from World Wide Web: <http://www.husky.ca/products_main/quadloc-index.html>.

[9] Weingart J.: Efficiency of a modern Hydraulic Injection Moulding Machine. *Publikationen des Instituts für Fluidtechnik*, Dresden, 2002.

[10] Shabana A. A.: *Dynamics of Multibody Systems - 2nd Edition.* Cambridge: Cambridge University Press, 2003.

[11] García de Jalón J., Bayo E.: *Kinematic and Dynamic Simulation of Multibody Systems - The Real-Time Challenge.* Berlin; Heidelberg; New York: Springer Verlag, 1994.

[12] *ADAMS/Solver Help,* MSC.Software, 2004.

[13] Gasch, R., Knothe, K.: *Strukturdynamik, Band 2*. Berlin; Heidelberg; New York: Springer Verlag, 1987.

[14] Guyan R. J.: Reduction of Stiffness and Mass Matrices. *AIAA Journal,* Vol. 3, No. 2, p 380, 1965.

[15] Craig R. R. Jr.: Substructure Methods in Vibration. *Transaction of the ASME,* Vol. 117, pp 207-213, 1995.

[16] Craig R. R. Jr.: A Review of Time-Domain and Frequency-Domain Component Mode Synthesis Methods. *International Journal of Analytical and Experimental Modal Analysis,* Vol. 2, pp 59-72, 1987.

[17] Seshu P.: Substructuring and Component Mode Systhesis. *Shock and Vibration,* Vol. 4, No. 3, pp 199-210, 1996.

[18] Craig R. R. Jr.: *Structural Dynamics. An Introduction to Computer Methods.* New York: John Wiley and Sons, 1981.

[19] MacNeal R. H.: A Hybrid Method of Component Mode Mode Synthesis. *Journal of Computers and Structures,* Vol. 1, No. 4, pp 581-601, 1971.

[20] Rubin S.: Improved Component Mode Representation for Structural Dynamic Analysis. *AIAA Journal,* Vol. 13, No. 8, pp 995-1006, 1975.

[21] Craig R. R. Jr., Chang C-J.: On the Use of Attachment Modes in Substructure Coupling for Dynamic analysis. *AIAA Paper No. 77-405, AIAA/ASME 18th Structures, Structural Dynamics and Material Conference*, San Diego, 1977.

[22] Hurty W. C.: Dynamic Analysis of Structural Systems using Component Modes. *AIAA Journal,* Vol. 3, No. 4, pp 678-685, 1965.

[23] Craig R. R. Jr., Bampton M. C. C.: Coupling of Substructures for Dynamic Analyses. *AIAA Journal,* Vol. 6, No. 7, pp 1313-1319, 1968.

[24] Appendix D, Theoretical Background. *ADAMS/Flex Help,* MSC.Software, 2004.

[25] Theory Reference. *ANSYS 8.0 Documentation,* ANSYS Inc., 2000.

[26] Will D., Hubert S., Gebhardt N.: *Hydraulik, Grundlagen, Komponenten, Schaltungen - 2. Auflage.* Berlin; Heidelberg; New York: Springer Verlag, 2004.

[27] Nordmann R.: *Maschinenelemente und Mechatronik - Skript Block A.* Aachen: Shaker Verlag, 2000.

[28] *Hydraulics. Basic Principles and Components. The Hydraulic Trainer, Volume 1.* Bosch Rexroth AG, Erbach, 2003.

[29] Proportional and Servo Valve Technology*. The Hydraulic Trainer, Volume 2.* Bosch Rexroth AG, Erbach, 2003.

[30] Jelali M. , Kroll A.: *Hydraulic Servo-Systems, Modelling, Identification and Control.* Berlin; Heidelberg; New York: Springer Verlag, 2003.

[31] *DSHplus Component Manual.* Fluidon GmbH, Aachen, 1997.

[32] *DSHplus Module Manual, DSHplus-STC.* Fluidon GmbH, Aachen, 2003.

[33] *ADAMS/Controls function evaluation (continuous) mode details.* [Online]. 2004 [Accessed 30th October 2004]. Available from World Wide Web: <http://support.adams.com/kb/faq.asp?ID=kb10371.html>.

[34] Hostert C., Kollmeier K., Maas S., Nordmann R, Zuerbes A.: Simulation of the Locking Mechanism of an Injection Molding Machine. *NAFEMS Seminar: Analysis of Multi-Body Systems using FEM and MBS*, Wiesbaden, 2004.

[35] Lalanne M., Berthier P., Der Hagopian J.: *Mechanical Vibrations for Engineers.* Chichester: John Wiley and Sons, 1983.

[36] *FKM-Richtlinie, Rechnerischer Festigkeitsnachweis für Maschinenbauteile - 4., erweiterte Ausgabe.* Frankfurt am Main: VDMA Verlag, 2002.

[37] Hobbacher A.: *Empfehlungen zur Schwingfestigkeit geschweißter Verbindungen und Bauteile.* Düsseldorf: DVS Verlag,1997 (IIW-Empfehlungen).

[38] Hostert C., Maas S., Nordmann R, Zuerbes A.: Dynamic Simulation of an Injection Molding Machine. *VDI Tagung: Schwingungen in Verarbeitungsmaschinen*, Stuttgart, 2005.

[39] Johnson K.L.: *Contact Mechanics.* Cambridge: Cambridge University Press, 1985.

[40] Unbehauen H.: *Regelungstechnik 1, klassische Verfahren zur Analyse und Synthese linear kontinuierlicher Regelsysteme.* Braunschweig: Vieweg Verlag, 1997.

[41] Leigh J.R.: *Applied Digital Control - 2nd Edition*. New York: Prentice-Hall, 1992.

[42] Newtom G.C. Jr., Gould L.A., Kaiser J.F.: *Analytical Design of Linear Feedback Controls.* New York: John Wiley and Sons, 1957.

[43] Wagner W.: *Rohrleitungstechnik - 6. Auflage.* Würzburg: Vogel Verlag, 1993.

[44] Manhartsgruber B.: Application of Singular Perturbation Theory to Hydraulic Servo Drives - System Analysis and Control Design. *Proceeding of 1st Fluid Power Net International PhD Symposium,* pp. 339-352, Hamburg, 2000.

[45] Yao B., Bu F., Reedy J., Chiu G.T.C.: Adaptive Robust Motion Control of Single Rod Hydraulic Actuators: Theory and Experiments. *Proceedings of the American Control Conference,* pp759-763, San Diego, June 1999.

[46] Yu H., Feng Z., Wang X.: Nonlinear Control for a Class of Hydraulic Servo System. *Journal of Zhejiang University Science,* Vol.5, Issue 11, pp1413-1417, Hangzhou, 2004.

[47] Ambrugi, F., Braccesi, C., Cianetti, F.: Simulation of moving parts on flexible bodies using multybody approach. Test case on a reinforced highway bridge. Mechanical Dynamics, Universtà di Perugia, 2000.

[48] Hoshino, H., Zeischka, J.: Time varying surface loading of flexible bodies through MFORCE and load shape functions. Mechanical Dynamics, 2002.

[49] Richardson M.H., Schwarz B.J.: *Introduction to Operating Deflection Shapes.* Vibrant Technologie, Jamestown, 1999.

[50] Vold H., Schwarz B., Richardson M.H.: Measuring Operating Deflection Shapes Under Non-Stationary Conditions. *Proceedings of International Modal Analysis Conference XVIII*, San Antonio, 2000.

[51] Maia N., Silva J.: *Theoretical and Experimental Modal Analysis.* Baldock: Research Studies Press, 1997.

[52] Olsson H., Aström K.J., Canudas de Wit C., Gäfvert M., Lischinsky P.: *Friction Models and Friction Compensation* [Online]. 1997 [Accessed 4th March 2003]. Available from World Wide Web: <http://www.control.lth.se/~kja/friction.pdf>.

[53] Haug E. J.: *Computer Aided Kinematics and Dynamics of Mechanical Systems – Volume I: Basic Methods.* Allyn and Bacon,Massachusetts, 1989.

[54] Arnold B.: Analyse des dynamischen Verhaltens eines Dosenverschliessmechanismus mit verketteten Servomotoren. *VDI-Berichte 1887: Schwingungen in Verarbeitungsmaschinen*, VDI Verlag, Düsseldorf, 2005.

[55] Frank H., Albers A.: Systementwurf und -analyse bei Umstellung mechanisch realisierter Funktionalität auf ein mechatronisches System. *VDI-Berichte 1887: Schwingungen in Verarbeitungsmaschinen*, VDI Verlag, Düsseldorf, 2005.

[56] Horst H.-G., Wölfel H. P.: Aktive Schwingungsminderung in Verarbeitungsmaschinen. *VDI-Berichte 1887: Schwingungen in Verarbeitungsmaschinen*, VDI Verlag, Düsseldorf, 2005.

[57] Brecher C., Witt S., Queins M.: Coupled Simulation OF Structural Dynamics and Control Loops for the Development of high-dynamic Machine Tools. *NAFEMS Seminar: Mechatronics in Structural Analysis*, Wiesbaden, 2004.

[58] Weber B.: Simulation bei der Entwicklung von Fahrwerksregelsystemen. *NAFEMS Seminar: Mechatronics in Structural Analysis*, Wiesbaden, 2004.

[59] Papadopoulos E., Mu B., Frenette R.: Modeling and Identification of an Electrohydraulic Articulated Forestry Machine. *IEEE International Conference on Robotics and Automation*, Albuquerque, 1997.

[60] Guofu D., Zhonghyan Q., Shuangxia P.: Active Vibration Control of Excavator Working Equipment with ADAMS. *North American ADAMS User Conference*, Orlando, 2000.

[61] Bianchi G., Fassi I., Tosatti L. M.: A Virtual Prototyping Environment for Parallel Kinematic Machine Analysis and Design. *European ADAMS User Conference*, Rome, 2000.

[62] Deeken M.: Simulation of the Tribological Contacts in an Axial Piston Machine. *O+P Ölhydraulik und Pneumatik 47 Nr. 11-12*, 2003.